EX VIVO INVESTIGATION OF IRON HANDLING IN THE BRAIN

Sinead Healy

Galway Neuroscience Centre

College of Science

National University of Ireland, Galway

A thesis submitted to the National University of Ireland, Galway in fulfilment of the requirement for the Degree of Doctor of Philosophy

November 2016

DECLARATION

This dissertation is the result of my own work and includes nothing, which is the outcome of work done in collaboration except where specifically indicated in the text. It has not been previously submitted, in part or whole, to any university of institution for any degree, diploma, or other qualification.

Signed:_____

Date:_____

Sinead Healy, MSc, BSc
NUI Galway

ABSTRACT

Aberrant iron deposition in the brain is associated with aging and neurodegenerative disorders including multiple sclerosis, Alzheimer's disease and Parkinson's disease. It is unclear whether metabolic dyshomeostasis of iron is causative or is a consequence of brain pathology. An improved understanding of the mechanisms underlying iron handling might yield critical information relevant to neurodegenerative disease. The main focus of this work was to establish, validate and characterise a novel *ex vivo* model of iron loading. Having characterized and validated the iron homeostasis system in *ex vivo* cultures, compared with postnatal and adult tissue, we demonstrated differential uptake and toxicity of iron after 12 h exposure to 10 μM ferrous ammonium sulphate, ferric citrate or ferrocene. Having established the supremacy of ferrocene in this model, the cultures were then loaded with 0.1–100 μM ferrocene for 12 h. One μM ferrocene exposure produced the maximal 1.6-fold increase in iron compared with vehicle. This was accompanied by a 1.4-fold increase in ferritin transcripts and mild toxicity. Using dual-immunohistochemistry, we detected ferritin in oligodendrocytes, microglia, but rarely in astrocytes and never in neurons in iron-loaded slice cultures. At a transcript level, we also detected modest increases in the expression of several import molecules while the export molecules remained unchanged. Moreover, iron loading led to a 15% loss of OLIG2-positive cells and a 16% increase in number and greater activation of microglia compared with vehicle. However, there was no appreciable effect of iron loading on astrocytes. The development of such a model, which enables the study of inter- and intra-cellular iron movement and the cellular basis of iron-induced pathology within the complex brain milieu equips researchers with an improved platform to comprehensively study the intricate iron handling system. Indeed, we used this model to preliminarily study the putative intersection between iron metabolism and the unfolded protein response in the CNS. In the iron-loaded slice cultures there were modest increases in transcripts of chaperones and transcription factors associated with the UPR. Moreover, we found that concurrent activation of the unfolded protein response leads to the amelioration of iron accumulation and the resulting toxicity and glial perturbations seen following iron-loading. Finally, given that critical role of image analysis is this work, we critically appraised image segmentation algorithms to the develop, optimize and validate an image analysis workflow for handling the complex micrographs of glial immunohistochemistry acquired from thick 3D *ex vivo* hippocampal slice cultures.

ACKNOWLEDGEMENTS

I would like to thank many of the special people who assisted me through the completion of the thesis. First, I would like to sincerely acknowledge the support, guidance and encouragement that I have received throughout the last few years from my supervisor, Dr. Una FitzGerald. I would also like to express my deepest gratitude to my co-supervisor Dr. Jill McMahon who has been a wonderful mentor, advisor and friend, all in one, and for her constant assistance that was indispensable for my research work (not to mention her critical contribution to the many unnecessary font and color design decisions for each and every poster and presentation!). To my GRC, thank you all for your suggestions and advice during the course of my studies.

I wish to express my gratitude to Michelle Naughton for her assistance, support, and friendship. My time in the lab would not have been the same without her. Thanks also to all the other members of the lab, both past and present, for their help and support – Mary Ni Fhlathartaigh, Alan Hoban, Sravanthi Rao and Enrico Bagnoli. An extended thanks to everyone in 1 North Wing who had to endure some loud and long conversations and games in the office. Special thanks to Adriona Kelly and James Britton (friends and desk neighbours), who on top of this behaviour, also put up with my selfish tendency to steal and use their chairs for footrests. Thanks also to Vaibhav Patil and Azim Patar, who have been helpful and supportive in managing and organizing tissue preps between us all. And also to the many individuals in the Biomedical Sciences building who were kind enough to help along the way, thank you!

To my fantastic family, I can't thank you enough for encouraging me to do what I wanted. Without your love and support, this journey would have been impossible. Also, my friends deserve a mention here too, for all the support and kindness they have shown me through this time, including my housemate, Alan Kirwan, who, in particular, had to put up with the trials and tribulations of my thesis writing phase at home.

I would also like to acknowledge Kayla Friedman and Malcolm Morgan of the Centre for Sustainable Development, University of Cambridge, UK for designing the Microsoft Word thesis template used to produce this document that made my life much simpler!

CONTENTS

1 GENERAL INTRODUCTION 1

1.1 IRON 1

1.2 IRON LOCALIZATION IN THE BRAIN 1

1.3 IRON MANAGEMENT IN THE BRAIN 2

1.4 CONSIDERATIONS FOR DESIGNING *IN VITRO*/*EX VIVO* IRON LOADING EXPERIMENTS 9

1.4.1 Reagents 9

1.4.2 Iron Concentration 11

1.4.3 Addition of serum and ascorbate 12

1.4.4 Iron Measurement 15

1.5 SUITABILITY OF *IN VITRO* AND *EX VIVO* MODELS FOR IRON LOADING STUDIES 17

1.5.1 Primary cell studies 17

1.5.2 Studies with cell lines of neurons, microglia and oligodendrocytes 18

1.5.3 Ex vivo slice cultures 19

1.6 DIFFERENTIAL IRON ACCUMULATION AND TOXICITY IN CULTURED CNS CELLS 20

1.7 IMPORTANCE AND RELEVANCE OF *EX VIVO* IRON LOADING MODELS 22

1.8 THE ENDOPLASMIC RETICULUM 28

1.9 UNFOLDED PROTEIN RESPONSE 28

1.9.1 Pathway overview 29

1.9.2 BiP 31

1.9.3 CHOP 31

1.10 UPR CROSSTALK WITH IRON METABOLISM 33

1.11 IRON, UPR AND NEURODEGENERATIVE DISEASE 33

1.11.1 Multiple Sclerosis 34

1.11.2 Alzheimer's disease 35

1.12 HYPOTHESIS AND AIMS 37

2 MATERIALS AND METHODS 38

2.1 MATERIALS 39

2.2 TISSUE CULTURE 41

2.2.1 Animals 41

2.2.2 Slice Culture Preparation and Maintenance 41

2.3 TISSUE CULTURE TREATMENTS 43

2.3.1 Iron Loading 43

2.3.2 UPR Activation 43

2.4 IRON DETECTION 44

2.4.1 Ferrozine Assay *44*
2.4.2 Bradford *44*
2.5 VIABILITY ASSAYS 45
2.5.1 LDH Assay *45*
2.5.2 MTT *45*
2.6 RNA EXPRESSION ANALYSIS 46
2.6.1 RNA extraction *46*
2.6.2 DNase treatment and cDNA synthesis *46*
2.6.3 Real time PCR *47*
2.6.4 Data Analysis of Gene expression *48*
2.6.5 Primers *48*
2.7 IMMUNOHISTOCHEMISTRY 52
2.8 IMAGE ACQUISITION AND PROCESSING 54
2.8.1 Image Acquisition *54*
2.8.2 Image Analysis *54*
2.8.3 Image Analysis Methodology Validation *56*
2.9 STATISTICAL ANALYSIS 57
3 CHARACTERISATION AND COMPARISON OF THE IRON HOMEOSTASIS MOLECULES IN NEONATAL AND *EX VIVO* BRAIN 58
3.1 INTRODUCTION 59
3.2 AIMS: 60
3.3 SUMMARY OF METHODOLOGY 60
3.4 RESULTS 61
3.4.1 Primer Optimisation *61*
3.4.2 Levels of iron in cultured slices are representative of those found in vivo *62*
3.4.3 Expression of iron storage transcriots in the developing hippocampus *62*
3.4.4 Expression of iron homeostasis transcripts in the developing rat hippocampus *64*
3.4.5 Expression of iron homeostasis transcripts in the developing rat cerebellum *68*
3.4.6 Homogeneous expression of iron homeostasis molecules detected in P10 CNS .. *71*
3.5 DISCUSSION 75
3.6 CONCLUSION 78
4 GLIAL ALTERATIONS IN RESPONSE TO IRON LOADING IN A NOVEL *EX VIVO* HIPPOCAMPAL SLICE MODEL 79
4.1 INTRODUCTION 80
4.2 AIMS OF THIS STUDY 80

4.3 SUMMARY OF METHODOLOGY 81
4.4 RESULTS 81
4.4.1 Iron Reagent Comparison 81
4.4.2 One µM ferrocene exposure leads to maximal iron accumulation 83
4.4.3 Optimisation of antibodies 85
4.4.4 Ferritin accumulates in oligodendrocytes and microglia 88
4.4.5 Real-time PCR analysis of transcript of iron homeostasis molecules 88
4.4.6 Iron loading alters the cellular expression of export and import molecules 92
4.4.7 Iron loading alters number and morphology of glial cells 92
4.5 DISCUSSION 99
4.6 CONCLUSION 104
5 IRON METABOLISM AND THE UPR IN THE CNS 105
5.1 INTRODUCTION 106
5.2 AIMS 106
5.3 SUMMARY OF METHODOLOGY 107
5.4 RESULTS 108
5.4.1 Impact of iron loading on the UPR 108
5.4.2 Impact of the UPR on iron metabolism 110
5.4.3 UPR activation prevents ferrocene-induced iron accumulation and glial perturbations 113
5.4.4 Glial morphology 119
5.5 DISCUSSION 122
5.6 CONCLUSION 124
6 EVALUATION OF BINARISATION ALGORITHMS FOR IMAGE ANALYSIS OF GLIAL CELLS IN *EX VIVO* SLICE CULTURES 125
6.1 INTRODUCTION 126
6.2 AIMS OF THIS STUDY 127
6.3 SUMMARY OF METHODOLOGY 127
6.4 RESULTS 129
6.4.1 Qualitative evaluation of image presentation approaches for representing the z-stack data of astrocyte, oligodendrocyte and microglial staining in slice cultures 129
6.4.2 Qualitative visual evaluation of binarisation output of MIP IHC 131
6.4.3 Quantitative evaluation of algorithm binarisation of astrocyte images 134
6.4.4 Quantitative evaluation of algorithm binarisation of oligodendrocyte images 139
6.4.5 Quantitative evaluation of algorithm binarisation of microglia 143

6.5 DISCUSSION 147
6.6 CONCLUSION 152
7 DISCUSSION 153
7.1 DISCUSSION 154
7.2 CONCLUDING REMARKS 163
7.3 FUTURE PERSPECTIVES 163
8 REFERENCES 165

LIST OF TABLES

TABLE 1.1 PRESENCE OF IRON AND PROTEINS RELATED TO IRON METABOLISM IN BRAIN CELLS 7

TABLE 1.2 COMMON IRON REAGENTS ADDED TO *IN VITRO* SYSTEMS 14

TABLE 1.3 IRON LOADING IN ASTROCYTES 23

TABLE 1.4 IRON LOADING STUDIES IN PRIMARY NEURONS 24

TABLE 1.5 IRON LOADING STUDIES IN PRIMARY MICROGLIA 25

TABLE 1.6 IRON LOADING STUDIES IN OLIGODENDROCYTE-LINEAGE CELLS (PRIMARY AND CELL LINE) 26

TABLE 1.7 IRON LOADING STUDIES IN MIXED AND CO-CULTURES 27

TABLE 1.8 IRON AND ACTIVATED UPR IN NEURODEGENERATIVE AND NEUROINFLAMMATORY DISEASE 36

TABLE 2.1 PRIMER DETAILS FOR GENES ANALYSED BY REAL-TIME PCR 51

TABLE 2.2 ANTIBODY SOURCE AND DILUTION USED FOR IMMUNOHISTOCHEMISTRY 53

TABLE 3.1 OPTIMISATION OF PRIMERS THAT WERE USED IN THIS STUDY 61

TABLE 5.1 PUTATIVE BINDING SITES OF UPR TRANSCRIPTION FACTORS IN IRON HOMEOSTASIS MOLECULES 111

TABLE 6.1 SUB-DIVISION OF GLOBAL AUTO-THRESHOLD ALGORITHM BY METHODOLOGY 129

LIST OF FIGURES

FIGURE 1.1: SCHEMATIC OF IRON HOMEOSTASIS SYSTEM IN CNS CELLS. 6

FIGURE 1.2: SCHEMATIC OF THE UNFOLDED PROTEIN RESPONSE SIGNALING PATHWAY. 32

FIGURE 2.1: SLICE CULTURE PREPARATION. 42

FIGURE 2.2: DETECTION OF TOTAL IRON CONTENT BY COLORIMETRIC ASSAY..... 44

FIGURE 2.3: STANDARD CURVE. REPRESENTATIVE GRAPH DEPICTING THE 5-POINT STANDARD CURVE OF 10-FOLD DILUTION SERIES FOR FTL 49

FIGURE 2.4: PCR MELT CURVE. REPRESENTATIVE GRAPH OF THE MELT CURVE OF A GENE PRODUCT..... 50

FIGURE 3.1: BASAL IRON CONTENT COMPARISON WITH PUBLISHED VALUES..... 62

FIGURE 3.2: COMPARISON OF IRON AND IRON HANDLING PROTEINS IN *EX VIVO* SLICE CULTURES AND AGE-EQUIVALENT IN VIVO TISSUE 63

FIGURE 3.3: IRON CONTENT, AND GENE EXPRESSION OF IRON STORAGE MOLECULES IN THE DEVELOPING POSTNATAL RAT HIPPOCAMPUS..... 65

FIGURE 3.4: GENE EXPRESSION OF IRON IMPORTERS IN THE DEVELOPING RAT HIPPOCAMPUS .. 66

FIGURE 3.5: GENE EXPRESSION OF IRON EXPORTERS IN THE DEVELOPING RAT HIPPOCAMPUS . 67

FIGURE 3.6: GENE EXPRESSION OF IRON STORAGE MOLECULES IN THE DEVELOPING POSTNATAL RAT CEREBELLUM..... 68

FIGURE 3.7: GENE EXPRESSION OF IRON IMPORTERS IN THE DEVELOPING POSTNATAL RAT CEREBELLUM..... 69

FIGURE 3.8: GENE EXPRESSION OF IRON EXPORTERS IN THE DEVELOPING POSTNATAL RAT CEREBELLUM..... 70

FIGURE 3.9: IRON CONTENT, AND GENE EXPRESSION OF IRON STORAGE MOLECULES THROUGHOUT P10 BRAIN 72

FIGURE 3.10: GENE EXPRESSION OF IRON IMPORTERS THROUGHOUT P10 BRAIN 73

FIGURE 3.11: GENE EXPRESSION OF IRON EXPORTERS THROUGHOUT P10 BRAIN 74

FIGURE 4.1: TEN μM IRON REAGENT COMPARISON 82

FIGURE 4.2: ONE μM IRON REAGENT COMPARISON.....83

FIGURE 4.3: ONE MM FERROCENE PRODUCED MAXIMAL IRON ACCUMULATION. 84

FIGURE 4.4: REPRESENTATIVE SINGLE-PLANE CONFOCAL IMAGES DEMONSTRATING THE OPTIMISED FLUORESCENT STAINING OF CELL SPECIFIC MARKERS IN ORGANOTYPIC HIPPOCAMPAL SLICE CULTURES. 86

FIGURE 4.5: OPTIMISATION OF IMMUNOHISTOCHEMICAL DETECTION OF IRON HANDLING MOLECULES IN ORGANOTYPIC HIPPOCAMPAL SLICE CULTURES 87

FIGURE 4.6: DUAL IMMUNOFLUORESCENT DETECTION OF FERRITIN EXPRESSION IN CNS CELLS IN VEHICLE AND IRON-LOADED SLICE CULTURES 90

FIGURE 4.7: PCR ANALYSIS OF IRON HANDLING MOLECULES**ERROR! BOOKMARK NOT DEFINED.**

FIGURE 4.8: DUAL IMMUNOFLUORESCENT DETECTION OF DMT1 IN MICROGLIA IN VEHICLE AND IRON-LOADED SLICE CULTURES 93

FIGURE 4.9: DUAL IMMUNOFLUORESCENT DETECTION OF DMT1 IN OLIGODENDROCYTE-LINAGE CELLS IN VEHICLE AND IRON-LOADED SLICE CULTURES 94

FIGURE 4.10: DUAL IMMUNOFLUORESCENT DETECTION OF FERROPORTIN IN MICROGLIA IN VEHICLE AND IRON-LOADED SLICE CULTURES 95

FIGURE 4.11: COLOCALISATION ANALYSIS OF IRON MOLECULES WITH OLIGODENDROCYTES AND MICROGLIA. 96

FIGURE 4.12: EFFECT OF 1 MM FERROCENE LOADING ON THE NUMBER AND MORPHOLOGY OF MICROGLIA. 97

FIGURE 4.13: EFFECT OF 1 MM FERROCENE LOADING ON THE NUMBER AND MORPHOLOGY OF GLIAL CELLS 98

FIGURE 5.1: UPR CHAPERONE MRNA EXPRESSION IN IRON-LOADED SLICE CULTURES 108

FIGURE 5.2: UPR TRANSCRIPTION FACTOR MRNA EXPRESSION IN IRON-LOADED SLICE CULTURES. 109

FIGURE 5.3: ACTIVATION OF THE UPR. 112

FIGURE 5.4: EFFECT OF UPR ACTIVATION ON MRNA EXPRESSION OF IRON STORAGE MOLECULES. 112

FIGURE 5.5: EFFECT OF UPR ACTIVATION ON IRON LOADED SLICE CULTURES. 113

FIGURE 5.6: DUAL IMMUNOFLUORESCENT DETECTION OF CHOP IN OLIGODENDROCYTE-LINEAGE IN VEHICLE, IRON-LOADED AND UPR ACTIVATED SLICE CULTURES 115

FIGURE 5.7: DUAL IMMUNOFLUORESCENT DETECTION OF CHOP IN MICROGLIA IN VEHICLE, IRON-LOADED AND UPR ACTIVATED SLICE CULTURES 116

FIGURE 5.8: DUAL IMMUNOFLUORESCENT DETECTION OF ATF6 IN NUCLEI OF NEURONS AND GLIAL CELLS IN VEHICLE, IRON-LOADED AND UPR ACTIVATED SLICE CULTURES 117

FIGURE 5.9: DUAL IMMUNOFLUORESCENT DETECTION OF ATF6 IN OLIGODENDROCYTE-LINEAGE CELLS IN VEHICLE, IRON-LOADED AND UPR ACTIVATED SLICE CULTURES 118

FIGURE 5.10: EFFECT OF CONCURRENT UPR ACTIVATION AND IRON-LOADING ON THE NUMBER OF OLIG2-POSITIVE CELLS 120

FIGURE 5.11: EFFECT OF CONCURRENT UPR ACTIVATION AND IRON-LOADING ON THE NUMBER AND MORPHOLOGY OF MICROGLIA 120

FIGURE 6.1: BROCHER'S SEMI-QUANTITATIVE COLOUR-CODED EVALUATION OF SEGMENTATION COMPARING 16 GLOBAL AND 9 LOCAL AUTOTHRESHOLDING ALGORITHMS IN FIJI 128

FIGURE 6.2: QUALITATIVE EVALUATION OF THE AVAILABLE APPROACHES FOR IMAGE PRESENTATION OF GLIAL CELLS IN *EX VIVO* SLICE CULTURES 130

FIGURE 6.3: REPRESENTATIVE MAXIMUM INTENSITY PROJECTIONS AND SUBSEQUENT OUTPUT BINARISATION GENERATED FROM SINGLE USER-CHOSEN ARBITRARY NUMERICAL THRESHOLDS. 132

FIGURE 6.4: REPRESENTATIVE MAXIMUM INTENSITY PROJECTIONS AND SUBSEQUENT OUTPUT BINARISATION GENERATED FROM SINGLE USER-CHOSEN ARBITRARY NUMERICAL THRESHOLDS. 134

FIGURE 6.5: PERFORMANCE EVALUATION OF IMAGE SEGMENTATION ALGORITHMS ON Z-STACK MICROGRAPHS OF ASTROCYTES IN *EX VIVO* SLICE CULTURES 137

FIGURE 6.6: QUANTITATIVE ASSESSMENT OF THRESHOLD PERFORMANCE USING RELATIVE QUALITY, SPECIFICITY, ACCURACY AND SENSITIVITY PARAMETERS 138

FIGURE 6.7: PERFORMANCE EVALUATION OF IMAGE SEGMENTATION ALGORITHMS ON Z-STACK MICROGRAPHS OF OLIGODENDROCYTE-LINEAGE CELL NUCLEI 141

FIGURE 6.8: QUANTITATIVE ASSESSMENT OF THRESHOLD PERFORMANCE USING RELATIVE QUALITY, SPECIFICITY, ACCURACY AND SENSITIVITY PARAMETERS 142

FIGURE 6.9: PERFORMANCE EVALUATION OF IMAGE SEGMENTATION ALGORITHMS ON Z-STACK MICROGRAPHS OF IBA1 STAINING IN EX VIVO SLICE CULTURES 145

FIGURE 6.10: QUANTITATIVE ASSESSMENT OF THRESHOLD PERFORMANCE USING RELATIVE QUALITY, SPECIFICITY, ACCURACY AND SENSITIVITY PARAMETERS.....146

List of Abbreviations and Acronyms

AAS	atomic absorption spectroscopy
AD	Alzheimer's disease
AFU	arbitrary fluorescence units
APP	amyloid precursor protein
ATF6	activating transcription factor 6
BiP	B-cell immunoglobulin-binding protein
BS	brain stem
BSA	bovine serum albumin
CB	cerebellum
CHOP	CCAAT/enhancer binding protein (C/EBP)homologous protein
CNS	central nervous system
Cp	ceruloplasmin
CREBH	cyclic AMP response element-binding protein H
CRT	calreticulin
CSF	cerebrospinal fluid
CTX	cortex
DAPI	diamino-2-phenylindole
DMSO	dimethylsulfoxide
DMT1	divalent metal transporter 1
DYCTB	duodenal cytochrome B
EAE	experimental autoimmune encehalomyelitis
EIF2a	eukaryotic initiation factor 2a
ER	endoplasmic reticulum
ERAD	ER-associated dagradation
FAC	ferric ammonium citrate
FAS	ferrous ammonium sulphate
FBS	foetal bovine serum
Ferr	ferritin
ferric-NTA	ferric nitrilotriacetate
FPN	ferroportin
FS	ferrous sulphate

FTH	ferritin heavy chain
FTL	ferritin light chain
Fz	ferrozine assay
GADD 34	DNA damage-inducible protein 34
GFAP	glial fibrillary acidic protein
gpiCp	gpi-ceruloplasmin
HCP1	haem carrier protein 1
HD	Huntington's disease
HEPH	hephaestin
HO1	haemoxygenase 1
HSP	heat shock protein
IBA1	Ionized calcium binding adaptor molecule 1
IRE	iron regulatory elements
IRE1	inositol-requiring enzyme 1
IRP	iron regulatory protein
LA-ICP-MS	laser ablation inductively coupled plasma mass spectrometry
LDH	lactate dehydrogenase
Lf	lactoferrin
LfR	lactoferrin receptor
LIP	labile iron pool
MB	mid brain
Mf	melanoferrin
MIP	maximum intensity projection
MRI	magnetic resonance imaging
MS	multiple sclerosis
MtfR	melanotransferrin receptor
MtFt	mitochondrial ferritin
NTBI	non transferrin bound iron
OB	olfactory bulb
OL	oligodendrocyte
OLIG2	oligodendrocyte lineage transcription factor 2
OPC	oligodendrocyte percursor cell
PD	Parkinson's disease
PDI	protein disulphide isomerase

PERK	pancreatic ER kinase-like endoplasmic reticulum kinase
RER	rough ER
RFU	relative fluorescence units
SER	smooth ER
SXRF	Synchrotron x-ray fluorescence
Tf	transferrin
TfR	transferrin receptor
Tim2	T cell immunoglobulin and mucin domain 2
Tm	tunicamycin
TMH-ferrocene	3,5,5-trimethyl-hexanoyl ferrocene
UPR	unfolded protein response
UTR	untranslated region

1 General Introduction

1.1 Iron

Iron is one of the most abundant metals, not just on Earth but found throughout the universe on the sun and many stars, and is essential to nearly all known life forms from the very first organisms with the exception of some bacteria (Sheftel et al. 2012). This potentially toxic transition metal, its regulation and functioning, is critical for the body and in the brain. There are approximately 3-5 grams of iron in the human body (Salvador 2010), which is equivalent to the amount of iron in a 3-inch nail, and this iron is located primarily in hemoglobin (70%) and ferritin stores in cells throughout the body (25%) (Gaasch et al. 2007). The remainder is found within proteins facilitating the metabolic energy needs of the body e.g. cellular respiration and DNA repair and synthesis (Núñez et al. 2012; Crichton et al. 2011; Todorich et al. 2009; Hallgren & Sourander 1958). Proper maintenance of these iron levels is critical and disturbed iron homeostasis poses a considerable threat to cells and tissues and is, indeed, associated with numerous diseases (Núñez et al. 2012; Crichton et al. 2011; Todorich et al. 2009; Hallgren & Sourander 1958).

1.2 Iron localization in the brain

Iron, an abundant metal in the brain, is indispensable for normal central nervous system (CNS) function, being a crucial cofactor for enzymes involved in neurotransmitter synthesis, energy metabolism, myelin production, oxygen transport, DNA synthesis and repair, and respiratory activity (Núñez et al. 2012; Crichton et al. 2011; Todorich et al. 2009; Hallgren & Sourander 1958). The redox-active nature of iron means that it can generate free radicals via the Fenton reaction and cause tissue damage if not properly managed. The CNS is particularly sensitive to damage caused by reactive oxygen species that are generated from redox reaction for several reasons (Molina-Holgado et al. 2007). There is high oxygen consumption per unit mass, high polyunsaturated fat content in the form of myelin, a high metabolic production of hydrogen peroxide and a relatively high concentration of iron in different regions (Hallgren & Sourander 1958). Therefore, iron metabolism requires a tightly-controlled regulatory system to minimize potential deleterious effects without compromising availability for essential cellular functions. Consequently, neurons, astrocytes, microglia and oligodendrocytes are all equipped with different sets of iron-related molecules to manage iron levels. A detailed description of these molecules, including their function and location, is provided in the next section.

1.3 Iron management in the brain

Neurons, astrocytes, oligodendrocytes and microglia each express distinctive profiles of iron regulatory proteins (Fig. 1.1 and Table 1.1) with each cell type having different proteins responsible for uptake, storage, use and export of iron. The amount of each protein expressed varies greatly depending on the cell type and its iron status, brain region, developmental age, detection method and species. Iron regulation, in general, has already been comprehensively reviewed (R. Ward et al. 2014; Crichton et al. 2011; Rouault 2013). Provided here is a brief overview of the cellular iron homeostasis machinery acting to prevent iron mismanagement with the CNS.

In cerebrospinal fluid (CSF) and brain interstitial fluid, iron exists in both ferric (Fe^{3+}) and ferrous (Fe^{2+}) forms. In its ferric state, iron is predominantly complexed to transferrin but can also bind lactoferrin (Lf) and melanotransferrin (Mf), additional members of the transferrin family, and also ferritin (Qian & Shen 2001; Moos et al. 2007; Jiang et al. 2016). Indeed, given the low concentration of transferrin and iron normally present in the brain interstitial fluid, the binding capacity of transferrrin (Tf) is usually saturated meaning that this excess of non-transferrin bound iron (NTBI) binds low molecular weight complexes like ascorbate, citrate and ATP (Hare, Ayton, et al. 2013; Gaasch et al. 2007; Lane & Richardson 2014; R. Ward et al. 2014). NTBI can exist in both ferrous and ferric forms depending on the microenvironment and availability of ferric reductases, such as duodenal cytochrome B (DCYTB) present on astrocytes. Although CNS cells are provided with both transferrin and non-transferrrin-bound iron as potential sources of iron, these sources are not necessarily available to a particular cell depending on the iron uptake proteins present.

There are several potential routes for iron uptake (Figure 1.1). Divalent metal transporter 1 (DMT1) and the transferrin receptor (TfR) are responsible for ferrous and ferric iron uptake, respectively, and are differentially expressed in each cell type and between anatomical brain regions. Transferrin receptors are present in neurons and oligodendrocyte precursor cells, absent in microglia and irregular in astrocytes and oligodendrocytes, whereas DMT1 is found in neurons, astrocytes, microglia and weakly/rarely in oligodendrocytes (Siddappa et al. 2002; Song et al. 2007; Moos et al. 2000; Burdo et al. 2001; Moos 1996; Kaur & Ling 1995; Connor & Menzies 1995). Conversely, T cell immunoglobulin-domain and mucin domain protein2 (tim-2,) a ferritin receptor, is exclusively expressed on oligodendrocytes (Todorich et al. 2008;

Schulz et al. 2011) and the melanotransferrin receptor has been found only on microglia in the brain of Alzheimer's disease sufferers (Jefferies et al. 1996). In addition, HCP1, which transports haem as an intact metalloporphyrin with iron, has been found to be expressed on cultured neurons and astrocytes (Dang et al. 2011; Dang et al. 2010). In the cytosol, inducible haem-oxygenase 1 (HO-1) degrades this metalloporphyrin to bilirubin, thereby releasing iron. Finally, extracellular iron-binding glycoproteins, such as lactoferrin and melanotransferrin, mentioned above, can contribute to iron uptake in cells (Fillebeen et al. 2001; Kawamata et al. 1993; An et al. 2009; Jefferies et al. 1996) but the contributions of these proteins to brain iron metabolism remains to be elucidated in more detail.

After uptake, iron may be stored, used or exported (Figure 1.1). Although detected in all cell types, oligodendrocytes are the predominant iron-positive cells in the normal human brain (Connor & Menzies 1990). Iron is safely stored in a ferritin shell, comprising ferritin heavy- and/or light-chain subunits depending on cell type and region in question. Oligodendrocytes have the highest level of ferritin and express both heavy- and light-chain subunits (Han et al. 2002; Cheepsunthorn et al. 1998; Zecca et al. 2004). In contrast, neurons and astrocytes have much less, if any, detectable ferritin under normal conditions and they express only ferritin heavy-chain and light chain, respectively (L. Wang et al. 2011; Snyder et al. 2010; Connor & Benkovic 1992; Connor et al. 1990). Like astrocytes, microglia express only ferritin light-chain (Connor et al. 1990; Simmons et al. 2007). These cytosolic ferritin chains have different functions: the heavy-chain has ferroxidase activity and catalyses the rapid oxidation of Fe^{2+} to Fe^{3+}, whereas the light-chain is more efficient at iron storage (Friedman et al. 2011; Finazzi & Arosio 2014). Moreover, mitochondrial ferritin, the third and most recently identified ferritin, has been demonstrated in neurons and oligodendrocytes (L. Wang et al. 2011; Snyder et al. 2010; Zecca et al. 2004). Like ferritin heavy-chain, mitochondrial ferritin has ferroxidase activity but its primary function is thought to be protection against iron-dependent oxidative injury (Santambrogio et al. 2007; Snyder et al. 2010; Jeong et al. 2009).

Excess iron, i.e. iron that is not recruited into cellular functions, sequestered in ferritin or comprising the cytosolic labile iron pool (LIP), can be transported from the cell so that normal iron levels are maintained. Ferroportin, which is the only known iron exporter, releases only ferrous iron (Wu et al. 2004; Schulz et al. 2011; Boserup et al. 2011; J. Wang et al. 2007). It is assisted in this function by associated ferroxidases (hephaestin and/or gpi-ceruloplasmin; heph and gpiCp) (Møllgård et al. 1988; Gebril et al. 2011; J. Wang et al. 2007; Schulz et al. 2011). Amyloid precursor protein (APP) has also been

reported to have ferroxidase activity and assist in iron export via ferroportin (Duce et al. 2010; Skaper et al. 2009). Conversely, the iron-regulatory hormone hepcidin (expressed in each cell type and secreted into interstitial fluid) prevents iron release via this route by causing internalization and degradation of ferroportin (FPN) (Qian et al. 2014; Raha et al. 2013).

By altering the expression levels of iron-related molecules, cells control the amount of iron acquired, used, sequestered and exported. Cytoplasmic RNA binding proteins, known as the iron regulatory proteins (IRP1 and IRP2), are expressed by each cell type (Siddappa et al. 2002; Huang et al. 2006). Under low iron conditions, IRPs bind to iron regulatory elements (IREs; characteristic stem and loop structures of some mRNAs). IRPs prevent mRNA translation by binding to IREs at the 5'-untranslated region (UTR) and allow translation by binding 3'-UTR and stabilising mRNA (R. Ward et al. 2014; Crichton et al. 2011; Rouault 2013). In addition to this IRE/IRP post-transcriptional regulation, ferroportin expression is also regulated at a post-translational level by hepcidin internalization of ferroportin. Moreover, hepcidin has been shown to reduce brain iron content in iron-overloaded rats and to decrease the expression of TfR1, DMT1 and ferroportin in cultured neurons and astrocytes (Du et al. 2011; Du et al. 2014). Interestingly, a hepcidin-independent internalization has also been described (D. M. Ward & Kaplan 2012).

Furthermore, this iron regulatory system matures throughout postnatal development. Notably, iron is stored in microglia early in postnatal development before the role, reportedly, being taken over by oligodendrocytes during maturation (Connor & Menzies 1995; Cheepsunthorn et al. 1998). Iron, transferrin and ferritin are found at their highest concentrations at birth and thereafter decrease steadily during the first three weeks of life (Roskams & Connor 1994; Y. Li et al. 2013; Siddappa et al. 2002). On the other hand, there is increased expression of DMT1, IRP1 and IRP2 in hippocampal neurons during this timeframe (Siddappa et al. 2002). Transferrin receptors, however, which are undetectable in microglia in older rats, are strongly expressed in amoeboid microglia during the first two postnatal weeks (Kaur & Ling 1995). Similarly, transferrin receptor, which is consistently and highly expressed in oligodendrocyte precursor cells, is apparently downregulated in maturing oligodendrocytes with minimal, if any, expression noted in mature oligodendrocytes *in vivo* (Leitner & Connor 2012; Todorich et al. 2009). However, increased expression of transferrin receptor and ferritin heavy-chain in the grey matter of human brain has been reported (Hulet et al. 1999).

Substantial details about intricate iron homeostasis machinery, as summarised here, have been gleaned from research on post-mortem human brain, *in vitro* and *in vivo* studies (Table 1.1) and has provided considerable insight into these processes in health and disease (section 1.11). Nevertheless, there are still evident gaps in information and some discrepancies that need to be clarified. For instance, although astrocytes and neurons have recently been reviewed in detail with regard to iron (Dringen et al. 2007; Salvador 2010), much less attention has been given to oligodendrocytes and microglia despite the crucial roles these cells play in iron handling (Schulz et al. 2011; Zhang et al. 2006; Todorich et al. 2009) and. Well-designed *in vitro* or *ex vivo* model systems will be essential if these unresolved details are to be considered (section 1.14).

Although histochemical analyses of post-mortem brain samples and MRI studies provide information regarding the location of iron deposition, these methods cannot be readily used to address iron movement and on-going damage at a cellular level, and they are not easily quantifiable. Moreover, the majority of post-mortem brains studied are from patients who have undergone treatment; findings from these studies only give an insight into the drug-treated and entrenched disease state, leaving the interpretation of results complex and limited. For instance, L-DOPA treatment in patients with Parkinson's disease has been shown to result in increased CSF ceruloplasmin (Boll et al. 1999), whereas L-DOPA treatment *in vitro* increased DMT1 expression (Chang et al. 2005). Such findings highlight the importance of designing and utilising an appropriate model system so that a clear picture of iron handling might be described. To this end, a number of studies have exploited *in vitro* and *in vivo* models in conjunction with, or as an alternative, to investigation of the human brain, in order to investigate iron handling in the context of neurodegeneration. In the next section, the details and critical parameters of these *in vitro* studies will be systematically reviewed, while a detailed account of iron metabolism in neurodegeneration is given later in section 1.11.

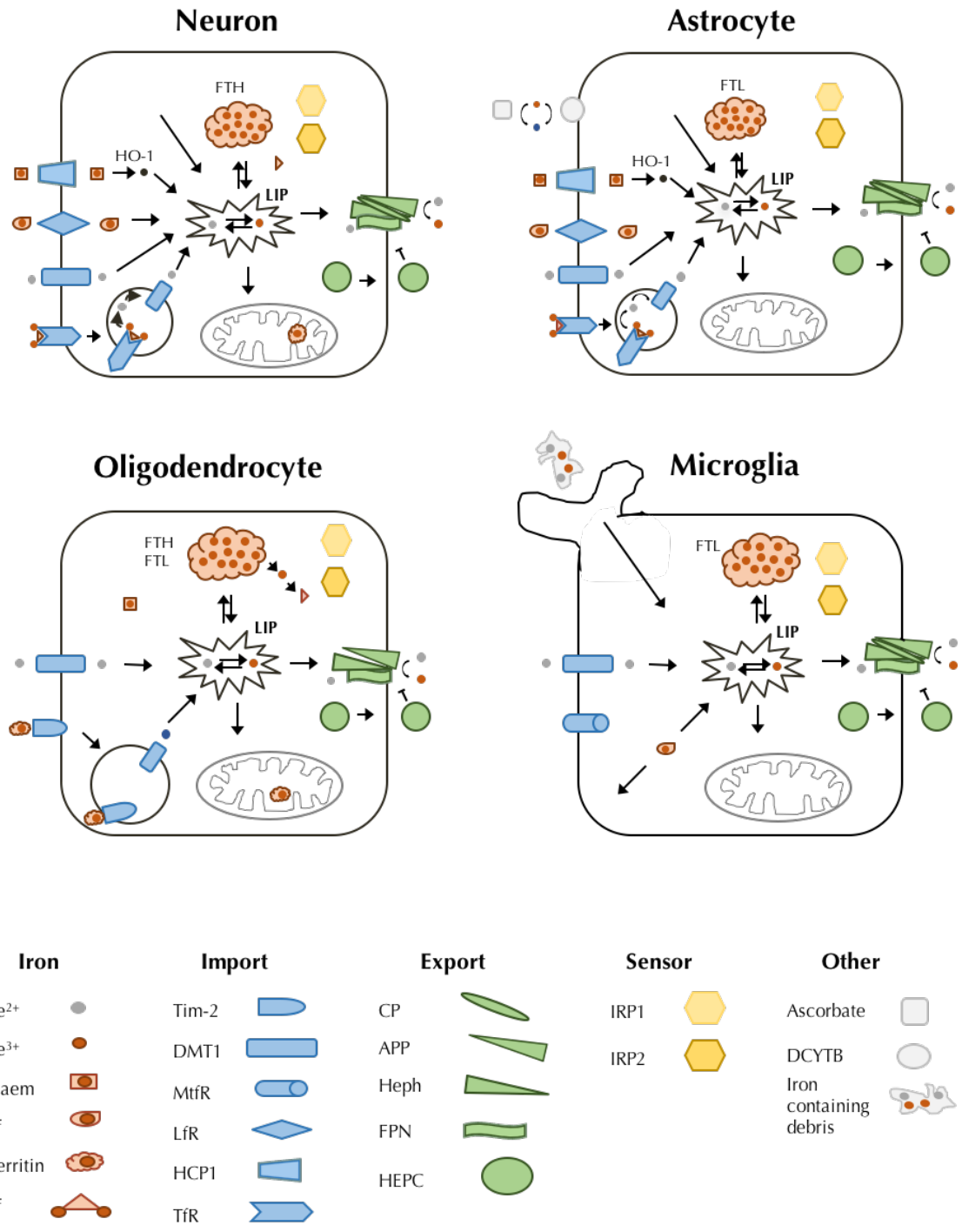

Figure 1.1: Schematic of iron homeostasis system in CNS cells. Neurons, astrocytes, oligodendrocytes and microglia each express a distinctive profile of iron related proteins for the management of cellular iron homeostasis. This tightly controlled regulatory system ensures toxic accumulation is limited without compromising the availability of iron for cellular needs and is perturbed in neurodegenerative disease. Abbreviations: APP, amyloid precursor protein; Cp, ceruloplasmin; DCYTB, duodenal cytochrome B; DMT1, divalent metal transporter, Fe^{2+}, ferrous iron; Fe^{3+}, ferric iron; FPN, ferroportin; FTH, ferritin heavy chain; FTL, ferritin light chain; FtMt, mitochondrial ferritin; HEPC, hepcidin; Heph, hephaestin; HO-1, haem-oxygenase 1; IRP1, iron regulatory protein 1; IRP2, iron regulatory protein 2; Lf, lactoferrin; LfR, lactoferrin receptor; transferrin, Tf; TfR, transferrin receptor. Image source: Sinead Healy.

Table 1.1 Presence of iron and proteins related to iron metabolism in brain cells

Function	Protein	Neurons		Astrocytes		Oligodendrocytes		Microglia	
		In vitro	*In vivo*	*In vitro*	*In vivo*	*In vitro*	*In vivo*	*In vitro*	*In vivo*
Export	FPN	5,6,12,13,14,15	16,17,19,20,21	8,12,22,23	16,17,21 19	17	16 **C** [17,19,21]	12, 22	21 19
	GPI-CP	24 25	25,26,27,28	22,23,25,29 24	18,25,26,27,28,30	**B** [17]	26	22	30
	HEPC	13 12	113,20,31,32	12	13,20		**E** [20]	12	13
	HEPH	5 17	21	17	21	**C** [17]	17, 21	17	21
	APP	15,33,34,35	36,37	33,34,35,38,39	36,37	34,40	36,37	35,38	37
Import	DMT1	6,12,14,41	7,18,42,43,46 **A** [44]	8,12,22,23,41,45	36,37		**A**[7,46 44] 43	11,12,22	43
	DCYTB			23,45	47				
	TfR1	6,14	7,48,61	49 23	7 **D**[48] 49,50	49,52,70 53	7 **D**[48] **F**[56] 51,54,56	**G**[11,57]	**G**[54] 51
	Tim2		58		58	58	17,58		
	HCP1	59		59					
	LfR	76	60		**A**[60]				
	Lf		17,58		**A**[63]		**A**[63]	76	62,64 **A**[63]
	MtfR		61		61		61		**H**[61]
Storage	Ferr	10	23	10,49	23	10	2	10	2,65
	FTL		66 48,67,68	8,22	48,66 **D**[67]	10	48,66,67,68,69	22	48,66,69
	FTH		48,67,68	22	66	10,70	66,67,68	22	48,66
	MtFt	71	71,72,72,74		72		73		
	Tf	52	**A**[2,26,44]	52	**A**[2] 3	10 75	2,3,48,75		2
Sensor	IRP1	5,6	7	8	7,9	10	7	11	9
	IRP2	6	7		7,9	10	7	11	9
Iron		1	2,3	1	**A**[2]	4	2	1	**A**[2]

*Presence confirmed (*green*); absence confirmed (*blue*); presence or absence not reported so far (pink). Notes:* [A] staining reported to be light/weak, and/or rare/inconsistent/sparse and sometimes only in curtained regions in aged/diseased brain; [B] cultured oligodendrocytes express Cp only at mRNA level and not protein level; [C] only present on mature oligodendrocytes; [D] highly expressed in the striatum but minimal expression in other regions; [E] Co-localised to MBP, which suggest hepcidin expression by oligodendrocytes in human brain and present on oligodendrocytes in APP-tg mice; [F] only detected in microglia in senile plaques in Alzheimer´s disease, [G] only present in early postnatal microglia; [H], confined to grey matter. *References:* 1 (Bishop et al. 2011); 2 (Connor et al. 1990); 3 (Connor & Benkovic 1992) 4 (Morath & Mayer-Pröschel 2001); 5 (Song et al. 2010); 6 (J. Wang et al. 2013); 7 (Siddappa et al. 2002); 8 (Zhang et al. 2013); 9 (Huang et al. 2006); 10 (Hoepken 2005); 11 (Rathnasamy et al. 2011); 12 (Urrutia et al. 2013) 13 (Qian et al. 2014); 14 (Du et al. 2009); 15 (Wong et al. 2014); 16 (Wu et al. 2004); 17 (Schulz et al. 2011); 18 (L. Li et al. 2011) 19 (Boserup et al. 2011) 20 (Raha et al. 2013) 21 (J. Wang et al. 2007); 22 (Rathore et al. 2012); 23 (Jeong 2003); 24 (Hare et al. 2012); 25 (Klomp et al. 1996); 26 (Møllgård et al. 1988); 27 (Loeffler et al. 1996); 28 (Hwang et al. 2004); 29 (B. N. Patel 1997); 30 (Gebril et al. 2011) 31 (Zechel et al. 2006) 32 (Sun et al. 2012) 33 (Rohan de Silva et al. 1997); 34 (Mizuguchi et al. 1992); 35 (LeBlanc et al. 1991); 36 (Mita et al. 1989); 37 (Schmechel et al. 1988); 38 (Haass et al. 1991); 39 (Gray & A. J. Patel 1993) 40 (Skaper et al. 2009); 41 (Pelizzoni et al. 2012); 42 (Huang et al. 2004); 43 (Song et al. 2007); 44 (Moos et al. 2000); 45 (Tulpule et al. 2010); 46 (Burdo et al. 2001) 47 (Loke et al. 2013); 48 (Connor & Menzies 1995); 49 (Hoepken et al. 2004); 50 (Jeong 2006); 51 (Moos 1996); 52 (de Los Monteros et al. 1988); 53 (Todorich et al. 2009); 54 (Kaur & Ling 1995); 55 (Hulet et al. 1999) 56 (Hulet et al. 2002); 57 (Rathnasamy et al. 2014); 58 (Todorich et al. 2008); 59 (Dang et al. 2011); 60 (Faucheux et al. 1995); 61 (Jefferies et al. 1996); 62 (Fillebeen et al. 2001); 63 (Kawamata et al. 1993); 64 (An et al. 2009); 65 (Simmons et al. 2007) 66 (Han et al. 2002) 67 (Cheepsunthorn et al. 1998); 68 (Zecca et al. 2004); 69 (Lopes et al. 2008); 70 (Y. Li et al. 2013); 71 (L. Wang et al. 2011); 72 (Jeong et al. 2009); 73 (Snyder et al. 2010); 74 (Santambrogio et al. 2007); 75 (Klomp et al. 1996) 76 (J. Wang et al. 2015)

1.4 Considerations for designing *in vitro*/*ex vivo* iron loading experiments

Various iron reagents have been added to *in vitro* systems (i.e. "iron-loading") to promote oxidative stress, toxicity, lipid peroxidation and iron accumulation (Table 1.2). Additionally, iron loading reagents, concentrations, exposure periods and experimental conditions have varied dramatically between studies, begging the question: what is the ideal (and/or consensus for) iron-loading paradigm for studying iron in the context of neurodegeneration? Each of these factors, in turn, will be evaluated below followed by a discussion on the suitability of in vitro and ex vivo models for iron loading studies in section 1.5.

1.4.1 Reagents

Table 1.2 summarizes the 9 different iron reagents that have been used in iron loading studies. These are: ferric ammonium citrate (FAC), ferric citrate, ferric nitrilotriacetate (ferric-NTA), ferrous sulfate, ferrous ammonium sulfate (FAS), ferrous chloride, ferric chloride, ferrocene and 3,5,5-trimethyl-hexanoyl ferrocene (TMH-ferrocene).

Ferric (Fe^{3+}) iron, typically present as ferric ammonium citrate (FAC) or ferric chloride, tends to be the preferred choice of reagent for iron-loading in primary astrocyte cultures. However, FAC loading under similar experimental conditions in different studies has been shown to produce substantial discrepancies in the extent of iron accumulation. For instance, primary astrocytes loaded with 100 µM FAC for 24 h had increased iron content by 7-, 21 and 80-fold in three different studies (Hoepken et al. 2004; Riemer et al. 2004; Bishop et al. 2011). This criticism, of course, can be levelled at other iron reagents too and, indeed, might be partially accounted for by differing experimental conditions like ascorbate, serum and tissue source (see section 1.4.3). However, the other reagents do not seem to produce as much variability in iron accumulation between studies or, if they do, the concentration, cell type and/or exposure times do not match exactly and a direct comparison cannot be made. Ferric citrate is a particularly attractive reagent because citrate is a true physiological chelator of iron. In the interstitial fluid of the brain, iron binds to citrate and other small organic molecules like ATP or ascorbate and these complexes make up the physiological pool of non-transferrin bound iron (NTBI) (Gaasch et al. 2007). However, ferric citrate is not readily soluble in water or medium and can precipitate out of solution unless it is chelated to excess citrate at a ratio of 1.5 upwards (Brunner-Döpper et al. 1998). In HeLa cells, the maximum recommended citrate concentration is 50 µM thereby limiting iron

loading concentrations to those under 30 μM. The final ferric iron reagent, namely ferric-NTA, has also been used as an iron loading reagent but is less commonly chosen.

It is ferrous (Fe^{2+}) iron that participates in the Fenton reaction to produce free radicals and oxidative stress. Given that oxidative stress is associated with several neurodegenerative diseases, ferrous iron reagents are more likely to be a pathologically relevant sources of iron than ferric ammonium citrate or ferric citrate, which are much less likely to participate in the Fenton reaction. However, at neutral pH in culture medium, free ferrous iron is oxidized such that iron applied as ferrous sulfate, ferrous ammonium sulfate or ferrous chloride is likely to be rapidly oxidized to ferric iron. Therefore, ferrous iron must be maintained in its reduced state in medium by adding compounds such as ascorbate (see section 1.4.3).

A third, less common, option for iron-loading is ferrocene and its derivatives (Nielsen & Heinrich 1993). Ferrocene, unlike typical ferric and ferrous reagents, is lipophilic and readily crosses the cell membrane without engaging the rigorous iron regulatory system that acts to reduce uptake mechanisms under iron loading conditions. Previous studies in whole animals and in cultured hepatocytes have demonstrated that 3,5,5-trimethyl-hexanoyl-ferrocene (TMH-ferrocene) is bioavailable, chelatable and incorporated into ferritin. Furthermore, ferrocene iron loading recapitulates iron uptake patterns found in hemochromatosis (Cable & Isom 1999; Cable et al. 2007). Despite these appealing characteristics, ferrocene has gone largely unappreciated for *in vitro* CNS cell iron loading with the exception of several publications by the Connor research group. They reported that astrocytes pre-treated with TMH-ferrocene, but not FAS or FAC, were more susceptible to oxidative stress (Robb & Connor 1998) and have subsequently used this reagent for later iron loading studies.

Notably, Hohnholt et al. (2010) demonstrated that FAS, FAC or ferrous chloride exposure for 48 h equally increased iron content in OLN-93 cells. This was particularly evident at the 30 μM concentration. Exposure to 100 or 300 μM concentrations, however, produced ostensibly different cellular iron content between groups. These differences, however, were statistically insignificant, which suggests the iron source might not be important. However, it is crucial that the cells are capable of taking up the iron supplied. Todorich et al (2011), after demonstrating a loss in viability in transferrin-deprived OPCs, concluded that transferrin-deprived OPCs could not be rescued by FAC supplementation because FAC failed to prevent the loss in their viability; on the other hand, viability was not reduced in transferrin-deprived cells that were treated with the same molar concentration of membrane permeable TMH-ferrocene (Todorich et al. 2011). Since

astrocytes, microglia and mature oligodendrocytes generally do not express transferrin receptors (see section 1.3), and the existence of another ferric importer is not currently known, iron must be supplied to these cells in ferrous form. The case is different for astrocytes, which although not expressing transferrin receptors, have membrane-bound ferric reductases that can reduce ferric iron to the ferrous state and thereby allow the uptake of ferrous iron (from a ferric source) via DMT1. Moreover, in the brain, non-transferrin-bound iron is thought to be mainly ferrous rather than ferric because of the high concentration of extracellular ascorbate and the low level of ferroxidase activity (mainly ceruloplasmin) in the cerebrospinal fluid (Bradbury 1997; Lane et al. 2010; Lane & Richardson 2014)

1.4.2 Iron Concentration

Choosing a pathologically relevant iron concentration is another important consideration. Iron in the CSF, which is thought to be reflective of interstitial content, has been reported at low and variable concentrations i.e. 0.75±0.048, 0.29±0.72, 1.12±0.51, 0.55±0.27, 0.2-1.1, 0.01–0.1, 0.4-1.2, μM (Bradbury 1997; Núñez et al. 2012; Gaasch et al. 2007). However, values of free redox-active iron (rather than total iron) in the CSF are more consistent: 0.27±0.04, 0.55±27 and 0.3–0.75 μM (Lavados et al. 2008; Gaasch et al. 2007). Taken together, these values range from 0.01-1.2 μM and have mid-range value of approximately 0.6 μM. Consequently, any concentration above this value could be considered supraphysiological. Therefore, iron loading at 1.2, 6, 12 and 30 μM would represent 2-, 10-, 20- and 50-fold increase over normal CSF iron content, respectively, and could encompass the extracellular elevation of iron that cells might experience in neurodegenerative disease. Consistent with this, in Alzheimer's disease, iron content in plaques compared adjacent cortical tissue is about 1.6-fold higher (1 mM and 0.65 mM, respectively).

In the literature, a wide range of iron concentrations (0.1-1000 μM) has been used in iron loading experiments *in vitro* (Table 1.3-1.7*)*. However, most of these studies fail to explicitly justify how the iron loading concentration chosen relates to pathophysiological iron concentrations and, in some instances, are perhaps unlikely to accurately reflect realistic pathological concentrations. Moreover, the exposure time is also artificial; iron loading studies, which have ranged from acute to short-term (i.e 3 minutes to 48 hours), cannot accurately reproduce the chronic conditions underlying iron deposition and aberrations in neurodegenerative disease or aging. Indeed, Pelizzoni et al. (2011) explain that the high iron loading in their study (i.e. FAS concentration up to 100 μM for 3

minutes) was used for technical rather than physiological or pathological reasons, but propose such high concentrations might be probable in disease. Other studies may have used their demonstration of toxicity and iron accumulation *in vitro* as surrogate indicators for a pathologically relevant dose. Although these values vary between studies, reagents, exposure time and cell types, iron accumulation and toxicity reliably occur between 10-40 μM in all cells (excluding astrocytes, which do not seem to be susceptible to iron toxicity). Given the lack of studies assessing iron at lower concentrations, it is possible that iron might also be toxic at these lower concentrations. Conversely, several studies, such as Morath et al. (2001) have used iron loading to study oligodendrocyte development and proliferation rather than mimicking iron overload in disease and, as such, cannot necessarily be taken into consideration for determining a pathologically relevant iron dose.

1.4.3 Addition of serum and ascorbate

Two other important experimental conditions that are very variable between studies are the levels of serum and ascorbate added to culture medium (tables 1.3-1.7). Transferrin, which is present in serum, binds to supplemented iron. As a result, this transferrin-bound iron can only be imported into cells via transferrin receptor and this might limit or exclude the participation of transferrin-independent uptake mechanisms such as DMT1. On the other hand, the absence of serum (and therefore the absence of lactoferrin and melanotransferrin that are present in serum) might rule out the participation of the lactoferrin or melanotransferrin pathways. Both of these proteins have been suggested as potential routes of non-transferrin-bound-iron uptake and might be relevant in disease pathogenesis. It is also possible that transferrin expressing cells might release transferrin into the medium during experimental treatment and that ferric iron would bind the released transferrin and then be taken up via transferrin receptors.

Ascorbate supplementation is another important consideration. Ascorbate is abundant within brain tissue and plays a multi-faceted role in iron metabolism (Lane & Richardson 2014). Indeed, the rate of iron accumulation in cultured ascorbate-deficient astrocytes was shown to be only half that of ascorbate-replete astrocytes (Lane et al. 2010). Similarly, iron-induced cellular injury in ascorbate-deficient hippocampal cultures was also much less than in ascorbate-replete cultures (Zhang et al. 1993), suggesting that this ascorbate-deficiency (i.e. standard culture conditions) might not offer a physiologically relevant system for iron loading studies. Nevertheless, we note that most iron loading studies have been performed in ascorbate-deficient conditions.

Iron loading studies that have used ascorbate supplementation typically did so at a 1:44 molar ratio of iron to ascorbate to maintain iron in its ferrous state, often at the expense of sacrificing physiological ascorbate concentration i.e. 200– 400 µM in the extracellular fluid of the brain (Rice 1999). For instance, Tulpule et al. (2010) used 5 mM ascorbate supplementation, a concentration ten times higher than extracellular physiological ascorbate, ensuring that 90% of 100 µM FAC was maintained in a ferrous state for 5 hours. Conversely, Liu et al. (2003) treated organotypic slice cultures with 0.5 mM ascorbate and 200 µM ferrous sulfate, which is likely to have maintained basal ascorbate concentration near *in vivo* levels but meant that iron was present in the medium as both ferric and ferrous forms.

Consequently, we propose that the optimal trade-off between physiological ascorbate and supraphysiological iron supplementation would be 500 µM and 10 µM, respectively. Such supplementation is likely to be a suitable concentration for future studies attempting to mimic iron accumulation and toxicity in CNS disease. Serum, if used, should be from the same batch (tested for concentration of iron and iron-binding proteins present) and should be used at a reduced percentage to ensure that non-transferrin-bound-iron is available and can bind to ascorbate as it would normally in the brain. Exposure time and type of iron reagent are less important considerations that should be chosen empirically to define reliable iron accumulation conditions *in vitro*. Another significant aspect of designing an *in vitro* iron-loading experiments is the method by which the iron levels are to be detected – the analytical procedures that have been used will be described and evaluated in detail in the following sub-section.

Table 1.2 Common iron reagents added to *in vitro* systems

Reagent	Formula (MW)	Structure	Solubility	S	L	MP
FAC	$C_6H_8O_7 \cdot xFe^{3+}\, yNH_3$ (Variable)	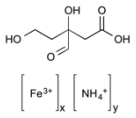	Very water soluble (<0.1 g/ml)	Y	Y	N
Ferric Chloride	$FeCl_3$ (162.2)		Water soluble (<5.7 M)	Y	Y	N
Ferric Citrate	$C_6H_5FeO_7$ (244.94)	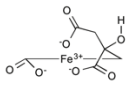	Dissolves in hot H_20 (<40 mM)	Y	Y	N
Ferric-NTA	$C_6H_6FeNO_6$ (243.96)	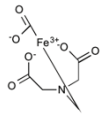	Water soluble (<5.25 mM)	-	-	N
FAS	$(NH_4)_2Fe(SO_4)_2 \cdot 6H_2O$ (392.14)	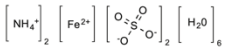	Water soluble (<180 mM)	N[b]	Y	N
Ferrous sulfate (FS)	$FeSO_4$ (151.91)		Water soluble (<1.9 M)	N[a]	Y	N
Ferrous Chloride	$FeCl_2$ (126.75)		Water soluble (<4.9 M)	N	-	N
Ferrocene	$Fe(C_5H_5)_2$ (186.03)	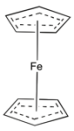	DMSO soluble (>500 mM) [c]	Y	Y	Y
TMH-Ferrocene (TMHF)	$Fe(C_5H_5)_2C_9H_{17}O$ (327.31)	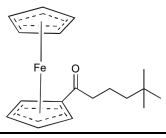	DMSO soluble [c]	Y	Y	Y

Abbreviations: FAC, ferric ammonium citrate; Ferric-NTA, ferric nitrilotriacetate; L, light sensitive; MP, membrane permeable; MW, molecular weight; RT, room temperature; S, stable. TMH-ferrocene, 3,5,5-trimethyl-hexanoyl ferrocene. Notes: [a] Oxidizes in media (in absence of ascorbate), [b] air sensitive and more resistant to oxidation than FS. [c] DMSO soluble (& other non-polar solvents).

1.4.4 Iron Measurement

A variety of analytical techniques, each with advantages and disadvantages, have been used to determine the iron content in cultured cells (Tables 1.3-1.7). These include: atomic spectroscopy, colorimetric assays, histological techniques and fluorescent indicators.

Atomic absorption spectroscopy (AAS) is perhaps the most accepted analytical technique for iron analyses, but it has not yet been widely adopted for *in vitro* studies (Table 1.3-Table 1.7). The sensitivity and reliability of iron quantification offered by this method is likely offset by its undesirable characteristics; sample preparation is cumbersome, expensive and potentially hazardous as iron is released by ashing the sample with hot concentrated acid. Moreover, it does not provide information on the cellular and subcellular distribution of iron. Consequently, AAS seems to be an undesirable first-choice method for researchers that have an infrequent or occasional requirement to measure iron and who may not have easy access to specialized equipment. In this case, colorimetric methods may be preferable. Indeed, the ferrozine assay is a sensitive, simple, reproducible and accessible method that is widely used for detecting iron content in cultured CNS cells and comparable results were obtained between the ferrozine assay and AAS (Riemer et al. 2004; Fish 1988). Further benefits include: the availability of convenient commercial kits, selective measurement of ferrous and ferric iron in the same environment and the low-cost set-up. However, the ferrozine assay suffers from similar limitations as AAS in that it does not provide any spatial information.

Perls' staining, which is one of the oldest methods for visualizing iron, remains widely used today because it is inexpensive, simple, specific and does not require specialized equipment or expertise (Hare et al. 2012; McRae et al. 2009; Meguro et al. 2007). Briefly, iron reacts with potassium ferrocyanide and produces an insoluble blue complex. Cellular and subcellular iron content can then be readily visualized by conventional light or electron microscopy. However, complications can arise during sample preparation and storage steps when there is a risk of iron contamination from the environment or iron leaching from fixed samples. Also, the use of this technique has been somewhat limited because it is relatively insensitive (even when enhanced with diaminobenzdine) and does not enable quantification. Fluorescence histochemistry, using metal indicators such calcein-AM, phen green SK or fura-2, is a more sensitive and quantifiable approach that allows researchers to determine the chelatable iron pool of live cells (Tenopoulou et al. 2007; Prasanthi et al. 2011; Comporti 2002).

Calcein-AM is the most commonly used fluorescence metal indicator. It is a membrane-permeant, non-fluorescent molecule that becomes fluorescent upon intracellular cleavage by cytoplasmic esterases to membrane-impermeant calcein. Calcein is then quenched in the presence of iron and the degree of quenching then gives an estimate of the amount of iron present. Calcein is pH-independent, stable, rapidly quenched and shows high affinity for both ferric and ferrous iron, which makes it a good indicator of the labile iron pool. Calcein, unlike Perls', detects only cytosolic iron rather than the total cellular iron because it is unable to access sub-cellular compartments such as the endoplasmic reticulum, mitochondria or lysosomes.

Finally, a third approach for visualizing iron is to use ferritin immunohistochemistry as a surrogate marker (Schulz et al. 2011; Zarruk et al. 2015). This way it is possible to both visualize and quantify iron (although indirectly) without specialised instrumentation or technical expertise that is required for elemental analysis techniques such as laser ablation inductively coupled plasma mass spectrometry (LA–ICP-MS) or Synchrotron x-ray fluorescence (SXRF) visualized with microtomography, which (to our knowledge) have not yet been used within an *in vitro* CNS iron loading context.

In summary, approaches that combine histological and biochemical techniques provide reliable spatial and quantitative information while remaining widely accessible and straightforward. Nevertheless, this still disregards the alterations in underlying iron-related proteins that are responsible for maintaining iron homeostasis and provides an incomplete picture of cellular iron status. A more comprehensive account might be described by also using histochemical or molecular techniques, such western blotting or quantitative PCR, to determine the expression levels of iron-related proteins within different cell types. Having reviewed the experimental conditions and detection methods above in this section, next it is necessary to consider the inherent suitability of the different *in vitro* and *ex vivo* models that have been used for iron loading.

1.5 Suitability of *in vitro* and *ex vivo* models for iron loading studies

1.5.1 Primary cell studies

Focusing on only one cell type enables researchers to study functional aspects of a particular cell type unencumbered by effects from surrounding cells and external factors but at the cost of ignoring the complex iron handling relationship between cell types. Experiments that lack the complete brain environment cannot completely replicate the *in vivo* situation and might leave gaps in translatability. For instance, Qian et al. (2014) showed that LPS increased hepcidin expression in neurons only when they were co-cultured with microglia. Similarly, Oshiro et al. (2008), who compared all three cell types grown as single cultures, astrocyte-neuronal co-cultures and microglia-neuronal co-cultures, found that 50 μM ferric citrate was sufficient to impair viability in neurons and microglia, whereas astrocyte viability was unaffected at this concentration and actually increased when ferric citrate was added at 100 and 200 μM. Notably, however, 200 μM ferric citrate treatment did not impair viability of co-cultures, leading the authors to suggest that astrocytes and microglia protect neurons against iron toxicity (Oshiro et al. 2008).

To date, very little work has been carried out studying iron loading in mixed, organotypic or co-cultures (see section 1.5.3 and table 1.7). Nevertheless, the superiority of such platforms over monocultures has been recognized in studies that have assessed iron uptake from nanoparticles. Briefly, the iron was predominantly taken up by microglia in organotypic and/or mixed cultures while uptake in the other cell types present remained modest; this was quite unlike the dramatic uptake of iron nanoparticles that occurred in monocultures of astrocytes, neurons and oligodendrocytes (Pinkernelle et al. 2012; Petters et al. 2014). Although nanoparticle uptake represents quite a different mechanism of iron uptake than that from iron reagents, such findings highlight the importance of studying the full set of CNS cells together to obtain a true picture of iron homeostasis.

The detected expression of various iron homeostasis proteins in cultured neurons does not completely agree with expression detected *in vivo* (Table 1.1). Iron, which has been reported in cultured neurons, has not been detected in *in vivo* neurons (Bishop et al. 2011; Connor & Benkovic 1992; Connor et al. 1990). Similarly, the presence of hepcidin, hephaestin and ceruloplasmin has been confirmed in *in vivo* brain tissue, but there have

been contradictory reports about the presence of these proteins in cultured neurons (Urrutia et al. 2013; Qian et al. 2014; Sun et al. 2012; Song et al. 2010; Schulz et al. 2011; Hwang et al. 2004; Hare et al. 2012; Klomp et al. 1996; J. Wang et al. 2007; Raha et al. 2013). Furthermore, primary CNS monocultures and mixed glial cultures are normally derived from embryonic or early neonatal rat and more closely mimic the developmental situation rather that the adult one. For instance, transferrin receptors were found to be expressed in amoeboid microglia in neonatal rats but were undetectable in older rats (Kaur & Ling 1995). The presence of this transient iron uptake route in cultures of neonatal microglia might produce spurious iron accumulation findings. Also, IRP1 and IRP2 have not reached their mature expression in the neonatal brain and thus are unlikely to be operating normally in corresponding primary cultures (Siddappa et al. 2002). Additionally, these aforementioned studies do not necessarily measure the accumulation of iron, nor do they focus on iron deposition, leading to a large gap in our knowledge (Tables 1.3-1.7).

1.5.2 Studies with cell lines of neurons, microglia and oligodendrocytes

Several iron-loading studies have opted to use cell lines in lieu of primary neurons, microglia or oligodendrocytes possibly because the preparation of these primary cells can be time-consuming and cumbersome whereas many cell lines are homogenous, inexpensive and proliferate quickly. Astrocytes, however, which are most readily generated and cultured, have not been substituted with a cell line replacement in iron loading studies.

The SH-SY5Y human neuroblastoma line differs from its primary neuronal counterparts in that SH-SY5Y cells have a greater resistance to iron toxicity and a larger labile iron pool (Pelizzoni et al. 2011; Aguirre et al. 2005). Nevertheless, Olivieri et al. (2011) report similar increases in cellular iron retention (in the absence of ferroxidase activity) in both primary neurons and SH-SY5Y cells. Also, Aguirre et al. (2005) confirm that SH-SY5Y cells, like primary neurons, display an active iron regulatory system.

Qian et al. (2014) exploited the BV-2 microglia cell line rather than using primary microglia in their co-culture with primary neurons. Although Cheepsunthorn et al. (2001) assert that HAPI cells (an immortalised rat microglia line) possess the functional properties and phenotype of microglia, discrepancies in the response of HAPI cells to LPS stimulation have been reported and call into question their usefulness (and, by extension, other microglial lines) in the place of primary microglia (Horvath et al. 2008).

In the human oligodendrocyte precursor cell line OLN-93, 30 µM iron (FAS, FAC or $FeCl_2$) loading for 48 h increased iron content in OLN-93 cells by about 1.7-fold without affecting viability, which is in line with the findings reported in primary OPCs and oligodendrocytes (Zhang et al. 2005). However, the basal iron content in OLN-93 cells is quite variable; Hoepken (2005) and Hohnholt (2011) reported values of 15.0 ± 1.1 and 29.9 ± 37.7 nmol/mg, respectively. Moreover, both authors commented that these values for iron content in OLN-93 cells were much higher than previous reports of iron content in primary OPCs i.e. 3 nmol/mg and 1 nmol/mg by Thorburne and Juurlich (1996) (as cited in Hohnholt et al. 2010 and Morath and Proschel (2001).

1.5.3 Ex vivo slice cultures

Organotypic slice cultures, which are efficient and reliable *ex vivo* models, combine the accessibility and convenience of *in vitro* models with the preservation of most of the complex brain milieu present in *in vivo* studies (Humpel 2015a; Cho et al. 2007; Gähwiler et al. 1997). Furthermore, organotypic slice cultures can be derived from older postnatal animals and continue to develop normally, which is one step closer to reflecting the sophisticated iron regulatory system in adult CNS. However, only one study (see Table 1.7) has exploited the use of this platform for loading iron, but this focused only on iron in oxidative stress and did not attempt to model or measure iron deposition or changes in iron molecules from oxidative stress (R. Liu et al. 2003). In this study, 25 µM ferrous sulfate exposure for 24 h was shown to decrease the viability of organotypic slice cultures. Although this value represents slice viability, the authors speculated that the measured increase in LDH release was derived mostly from neuronal death and that the glia viability was only affected after 300 µM ferrous sulfate exposure (R. Liu et al. 2003). Another study, which did not load or measure iron, investigated changes in iron homeostasis caused by 27-OHC and CHOP siRNA(Prasanthi et al. 2011). Thus far, organotypic cultures appear to be unappreciated for their potential in studying iron handling in the CNS.

1.6 Differential iron accumulation and toxicity in cultured CNS cells

In vitro iron loading in glia and neurons results in differential iron accumulation and toxicity. Astrocytes, in particular, are capable of withstanding high iron loading (Table 1.3). Indeed, exposure of primary astrocytes to 100 μM FAC for 24 h impaired viability in only one of three studies (Bishop et al. 2011; Riemer et al. 2004; Hoepken et al. 2004). Consistent with these findings, other studies that used different iron reagents, concentrations and exposure times also reported unchanged astrocyte viability (Keenan et al. 2010; Jeong 2006; Tulpule et al. 2010; Bishop et al. 2011; Rathore et al. 2012; Kress et al. 2002; Robb & Connor 1998). Conversely, one study reported increased viability and proliferation due to iron loading and suggested that the iron might have acted as a growth factor rather than a stressor (Oshiro et al. 2008). The magnitude of iron accumulation, unlike viability, proved quite inconsistent from experiment to experiment. Although 10 μM FAC loading produced similar increases in iron content (i.e. 2-fold, 3-fold and 8-fold), the 21-, 7- and 80-fold increase in iron from 100 μM FAC is quite variable (Riemer et al. 2004; Hoepken et al. 2004; Bishop et al. 2011). $FeCl_3$ exposure paradigms also caused variable intracellular iron accumulation; 33 μM loading for 3 h caused a 50-fold increase whereas 25 μM exposure for 2 h only increased iron content by 4-fold (Keenan et al. 2010; Bishop et al. 2010). On the other hand, 25 μM iron loading ($FeCl_3$ for 2 h or FAC for 3 h) produced similar 4-fold and 2-fold increases in astrocyte iron content (Bishop et al. 2010; Tulpule et al. 2010). Collectively, these studies demonstrate a massive uptake of iron into astrocytes without compromising viability, which suggests that astrocytes are able to cope well with iron accumulation.

Neurons, however, appear to be more vulnerable to iron overload and toxicity than astrocytes (Table 1.4). Neurons were shown to have impaired viability and lower total iron accumulation compared with astrocytes when subjected to the same acute high iron overload conditions (Pelizzoni et al. 2011; Kress et al. 2002). Short-term ferrous sulfate, ferric chloride/ferrous chloride and ferric chloride exposure led to a decrease in neuronal viability at 10, 7 μM and 50 μM, respectively (Zhang et al. 1993; Pike et al. 1997; Oshiro et al. 2000). Of these studies, only the latter measured intracellular iron content; the 1.5-fold increase in iron uptake was in line with the iron increase reported by Pelizzoni et al. (2011) and Kress et al. (2002) (i.e. 6-fold and 5-22% quenching). Bishop et al. (2011), however, found that iron exposure produced a 25-fold increase in iron content without any change in viability (i.e. 2.5-fold less iron accumulation compared with

astrocytes in the same study). The authors speculated that different populations of neurons might have a heterogeneous response to iron toxicity, which seems plausible given that the different experimental designs in other studies produced reasonably consistent responses. However, it is worth noting that these neurons were not only derived from the cerebellum rather than the forebrain, but also from postnatal mice rather than embryonic rats. It is possible that the iron demands and the maturation of the iron regulatory system in these cells might be quite different. Nevertheless, despite discrepancies in the degree of toxicity and total iron accumulated, it is clear that *in vitro* neurons are capable of accumulating iron but their capacity to do so safely is quite limited. This is in line with *in vivo* findings.

Microglia appear to be moderately well able to withstand the toxic effects of iron loading (Table 1.5). The viability of these cells was shown to be unaffected by exposure to 100 μM FAC for 24 h (Bishop et al. 2011). Nevertheless, this treatment caused a dramatic 170-fold increase in iron content compared with control. Moreover, the authors noted that microglia accumulated 4.7-fold more iron than astrocytes and 8-fold more than neurons that underwent the same treatment. Conversely, other studies have described reduced viability of microglia after exposure to 50 μM ferric citrate, 40 μM ferric chloride or 80 μM TMH-ferrocene (Oshiro et al. 2008; Rathore et al. 2012; Bishop et al. 2010). In only one of these studies was iron uptake compared with the iron content of untreated cells. Loading was found to cause a modest increase of 1.65-fold in iron influx and minimal efflux was recorded. Generally speaking, microglia *in vitro* seem to be more resistant to iron toxicity than neurons but less so than astrocytes, which fits in well with the idea of microglia protecting neurons from oxidative and/or iron damage *in vivo*. Ferritin positivity and iron accumulation is associated with dystrophic microglia in aged brains, as well as those with Alzheimer's disease, Huntington's disease and Multiple Sclerosis (Lopes et al. 2008; Simmons et al. 2007; Hametner et al. 2013; Streit et al. 2014). Nevertheless, the characterization of the iron handling system in microglia has lagged that of the other cell types. The existence (often discrepant or unreported; Figure 1.1 and Table 1.1) of several iron-related proteins in microglia, such as DCYTB, mitochondrial ferritin, mellanotransferrin receptor, lactoferrin and Tim2 remains to be clarified both *in vitro* and *in vivo*.

Very few iron-loading studies have been carried out on primary oligodendrocytes or oligodendrocyte precursor cells (OPCs) (Table 1.6). Instead, researchers tend to employ a cell-line substitute (see section 1.5.2). Nevertheless, it has been shown that 20 μM TMH-ferrocene loading for 24 h increased OPC iron content measured as a 1.25-fold

decrease in calcein-am signal) without any effect on viability (Zhang et al. 2005). Indeed, it was only at a 40 μM concentration that 24 h TMH-ferrocene exposure impaired viability. Notably, this compromised OPC viability occurred at only half the concentration at which viability in microglia was impaired (Zhang et al. 2006). In addition, it has been shown that a 48 h exposure to 100 ng/ml FAC increased iron content in oligodendrocytes by 2-fold without affecting viability (Morath & Mayer-Pröschel 2001). On the other hand, a 5 minute exposure to 75 μM $FeCl_2$ led to reduced oligodendrocyte viability (Kress et al. 2002). By comparison, neuronal and astrocyte viability was unaffected by treatment with 75 μM $FeCl_2$ or, indeed, 150 μM $FeCl_2$ (Kress et al. 2002). In summary, this section has reviewed the literature relating to the differential iron accumulation and toxicity in cultured CNS cells and it appears that oligodendrocyte-lineage cells and then neurons, seem to be the most vulnerable to manipulation of their iron status.

1.7 Importance and relevance of *ex vivo* iron loading models

Collectively, the existing efforts to model iron loading in monocultures, the limitations of such work, not to mention the improved understanding of the functioning of iron homeostasis machinery and findings of differential accumulation of iron in glial and neuronal cells, are of considerable interest in the context of aberrant iron deposition in neurodegenerative disease. Indeed, recent evidence has demonstrated not only iron metabolism, but also the activation of the unfolded protein response as common pathological processes contributing towards neurodegenerative diseases (Table 1.8 and section 1.11). However, these processes are not fully understood or defined; in particular, the crosstalk between iron metabolism and endoplasmic reticulum stress in CNS remains distinctly understudied and underappreciated (section 1.11). A novel validated, reliable and robust *ex vivo* model of iron loading might represent an excellent platform to address the molecular mechanisms underlying such events. The development of a model is only possible by appreciating and building on the wealth of existing studies and approaches, which have been comprehensively scrutinised and summarised in above sections. Next, the endoplasmic reticulum and the unfolded protein response will be summarised as prelude to iron UPR interplay.

Table 1.3 Iron Loading in astrocytes

Experimental Conditions				Experimental Measurements			References
Reagent	Exposure	S	AA	Detection	Iron Content	Viability	
$FeCl_2$	75/150 μM & Pyr; 5 min	Y	N	Fura-2 AM	14-fold quenching (140→10 AFU)	±	(Kress et al. 2002)
$FeCl_3$	33 μM; 3 h	N	N	Fz	↑ 50-fold to 100 nmol/mg	±	(Keenan et al. 2010)
$FeCl_3$	25-100 μM; 0-2 h	N	Y	Fz & Perls	25 & 100 μM; 2 h: ↑ 4- & 20-fold to 32 & 160 nmol/mg, respectively	±	(Bishop et al. 2010)
$FeCl_3$	40 μM; 6 & 24 h	N	Y	Radiolabeled	Influx: ↑1.3-fold (100→130%)	+	(Rathore et al. 2012)
$FeCl_3$	40 μM; 12, 24 & 48 h	N	Y	Radiolabeled	0.1 pmol/10^6 cells/h influx	n/d	(Jeong 2003)
FAC	10-1000 μM; 8, 24 & 48 h	Y	N	AAS	10 & 100 μM; 8/24 h: ↑ 3- & 7-fold to 25 & 65 nmol/mg, respectively	↓ >100 μM 24 h	(Hoepken et al. 2004)
FAC	10-100 μM; 24 h	N	N	AAS & Fz	10 &100 μM: ↑ 2- & 21-fold to 20 & 240 nmol/mg, respectively	± >100 μM	(Riemer et al. 2004)
FAC	10-100 μM; 6 & 24 h	N	N	Fz	100 μM; 6 & 24h: ↑ 60- & 80-fold to 230 & 40 nmol/mg, respectively	±	(Bishop et al. 2011)
FAC	25-100 μM; 3 h	N	Y	Fz	25 & 100 μM: ↑ 2- & 11-fold to 24 & 100 nmol/mg, respectively	±	(Tulpule et al. 2010)
FC	3/30 μM; 1 h	N	Y	Radiolabeled & calcein-AM	2-fold quenching (100-50%)	n/d	(Lane et al. 2010)
FC	50-200 μM; 1 h	Y	N	Radiolabeled	15.7 x 10^3 dpm (TFIU activity)	↓>100 μM	(Oshiro et al. 2008)
FS	500 μM; 15 min	Y	N	n/d	n/d	n/d	(Erikson & Aschner 2006)
Fe-NTA	7 μM & IS; 18 h	Y	N	AAS	Values not reported for iron alone	n/d	(Urrutia et al. 2013)
FAC/FAS, TMHF	100 μg/ml, 10 mM; 1-2 d	N	N	n/d	n/d	± FAC/FAS	(Robb & Connor 1998)

Abbreviations: AA, ascorbate; AAS, atomic absorption spectroscopy; AFU, arbitrary fluorescent units; FAC, ferric ammonium citrate; FAS, ferrous ammonium sulfate; FC, ferric citrate; Fe-NTA, ferric nitrilotriacetic acid; FS, ferrous sulfate; FTH, ferritin heavy chain; Fz, ferrozine assay; IS, inflammatory stimuli; Pyr, Pyrithione; S, serum; TFIU, transferrin-independent uptake; TMPF, TMP-ferrocene. All tissue derived from rats or mice. [a] LDH, [b] Trypan Blue. Symbols: '↓' = decrease, '↑ ' = increase, '± ' = unchanged and 'n/d' = not done.

Table 1.4 Iron Loading studies in primary neurons

Experimental Conditions				Experimental Measurements			References
Reagent	Exposure	S	AA	Detection	Iron Content	Viability	
$FeCl_2$	75 or 150 μM & Pyr; 5 min	Y	N	Fura-2 AM	7-fold quenching (110 to 16 AFU)	↓[b]>150 μM	(Kress et al. 2002)
$FeCl_3$	50-200 μM; 24 h	N	N	Radiolabeled	50 μM: ↑ 1.5-fold (TFIU activity)	↓[d]>50 μM	(Oshiro et al. 2000)
$FeCl_2$, $FeCl_3$	0.1-100 μM; 18-24 h	N	N	n/d	n/d	↓[a] >7 μM	(Pike et al. 1997)
FAC	10-100 μM; 6 & 24 h)	N	N	Fz	100 μM; 6 h: ↑ 25-fold to 115 nmol/mg	+ [b]	(Bishop et al. 2011)
FC	50-200 μM; 1 h)	Y	N	Radiolabeled	7.7 x 10^3 dpm (TFIU activity)	↓[d]>50 μM	(Oshiro et al. 2008)
FS	0.1-100 μM; 3 h	Y	Y/N	n/d	n/d	↓[a] >10 μM	(Zhang et al. 1993)
Fe-NTA	40 μM & IS; 18 h	N	N	AAS	Values not reported for iron alone	n/d	(Urrutia et al. 2013)
FAS, FAC	0.3-100 μM, 100 μM and Pyr; 3 & 60 min	Y	N	Calcein-AM & Fura-2 AM	1, 10 & 100 μM FAS & 100 μM FAC: 5, 12, 22 & 6% quenching	↓ [c]>100 μM FAS	(Pelizzoni et al. 2011)

Abbreviations: AA, ascorbate; AAS, atomic absorption spectroscopy; FAC, ferric ammonium citrate; FAS, ferrous ammonium sulfate; FC, ferric citrate; Fe-NTA, ferric nitrilotriacetic acid; FS, ferrous sulfate; FZ, ferrozine assay; Pyr, Pyrithione, S, serum; TFIU, transferrin-independent uptake. All tissue derived from rats or mice. [a] Counts, [b] LDH, [c] MTT, [d] Trypan Blue. Symbols: '↓' = decrease, '↑ ' = increase, '± ' = unchanged and 'n/d' = not done.

Table 1.5 Iron Loading studies in primary microglia

Experimental Condition				Experimental Measurements			References
Reagent	Exposure	S	AA	Detection	Iron Content	Viability	
$FeCl_3$	20 μM; 6 & 24 h	N	Y	Radiolabeled	Influx: ↑ 1.65-fold (100→165%)	↓[a] >40 μM	(Rathore et al. 2012)
FAC	10-100 μM; 6 & 24 h	N	N	Fz	100 μM; 6 h: ↑ 170-fold to 1.5 μmol/mg	+[b]	(Bishop et al. 2011)
FC	50-200 μM; 1 h	Y	N	Radiolabeled	6.8 x 10^3 dpm (TFIU activity)	↓[a] >50 μM	(Oshiro et al. 2008)
Fe-NTA	7 μM & IS; 18 h	Y	N	AAS	Values not reported for iron alone	n/d	(Urrutia et al. 2013)
TMHF	10-160 μM; 24 h	Y	N	n/d	n/d	↓[c] >80 μM	(Zhang et al. 2006)

Abbreviations: AA, ascorbate; AAS, atomic absorption spectroscopy; FAC, ferric ammonium citrate; FC, ferric citrate; Ferr, ferrocene; Fe-NTA, ferric nitrilotriacetic acid; FZ, ferrozine assay; IS, inflammatory stimuli; S, serum; TMPF, TMP-ferrocene. All tissue derived from rats or mice. [a] Trypan Blue, [b] LDH, [c] MTT. Symbols: '↓' = decrease, '↑ ' = increase, '$\pm$ ' = unchanged and 'n/d' = not done.

Table 1.6 Iron Loading studies in oligodendrocyte-lineage cells (primary and cell line)

	Experimental Conditions				Experimental Measurements			References
Cell	Reagent	Exposure	S	AA	Detection	Iron Content	Viability	
OL	$FeCl_2$	75 or 150 μM & Pyr; 5 min	Y	N	Fura-2 AM	8-fold quenching to 25 AFU	↓[a] > 75 μM	(Kress et al. 2002)
OL	FAC	100 ng/ml; 48 h	Y	N	AAS	↑ 2-fold to 83.7 ng/ml	±[b]	(Morath & Mayer-Pröschel 2001)
OPC	FAC, TMHF	0.25-5 μM, 55 μg/ml FTH	Y	N	Calcein-AM	Values not reported for iron alone	↓[a b] > 1 μM	(Todorich et al. 2011)
OPC	TMHF	10-160 μM & IS; 24 h	N	N	Calcein-AM	20 μM: 1.25 fold quenching (100→80%)	↓[b] > 40 μM	(Zhang et al. 2005)
OLN-93	FAC, FAS, $FeCl_3$	30, 100, 300, & 1000 μM; 48 h	Y	N	Fz & Perls	FAC 30 &100 μM: 48 h: ↑ 2- & 4-fold to 9 and 16 nmol/mg	± [a]	(Hohnholt et al. 2010)
OLN-93	FS	5 & 50 μM; 2 & 16 h	Y	N	Fz	5 μM, 2 & 16 h; ↑ 2.5 and 10-fold to 1.1 & 4 nmol/μg DNA,	±[c]	(Brand et al. 2008)
O-2A	FAC	100 ng/ml; 48 h	Y	N	AAS	↑ 2.7 to 196.4 ng/ml	+[b]	(Morath & Mayer-Pröschel 2001)

Abbreviations: AA, ascorbate; AAS, atomic absorption spectroscopy; AFU, arbitrary fluorescence units; FAC, ferric ammonium citrate; FAS, ferrous ammonium sulfate; FS, ferrous sulfate; FTH, ferritin heavy chain; Fz, ferrozine assay; IS, inflammatory stimuli; OL, oligodendrocyte; OPC, oligodendrocyte precursor cell, Pyr, Pyrithione; S, serum; TMHF, TMH-ferrocene. All tissue derived from rats or mice. [a] LDH, [b] MTT, [c] NR, Symbols: '↓' = decrease, '↑ ' = increase, '± ' = unchanged and 'n/d' = not done.

Table 1.7 Iron Loading studies in mixed and co-cultures

	Experimental Conditions				Experimental Measurements			References
Cell	Reagent	Exposure	S	AA	Detection	Iron Content	Viability	
OSC	FS		N	Y	n/d	n/d	↓ [a b] > 10 μM	(R. Liu et al. 2003)
OSC	FAS, FC & Ferr	1 & 10 μM; 12 h	N	Y	Fz	Ferr 1 μM: ↑ 1.6-fold	↓ [b] > 10 μM	(Healy et al. 2016)
1° N-M	FC	200 μM; 1 h	N	N	Radiolabeled	± (compared with N or M)	± [c]	(Oshiro et al. 2008)
N-AS	FC	200 μM; 1 h	N	N	Radiolabeled	± compared with N or A)	± [c]	(Oshiro et al. 2008)
Glia	$FeCl_3$	50-200 μM; 24 h	N	N	Radiolabeled	50 μM: ↑ 4-fold (TFIU activity)	↓ [c] > 50 μM	(Oshiro et al. 2008)
Glia	$FeCl_3$	1.6 mM & +/- Tf; 3-24 h	N	N	Radiolabeled	No & 10x Tf: ↑ iron uptake & retention & ↓ iron uptake	n/d	(Takeda et al. 1998)

Abbreviations: AA, ascorbate; FC, ferric citrate; FS, ferrous sulphate; FZ, ferrozine assay; N-AS, neuron-astrocyte co-culture; N-M, neuron-microglia co-culture; OSC, organotypic slice cultures; S, serum; TFIU, transferrin-receptor-indepedent-uptake.

1.8 The endoplasmic reticulum

The endoplasmic reticulum (ER) is a multifunctional organelle located within the cytoplasm in all eukaryotic cells. Structurally, the ER is a network of branched tubules found through the cell and is partially contiguous with the outer nuclear envelope, Golgi apparatus, mitochondria and the plasma membrane. The ER functions as a critical manufacturing and packaging factory of the cell. It is responsible for a vast array of functions, including the biosynthesis, folding, assembly, post-translation modifications of secretory and membrane-targeted proteins and calcium signalling.

There are two types of ER: rough ER (RER) and smooth ER (SER). These are inter-connected sub-compartments of the ER. The RER is a series of flattened sealed sacs with ribosomes attached to the cytoplasmic surface whereas the SER is a tubular interconnecting network and is not studded with ribosomes. The RER produces, folds and dispatches proteins. This process begins at the cytosolic surface before the proteins are translocated into the ER lumen where they are folded and matured. Stringent quality control checking is conducted here; any incorrectly formed or folded proteins are rejected (Kleizen & Braakman 2004). These rejects are inhibited from leaving and are either stored in the lumen or sent for recycling by eventual breakdown into amino acids. The proteins whose native conformations are met are permitted to exit and are delivered to the Golgi apparatus on route to their final destinations. The SER is mostly associated with lipid production and metabolism but also plays detoxification functions. The oxidizing environment, one of the most remarkable features of the ER, is a prerequisite to permit disulfide bond formation (Tu & Weissman 2004). Other specialized features of the ER lumen include its high protein concentration, high calcium concentration and an abundance of chaperones and folding enzymes (Marquardt et al. 1993; Kleizen & Braakman 2004; Ron & Walter 2007; Walter & Ron 2011)

1.9 Unfolded Protein Response

Despite the sophistication of the quality control mechanisms normally provided by the ER, it is certainly not infallible (Braakman & Hebert 2013; Kleizen & Braakman 2004; Gething 1997). Certain physiological states and exogenous stimuli compromise this specialized folding environment and produce a discrepancy between the demand for ER functions and its production capacity. These include: pathological events, perturbed intraluminal calcium, glycosylation, alteration of redox status, energy/nutrient

deprivation and hypoxia. The UPR can be induced following a chemical insult e.g. tunicamyin and thapsigargin.

The unfolded protein response (UPR) is a 'check-and-balance' program (Fig. 1.2 & section 1.9.1) activated upon disturbed homeostasis in the endoplasmic reticulum (i.e. ER stress). It acts to alleviate stress and restore normal ER function. The UPR accomplishes this goal through multiple synergistic strategies that encompass halting protein translation, degrading misfolded proteins, and activating the signaling pathways that lead to increasing the production of molecular chaperones involved in protein folding (M. Wang & Kaufman 2016; Schröder & Kaufman 2005). If these pro-survival objectives are not achieved within a certain time span or the disruption is prolonged, the UPR aims towards apoptosis.

1.9.1 Pathway overview

The UPR (Fig. 1.2) comprises three distinct but interconnecting pathways that are defined by the major ER-resident transmembrane proteins operating as proximal sensors – namely, inositol-requiring enzyme 1 (IRE1), activating transcription factor 6 (ATF6) and pancreatic ER kinase-like endoplasmic reticulum kinase (PERK) (Ron & Walter 2007; Walter & Ron 2011; Schröder & Kaufman 2005). IRE1 and PERK are type I transmembrane proteins with protein kinase activity, whereas ATF6 is a type II transmembrane protein encoding a transcription factor (M. Wang & Kaufman 2016; Schröder & Kaufman 2005). The ER-luminal domains of PERK, IRE1 and ATF6 interact with B cell immunoglobulin-binding protein (BiP/GRP78), a molecular chaperone and common activation trigger, and are thus kept inactivated under unstressed conditions (Pincus et al. 2010). However, as unfolded proteins clog up the ER, BiP preferentially binds to the misfolded proteins and dissociates from these sensors, leading to their activation (M. Wang & Kaufman 2016; Schröder & Kaufman 2005; Ron & Walter 2007). Each receptor initiates a different signaling pathways that ultimately leads either to the reduction of ER stress by suppressing protein synthesis and increasing expression of certain proteins required for the restoration of normal ER function or ultimately, if balance is not restored, apoptotic cell death.

Following BiP disassociation, PERK homodimerizes and autophosphorylates to activate its kinase domain. Activated PERK subsequently phosphorylates and inactivates the alpha subunit of eukaryotic initiation factor 2 (eIF2α). This, in turn, rapidly and temporarily inhibits global protein synthesis. Paradoxically, phosphorylation of eIF2α also increases translation of selected transcript factors, such as activating transcription

factor 4 (ATF4), to increase the capacity for protein transport in the ER. After translation, ATF4 enters the nucleus, where it activates UPR genes that encode proteins that are necessary for the antioxidant response and amino acid biosynthesis and transport. ATF4 also activates the transcription of CCAAT/enhancerbinding protein (C/EBP) homologous protein (CHOP), which forms heterodimers with ATF4 to upregulate genes with functions in the UPR, autophagy and mRNA translation. Intriguing, beyond the classical targets, CHOP has also been recently linked to iron homeostasis (see section 1.9). Once ER protein folding homeostasis is restored, ATF4 and CHOP induce transcription of growth arrest and DNA-damage-inducible protein 34 (GADD34) to de-phosphorylate eIF2α- and restart global mRNA translation, which is critical if cells are to survive an acute insult, and defines a negative feedback loop.

ER stress signals are also integrated and transmitted through the IRE1 pathway. The structural homology shared by the luminal domains of PERK and IRE1 renders identical activation mechanisms. However, this pathway, unlike PERK, does not act to inhibit global translation but rather increases the cell's capacity for protein folding, transportation and degradation (M. Wang & Kaufman 2016; Schröder & Kaufman 2005). Activated IRE1 induces endoribonuclease activity that selectively cleaves a 26-nucleotide intron from X-box-binding protein (XBP1) mRNA. This process produces a stable active transcription factor (spliced XBP1; XBP1s) that induces component of the ER-associated degradation (ERAD) pathway, such as Derlin 1 and Derlin 2, along with chaperones such as BiP and P58, as well as modulators of lipid synthesis and ER expansion (M. Wang & Kaufman 2016; Schröder & Kaufman 2005).

The third pathway, ATF6, is critical for the adaptive response to ER protein misfolding. Following dissociation from BiP, ATF6 moves to the Golgi apparatus, where it is cleaved by S1 and S2 proteases to produce its active 50 KDa form. Then, upon trafficking to the nucleus, activated ATF6 induces the expression of a cohort of ER proteins which include chaperones, such as BiP and GRP94, folding enzymes and ERAD components. Although activated ATF6 is mainly considered to be a pro-survival molecule, the over-expression of ATF6 can induce CHOP mRNA expression. Also of note, activated ATF6 can also up-regulate the unspliced XBP1 (XBP1u) mRNA, supplying the IRE1 pathway with its substrate (Ron & Walter 2007). Reciprocally, uXBP1 triggers activated ATF6 degradation, acting as negative regulator of the ATF6 signaling cascade (Schröder & Kaufman 2005; Walter & Ron 2011). Following this overview of the unfolded protein response pathways, a more detailed account of BiP and CHOP is given in the following sub-sections.

1.9.2 BiP

Molecular chaperones are proteins that assist in the folding and unfolding of proteins, thereby helping those struggling and/or problematic proteins attain their correct 3D conformation (Braakman & Hebert 2013). Chaperones achieve this by preserving maturing polypeptides in a soluble, folding-competent state, thereby counteracting misfolding and aggregation, rather than conveying structural information or accelerating the folding steps. BiP, otherwise also known as glucose-regulated protein (GRP78), is prominent among the multitude of chaperones constitutively expressed in the ER and serves as a classical marker of UPR activation. It is a member of the heat shock protein 70 (HSP70) family of molecular chaperones. BiP contains an N-terminal domain with the ATPase catalytic site and a C-terminal substrate-binding domain (Gething 1999). BiP chaperoning involves repetitive ATP/ADP cycles through which an unfolded polypeptide is transiently bound and released as it progresses towards its native state (Gething 1999).

1.9.3 CHOP

CHOP, otherwise known as growth arrest and DNA damage-inducible 153 (GADD153) is a member of the C/EBP family (Oyadomari & Mori 2004). It is a 29 kDa factor that is expressed at low levels in unstressed cells and can be strongly induced in response to numerous cellular stressors including UV light, genotoxic agents, glucose deprivation and amino acid starvation and ER stress (Oyadomari & Mori 2004). CHOP heterodimerizes with other members of the C/EBP transcription factor family thus preventing their homodimerization and binding to DNA sequences specific for the homodimers. Although CHOP can be induced by the 3 arms of the UPR, the PERK/eIF2a pathway is the primary mediator of CHOP induction (M. Wang & Kaufman 2016; Schröder & Kaufman 2005). The induction of CHOP by ER stress is almost fully attenuated in PERK null cells and in eIF2aS51A cells that have a non-phosphorylatable form of eIF2a (Harding et al. 2000). Nevertheless, the ATF6 and Ire1/XBP-1 signalling pathways are still required for optimal induction of CHOP during ER stress.

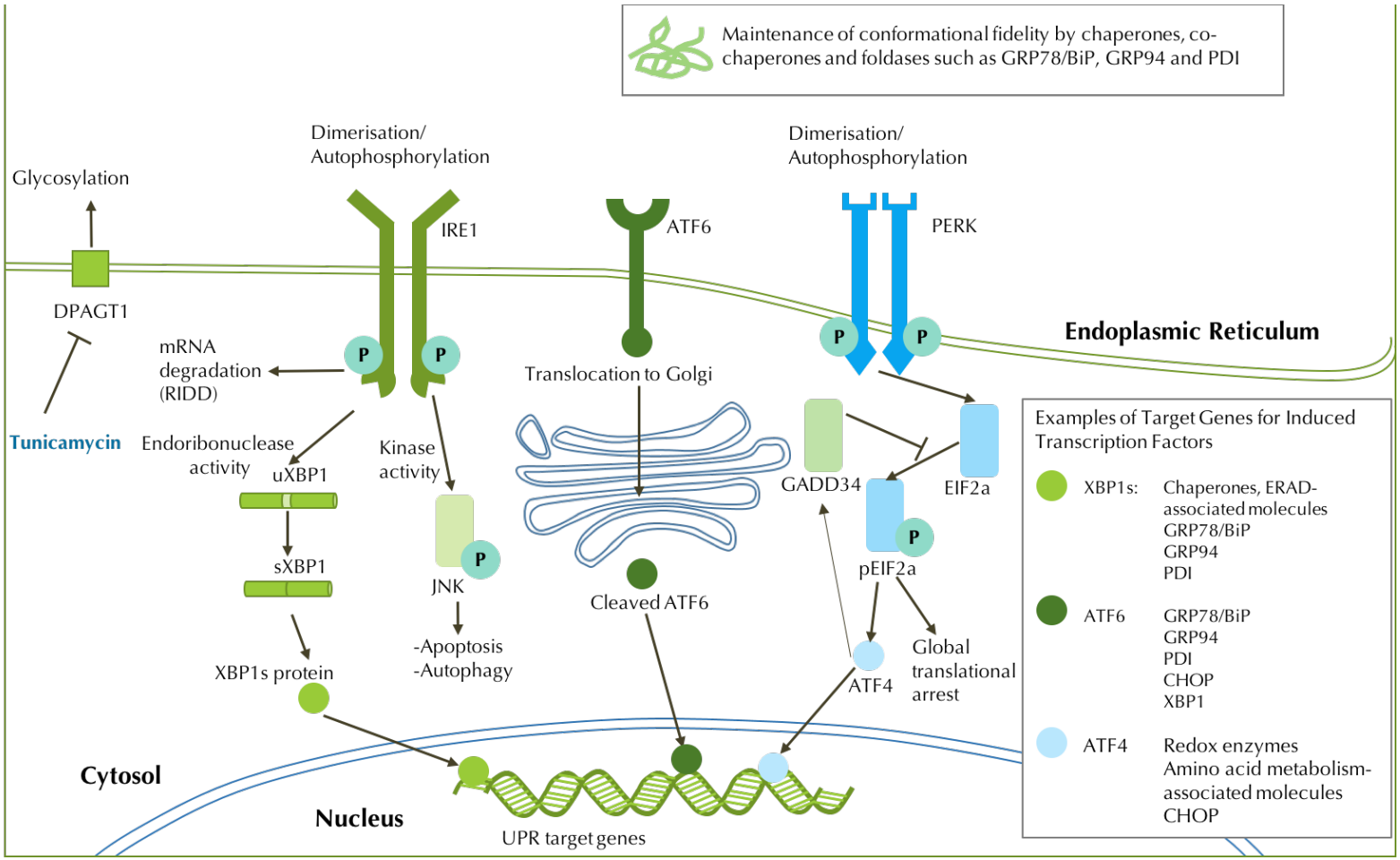

Figure 1.2: Schematic of the unfolded protein response (UPR) signaling pathway. Upon accumulation of unfolded proteins in the ER, BiP detaches from the three transmembrane sensors, PERK, ATF6 and IRE. The activated transmembrane receptors then induce the expression of chaperone proteins and transcription factors. The UPR can be chemically induced e.g using tunicamycin exposure. Tunicamycin inhibits DPAGT1, a protein required for N-linked protein glycosylation in the ER. Inhibition of glycosylation leads to a build up of improperly folded proteins to which BiP preferentially binds and thereby leads to the activation of the UPR. Image source: Dr. Jill McMahon.

1.10 UPR crosstalk with iron metabolism

In recent years, increasing evidence of the crosstalk between iron metabolism and the UPR has emerged. For example, the expression of ER chaperones BiP and calreticulin was up-regulated in astrocytoma cells that were loaded with iron (Ye & Connor 2000) and BiP expression was increased in hepatocytes in mice that were fed excess iron in their diet(Petrak et al. 2007). Also, iron-loaded hypoxic oligodendrocytes were found to express increased levels of BiP and IRE1 alongside ultrastructural evidence demonstrating a dilated ER, which was subsequently reduced by treatment with deferoxamine, an iron chelator (Rathnasamy et al. 2015).

Moreover, the UPR, in turn, modulates iron metabolism. The UPR has been shown not only to induce a biphasic pattern of expression of the iron regulatory hormone hepcidin, through CHOP action on hepcidin promoter-binding C/EBPα, but also to up-regulate at least 2 other iron-associated molecules (i.e. the iron exporter ferroportin and an iron storage molecule ferritin H) HepG2 cells (Oliveira et al. 2009). Another study demonstrated that the hepcidin gene is activated in a CREBH (cyclic AMP response element–binding protein H; an ER stress-activated trancription factor)-dependent fashion in HepG2 cells and in mice using chemical and immunological stressors (Vecchi et al. 2009). ER stress was also shown to induce hepcidin expression and caused hypoferremia and iron sequestration in the spleen of mice (Vecchi et al. 2009). Furthermore, silencing CHOP gene expression in organotypic adult rabbit hippocampal slices led to increased expression of IRP1, IRP2 and TfR1 while FTL and FTH expression was unchanged (Prasanthi et al. 2011). Finally, transferrin has been reported to be highly modulated by drug-induced CHOP overexpression or by *in vitro* transfection by CHOP antagonizing the C/EBP activation of the transferrin gene (You 2003). The existence of this putative connection in the context of neurodegeneration is intriguing and will be discussed in detail in the next section.

1.11 Iron, UPR and neurodegenerative disease

Recent evidence has highlighted iron metabolism and the unfolded protein response as common pathological processes associated with aging and contributing towards neurodegenerative diseases (Table 1.8). Selected examples, i.e multiple sclerosis and Alzheimer's disease, will be described in more detail in the following paragraphs.

1.11.1 Multiple Sclerosis

Multiple sclerosis (MS) is an inflammatory and degenerative condition that results in inflammation, loss of oligodendrocytes, demyelination, axonal damage and worsening neurological outcomes that significantly decrease quality of life (A. Williams 2015). Its aetiology is currently unknown and its pathogenesis is only partly understood (Frohman et al. 2006; A. Williams 2015; Lassmann & van Horssen 2011). Complex genetic traits as well as environmental factors determine the susceptibility to develop the disease (Sawcer et al. 2014). Dysregulation of iron metabolism, and activation of the UPR are increasingly being implicated in MS.

MRI and histological studies have shown global alterations in iron levels in the brains of patients with MS, with elevated iron detected in deep grey matter structures, and a decreased iron load in the normal appearing white matter (Table 1.8) (Stephenson et al. 2014; Hametner et al. 2013; Schuh et al. 2014; Bagnato et al. 2013; Haider et al. 2014). At a local level, both in MS and its primary animal model experimental autoimmune encephalomyelitis (EAE), iron perturbation has been localized in macrophages and microglia detected around the sites of inflammation and near demyelinated plaques, and, to a lesser extent, in astrocytes and damaged axons (Hametner et al. 2013; LeVine 1997; Schuh et al. 2014; Zarruk et al. 2015; R. Williams et al. 2011). Late active lesions were seen to have an increased iron load, whereas inactive or remyelinated lesions showed iron loads similar to or reduced compared with controls (Hametner et al. 2013). In MS and EAE, there are also changes in several iron-related molecules, e.g. increased amount of the iron storage molecules FTL, FTH and FtMt and also increased expression iron exporter HEPH in human brain (Hametner et al. 2013; Schuh et al. 2014; Zarruk et al. 2015)

Studies have also established ER stress and the UPR as participants in MS and EAE (Hetz 2014). Previous research from our lab group has found considerable evidence of UPR activation in MS (Cunnea et al. 2011; Mháille et al. 2008; Fhlathartaigh et al. 2013; McMahon et al. 2012). We have demonstrated BiP, CHOP and XBP1 immunoreactivity multiple cell types, including oligodendrocytes, astrocytes, T cells and microglia, in active grey and white matter lesions in post-mortem brain (Mháille et al. 2008; McMahon et al. 2012) and increased CHOP and ATF4 mRNA in demyelinating lesions (Cunnea et al. 2011). In line with our evidence, independent microarray studies have also demonstrated up-regulated ATF4 and BiP in MS lesions (Mycko et al. 2004; Cwiklinska 2003). In agreement with the human MS findings, peIF2α and CHOP were found to be elevated in oligodendrocytes and infiltrating T cells within white matter lesions of EAE

mice and rats (Lin et al. 2005; Lin et al. 2010; Chakrabarty et al. 2004; Fhlathartaigh et al. 2013) and our group detected significantly raised levels of CHOP, XBP1, pEIF2 α in EAE spinal cord lesions (Fhlathartaigh et al. 2013)

1.11.2 Alzheimer's disease

Alzheimer's disease (AD) is the most common cause of dementia. It is a progressive neurodegenerative disorder that is characterized by progressive cognitive impairment, memory loss and behavioural changes. Amyloid plaques and neurofibrillary tangles are the most prominent pathological hallmarks. The plaques are mainly composed of amyloid-beta peptides of 40-42 amino acids that are produced from the cleavage of amyloid precursor protein by secretases, whereas neurofibrillary tangles are composed of abnormally phosphorylated tau protein (Duran-Aniotz et al. 2014; Oshiro et al. 2011). A complicated array of molecular events has been implicated in the pathogenesis of AD, with increasing evidence that iron metabolism and the UPR might play a role.

Increased iron in AD was first reported over 60 years ago while its association with senile plaques, neurofibrillary tangles dates back 20 years and more recently iron has been demonstrated in the parietal cortex, motor cortex and hippocampus (Belaidi & Bush 2016; LeVine 1997). There is change in a number of iron-related molecules such as DMT1, FPN and Cp in the brains of AD patients (TODORICH & Connor 2004; Oshiro et al. 2011; Schrag et al. 2011; Connor et al. 1992). Moreover, LF expression was greatly up-regulated in both neurons and glia in affected AD tissue. It was very strongly associated with senile plaques, neurofibrillary tangles (Kawamata et al. 1993), while a subset of reactive microglia associated with senile plaques in AD brain express MTf, a phenomenon not seen in reactive microglia in the other pathological tissues examined or in other areas in AD (Jefferies et al. 1996).

Activation of UPR has been found as pathological feature in post-mortem AD brain tissue when compared to non-demented control brain tissue. Elevated levels of GRP78, peIF2α- and ATF4 have been observed in AD in the hippocampus and temporal cortex (Baleriola et al. 2014; O'Connor et al. 2008; Hetz & Mollereau 2014; Boserup et al. 2011). UPR activation was identified as an early pathological event with BiP and pPERK levels increasing in association with phosphorylated tau in glia and neurons prior the neurofibrillary tangle formation (Hoozemans et al. 2009; Nijholt et al. 2012). Undoubtedly, there is evidence for both iron and the UPR in neurodegenerative disease. However, the possible pathological significance of the connection between these mechanisms in these conditions remains largely unconsidered leading to our hypothesis.

Table 1.8 Iron and activated UPR in neurodegenerative and neuroinflammatory disease

Disease	Disease hallmarks	Pathological observations		Selected reviews
MS	CNS Inflammation Demyelination	Iron	↑ iron in grey & white matter ↓ HEPH	(Stephenson et al. 2014; LeVine et al. 2013)
			↑ iron in microglia	
		UPR	↑ BiP, CHOP, XBP1 & ATF4 in lesions	(Lin & Popko 2009) (Way & Popko 2016)
AD	ß-amyloid plaques Neurofibrillary tangles	Iron	↑ iron in plaques, neurofibrillary tangles & activated microglia	(TODORICH & Connor 2004) (Oshiro et al. 2011) (Schrag et al. 2011)
			↑ DMT1, ↓FPN ↓CP	
		UPR	↓ XBP1s, ↑ PDI in protein aggregates, ↑ pPERK in neurons and glia	(Hetz & Mollereau 2014) (Duran-Aniotz et al. 2014)
PD	DA neuron loss in SN Lewy body formation	Iron	↑ iron and IRP in SN ↓ ferritin in SN, ↑ iron in lewy bodies	(Jiang et al. 2016) (Belaidi & Bush 2016) (K. Li & Reichmann 2016)
		UPR	↑ pPERK, BiP, CHOP & ATF4 in DA neurons	(Halliday & Mallucci 2015) (Mercado et al. 2013)
HD	Huntingtin gene mutation	Iron	↑ iron in basal ganglia	(Batista-Nascimento et al. 2012) (Muller & Leavitt 2014)
		UPR	↑ XBP1 in striatum	(Hetz & Mollereau 2014)

Abbreviations: AD, Alzheimer's disease; DA, dopaminergic; PD, Parkinson's disease; PDI, Protein Disulfide Isomerase; MS, multiple sclerosis; SN, substantia nigra

1.12 Hypothesis and aims

Given the evidence supporting the physiological intersection of iron metabolism and the UPR in the CNS, the pathological significance of this crosstalk in neurodegenerative disease has emerged as an intriguing concept with potential therapeutic opportunities. Nevertheless, this idea has remained largely unconsidered to date – perhaps, partially, because the existing tools/platform (i.e. *in vitro* monocultures, extreme iron loading paradigms, and, to an extent, the basic knowledge on the iron homeostasis machinery; section 1.5, 1.4 and 1.3, respectively) required have been relatively impoverished. Consequently, this comprehensive account, which has integrated the published work on these topics, has been critical in the design and development of improved methodologies.

Hypothesis

The interplay between UPR and iron homeostasis is present in the CNS and functions under pathological conditions.

Aim

The major aim of this work was to develop a novel *ex vivo* model of iron loading to fulfil the unmet need for a relevant, low-cost and accessible platform that is critical to comprehensively investigating the iron homeostasis machinery, iron deposition and iron metabolism in the context of neurodegenerative disease. Such a platform would also enable investigation of the putative CNS crosstalk between iron metabolism and the UPR, and provide evidence of the relevance of this interplay in neurodegenerative disease given the tantalizing independent association reported.

Specific aims

Characterise iron homeostasis in the postnatal rat brain in context of developing and validating an *ex vivo* slice culture model generated from postnatal tissue.

i. Develop, optimise and characterise an *ex vivo* model of iron loading so that common hallmark of iron deposition and its perturbed handling occurring in neurodegenerative disease might be better understood in future studies.

ii. Characterise the reciprocal iron-UPR relationship in the brain.

iii. Establish and validate an image analysis workflow to handle micrographs of glial immunohistochemistry to reliably measure cell number and morphology.

2 Materials and methods

2.1 Materials

Tissue Culture Reagents

Ascorbic Acid (Sigma-Aldrich, A8960)

D-glucose (Sigma-Aldrich, G7021)

Hanks Balanced Salt Solution (Sigma-Aldrich, H6648)

Heat-inactivated Horse Serum (Sigma-Aldrich, H1270)

L-glutamine (Sigma-Aldrich, G7513)

Minimum Essential Medium (Gibco, 51200-087)

Minimum Essential Medium Eagle (Sigma-Aldrich, M7278)

N-acetyl-1-systeine (Sigma-Aldrich, A1965)

Penicillin/Streptomycin (Sigma-Aldrich, P4458)

Tris(hydroxymethyl)aminomethane (Sigma-Aldrich, 25289)

Tissue Culture Materials

6 well plates (Sarstedt, 83.1839)

Millicell Cell Culture Insert, 30mm hydrophilic PTFE, 0.4 µm (Millipore, PICM03050)

Tissue Culture Treatments

Dimethyl Sulfoxide (DMSO) (Sigma-Aldrich, D2650)

Ferric Citrate (Sigma-Aldrich, F3388)

Ferrocene (Sigma-Aldrich, F408)

Ferrous Ammonium Sulphate (Sigma-Aldrich, F1543)

Triton X-100 (Sigma-Aldrich, T9284)

Tunicamycin (Sigma-Aldrich, T7765)

Ferrozine Assay

Ammonium Acetate (Sigma-Aldrich, 372331)

Ferrozine (Sigma-Aldrich, 82950)

Hydrochloric Acid (Sigma-Aldrich, 320331)

Iron Standard Solution (Merck-Millipore, 1197810100)

Neocuproine (Sigma-Aldrich, N1501)

Potassium permanganate (Sigma-Aldrich, 31404)

Sodium L-ascorbate (Sigma-Aldrich, A7631)

Sodium Hydroxide (Sigma-Aldrich, 58045)

Viability Assays

LDH enzyme (Lactate dehydrogenase) (Cayman, 10009321)

NADH (Sigma-Aldrich, N8129)

Potassium phosphate dibasic (Sigma-Aldrich; P3786)

Potassium phosphate monobasic (Sigma-Aldrich P5655)

Sodium Pyruvate (Sigma-Aldrich, P8574)

Thiazolyl Blue Tetrazolium Bromide (Sigma-Aldrich, M2128)

RNA isolation

Chloroform (Sigma-Aldrich, C2432)

Diethyl pyrocarbonate (Sigma-Aldrich, D5758)

Ethanol (Sigma-Aldrich, E7023)

Glycoblue (Thermofisher Scientific, AM9515)

Isopropanol (Sigma-Aldrich, I9516)

RNaseZap® Wipes (Thermofisher Scientific, AM9786)

TissueRuptor (Qiagen, 9001273)

TriReagent (Sigma-Aldrich, T9424)

TissueRuptor Disposable probes (Invitrogen, 990890)

DNase Treatment and cDNA synthesis

DNase I Amplification Grade (Thermofisher-Scientific, 18068-015)

Random Primers (Thermofisher-Scientific, 48190-011)

Set of dATP, dCTP, dGTP, dTTP (Promega, U1240)

Superscript II Reverse Transcriptase (Invitrogen, 1804014)

Water for molecular biology (Sigma-Aldrich, W4501)

Real Time PCR

MicroAmp® Fast Optical 96-Well Reaction Plate (Applied Biosystems, 4346906)

Fast SYBR® Green Master Mix (Applied Biosystems, 4385612)

Primers (Sigma-Aldrich)

Protein Work

Bradford Reagent (Sigma-Aldrich, B6916)

Bovine Serum Albumin (Sigma-Aldrich, A7906)

2.2 Tissue Culture

2.2.1 Animals

Sprague–Dawley rats were obtained from Charles River Laboratories. All procedures were carried out in accordance European directive 2010/63/EU and were approved by the Animal Ethics Committee of NUI Galway.

2.2.2 Slice Culture Preparation and Maintenance

Organotypic hippocampal cultures were prepared from P10-11 male/female Sprague-Dawley rat pups (Fig 2.1) (Gähwiler et al. 2001). Following decapitation, the skin was removed from each head by cutting from the base of the skull up to the nose. The skull was cut from the vertebral foramen bilaterally along the midline towards the frontal lobe and gently peeled off with forceps to expose the brain. The brain was scooped out of the cavity and placed into a petri dish containing ice-cold dissection medium (i.e. MEM Eagle, 10 mM Tris, 0.5 mM L-ascorbate, 2 mM L-glutamine and 100 U/ml penicillin and 100 µg/ml streptomycin). Once the cerebellum and cerebral cortex were separated by a midline incision, the two hemispheres were then separated by cutting along the longitudinal cerebral fissure. The midbrain was removed using forceps until the hippocampus was exposed. The hippocampus was then gently rolled away from the hemisphere.

Transverse hippocampal slices with a thickness of 400 µm were prepared using a McIlwain tissue chopper. The slices were gently separated under a dissection microscope. The slices were transferred to sterile Millicell culture inserts (Merck Millipore, Cork, Ireland) and cultured at 34°C in 5% CO_2 for 10-11 days prior to experimental treatment. The medium (1.1 ml per well) was changed 1 day after plating and then 2-3 times a week subsequently. The culture medium used was as follows: 50% Minimum Essential Medium (MEM), 25% heat-inactivated horse serum (HIHS), 25% Hank's balanced salt solution (HBSS), 28 mM D-glucose, 2 mM L-glutamine, 0.5 mM L-ascorbate, 63 µg/ml N-acetyl cysteine, 100 U/ml penicillin and 100 µg/ml streptomycin. For serum-free culture medium, 25% HIHS was replaced with 25% MEM Eagle.

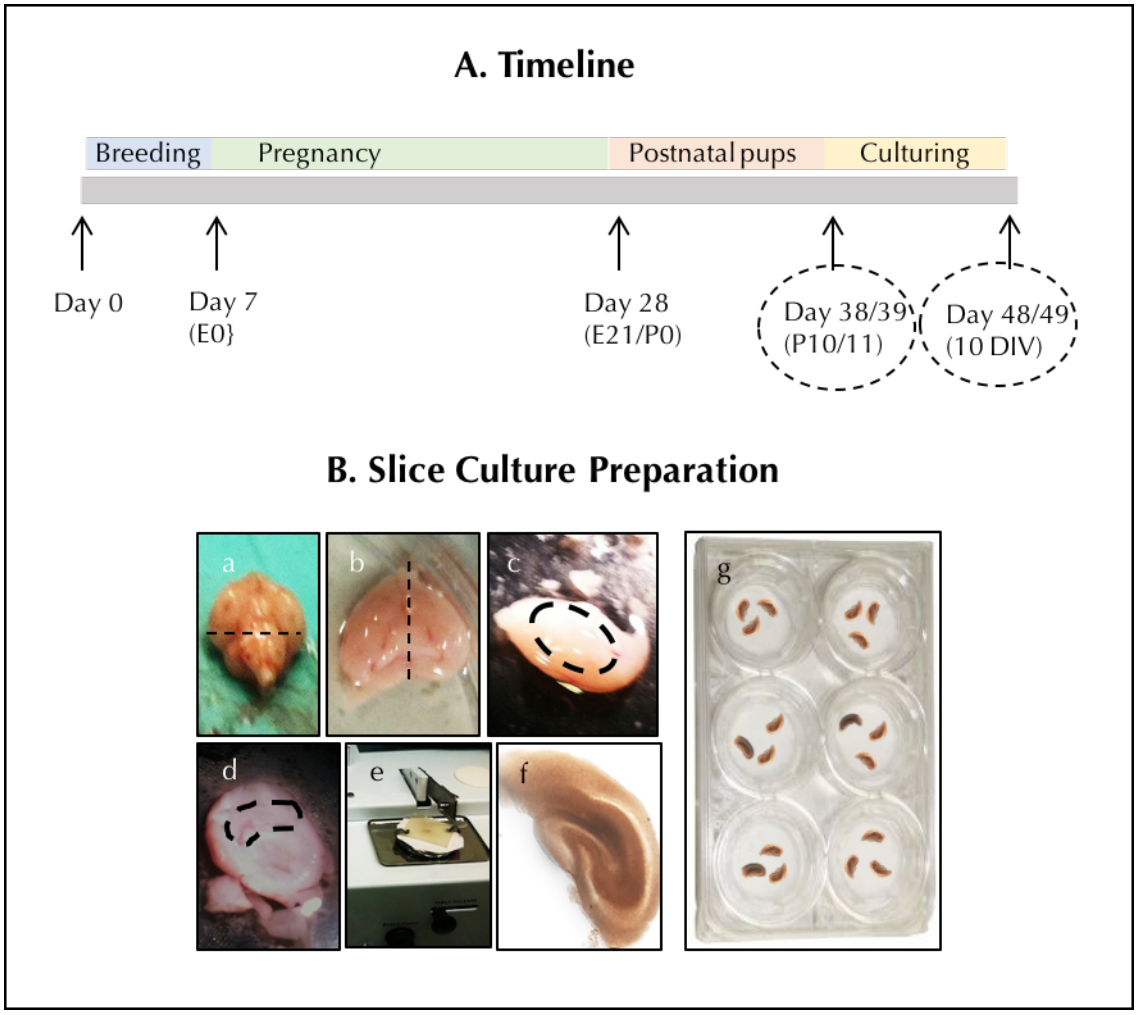

Figure 2.1: Slice culture preparation. A) Timeline of events. B) Step-by-step illustration of the dissection of hippocampus – (a) the cerebellum and cerebral cortex were separated by a midline incision, (b) the two hemispheres were then separated by cutting along the longitudinal cerebral fissure and (c) the midbrain was removed using forceps until (d) the hippocampus was exposed. The hippocampus was then gently rolled away from the hemisphere. Transverse hippocampal slices with a thickness of 400 µm were prepared using a (e) McIlwain tissue chopper and (f) gently separated under a dissection microscope and (g) transferred to sterile Millicell culture inserts.

2.3 Tissue Culture Treatments

2.3.1 Iron Loading

The following iron reagents were used: ferric citrate (FC), ferrous ammonium sulphate (FAS) and ferrocene (Sigma-Aldrich). These were chosen based on a literature search of previous iron loading studies and in order to encompass both ferric and ferrous forms of iron and also as a 'disguised form' of iron (i.e. one that bypasses import molecules) as ferrocene (Nielsen & Heinrich 1993; Rathore et al. 2012; Riemer et al. 2004; Hohnholt et al. 2010; Todorich et al. 2011; Robb & Connor 1998). Previous studies have shown that iron is released from ferrocene and its derivatives in various biological systems and undergoes normal physiological processing and metabolism (Stepnicka 2008; Madinaveitia 1965).

Iron loading was carried out in serum-free conditions. FC and FAS were reconstituted in dH_2O and ferrocene in DMSO. Cultures were washed once with pre-warmed serum-free medium and then incubated in this for 12 h prior to experimental treatment. Cultures were loaded with iron reagent or its respective vehicle for 12 h in serum-free medium. FC and ferrocene were stored as 5 mM stock solutions and kept light-protected at room temperature (RT). FAS was freshly prepared before use. The vehicle for FAS and ferric citrate was water and 0.1% DMSO for ferrocene.

2.3.2 UPR Activation

Tunicamycin (Tm), an inhibitor of n-glycosylation, was used to induce the UPR in slice cultures. Tunicamycin was stored as single-use 5 mg/ml aliquots at -20°C to ensure consistency. Using 12 h as a fixed time period to match the iron loading exposure, Tm concentrations ranging from 0.1-10 µg/ml were tested to determine which concentration activates the UPR without unduly compromising viability.

Tm exposure, like iron loading, was carried out in serum-free conditions. Cultures were washed once with pre-warmed serum-free medium and then incubated in this medium for 12 h prior to experimental treatment. Cultures were loaded with 5 µg/ml Tm, 1 µM ferrocene, 5 µg/ml Tm and 1 µM ferrocene or 0.2% DMSO (vehicle) for 12 h and then immediately harvested without recovery in fresh medium.

2.4 Iron Detection

2.4.1 Ferrozine Assay

The total amount of iron present (i.e. both ferrous and ferric) in the slice cultures and tissue dissectates was determined using a ferrozine-based colorimetric method (Riemer et al. 2004). Briefly, slices were solubilised in NaOH (220 µl at 50 mM) and then sonicated (Branson digital sonifier; 10% amplitude, 1 pulse per s for 10 s once for slice cultures and three times for dissectates). Bound iron was released using freshly prepared acidic potassium permanganate at 60°C for 2 h and detected after 30 min incubation with 60 µl iron detection reagent (6.5 mM ferrozine, 6.5 mM neocuproine, 2.5 M ammonium acetate, and 1 M ascorbic acid) by reading the absorbance of the ferrozine-iron complex at 550 nm in 250 µl reaction mixtures in wells of a 96-well plate (Riemer et al. 2004). For determination of the iron content, the absorbance of reaction mixtures containing samples was compared to that containing iron standards. Iron content was standardized to the protein content of slice cultures or tissue.

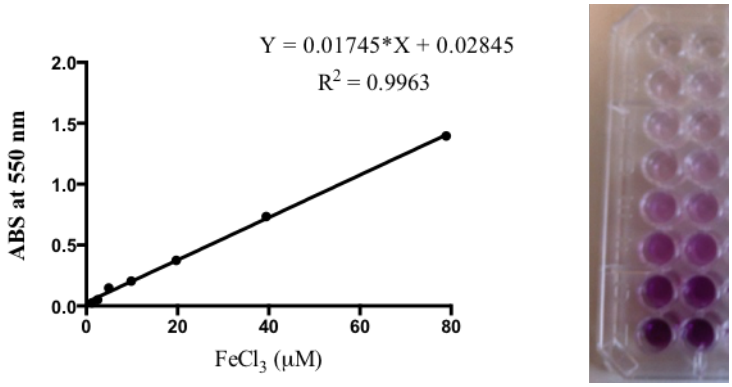

Figure 2.2: Detection of total iron content by colorimetric assay. There is a concentration dependent increase in absorbance of the ferrozine-iron complex read at 550 nm after application of $FeCl_3$ standards.

2.4.2 Bradford

The Bradford assay, a colorimetric protein assay (Bradford 1976), is based on the absorbance shift of the dye Coomassie Brilliant Blue G-250 dye from 465 to 595 nm upon protein binding. It is a quick, convenient and accurate means to detect protein concentration in samples. In triplicate wells in a 96-well plate, 2 µl of sample was mixed with 198 µl pf Bradford reagent. The protein concentration of the samples was determined from a bovine serum albumin (BSA) standard curve. The BSA standard solutions were prepared by dilution of a 500 mg/ml BSA stock to known concentrations ranging from 0-50 µg/ml, and included 2 µl lysis buffer. Absorbance was read at 595 nm.

2.5 Viability Assays

Two different cell viability assays were established in order to ascertain whether exposure to iron compound and ER stress inducers affected brain slice health: lactate dehyrdogenase (LDH) and MTT.

2.5.1 LDH Assay

Cell lysis and membrane damage can be determined by the lactate dehydrogenase (LDH) assay (Vassault 1974). LDH is a stable cytoplasmic enzyme present in all cells that is rapidly released into cell culture supernatant when the plasma membrane is damaged. It is a non-invasive and repeatable marker of cell viability.

Briefly, a 25 µl aliquot of supernatant was mixed with the 175 µl of reaction mixture (0.1 M phosphate buffer, pH 7.5, containing 100 mM sodium pyruvate and 0.1 mM NADH). The decrease in NADH absorbance, an index of LDH activity, was monitored at 340 nm for up to 10 min at room temperature in microtiter plate reader. Maximal LDH release (i.e. 100% cell death) was defined as the level of LDH present in supernatant following complete lysis with 0.5% Triton X-100.

2.5.2 MTT

The metabolic activity of cultures was assessed using an MTT [3-(4,5-Dimethylthiazol-2-yl)-2,5-Diphenyltetrazolium Bromide] assay in which the yellow tetrazolium salt is reduced largely through the action of mitochondria enzymes in viable cells to form purple formazan crystals (Mosmann 1983). MTT powder was dissolved in PBS to a 10x stock concentration of 5 mg/ml and stored at -20°C in 1 ml aliquots until required. For measurement of cell viability, MTT stock solution was added to each culture in the medium at a final concentration of 0.5 mg/ml and incubated for 30 minutes at 34°C. After incubation, slice cultures were scraped from the culture insert and transferred to 200 µl DMSO solution, in which the formazan crystals dissolve, and the absorbance was then read at 595 nm. All readings were normalised to DMSO-treated control cultures to give viability ratios and multiplied by 100 to give % viability.

2.6 RNA Expression Analysis

2.6.1 RNA extraction

RNA was isolated from slice cultures and *in vivo* brain tissue using TRIreagent as per the manufacturer's instructions. The samples were stored in 800 µl TRIreagent in 2ml RNase-free tubes at -80°C until required and then lysed using a tissue lyser (Qiagen, Manchester, UK). Once lysed, the samples were incubated at room temperature for 5 min to allow complete dissociation of nucleotide/protein complexes. Chloroform was added to the samples (160 µl/ sample) and samples were shaken vigorously by hand for 15 seconds. After a 5 min incubation at room temperature, samples were centrifuged at 12,000 x g for 15 min at 4°C.

The mixture separates into a lower (red) phenol-chloroform phase containing protein, an interphase containing DNA and the upper (colourless) aqueous phase containing the RNA. Approximately 300 µl of the aqueous phase was carefully transferred to a clean microcentrifuge tube (and the lower organic phase was stored at 4°C for protein extraction). The RNA was precipitated from the aqueous phase by adding 300 µl isopropanol and 1 µl glycoblue to enhance visibility of the RNA pellet. The samples were then placed at -80°C overnight, after which time they were spun as 12,00 x g for 10 min at 4°C. After centrifugation, the supernatant was discarded. The pellet was washed and centrifuged twice at 8,000 x g for 5 min at 4°C with 75% ethanol (800 µl/sample).

Finally, the pellet was air-dried for 5 min at room temperature. The RNA pellet obtained from the *ex vivo* slice cultures was re-suspended in 15 µl DEPC-treated water, whereas the pellet from the *in vivo* CNS tissue was re-suspended in 50 µl. The RNA concentration was quantified by spectrophotometry at 260/280 nm using the Nanodrop ND-2000 (Qiagen). The RNA had an A260/280 ratio between 1.8 and 2.1 indicating RNA was free from contaminants from the isolation procedure. The RNA was kept at -80°C until required.

2.6.2 DNase treatment and cDNA synthesis

Extracted RNA was treated with DNase to remove any DNA from the samples that could otherwise result in false positives. The DNase enzyme cleaves DNA non-specifically to leave 5' phosphorylated oligodeoxynucleotides. The DNase treatment was carried out according to the manufacturer's instruction (Thermofisher-Scientific, Dublin, Ireland). Briefly, 500 ng of RNA from *ex vivo* slice cultures or 1000 ng of RNA from *in vivo* brain dissectates was mixed with 1 µl of 10x DNase I reaction buffer and 1 µl DNase I. The mixture was diluted with RNase-free water to 10 µl and incubated for 15 min at room

temperature. The reaction was terminated by adding 1 µl of 25 mM EDTA and a 10 min incubation at 60°C.

Following DNase treatment, tubes were placed on ice for 2 min prior to reverse transcription. The cDNA was synthesised by reverse transcription using Superscript II (Thermofisher-Scientific). Briefly, 50 µM random primers, 10 mM dNTP, 0.1 M DTT, 200 units Superscript II and water as per manufacturer's instructions. Samples were run on a thermocycler using the following incubation steps: 25°C for 10 min, 40°C for 50 min and 70°C for 15 min. The cDNA was stored at -20°C until required.

2.6.3 Real time PCR

Quantitative real-time PCR (qPCR) is a type of reverse transcription PCR, which measures the amount of transcripts present in a sample in "real time". This method is based on the fluorescent measurement of the amplified product on termination of each cycles.

The SYBR Green detection system is the simplest and most economical choice for qPCR. Upon addition to the PCR reaction mixture, the SYBR Green dye immediately binds to any double-stranded DNA present and then binds to each new copy of double-stranded DNA formed during PCR. This results in increased fluorescence intensity that is proportional to the amount of double-stranded PCR product produced.

Gene expression was analysed by qPCR using the StepOne™ Real-Time PCR System (Applied Biosystems, Paisley, UK) and Fast SYBR® Green PCR Master Mix (Applied Biosystems), containing ROX as a reference dye. The qPCR reactions were run in 20 µl solutions in MicroAmp® Fast Optical 96-Well Reaction Plates (Applied Biosystems).

For each sample, the gene of interest and the reference gene were run in parallel in either duplicate or triplicate reaction solutions that contained forward and reverse primer, 2 µl of template cDNA, 10 µl of 2x Fast SYBR green master mix and nuclease-free water. In addition, a "no template" and a "negative reverse transcription" controls were included on each plate in order to demonstrate the absence of amplicon contamination. The plate was sealed and centrifuged at room temperature for 1 minute at x g to mix and move all contents to the bottom of the wells.

The PCR conditions suggested in the manufacturer's protocol were followed. This included an initial denaturation at 95°C for 20 sec, 40 cycles at 95°C for 3 sec and 60°C for 30 sec. A melt curve was generated after PCR amplification in order to investigate the specificity of the qPCR reaction and the presence of primer dimers.

2.6.4 Data Analysis of Gene expression

The ΔΔCt method (Applied Biosystems Research Bulletin No. 2 P/N 4303859) was used to quantify the data obtained by real-time PCR.

Cycle threshold (Ct) value, which is the number of cycles required for fluorescent signal to reach a detectable threshold, was obtained for each gene of interest and the reference gene for all experimental samples. ΔCt is calculated by subtracting the Ct values of the reference gene from the Ct values of the gene-of-interest for each sample. ΔΔCt is then calculated by comparing the ΔCt values for the sample of interest with that of the control sample.

The initial choice of 18s as a reference gene was based on experiments carried out by a previous PhD student who tested changes in a range of reference genes in postnatal cerebellum CNS tissue and confirmed that it was stably expressed between samples and conditions within this experiment. Nonetheless, stringent evaluation of the stability of 18s, ß-actin and GAPDH as potential reference genes in in the cDNA generated from the iron-loaded slice cultures experiments revealed that it was not as stable as ß-actin was between conditions. Consequently, 18s and ß-actin were used for *in vivo* and *ex vivo* studies, respectively

2.6.5 Primers

2.6.5.1 Primer Design

Primers are short synthetic oligo sequences that bind specifically to a DNA strand and act as a binding site for DNA polymerase to begin synthesizing the new DNA strand. It is necessary to critically design and evaluate primer characteristics prior to synthesis and use because SYBR Green binds non-specifically to any double-stranded DNA and may also bind to primer dimers or contaminating DNA or PCR product from mis-annealed primers and thereby lead to false positives.

Unless otherwise noted, all primers were designed using Primer3 software according to the guidelines suggested by Thornton et al. (2011). The following criteria were employed to ensure that optimal primers were designed: primer length (18-30 bases), melting temperature (60-63°C) GC content (45-55% with fewer than 5 sequential Gs), amplicon length (80-200 base pairs) and location (spanning exon junctions).

The secondary structure (e.g. hairpins, primer-dimers and self-dimers formed by inter- or intra-molecular forces) of the potential primers and the amplicon was visualized using Beacon Designer Free Edition and mFold software, respectively. Finally, BLAST (http://www.ncbi.nlm.nih.gov/BLAST/) searches were also conducted on all

primers to ensure unique specificity to the gene of interest. Table 2.2 details primer sequences.

The primers that were used were synthesized by Sigma-Aldrich and upon arrival were immediately dissolved in nuclease-free water to 100 µM stock solutions. Three µM working stock solutions were prepared from these stocks. All primer stocks were stored at -20°C.

2.6.5.2 Primer Optimisation

Standard curves were run for each set of primers prior to experimental usage to calculate and optimise their efficiencies. The delta delta Ct method assumes the gene-of-interest and reference gene both have 100% efficiencies. Efficiencies within 100% ±10% were considered acceptable, otherwise primers were discarded and new ones were redesigned and tested. A 100% efficiency corresponds to a slope of -3.32 and represents an exact doubling every cycle. The primer efficiencies were calculated according to the equation: $E = (10^{-1}/m^{-1}) * 100$, where m is the slope of the linear regression model fitted over log-transformed data of the input 1:10 diluted cDNA concentrations versus Ct values.

Five-point standard curves of 10-fold dilution series (1:10 to 1:1,000,000; see Figure 2.2 as an example standard curve) were prepared as follows: 20 µl neat cDNA was diluted 1:10 with 180 µl nuclease-free water and mixed well each step and repeated 4 times to generate 5 dilutions. Two µl of each dilution was added as cDNA (along with NTC and NRT), in duplicate or triplicate, to assess 2-3 primer concentrations (typically, 100, 300 and 500 nM).

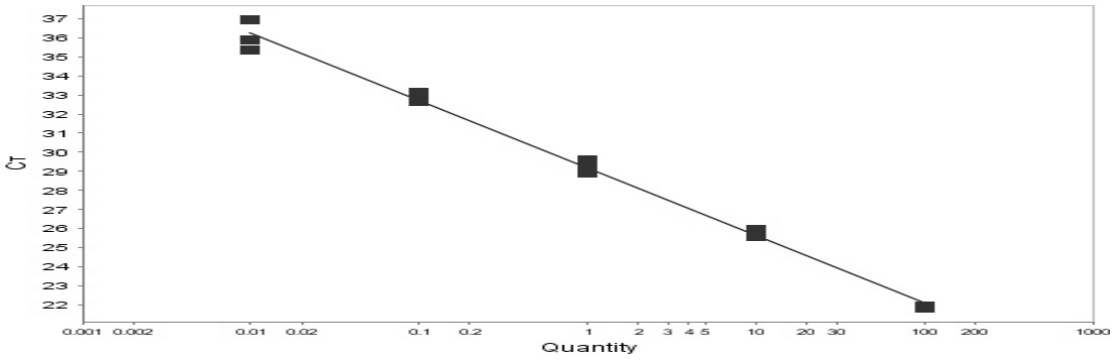

Figure 2.3: Standard curve. Representative graph depicting the 5-point standard curve of 10-fold dilution series for FTL. 300 nM is optimal concentration for both forward and reverse primers with an efficiency = 92% and $r^2 = 0.995$.

2.6.5.3 Melt Curve

A melt curve was generated after PCR amplification in order to investigate the specificity of the qPCR reaction and the presence of primer dimers. During melt curve analysis, products from the PCR are denatured by slowly increasing the temperature of the samples from 60°C to 90°C. The melt curve software plots the rate of change of the relative fluorescence units (RFU) with time (T) (-d(RFU)/dT) on the Y-axis versus the temperature on the X-axis. A significant change in fluorescent signal and peak signal occurs at the melting temperature (Tm) of the target amplicon.

Since each double-stranded DNA has its own Tm (based on its length and GC content), the presence of any potential unwanted PCR by-products such as primer-dimers or non-specific products can be identified on a melt curve because two or more peaks are obtained. A single peak on the melt curve analysis means that only one specific product is present (Fig. 2.4). Non-specific products tend to melt at a lower temperature than the target amplicon and present with low broad peaks.

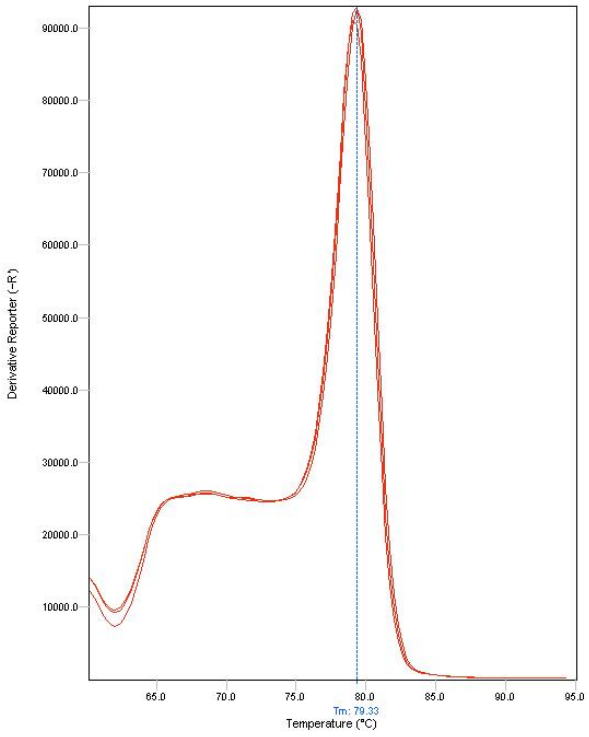

Figure 2.4: PCR melt curve. Representative graph of the melt curve of a gene product. The melt curve shows a single peak that indicates specificity of the primers used for PCR amplification.

Table 2.1 Primer details for Genes analysed by real-time PCR

Gene	Accession No.	Forward (5′-3′)	Reverse (5′-3′)
Iron			
FTL	nm_022500.4	ctcctcaagttgcagaacgaac	gttttaccccactcatcttg
FTH	nm_012848.2	atccccacttatgtgacttc	cttgtcaaagagatattctgcc
DMT1-IRE(+)*	nm_013173.2	gcctgtctgtctgtctttgc	cccagtgtttcccaactaaca
DMT1- IRE(-)*	nm_001031658.1	tagatgaccaacagcccaga	cacagccgttagctttaccc
FPN	nm_133315.2	agaggaggaattttgctgagg	tgccatgaccaagtcaagag
TfR1	nm_022712	accactcacccaagttacatcc	ggctgaaaatcccactatgc
Tf	nm_001013110.	aaccatatttgaggtcttgc	ctctttgccatctccatttc
gpiCp †	af202115.1	ggttactccactgccatgtg	gtgtatagagtatgttccagg
Cp †	nm_012532.2	tggtttatcgtgagtacacag	tctgcccaaatgacaggacc
Tim2	nm_001013855.1	ctgcaacatcctcagatgactc	ccaacatagaagcccttagtcg
HEPH	nm_133304	ccatcttctctgggctttactg	gcccaggtagtagtttcgaatg
UPR			
ATF4	nm_024403.2	tcagacaccggcaaggag	gtggccaaaagctcatctg
ATF6	nm_001107196.1	ggaccaggtggtgtcagag	gacagctctgcgctttgg
BiP	nm_013083.2	cctattcctgcgtcggtgtatt	ggttggacgtgagttggttc
CHOP	nm_024134.2	gaaatcgagcgcctgaccag	ggaggtgatgccaacagttca
CRT	nm_022399.2	agcagttcttggacggagatg	tgtttggattcgacccagc
XBP1s	nm_001004210	gagtccgcagcaggtgc	ggtccaacttgtccagaatgc
XBP1uns	nm_001004210	cagactacgtgcgcctctg	cttctgggtagacctctggg
Housekeeping			
ßactin ‡	nm_031144.3	cacactgtgcccatctatga	ccatctcttgctcgaagtct
18s ‡	m11188.1	aatcagttatggttcctttgtcg	gctctagaattaccacagttatccaa

Unless otherwise noted, all sequences were designed using Primer3. * denotes primer sequences taken from (Pelizzoni et al. 2012), † from (McCarthy & Kosman 2014) and ‡ from (Kraskiewicz & FitzGerald 2011) and ** from (Lin et al. 2005) . All primers were optimised to ensure specificity and optimal efficiency.

2.7 Immunohistochemistry

Slices were fixed in 4% paraformaldehyde (PFA) for 30 min followed by three washes in PBS and storage at 4°C in PBS containing 0.1% $NaNO_3$. In order to minimise reagent volume, membrane around the slices was trimmed using a scalpel allowing incubations to take place in a 24–well plate. Slices that were still attached to membranes were blocked and permeabilised for 1 h with 10% normal goat serum (NGS; NGS was replaced with 10% horse serum when using the Iba1 goat antibody) and 0.4% Triton X-100 in PBS. Subsequently, the slices were incubated with primary antibody (for single and dual labelling) in 2.5% NGS (or 2.5% horse serum) and 0.1% Triton X-100 in PBS for 48 h at 4°C and then washed three times for 15 min before incubation with the appropriate secondary antibody at 4°C overnight (see Table 2.2). Slice cultures were mounted in Vectashield containing diamino-2-phenylindole (DAPI) (Vector Laboratories, Peterborough, UK) to allow visualisation of nuclei. Negative "no primary antibody" controls were included. Slides were stored in the dark at 4°C until imaged.

The ferritin antibody (F5012, Sigma-Aldrich) used is mostly specific for ferritin light chain but ferritin heavy chain staining has also been described (Hametner et al. 2013; Shoham & Youdim 2002; Zarruk et al. 2015). Given that neurons have previously been described predominantly to contain the heavy subunit whereas microglia, astrocytes and oligodendrocytes contain the light subunit (Connor and Benkovic 1992; Connor et al. 1990; Roskams and Connor 1994) this antibody is mostly useful as a marker of iron accumulation in glia rather than neuronal cells.

Table 2.2 Antibody source and dilution used for immunohistochemistry

Antibody	Host/Isotype	Supplier	Catalogue No.	Dilution
Cell Markers				
Olig2	Mouse mAb	Millipore	MABN50	1:80 **1:100 1:150**
Olig2	Rabbit mAB	Millipore	AB9610	**1:500**
GFAP	Rabbit pAb	Dako	Z0334	**1:1000**
GFAP	Mouse mAb	Sigma	G3893	**1:500**
NeuN	Mouse mAb	Millipore	MAB377	**1:1000**
SMI-32	Mouse mAb	Abcam	AB28029	**1:1000**
Iba1	Goat pAb	Novus Biologicals	NB100-1028	**1:100** 1:200 1:400
Iba1	Rabbit pAb	Wako	091-10741	**1:1000**
Ox42 †	Mouse mAb	Millipore	CBL1512	unsuccessful
Iron Homeostasis				
DMT1	Rabbit pAb	Alpha Diagnostics	NRAMP23-S	1:250**1:600** 1:1000
Ferritin	Rabbit pAb	Sigma	F5012	1:100 **1:200** 1:400
FTL †	Rabbit pAb	Abcam	Ab69090	unsuccessful
Hepcidin †	Rabbit pAb	Abcam	Ab30760	unsuccessful
FPN	Rabbit pAb	Alpha Diagnostics	MTP11-A	1:250 **1:600** 1:1000
UPR				
ATF6	Rabbit pAb	Abcam	Ab37149	1:100 **1:150** 1:300
BiP/GRP78 †	Rabbit pAb	Abcam	Ab37149	unsuccessful
CHOP	Mouse mAb	Cell Signalling	L63F7	**1:100**
CRT	Mouse mAb	Abcam	Ab22683	unsuccessful
Secondary (Alexafluor)				
Anti-mouse 488	Goat pAb	Invitrogen	A11001	**1:1000**
Anti-rabbit 594	Goat pAb	Invitrogen	A11037	**1:1000**
Anti-goat 488	Donkey pAb	Invitrogen	A11055	**1:1000**

Dilutions highlighted in bold were the ones used following optimization. Abbreviations: mAb= monoclonal antibody, pAb=polyclonal antibody † optimization was unsuccessful despite varying fixation, permeabilisation and dilution steps.

2.8 Image acquisition and processing

2.8.1 Image Acquisition

All samples were imaged on a laser scanning confocal microscope (Olympus Fluoview 1000) using a 40x oil-immersion lens (numerical aperture of 1.3) equipped with blue argon laser (488 nm), green helium-neon laser (543) and 405 nm diode laser. Settings (laser power, voltage, gain and offset) were optimised for each antibody and kept consistent for subsequent imaging. Z-projection images were acquired to encompass the staining that was detectable within the slice (e.g. 5, 10 and 15 µm z-stack thickness for GFAP, OLIG2 and IBA1, respectively, with steps at 1 µm intervals).

2.8.2 Image Analysis

Images were processed using FIJI software (version 2.0.0-rc-49/1.51d). This platform was chosen for the following reasons: it requires only open source software and is cost-effective, flexible, freely inspectable, modifiable and redistributable and is readily usable for neuroscience researchers not having previous knowledge of algorithms or scripting language.

Due to morphological differences and the appearance of stained cells using different cell-specific antibodies, images of different glial cells were captured and analysed using different image analysis paradigms. These types of automated image analysis protocols are robust and well established in the literature and have numerous advantages in that they account for image variations, enable convenient and quick batch processing, avoid user bias and offer dozens of flexible options within a user-friendly interface.

Nevertheless, we are cognizant that such binary segmentation as that employed here is imperfect. Consequently, we have developed a way of selecting the optimal threshold segmentation algorithm for correctly identifying glial cells in hippocampal organotypic slice cultures by employing Brochener's Bio-Voxxel method (a full-description of the development, optimisation and evaluation of this workflow is given in chapter 6). We have also validated our methodology by double-counting oligodendrocyte-lineage cells using an alternative design-based stereological enumeration method on a cohort of images (2.8.3.2).

For the purposes of publication, the sample images of fluorescent staining have been enhanced as follows. All images were opened in Adobe Photoshop and modified using the sequence: Image>Adjustments>Brightness/Contrast to allow increased

contrast. The contrast values were increased by between 20 to 50 points in order to provide the clearest picture of immunofluorescent staining.

2.8.2.1 Microglia

To determine the activation status and number of microglia, six representative fields (15 µm z-stack with 1 µm intervals) were acquired per slice i.e. 36 per treatment group for a combined total of 216 images from 3 independent experiments. Based on the method of Morrison et al (2013), a custom macro was used to generate a maximum intensity projection image, subtract background using a rolling ball of 500 pixels and despeckle image. Once the image was binarised, the skeleton was extracted using the Skelentonise 2D/3D plugin that iteratively erodes particles to generate centrelines that are one pixel wide (i.e. a skeleton) while maintaining particle connectivity. At this point, the number of skeletons could be equated with microglial cell number.

The AnalyzeSkeleton plugin (http://imagejdocu.tudor.lu/) was then applied to the skeletonised images to determine the number of endpoints per frame (subsequently normalised to the number of skeletons per frame). The number of endpoints is a measure of microglia branching complexity and loss of complexity indicates activation (Morrison & Filosa 2013; Perry et al. 2010; Streit et al. 2009). Endpoint is defined as voxel that only has one neighbour and thus is the end of a branch.

2.8.2.2 Oligodendrocytes

In order to quantify changes in the oligodendrocyte population, seven fields (10 µm z-stack with 1 µm intervals) were acquired systematically throughout slice i.e. 42 images per treatment group, generating a combined total of 252 images from 3 independent experiments. Olig2-positive cells were counted using a custom macro (see Fig. S2 for details). Briefly, a maximum intensity projection image was generated for each z-stack, background was subtracted using a rolling ball of 50 pixels and thresholded using Otsu's method to produce a 8-bit binary image where the pixels that exceed this threshold were converted to a value of 255 (black), while pixels below this threshold were converted to a value of 0 (white). The watershed segmentation algorithm was then used, which separates clusters of nuclei that are very close together, or touching, into individual cells. Finally, using the *Analyse Particles* function, the total number of particles with a size greater than 20 μm^2 was determined.

2.8.2.3 Astrocytes

To determine if astrocytes were affected by exposure to iron, slices were stained using GFAP antibody and the area of GFAP-positive staining was quantified. Five representative fields (5 µm z-stack with 1 µm intervals) were acquired per slice culture i.e. 20 fields over 4 slices per treatment, to generate a total of 120 images from 3 independent experiments. The GFAP-positive area was determined by generating a maximum intensity projection image for each z-stack, subtracting background with a rolling ball of 50 pixels and applying Bernsen threshold, with a radius of 15 µm. Then, using the *Analyse Particles* function, the total area was determined. This area was expressed as percentage of the area of the total field.

2.8.3 Image Analysis Methodology Validation

2.8.3.1 Qualitative and Quantitative Binarization Evaluation

A subset of images, i.e. 16 maximum intensity projection images (i.e. 2 fields/slice, 2 slices/well, 2 wells/2 experiments), were used to evaluate threshold segmentation performance for identifying astrocytes, oligodendrocytes and microglia.

Brocher's semi-quantitative color-coded evaluation of segmentation (Brocher 2014), available within the Biovoxel plugin on ImageJ and FIJI platforms, compares the original test image against the 16 global and 9 local autothresholding algorithms. Global thresholds: Default, Huang, Intermodes, Isodata, Li, MaxEntropy, Mean, MinError, Minimum, Moments, Otsu, Percentile, RenyiEntropy, Shanbhag, Triangle and Yen. Local thresholds: Bernsen, Contrast, Mean, Median, Midgrey, Niblack, Otsu (local), Phansakar and Sauvola.

A single reference intensity value per image is used to classify each pixel as an object or non-object (i.e. background), giving 4 categories for each pixel: object-of-interest/cellular staining, (true positive; TP), background (true negative; TN) over-estimated (false positive; FP) and under-estimated (false negative; FN). To evaluate performance, the number of pixels assigned to each category is counted, and the following metrics are calculated: sensitivity, specificity, accuracy and relative quality.
Accuracy is derived from sensitivity (i.e. correctly identified positives) and specificity (correctly identified negatives) parameters. Relative quality is a measurement of absolute quality where 100% represents a perfect binary production of the test image i.e. every pixel is correctly labelled without missing object as background or mislabeling any background as an object.

2.8.3.2 Stereology

In order to validate the positive cell count that was detected from the automated maximum intensity projections, a subset of images was manually quantified using unbiased stereology principles (Schmitz & Hof 2005; Mayhew 1992). A Pearson correlation coefficient was computed to assess the relationship between two groups. Seventy-two images were counted from 2 independent experiments i.e. 3 fields/slice, 2 slices/well and 2 wells/treatment group, with stereology counting taking approximately 2 min per image. It was not considered feasible to spend the 9 h that manual stereology would require on all the 252 images acquired, which was why we only sampled approximately a third of the images.

The physical dissector method was used to count the number of OLIG2-postive cells present in the reference section that were not present in the corresponding look-up section according to unbiased stereology principles (Howard & Reed 2004). A constant 5 µm physical dissector height was used at z-slice 1 and 5 of the stack. This distance corresponds to approximately half to a third of the average particle size. Four small unbiased counting frames per sectional image were used for counting. This gives the numerical density that, along with the volume reference, is used to calculate the total number of cells per z-stack.

2.9 Statistical Analysis

Data was analysed using Prism 6 (GraphPad Software). All measurements were expressed as mean ± standard error of the mean (SEM) unless otherwise indicated. Normality was assessed using the Shapiro-Wilk test. Statistical analyses were carried out using Student's t-test, Mann-Whitney test or an ANOVA with Dunnet post-test, as appropriate, and as indicated in figure legends. A Pearson correlation coefficient was computed to assess the relationship between two groups. Differences were considered statistically significant if $P<0.05$.

3 Characterisation and comparison of the iron homeostasis molecules in neonatal and *ex vivo* brain

3.1 Introduction

Organotypic cultures are efficient and reliable *ex vivo* models that combine the accessibility and convenience of *in vitro* models with the preservation of most of the complex brain milieu present in *in vivo* studies (Cho et al. 2007; Gähwiler et al. 1997; Sundstrom et al. 2005; Daviaud et al. 2013; Humpel 2015a). Over the last two decades, numerous studies have contributed to development and optimisation of *ex vivo* brain slice cultures as a validated platform for studying normal and disease functions. Indeed, slice culture systems have been successfully established from a variety of CNS regions, including hippocampus, striatum, cortex, spinal cord and cerebellum, and have been used to model neurodegeneration and regeneration amongst a multitude of other studies (Cho et al. 2007; Gähwiler et al. 1997; Sundstrom et al. 2005; Daviaud et al. 2013; Humpel 2015a).

To date, however, the *ex vivo* brain slice platform has not been appreciated for its inherent advantages over *in vitro* monocultures or co-cultures in studying iron handling in the CNS. In addition to better matching cellular composition of the CNS, the *ex vivo* slice cultures also more closely resemble the mature CNS compared with monocultures because they are often derived from older postnatal animals and then typically continue to develop as normal while in culture prior to experimentation. Nevertheless, only Li et al. (2003) have exploited the use of this platform for loading iron. This study focused only on iron in oxidative stress and did not attempt to model or measure iron deposition or changes in iron molecules. Consequently, the overarching aim of my PhD project was to exploit the *ex vivo* platform as means to model and investigate iron perturbations in neurodegeneration in the CNS.

3.2 Aims:

As a prelude to the chapter 4, the work described in this chapter aimed to investigate the validity and advantages of the *ex vivo* slice culture platform, and how best to employ one of its numerous iterations towards the specific iron handling question.

Specific aims

i. Define the basal levels of iron and iron homeostasis molecules in *ex vivo* slice cultures and compare with age-equivalent in vivo tissue.

ii. Characterise the molecular profile of the iron homeostasis system in neonatal rat brain

3.3 Summary of methodology

Sprague-Dawley rat pups were bred from pregnant females obtained from Charles River. Day of birth was designated day 0 (P0). Animals were sacrificed by decapitation at P4, P7, P10 and P14, and by CO_2 asphyxiation at P21 and adult (>6 months; n=3 for RNA and n=6 for iron). Hippocampus (P4, P10, P14, P21 and adult), cerebellum (P7, P10, P14, P21 and adult) and P10 *in vivo* CNS tissue (hippocampus, cerebellum, brainstem, midbrain, olfactory bulb, cortex; n=3 for RNA and n=6 for iron analysis) were dissected and snap-frozen in Trireagent to develop a molecular characterisation of the iron homeostasis system in the rat brain

3.4 Results

3.4.1 Primer Optimisation

Postnatal CNS and liver tissue was used to generate cDNA to optimise primer concentration for PCR. Chapter 2 Figs 2.3 and 2.4 in chapter 2 depict a typical standard curve and melt curve used to demonstrate the suitability and validity of the primers for use in δδCt quantitation in real-time PCR. Table 3.1 provides primer sequences and concentrations of primers tested during optimisation. In total, 12 primers for different genes of interest were successfully assessed. Although the primers were mostly designed in-house using the Primer3 software, 4 primer sequences were taken from the literature and 1 primer, the reference gene 18s, was already available in the lab. Consequently, 18s was the only primer that had previously been optimised. We were able to confirm previous findings demonstrating 100% primer efficiency at 100/100 nM. In all cases, a standard curve for 2-3 different primer concentrations, typically 100/100, 300/300 and 500/500 nM for forward/reverse primers, were tested to determine the concentration that produced optimal efficiency and presented a good melt-curve profile. Despite several attempts on both self-designed and literature sourced primers, it was not possible to optimise primers for FtMt, DCYTB, hepcidin or lactoferrin because of unacceptable primer-dimers indicated on melt curve and/or poor primer efficiency

Table 3.1 Optimisation of primers that were used in this study

Primer	Concentration F/R (nM)	Efficiency (%)	R^2
FTL	300/300	92	0.995
FTH	100/100	100	0.985
Cp	100/100	93	0.96
gpiCP	100/100	94	0.99
Tf	100/100	89	0.92
TfR1	300/300	90	0.95
HEPH	100/100	91	0.92
Tim2	100/100	98	0.953
FPN	100/100	99	0.9
DMT (+IRE)	100/100	92	0.97
DMT (-IRE)	300/300	99	0.9
18s	100/100	107	0.998

Abbreviations: F, forward; R, reverse.

3.4.2 Levels of iron in cultured slices are representative of those found in vivo

We report, for the first time to our knowledge, that the iron content of these *ex vivo* slice cultures, which is 5.69±0.61 nmol iron/mg protein, is in line with the physiological iron content (i.e. 2-50 nmol/mg; Fig. 3.1) reported for cultured astrocytes, neurons, microglia and oligodendrocytes**.** In order to determine if levels of iron in cultured slices reflect those present in age-matched tissue *in vivo*, the amount of iron in *ex vivo* P10/P11-harvested hippocampal slices that had been cultured for 10 days *in vitro* (DIV) was compared to the level of iron detected in hippocampal dissectates isolated from P21 rats. The iron content detected did not differ significantly (Fig. 3.2).

3.4.3 Expression of iron storage transcriots in the developing hippocampus

However, at the mRNA level, there was an up- or down-regulation of several iron homeostasis molecules. For the storage molecules, there was significant increase in the levels FTL transcripts although FTH was unchanged in *ex vivo* slice cultured compared with the *in vivo* P21 tissue (Fig. 3.2). Similarly, two of the four import molecules were significantly down-regulated, i.e. TfR1 and DMT (-IRE), whereas Tf and DMT (+IRE) were unchanged. The direction of change in the expression of iron export proteins differed. That is, in cultured slices, FPN, gpiCP and HEPH transcripts were significantly down-regulated, up-regulated or unchanged, respectively. To help put these perturbations into context, we assessed the transcript expression in the postnatal hippocampus *in vivo* at P4, P10, P14, P21 and adult (>6 months).

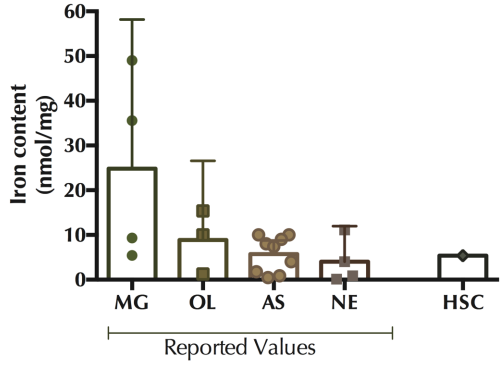

Figure 3.1: Basal iron content comparison with published values. Iron content in cultured CNS cells varies between studies and between cells types (each data point represents the mean of one published study; data expressed as mean ± SEM). To the best of our knowledge, only one published study, i.e. our work demonstrating iron content of P10/11+10 slice cultures, has reported the iron content in hippocampal slice culture.. Abbreviations, AS, astrocytes; HSC, hippocampal slice culture, MG, microglia; NE neurons and OL, oligodendrocytes.

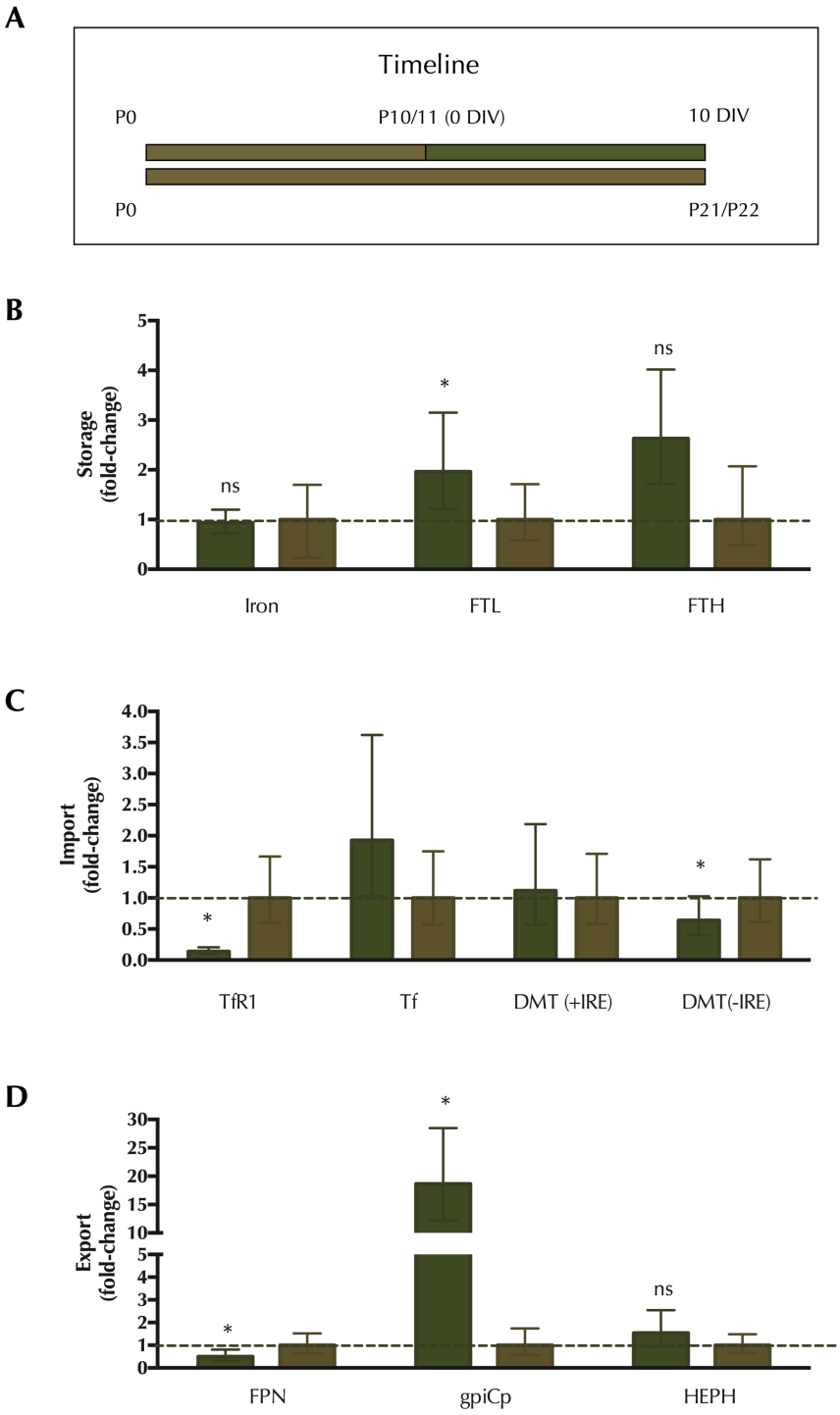

Figure 3.2: Comparison of iron and expressed RNA transcripts of iron handling proteins in *ex vivo* slice cultures and age-equivalent *in vivo* tissue. (A) Timeline. P10/11+10DIV *ex vivo* tissue is temporally equivalent to P21 *in vivo* tissue. (B) Storage Molecules. (C) Import molecules. (D) Export molecuels. There is no difference in iron content or transcripts of FTH, Tf, DMT (+IRE) or HEPH. However, levels of FTL, TfR1, DMT (-IRE), FPN and gpiCp are significantly higher or lower. Results are expressed as fold-change of P21 *in vivo* tissue, which is indicated by the dashed line. Values are mean ± 95% confidence interval (n=3 animals for mRNA and n=6 animals for iron content). * denotes difference between *ex vivo* slice cultures and *in vitro* tissue.

3.4.4 Expression of iron homeostasis transcripts in the developing rat hippocampus

Firstly, we assessed the expression of iron and its storage proteins, FTH and FTL, in the developing hippocampus (Fig. 3.3). A decrease in iron content was observed in the maturing postnatal hippocampus *in vivo* (aged P7-adult; n=6; Fig. 3.3; $P<0.05$). There was a trend towards down-regulated FTL transcripts that did not reach statistical significance. A 2- and 1.2-fold higher mean expression of FTL was seen at P4 and P10 samples, respectively, when compared with adult and no difference at P14 or P21 when compared to adult. Conversely, there were significantly fewer FTH transcripts detected in hippocampal tissue at each postnatal time point (with the exception of P10) when compared with transcript levels in adult samples. The postnatal tissue at P4, P14 and P21 all had comparable levels of FTH transcript, which were approximately half those detected in adult tissue.

Although there were few statistically significant differences in the expression of the import molecules, there were several interesting trends towards up- or down-regulation in several molecules (Fig. 3.4). Tim2, for instance, was expressed between 2-to 6-fold higher in the postnatal hippocampal tissues compared with adult, but this trend did not reach statistical significance. Tf expression was considerably and significantly lower at P4, P10, P14 compared with P21 and adult hippocampal tissue, whereas there was an apparent lower, albeit non-significant, expression at P21 against adult. TfR1 expression remained consistently expressed at all time points. DMT (-IRE) was detected at significantly lower transcript levels at P4 compared with adult. P10, P14 and P21 samples had slightly higher levels of DMT (-IRE) transcript from P4, but this was not found to be significantly increased, or alternatively, significantly lower than adult. The expression of DMT1 (+IRE), on the other hand, was the highest at P4 and P10, undergoes a significant and transient drop at P14, and then is increased again in P21 and adult

A similar pattern was detected in the export molecules (Fig. 3.5). There were no significant differences in gpiCP and Cp transcript levels during development. However, there was a trend towards a lower expression at P10 and P14 compared with P4 and then a subsequent trend towards an increase at P21 and adult. There was a similar u-shaped expression pattern seen for HEPH except that the difference was significant at each time point when compared to adult levels, and also at P10 and P14 versus P21, and P4 versus P10. FPN expression, however, was approximately 2-fold higher at P4, P10, P14 and P21 compared to adult, with the p21 increase being statistically significant.

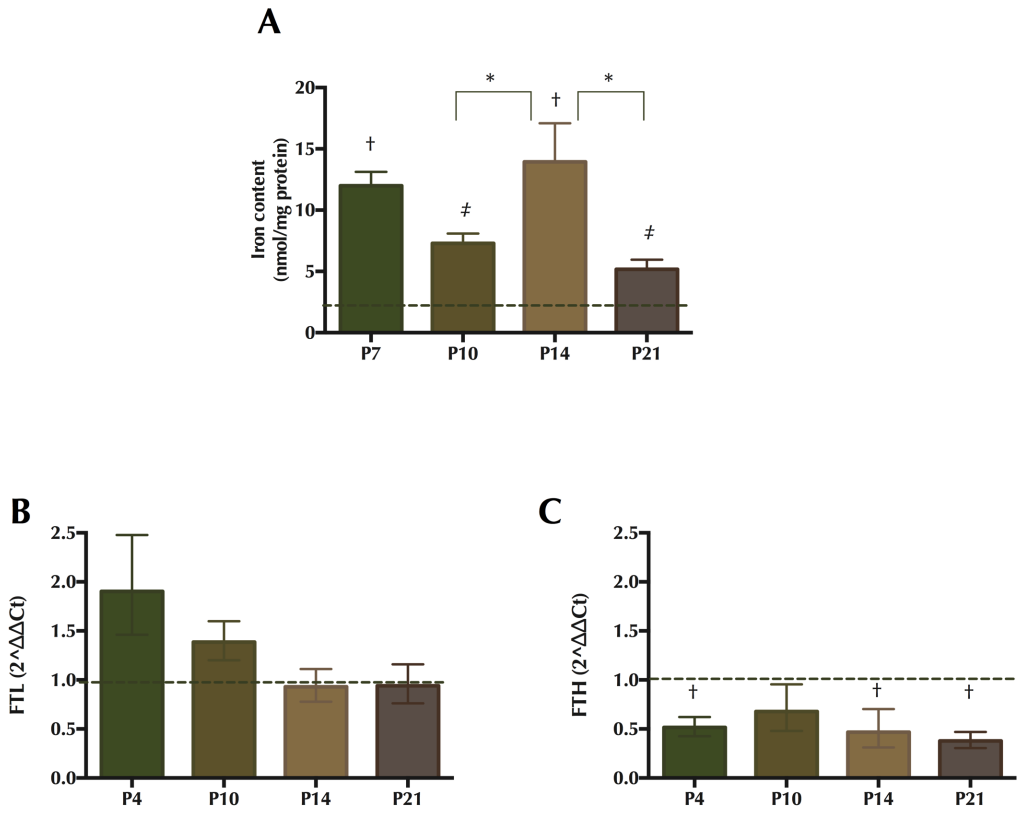

Figure 3.3: Iron content, and gene expression of iron storage molecules in the developing postnatal rat hippocampus. (A) Iron content. Generally iron content decreases in the developing hippocampus (P14 being the exception). (B) Iron storage molecules FTL and (C) FTH. There is a trend towards decreasing FTL transcripts in neonatal compared adult hippocampal tissue although FTH transcripts were typically much lower in neonates. Results are expressed as fold-change of adult, which is indicated by the dashed line. Values are mean ± 95% confidence interval (n=3 animals for mRNA and n=6 for iron content). † denotes difference from adult, ‡ from p21 and * denotes difference any age as indicated by the lines.

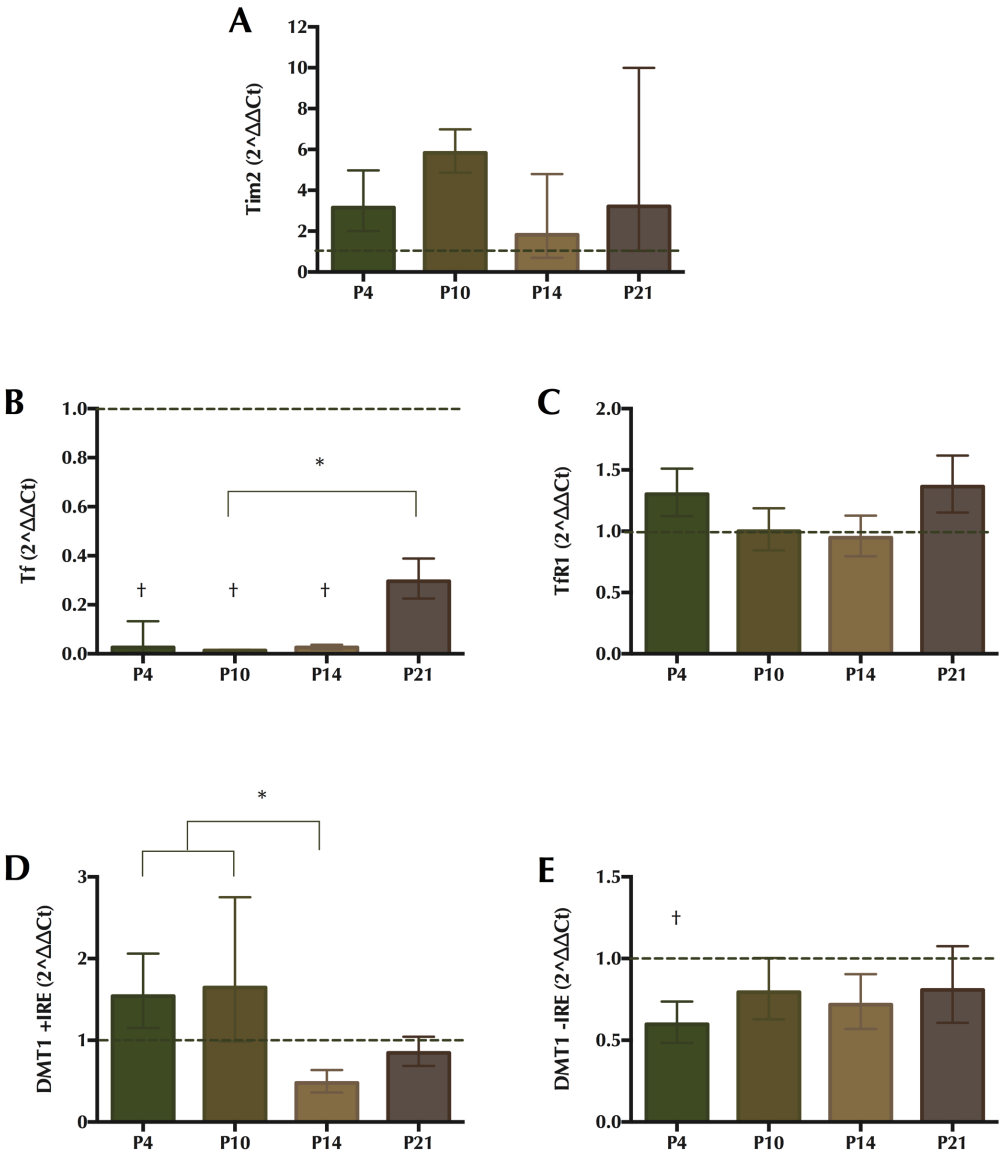

Figure 3.4: Gene expression of iron importers in the developing rat hippocampus. Transcript expression of (A) Tim2, (B) Tf, (C) Tfr1, (D) DMT1 (+IRE) and and (E) DMT1 (-IRE). There is a trend towards a decreased transcript expression of Tf and DMT1 (-IRE) in neonatal compared with adult hippocampal tissue, while Tim2 tends to be expressed a higher levels and there is minimal difference in TfR1. Results are expressed as fold-change of adult, which is indicated by the dashed line. Values are mean ± 95% confidence interval (n=3 animals). † denotes a significant difference from adult, ‡ from p21 and * from any age as indicated by the lines.

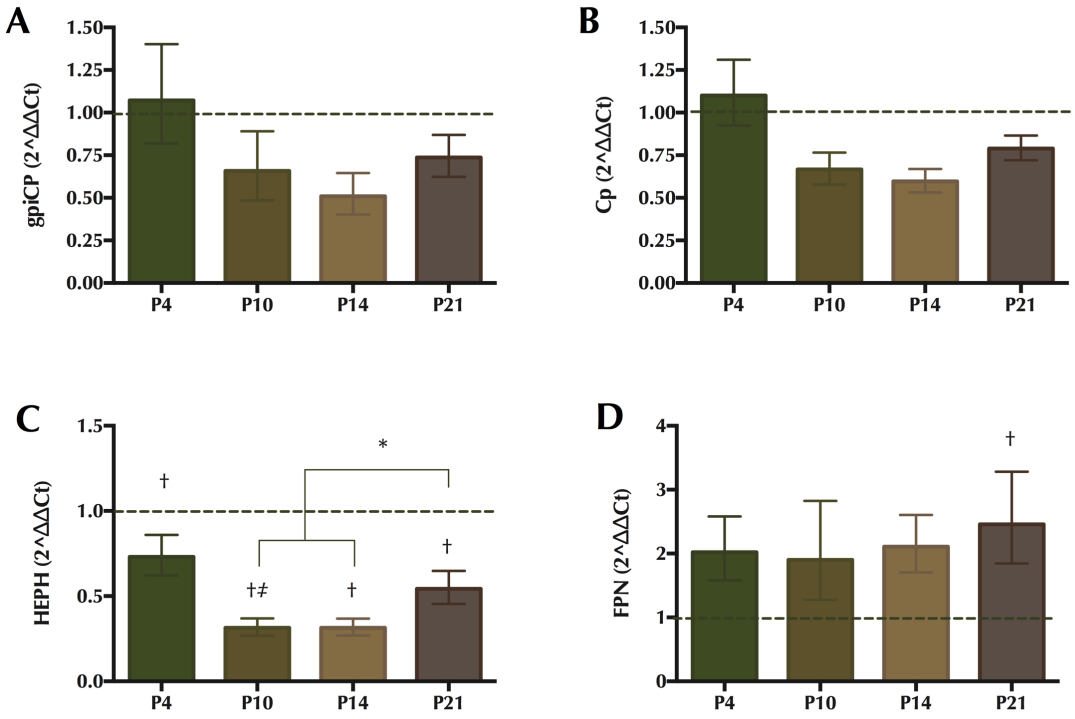

Figure 3.5: Gene expression of iron exporters in the developing rat hippocampus. Transcript expression of (A) gpiCP, (B) Cp, (C) HEPH and (D) FPN. There is a trend towards a lower transcript expression of gpiCp, Cp, and HEPH in neonatal tissue compared with adult, whereas FPN is the opposite. Results are expressed as fold-change of adult, which is indicated by the dashed line. Values are mean ± 95% confidence interval (n=3 animals). † denotes a significant difference from adult, ‡ from p21 and * from any age as indicated by the lines.

3.4.5 Expression of iron homeostasis transcripts in the developing rat cerebellum

These same molecules were then investigated in postnatal cerebellum that was taken from the same brain tissue, in order to assess if a similar pattern of expression would be detected (Fig, 3.6, 3.7 and 3.8). As with the hippocampal tissue, there were several intriguing trends, but we often could not detect significant differences. We detected a similar pattern of FTL and FTH levels in the cerebellum that was described in the hippocampus i.e. a trend towards a concurrent decreased FTL expression in adult and significantly increased FTH expression compared with postnatal tissue.

Similarly, Tf expression increased during postnatal cerebellar development. The Tf levels were significantly lower between each time point tested, with the exception of P7 compared with P10, and P21 compared with adult. Meanwhile, TfR1 expression was consistently about 2-fold higher at each postnatal time compared with adult and tim2 transcripts were inconsistently patterned. The pattern of ferroxidases levels in the cerebellum was dissimilar to that described in the hippocampus. The expression was highest at P4, dropped considerably by P10 to about 2-fold higher than adult levels, and remained at this level at P14 and P21. There was a significant difference between P4 and adult but significance was not reached at any other time point. Unlike in the developing hippocampus, FPN transcripts were detected at comparable levels at P7 and adult, but the interim ages were significantly elevated by 2- to 5-fold.

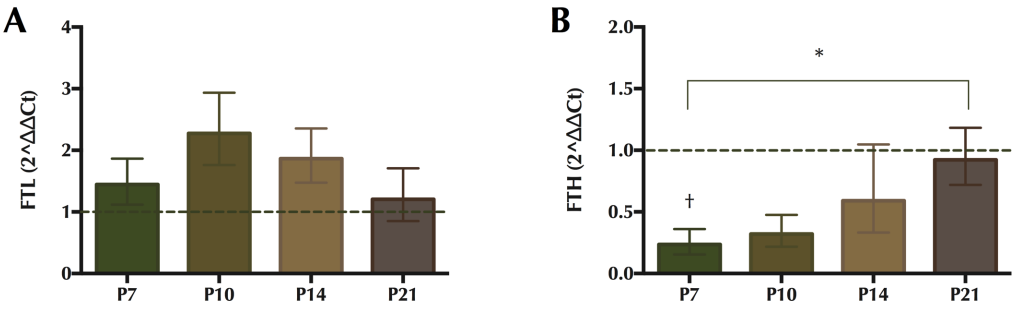

Figure 3.6: Gene expression of iron storage molecules in the developing postnatal rat cerebellum. (A) FTL and (B) FTH. There was little difference detected in FTL transcripts the developing cerebellum. However, there was a trend towards increased FTH transcripts in the developing cerebellum. Results are expressed as fold-change of adult, which is indicated by the dashed line. Values are mean ± 95% confidence interval (n=3 animals). † denotes a significant difference from adult, ‡ from p21 and * from any age indicated by the lines.

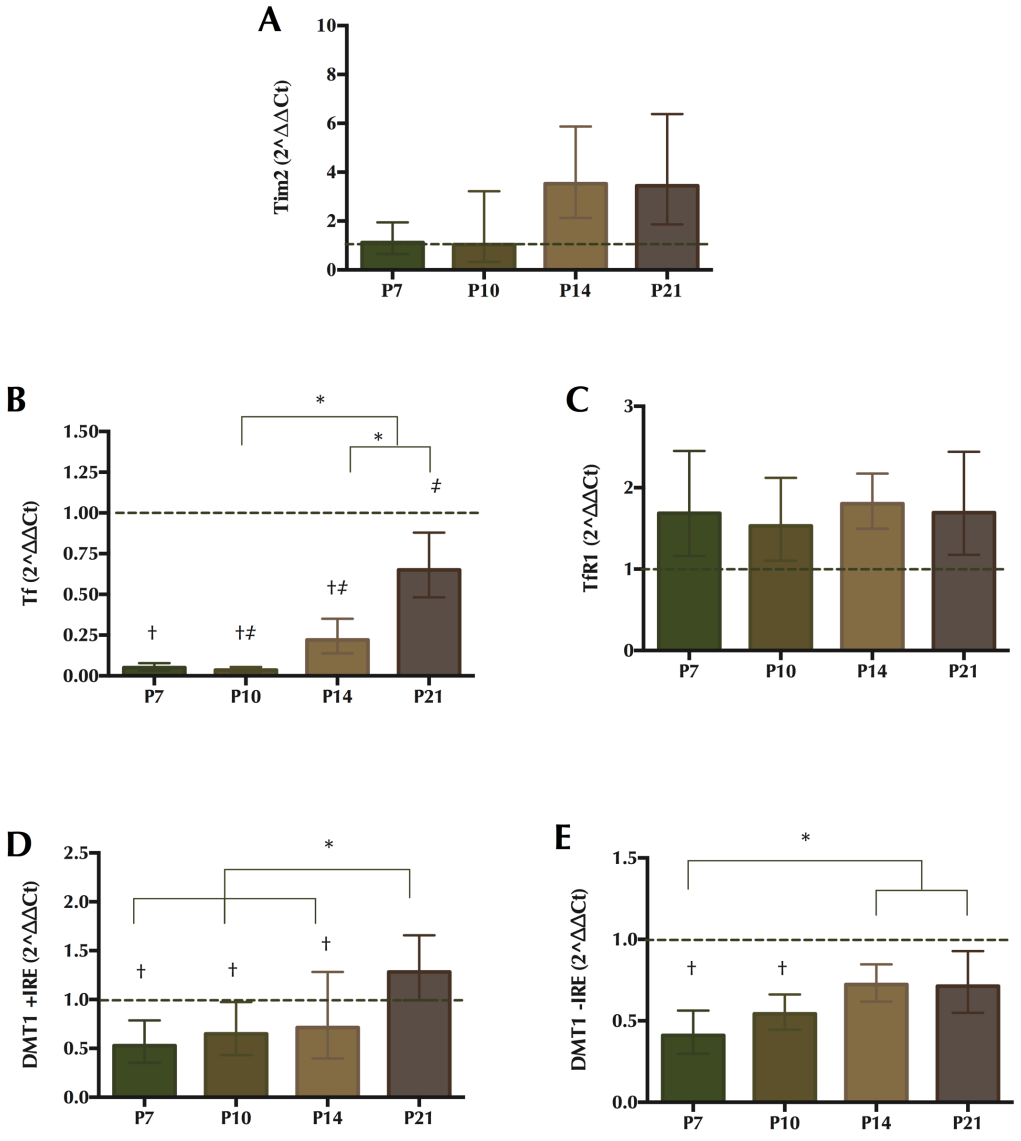

Figure 3.7: Gene expression of iron importers in the developing postnatal rat cerebellum. Transcript expression of (A) Tim2, (B) Tf, (C) Tfr1, (D) DMT1 (+IRE) and and (E) DMT1 (-IRE). There is a trend towards decreased transcript expression of Tf, DMT1 (-IRE) and DMT (+IRE) compared with adult while TfR1 transcript levels are increased. Results are expressed as fold-change of adult, which is indicated by the dashed line. Values are mean ± 95% confidence interval (n=3 animals). † denotes a significant difference from adult, ‡ from p21 and * from any age as indicated by the lines.

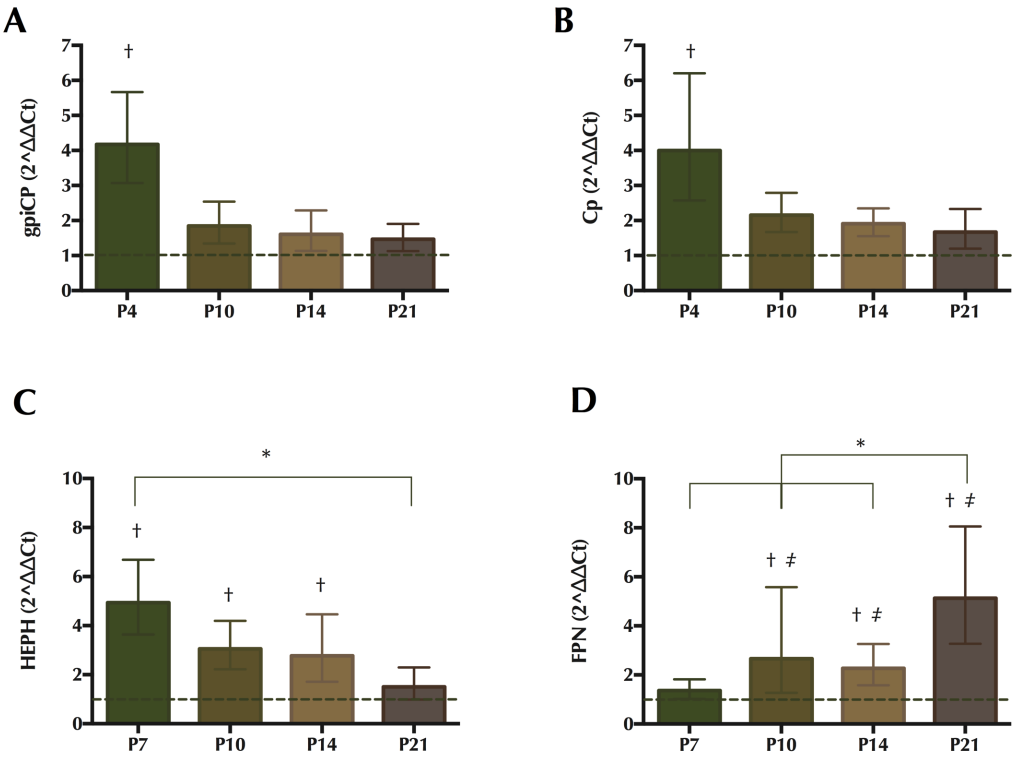

Figure 3.8: Gene expression of iron exporters in the developing postnatal rat cerebellum. Transcript expression of (A) gpiCP, (B) Cp, (C) HEPH and (D) FPN. There is a trend towards increased HEPH, FPN and gpiCp but a decrease Cp in neonatal tissue compared with adult. Results are expressed as fold-change of adult, which is indicated by the dashed line. Values are mean ± 95% confidence interval (n=3 animals). † denotes a significant difference from adult, ‡ from p21 and * from any age as indicated by the lines.

3.4.6 Homogeneous expression of iron homeostasis molecules detected in P10 CNS

To discover how levels of iron in rat hippocampus *in vivo* compared to those in other brain regions, quantities of iron were measured in dissectates from the 10 day-old hippocampus, olfactory bulb, cerebellum, cortex, brainstem and midbrain (Fig. **3**.9). Hippocampal iron content was 7.3±0.67 nmol/mg, which did not differ significantly from iron content in the cerebellum (5.7±0.60 nmol/mg), cortex (11±2.3 nmol/mg) or olfactory bulb (8.4±1.9 nmol/mg). However, iron content was significantly higher in the brain stem (17±1.3 nmol/mg) and midbrain (MB; 16±2 nmol/mg) when compared to the hippocampus ($P<0.01$).

There was little indication of a trend towards differences for most iron homeostasis transcripts, let alone differences that reached statistical significance. This is indicative of a generic CNS expression at this stage (Figs 3.9, 3.10 and 3.11). FTL and FTH transcripts were expressed at comparable levels throughout the different regions in the P10 brain with the exception of a significant difference in FTL levels between the cerebellum and hippocampus. Similarly, there was little difference in DMT1 (-IRE) and DMT (+IRE) levels. Tf expression was significantly higher in the brainstem but consistently lowly expressed across the other regions, while TfR1 was consistent across most regions except the hippocampus, which had slightly lower expression. Of interest, however, Tim2 expression was quite high in the cerebellum and hippocampus, and especially low in the cortex, whereas it was similar in the brainstem, midbrain and olfactory bulb. Finally, FPN was consistently expressed between the regions, whereas HEPH was somewhat variable, being especially high in the cerebellum but low in the hippocampus i.e. the only comparison with a significant difference.

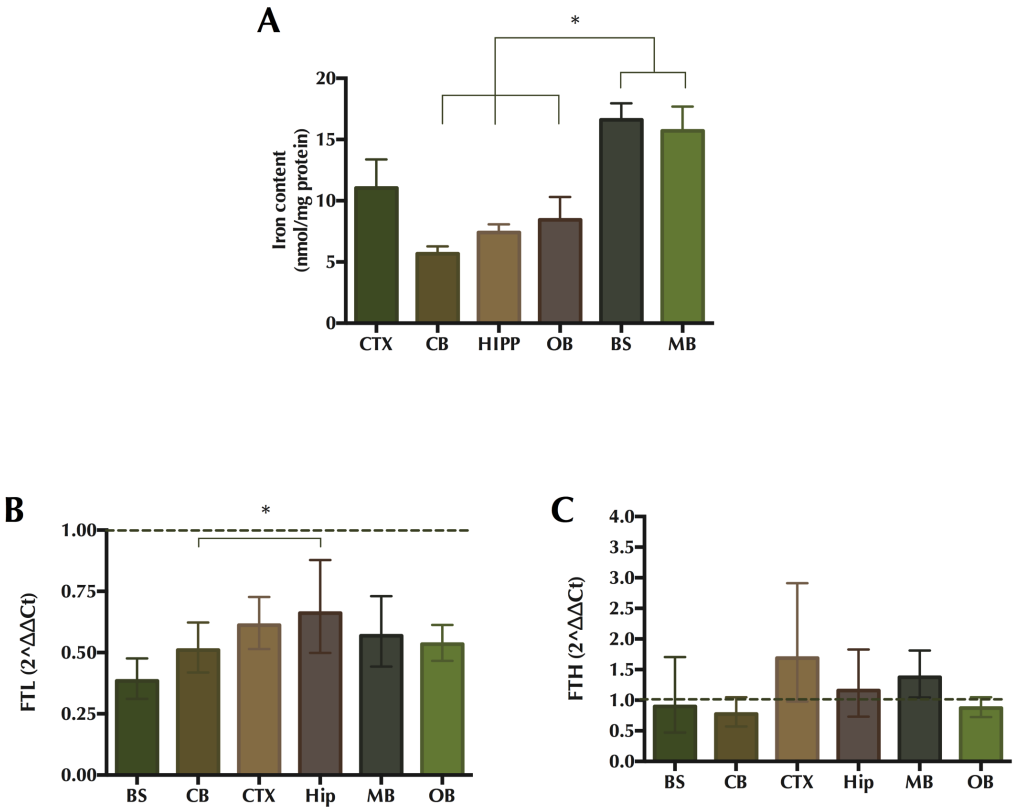

Figure 3.9: Iron content and gene expression of iron storage molecules throughout P10 brain. (A) Iron content. Hippocampal iron content matches levels of iron detected in cerebellum (CB), olfactory bulb (OB) and cortex (CTX) but is lower than the midbrain (MB) and brainstem (BS) at P10. Transcript expression of (B) FTL and (C) FTH. Transcript expression of FTL and FTH is consistent throughout the regions. Results are expressed as fold-change of liver, which was used as a positive control and is indicated by the dashed line. Values are mean ± 95% confidence interval (n=3 animals for mRNA and n=6 for iron content). * denotes a significant difference between regions that are indicated by the lines.

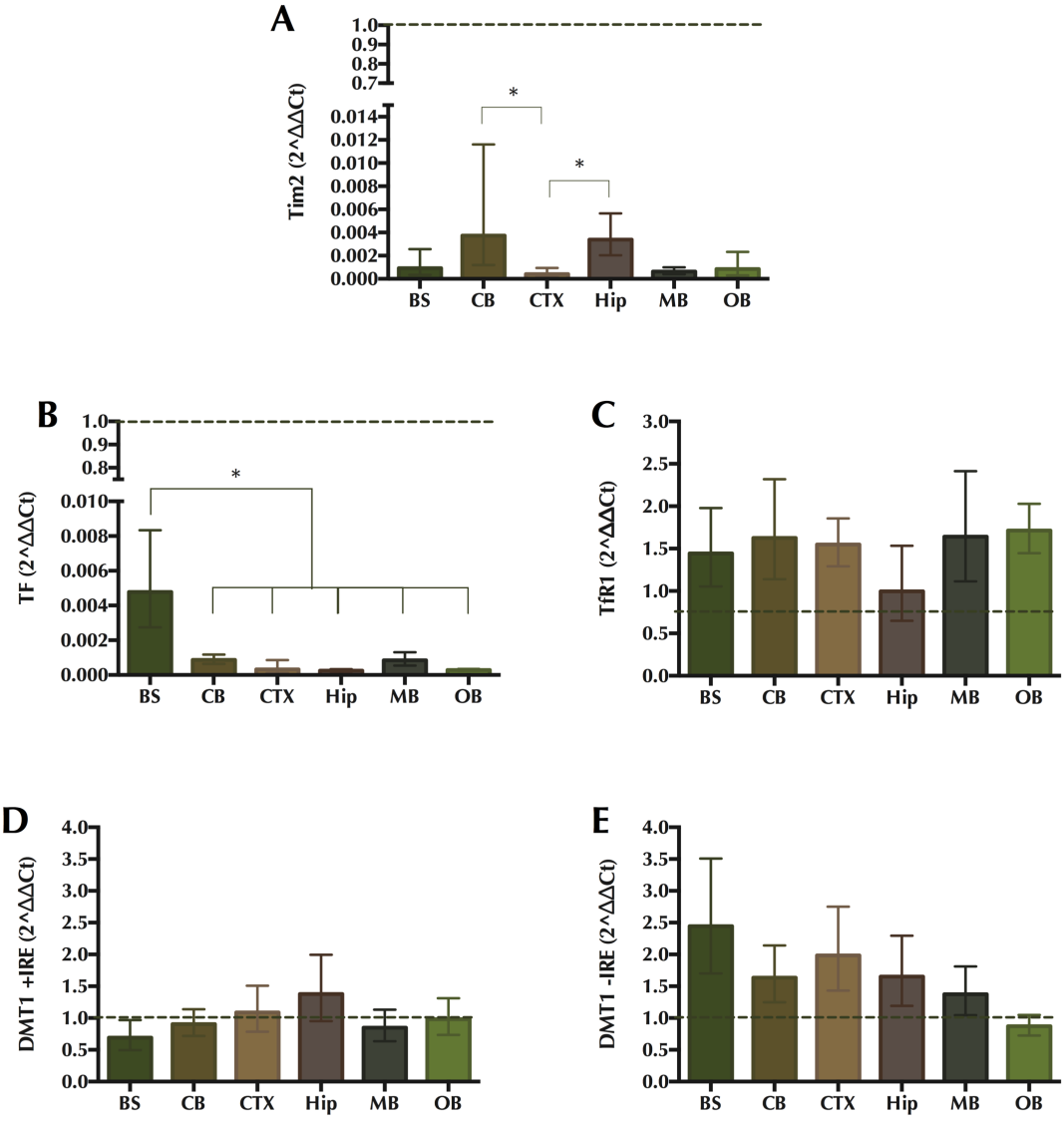

Figure 3.10: Gene expression of iron importers throughout P10 brain. Transcript expression of (A) Tim2, (B) Tf, (C) Tfr1, (D) DMT1 (+IRE) and and (E) DMT1 (-IRE). Generally, gene expression is quite similar between regions. Results are expressed as fold-change of liver, which was used as a positive control and is indicated by the dashed line. Values are mean ± 95% confidence interval (n=3 animals). * denotes a significant difference between regions that are indicated by the lines.

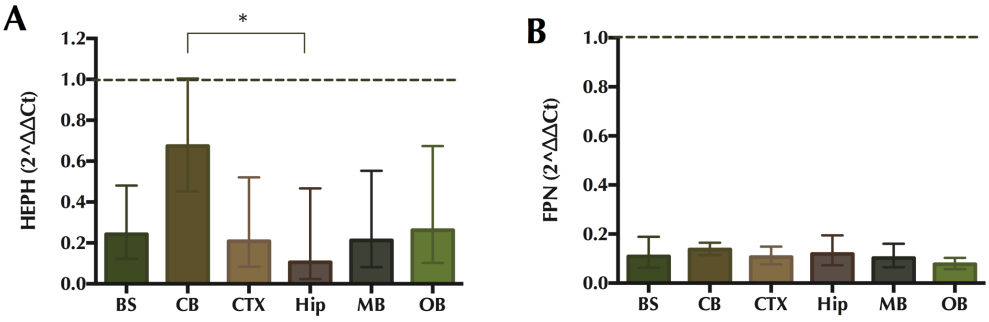

Figure 3.11: Gene expression of iron exporters throughout P10 brain. Transcript expression of (A) HEPH and (B) FPN. There is a trend towards regional variation in HEPH. However, there is no difference in FPN expression throughout the neonatal P10 CNS. Results are expressed as fold-change of liver, which was used as a positive control and is indicated by the dashed line. Values are mean ± 95% confidence interval (n=3 animals). * denotes a significant difference between regions that are indicated by the lines.

3.5 Discussion

Organotypic *ex vivo* slice cultures of brain tissue were first introduced over sixty years ago and then later popularised by Gähwiler and Stoppini with the development of the roller tube technique and interface-method, respectively, constituting a major breakthrough in the field of neuroscience (Humpel 2015a; Gähwiler et al. 1997). More recently, this technique underwent further refinement and modifications by several groups, spawning multiple preparation methods (Noraberg et al. 2005; De Simoni & MY Yu 2006; Stahl et al. 2009) and seems to be particularly well suited as an experimental platform for modelling brain iron deposition and mismanagement that is associated with neurodegeneration. It is fast, flexible and robust. The full cast of glia, microglia and nerves cells present in this controlled environment enables investigation of iron homeostasis at a cellular level. However, the concept of mimicking iron accumulation in brain slices is completely novel, therefore a basic paradigm must be developed and validated.

For instance, slice cultures, in general, are described as continuing to develop as normal. Indeed, previous work has demonstrated that *ex vivo* slices from P7 hippocampus that were cultured for 1, 2 or 3 weeks *in vitro* were developmentally equivalent to brain tissue dissected at P14, 17 or 21, respectively, with regard to neuronal morphological features like number of primary branches and spine density (Cho et al. 2007). Also the slice cultures were shown to adopt patterns of protein expression and synaptic activity of the adult hippocampus (Cho et al. 2007). However, *ex vivo* slice preparation, which invariably cuts axons, has been shown to generate more complex neurons and also cause an extensive proliferation of astrocytes leading to a type II astrocytic glial cover on the sectioned hippocampal surface, inherently distorts certain aspects of the cytoarchitecture (Cho et al. 2007). Consequently, it is not clear whether the iron homeostasis system would follow a normal developmental pattern. The discovery of whether this is true represents the major goal of this chapter.

Firstly, we established that the basal iron content in the *ex vivo* cultures is, indeed, in line with the physiological iron content (i.e. 2-50 nmol/mg; Fig. 3.1) that has been reported for primary monoculture of astrocytes, neurons, microglia and oligodendrocytes (Bishop et al. 2011; Bishop et al. 2010; Hare, Grubman, et al. 2013; Hoepken et al. 2004; Hohnholt et al. 2010; Keenan et al. 2010; Luther et al. 2013; Morath & Mayer-Pröschel 2001; Riemer et al. 2004; Tulpule et al. 2010; Urrutia et al. 2013). Next, we

demonstrated that the level of iron in control cultured hippocampal slices is representative of endogenous iron content in the age-equivalent hippocampus *in vivo*.

Although such findings might be considered to indicate that the underlying iron regulatory system is likely continue to mature *ex vivo* as it would normally (Siddappa et al. 2002), and therefore more closely mimics the aged brain compared with the immature system present in neonatal primary cultures, we found that there are several differences in the levels of transcripts encoding of iron homeostasis molecules. FTL and gpiCp were significantly up-regulated in the *ex vivo* hippocampal slice cultures compared with aged-match *in vivo* hippocampus, while TfR1 and FPN were significantly down-regulated and there was no difference determined for FTH, DMT (+IRE) or HEPH. To help up put these perturbations into context, we assessed the transcript expression in the postnatal hippocampus at P4, P10, P14, P21 and adult (>6 months).

There was an overall decrease in total iron content during this period, with the exception of P14 in which iron content was elevated. Although this is the first study, to our knowledge, to characterise postnatal hippocampal iron concentration in detail, our findings do parallel a previous report that iron decreases in cortex, cerebellum and midbrain during postnatal development (Roskams & Connor 1994). In the developing rat hippocampus, there appeared to be no common pattern to the alteration in mRNA levels of the 11 iron homeostasis molecules that were tested. In order to assess if a similar variation in the levels of iron-associated transcripts would be detected in the developing rat cerebellum, we investigated the levels of expression the iron homeostasis molecules across a range of postnatal ages. The transcript profile in the postnatal cerebellum did not match of the hippocampus. This is not wholly unexpected given that the hippocampus and cerebellum are distinctive structures on quite different developmental trajectories. Broadly, these findings indicate that choice of region is more than a matter of technical and logistical consideration although these are of critical importance in terms of viability, consistency and yield. The region choice must be reasonably reflective of the global iron homeostasis system in CNS and not skewed by specific regional idiosyncrasies.

Consequently, we next characterised the expression of iron and all these iron homeostasis molecules at P10, a typical age at which *ex vivo* slice cultures might be generated. Early postnatal periods (e.g. p5 to p10) are ideally suited for culturing because the essentials of the cytoarchitecture are already established in most brain areas and the nerve cells survive explantation more readily. Hippocampal iron levels were the same as those in the cerebellum and olfactory bulb and were half those in the cortex, brainstem

and midbrain. Despite regional differences in iron content in the P10 brain, the expression of iron homeostasis molecules was found to be quite similar at this age. Presumably, the regional differences that have been described for several of these molecules in the adult must emerge at an older age.

This suggests, that in general terms, a hippocampal slice culture platform is a useful starting point for studying iron regulation in the brain given that 1) the hippocampus in itself is robust region for generating slice cultures, producing reproducible results, and 2) there is a moderate iron content at P10 and a similar level of expression of the iron homeostasis molecules compared with the other regions. We do acknowledge, however, that there are inherent differences in the iron homeostasis system present in the *ex vivo* hippocampal slice cultures when compared with age-equivalent tissue. We believe that the altered mRNA expression of iron homeostasis molecules detected *ex vivo* is not necessarily a consequence of immature or delayed development, but most likely resulting from the differences in cellular composition from the culturing processes (e.g. astrocyte proliferation). It may be that the mechanical transection of fibres obtained during slice preparation has induced sustained hippocampal injury in the slice cultures, and this might account for the changes in the expression of the iron homeostasis detected compared with age matched tissue. Therefore, our model does not perfectly recapitulate the iron homeostasis system in mature normal CNS. However, it does offer a reasonable version of this system given that all the elements of the iron homeostasis machinery are present at mostly appropriate levels, and therefore our model represents a considerable improvement over current *in vitro* primary monoculture alternatives, but it not necessarily a model of homeostatic iron handling even prior to iron-loading.

Finally, we note that one of the critical weaknesses in this study was our inability to detect significant differences because of insufficient power. Post-hoc power analysis indicated that this study, using n=3 samples per time point for mRNA samples, was under-powered (with the exception of iron analyses where n=6 and *ex vivo* compared with *in vivo* samples in which n=3 was sufficient for the t-test used). This low-power explains the lack of significant differences determined in the hippocampal and cerebellar characterisations despite interesting trends. Also, as this characterisation relied exclusively on RNA, it would be considerably stronger if protein data from western blot or immunohistochemistry could be included.

3.6 Conclusion

The hippocampus represents a reasonable surrogate platform of the CNS for modelling iron homeostasis *ex vivo*. It is a discrete, viable and consistent structure that yields an excellent number of slice cultures for experimentation. Our comprehensive characterisation of iron and iron homeostasis molecules indicates that the hippocampus has moderate iron content and homogeneous expression of iron homeostasis molecules compared with other regions at P10. At a mRNA level, the expression of the iron homeostasis molecules at P21 generally matches that of the adult, and that P10/11 hippocampal slices cultured for 10 days is an adequate match, although imperfect, of the P21, indicative of that all elements of the iron homeostasis machinery are present and mostly appropriate levels. This new approach may represent a promising tool for studying iron metabolism, which is still incompletely understood in the CNS, and might bridge the gap between *in vitro* and *in vivo* work.

4 Glial alterations in response to iron loading in a novel *ex vivo* hippocampal slice model

4.1 Introduction

Aberrant iron deposition in the brain is associated with aging and neurodegenerative disorders including Multiple Sclerosis, Alzheimer's disease and Parkinson's disease (Crichton et al. 2011; Hallgren & Sourander 1958; Hametner et al. 2013; Stephenson et al. 2014; Oshiro et al. 2011). However, to date, despite the heightened research interest in the endogenous iron handling system and valuable insight generated from post-mortem brain samples and monocultures, it still remains unclear whether metabolic dyshomeostasis of iron is causative or is a consequence of brain pathology. An improved understanding of the mechanisms underlying iron handling might yield critical information relevant to neurodegenerative disease.

The focus of this chapter is to establish and characterise a novel *ex vivo* model of iron loading (Healy et al. 2016). The development of such a model, which enables the study of inter- and intra-cellular iron movement and the cellular basis of iron-induced pathology within the complex brain milieu (Cho et al. 2007; Humpel 2015a), would equip researchers with an improved platform to comprehensively study the intricate iron handling system.

4.2 Aims of this study

The primary goal of the work described in this chapter was to develop an *ex vivo* model of iron accumulation and then establish a profile of expression of iron handling proteins in neuronal and glial cells.

Specific aims were to:

i. Compare iron accumulation and toxicity following exposure to different iron reagents.

ii. Define a profile of iron handling proteins involved in uptake, storage and export following iron loading.

iii. Characterise protein expression of ferritin, ferroportin and DMT1 using dual immunohistochemistry in glial cells.

iv. Quantify the effect of iron loading on the morphology and number of oligodendrocytes, astrocytes, microglia and neurons.

4.3 Summary of Methodology

A novel *ex vivo* model of iron loading was established by exposing cultured hippocampal slices to various iron reagents (ferric citrate, ferrous ammonium sulphate and ferrocene) for 12 h in serum-free medium. Following exposure, the slice cultures were harvested for comprehensive molecular, immunohistochemical, viability or biochemical analyses. The details of methods used are provided in chapter 2. Also, see chapter 6 or complete description of the development, optimisation and evaluation of an image analysis workflow for handling and quantifying z-stack micrographs of glial immunohistochemistry taken from *ex vivo* slice cultures.

4.4 Results

4.4.1 Iron Reagent Comparison

The following iron reagents were compared: ferric citrate (FC), ferrous ammonium sulphate (FAS) and ferrocene. These were chosen based on a literature search of previous iron loading studies and in order to encompass both ferric and ferrous forms of iron and also a 'disguised form' of iron (i.e. one that bypasses import molecules) as ferrocene. Ten µM iron concentration was chosen as a physiologically relevant concentration for iron overloading based on the iron content that has been detected in normal human cerebrospinal fluid (CSF) (Bradbury 1997; Gaasch et al. 2007; LeVine et al. 1999; LeVine et al. 1998). The composition of the CSF, i.e. 0.1-1.2 µM iron, is considered to reflect that of the interstitial fluid surrounding the neurons and glia and therefore 10 µM represents a reasonable supraphysiological concentration. It is, however, considerably lower than iron concentrations of neonatal glia and neurons that has been reported in the literature (summarised in Fig. 3.1), which, on average and approximately, contain 10 mM iron (while the hippocampal slice cultures have 7.7 mM).

Ten µM ferrocene produced a significant 1.3-fold increase in the levels of iron in slice cultures when compared with vehicle ($P < 0.05$; Fig. 4.1A). This ferrocene-induced increase in iron content was accompanied by minor toxicity, as indicated by a 1.4-fold increase in LDH release compared with vehicle ($P<0.05$; Fig. 4.1B). By comparison, FAS and FC produced only a 1.2-fold or no increase in iron content, respectively (Fig. 4.1A). Nevertheless, FAS loading also caused a significant 1.3-fold increase in LDH activity, whereas FC had no effect (Fig. 4.1B). This experiment was repeated using 1 µM ferrocene, 1 µM FAS and 1 µM FC and, once again, the use of ferrocene was shown to result in a significant increase in brain slice iron levels (Fig. 4.2A). Although non-significant, the 1

μM iron reagent exposure led to slightly elevated fold-increases in iron content compared to vehicle than that which had been achieved with the 10 μM iron reagent exposure. There was no significant difference in protein content between cells incubated with iron reagents compared with vehicle (Fig. 4.2B).

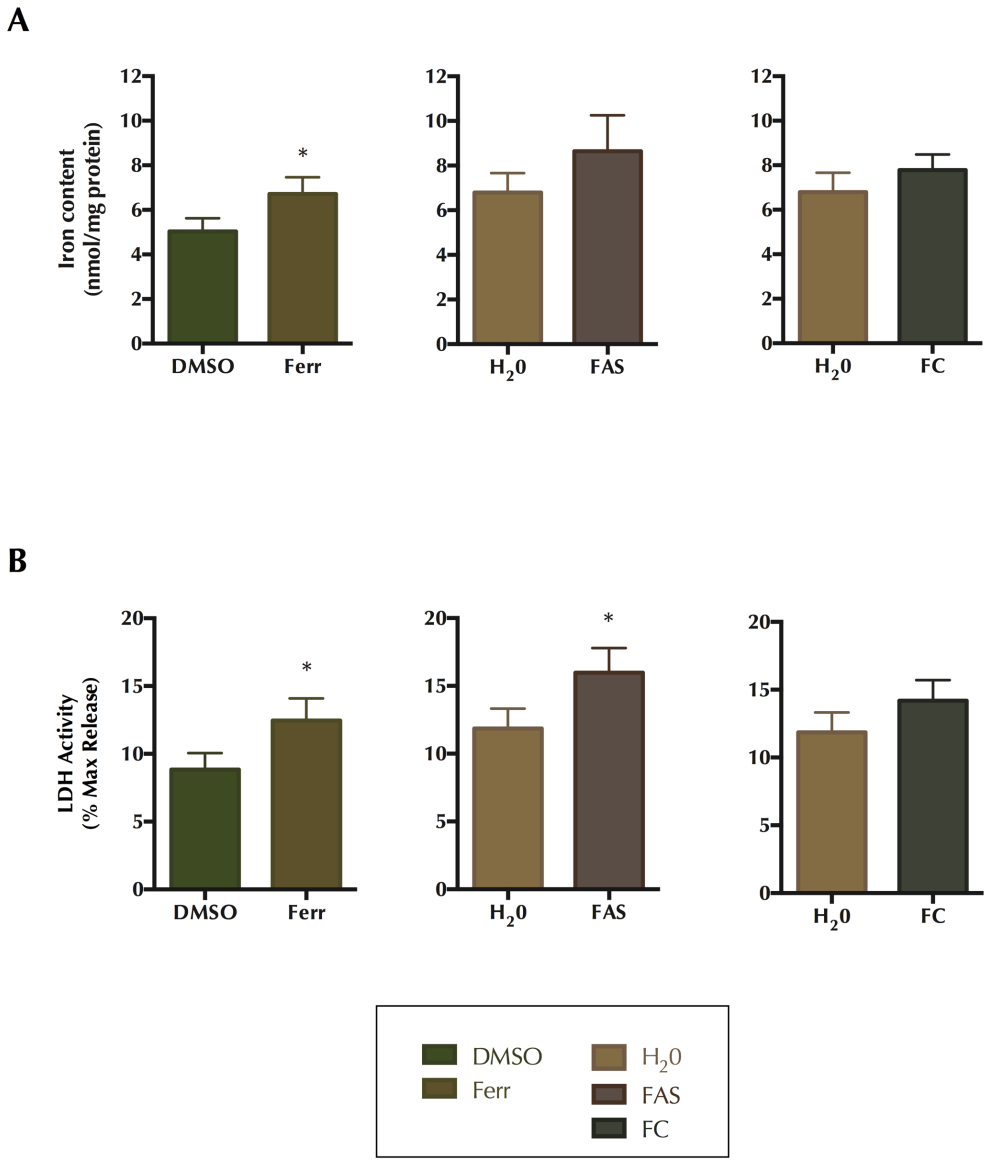

Figure 4.1: Ten μM iron reagent comparison. Cultures were treated for 12 h with 10 μM ferrocene, FAS or FC. (A) Iron Content. Ferrocene produced a significant 1.3-fold increase in iron content compared with DMSO (6.7 ± 0.76 and 5 ± 0.60, respectively). (B) Viability. Delivery of both FAS and ferrocene resulted in impaired viability whereas FC had no detectable effect. Values are expressed as mean ± SEM from 3 separate experiments. *P<0.0 compared with vehicle.

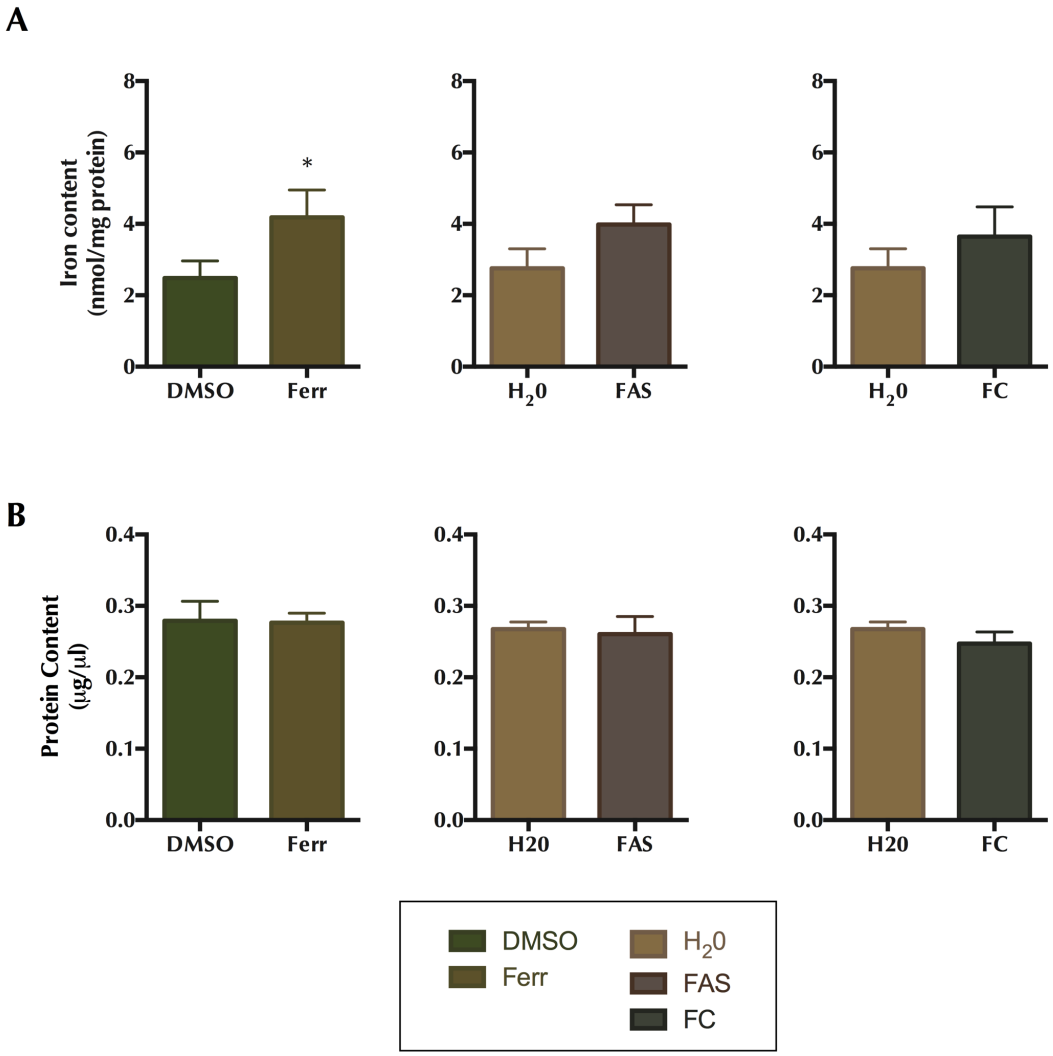

Figure 4.2: One µM iron reagent comparison. Cultures were treated for 12 h with 10 µM ferrocene, FAS or FC. (A) Iron Content. Ferrocene produced a significant 1.7-fold increase in iron content compared with DMSO whereas FAS and FC exposure resulted in non-significant increases in iron. (B) Protein. Iron exposure did not affect protein content. Values are expressed as mean ± SEM from 3 separate experiments. *P<0.05 compared with vehicle.

4.4.2 One µM ferrocene exposure leads to maximal iron accumulation

Having established the supremacy of 10 µM ferrocene over the same concentration of FC or FAS in this model, a dose-response experiment was completed by testing the effects on cultured hippocampal slices of a 12-hour exposure of 0.1-100 µM ferrocene. Ferrocene loading at 1 and 10 µM produced significant increases in iron content ($P<0.05$; Fig. 4.3A). One µM ferrocene produced a maximal 1.6-fold increase in iron content compared with vehicle (8.05±0.98 and 4.97±0.57 nmol/mg, respectively). Using an LDH assay, we showed that all ferrocene concentrations tested here increased LDH activity by approximately 1.3-fold ($P<0.05$; Fig. 4.3B).

To confirm iron accumulation, we also assessed the expression of ferritin light chain and ferritin heavy chain (i.e. FTL and FTH; surrogate markers for iron accumulation) in 1 μM ferrocene-loaded cultures. FTL and FTH transcripts were up-regulated 1.3- and 1.6-fold compared with vehicle-treated cultures although this did not reach statistical significance (Fig. 4.3C). Using an MTT assay, we also measured metabolic activity of cultures exposed to 1 μM ferrocene. In contrast to the LDH viability data, no iron-induced loss in metabolic activity was detected (Fig. 4.3D).

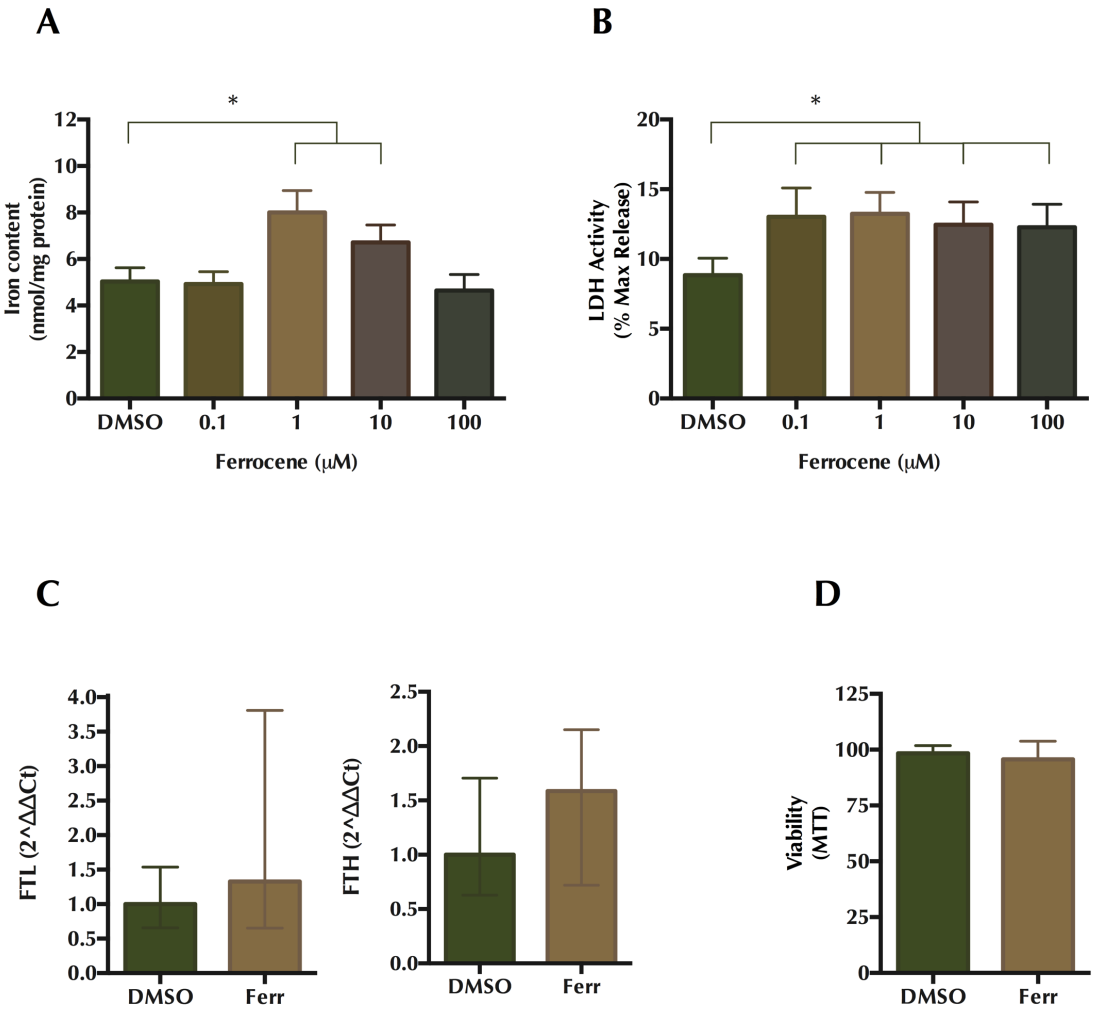

Figure 4.3: One μM ferrocene produced maximal iron accumulation. Cultures were loaded with 0.1-100 μM ferrocene for 12h to identify optimal concentration for iron loading. (A) Iron Content. One μM ferrocene produced a 1.6-fold increase in iron content compared with DMSO vehicle (8.05 ± 0.98 and 4.97 ± 0.57 nmol/mg, respectively). (B) LDH Assay. All concentrations of ferrocene resulted in impaired viability, as determined by LDH release. (C) One μM ferrocene, the maximal iron loading concentration, lead to modest up-regulation of Ferritin Light Chain (FTL) and Ferritin Heavy Chain (FTH) transcripts, respectively, (ferritin, an iron storage protein, is a surrogate indicator of iron accumulation) expression. (D) MTT. Values are expressed as mean ± SEM from 3 separate experiments for iron and viability data with qPCR data is expressed as mean ± 95% confidence interval from 5 experiments. * denotes $P<0.05$ compared with vehicle.

4.4.3 Optimisation of antibodies

Hippocampal slice cultures were used to optimize staining conditions. A range of concentrations of primary antibody were tested. The primary antibody dilutions tested for cellular markers were based on those that have been previously identified by our group in frozen postnatal cerebellum sections (Naughton et al. 2015). For the iron handling proteins, the dilutions tested varied from 1:100 to 1:1000 in accordance with manufacturer's guidelines.

In order to determine which cell types express the iron and UPR proteins, dual immunofluorescent staining was carried out. Before carrying out dual labelling, conditions for single labelling using immunofluorescent staining of monoclonal cell specific markers were first established (Fig. 4.4). The cell specific markers tested were as follows: Olig2 (oligodendrocyte-lineage cells), NeuN (neuronal nuclei), SMI32 (neurofilament), GFAP (astrocytes) and OX-42 (microglia). There was no fluorescent staining obtained in the negative controls following omission of primary antibody. Positive fluorescent staining was obtained for each monoclonal tested except Ox-42. However, polyclonal goat IBA1 was identified as an alternative for dual-labelling studies and positive fluorescent staining was demonstrated. Fig. 4.4 shows samples of positive staining for each cell type.

The fundamental goal of this project was to characterise alterations in the iron handling system following iron loading. It was necessary to select and optimise a subset of 5 iron molecules involved in iron storage, import and export processes: ferritin (neuronal and glia iron storage), ferritin-light chain (glial iron storage), DMT1 (iron uptake), ferroportin (iron export) and hepcidin (iron regulation/export). A series of antibody dilutions were tested as detailed in the Materials and Methods (Section 2.7 & Table 2.2). Fig 4.5 show samples of positive and negative (no primary antibody) staining for the antibody that were successfully optimised. The optimal working dilutions were identified for ferritin (1:200), ferroportin (1:600) and DMT1 (1:600). We were unable to demonstrate positive fluorescent staining for ferritin-light chain or hepcidin.

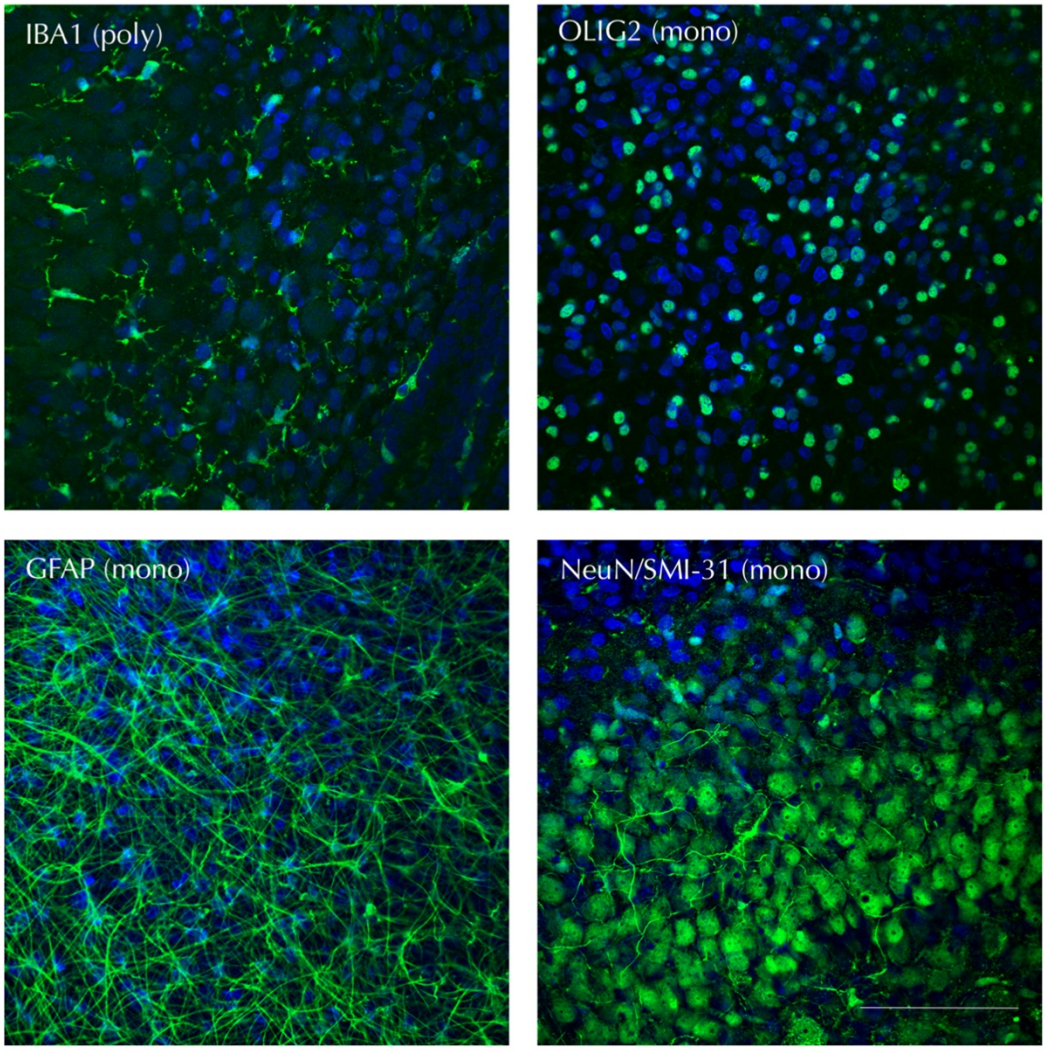

Figure 4.4: Representative single-plane confocal images demonstrating the optimised fluorescent staining of cell specific markers in organotypic hippocampal slice cultures. Upper left: microglia (IBA1), upper right: oligodendrocyte-lineage cells (OLIG2), lower left: astrocytes (GFAP) and lower right: neurons (NeuN/SMI-31). Scale bar = 100 µm.

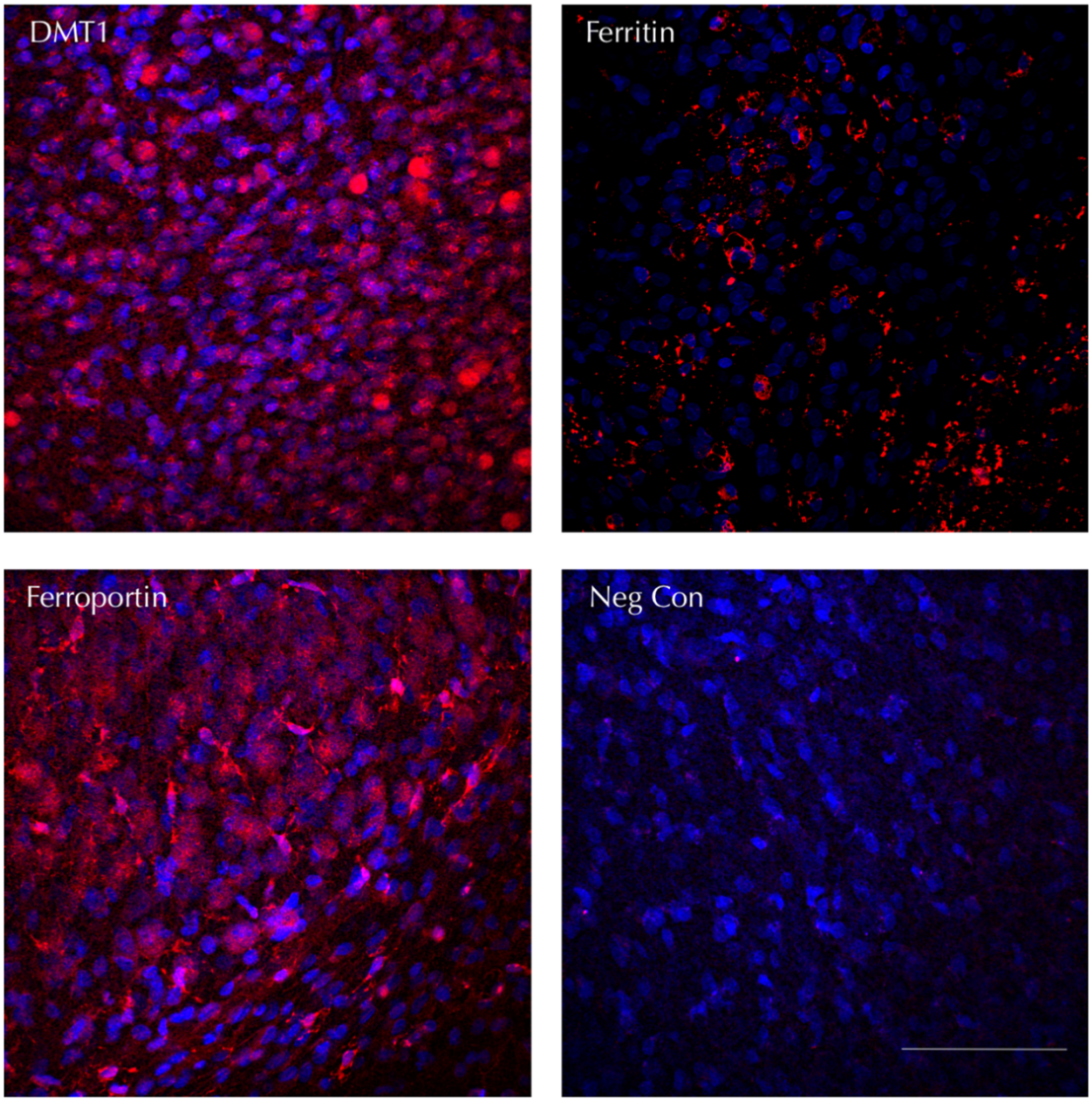

Figure 4.5: Optimisation of immunohistochemical detection of iron handling molecules in organotypic hippocampal slice cultures. Maximum intensity projection images of DMT1, ferroportin, ferritin and negative control. In negative controls, omission of primary antibody abolished immunoreactivity demonstrating the lack of non-specific binding of the secondary antibodies. Cultures were counterstained with DAPI (blue) to visualise the nuclei. Scale bar = 100 µm.

4.4.4 Ferritin accumulates in oligodendrocytes and microglia

Ferritin, an iron storage molecule that has been shown to be increased with increased iron accumulation, was used as a surrogate marker for iron to further determine the cellular localisation of the accumulated iron.

Double immunofluorescence labelling with cell type-specific antibodies and an antibody to ferritin showed ferritin expression in oligodendrocytes and microglia once they were treated with 1 μM ferrocene (Fig. 4.6A & B). In contrast, ferritin expression was rarely detectable in astrocytes and was not detectable in neurons (Fig. 4.6C & D). In control conditions, ferritin immunostaining was found at low levels predominantly in oligodendrocytes and, to a lesser extent, microglia. However, astrocytes and neurons did not have detectable ferritin under control culture conditions examined.

4.4.5 Real-time PCR analysis of transcript of iron homeostasis molecules

Dysregulation of the molecular mechanisms involved in iron handling might contribute to the increased iron accumulation or its absence in different cell types. We therefore examined the mRNA expression of molecules mediating cellular iron uptake and efflux in iron-loaded slice cultures. Real time PCR was carried out on the cDNA of vehicle- or iron-loaded slice cultures to detect transcripts of 6 iron homeostasis molecules: DMT1 (–IRE splice variant), DMT1 (+IRE splice variant), TfR1, transferrin, FPN and gpiCp (Fig. 4.7).

In general, there was an upward trend towards increased mRNA levels of these uptake proteins (Fig 4.7A). DMT1, a ferrous iron importer, exists in splice variant forms, one that is controlled by IRP regulation (+IRE) and one that is not (-IRE). The former is up-regulated 1.3-fold while the latter is up-regulated 2.3-fold. TfR1, along with transferrin, which are responsible for ferric iron uptake, are also affected by iron loading and were up-regulated and down-regulated to 1.4- and 0.8-fold, respectively. There was minimal difference in the regulation of iron export proteins that were tested with a slight 1.2-fold upward trend in FPN transcripts and a 0.9-fold downward trend in gpiCp (H4.7B).

Several attempts had been made to optimise 2 sets of self-designed hepcdin primers and 3 sets taken from the literature using cDNA generated from hippocampal slice culture samples, adult *in vivo* CNS tissue and liver but were uniformly unsuccessful. Similarly, although primers had been optimised, validated and employed for hephaestin and Tim-2 in cDNA from *in vivo* CNS tissue, there were technical problems (i.e. low expression, and non-satisfactory melt curve) detecting expression in cDNA generated from slice cultures. Nevertheless, the 8 genes that were used in cDNA from iron-loaded

slice cultures were sufficient to demonstrate consistent trends of up-regulation although these did not reach statistical significance.

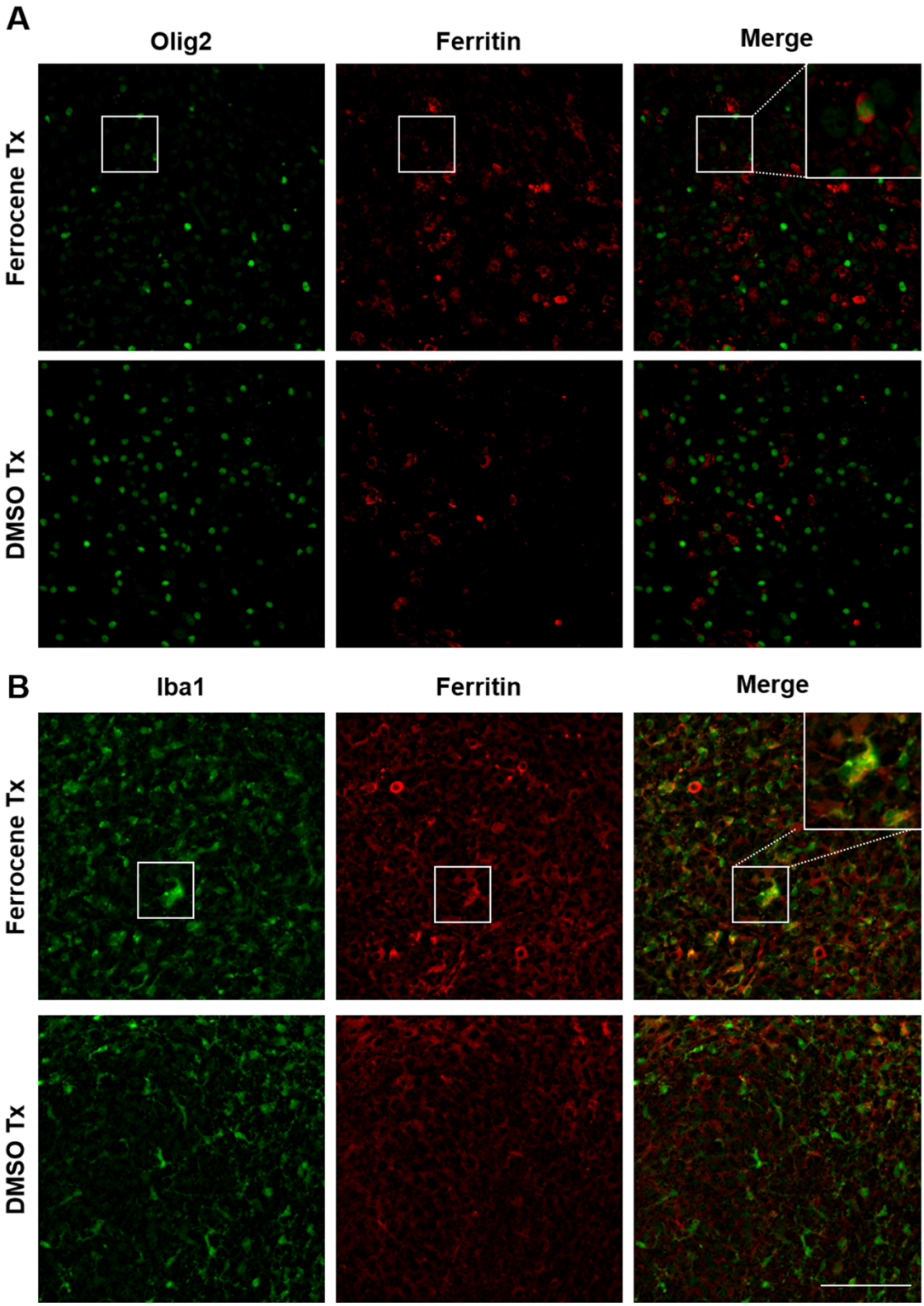

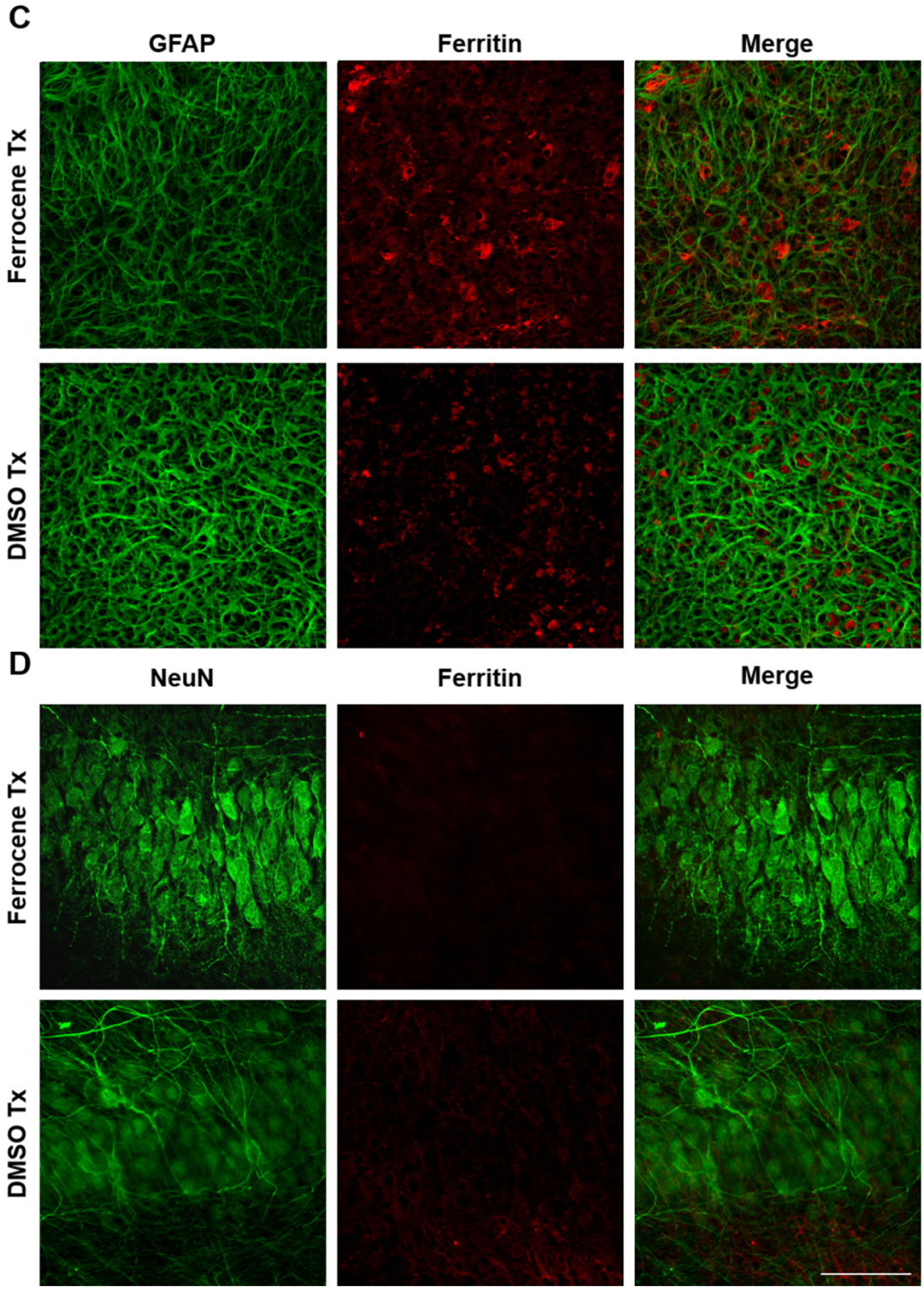

Figure 4.6: Dual immunofluorescent detection of ferritin expression in CNS cells in vehicle and iron-loaded slice cultures. Confocal images of (A) oligodendrocytes, (B) microglia, (C) astrocytes and (D) neurons. Insets show an enlarged version of the boxed area. Scale = 100 μm.

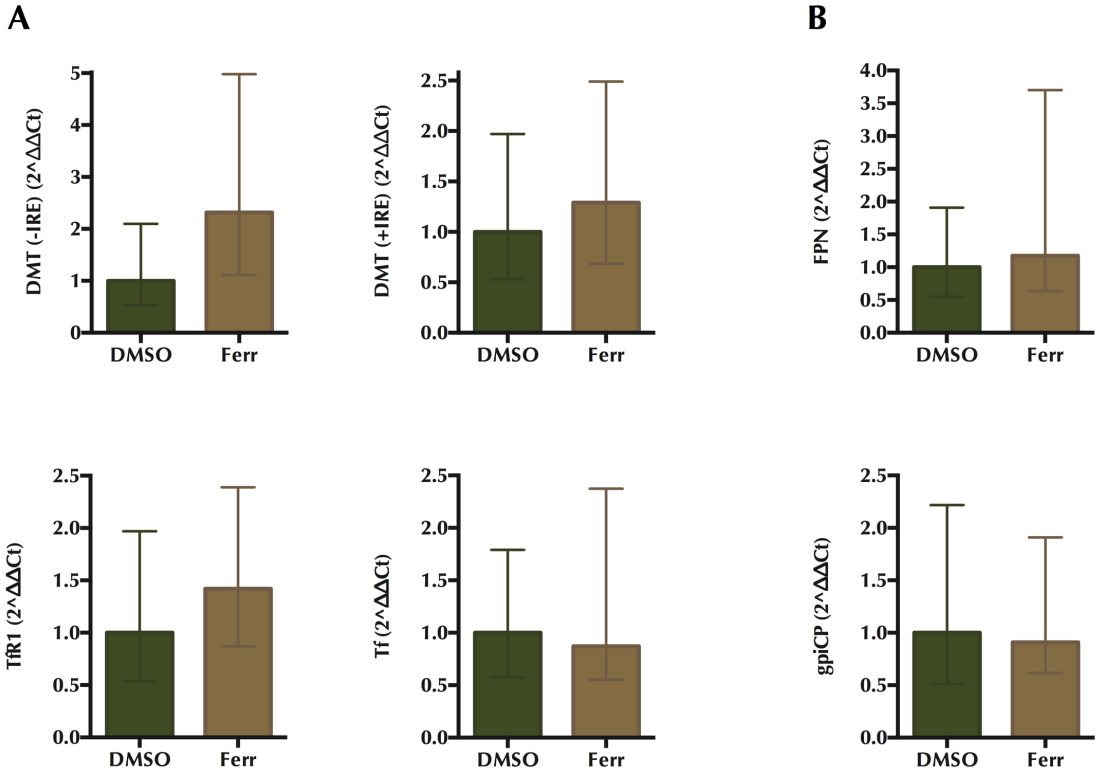

Figure 4.7: PCR analysis of iron handling molecules. (A) Import molecules. (B) Export molecules. There is a trend towards increased transcript expression of DMT (-IRE), DMT (+IRE) and TfR1 molecules, whereas there is a trend towards a possible decreased Tf, and minimal difference in transcript expression of export molecules. Values are mean ± 95% confidence interval (n=3 experiments).

4.4.6 Iron loading alters the cellular expression of export and import molecules

In order to characterise and to confirm alterations in cellular iron homeostasis following iron loading, dual immunofluorescent labelling and preliminary colocalisation analysis was used to detect the expression of selected uptake and export proteins in microglia and oligodendrocytes.

Representative images of DMT1 are shown in Figure 4.8 and Figure 4.9 and preliminary data from the colocalisation analysis is in Figure 4.11. This work confirmed, for the first time, to our knowledge, the presence of DMT1 in *ex vivo* microglia, while very few oligodendrocytes seemed to be associated with DMT1. Although dual labelling with neurons was not carried out, we could note the presence of DMT1 in cells that morphologically resemble and that are spatially consistent with that of neurons.

Interestingly, immunolabelling with DMT1 revealed differential expression level following iron loading. Consistent with the real-time PCR results, the expression of DMT1 was seen to be increased in microglia following iron exposure (Fig. 4.8 and Fig. 4.11B), whereas we seldom observed DMT1 positive staining associated with OLIG2-positive cells in control or iron-loaded slice cultures (Fig 4.11A).

Taken together, the staining pattern of ferritin and DMT1 in microglia is indicative of increase iron uptake and storage. Consequently, we further assessed the iron handling by dual labelling with the exporter ferroportin (Fig. 4.10 and Fig. 11C). A reduction in staining was seen, along with punctate deposits within the microglia, suggestive of internalisation.

4.4.7 Iron loading alters number and morphology of glial cells

Aside from the occurrence of cellular iron accumulation, iron loading with ferrocene also affected glial morphology and number. A significant 15% increase in the number of Iba1-positive microglia was observed (Fig. 4.12A & B). These cells also showed decreased complexity in branching morphology, as quantified by skeleton analysis (note: an endpoint is the end of a microglia process; please see section 2.8.2.1 for full details), with the mean number of microglia endpoints per cell decreasing by 17% from 17 ± 0.86 in vehicle-treated slice cultures to 14 ± 0.9 in iron-loaded slice cultures (Fig. 4.12A & B).

Conversely, there was a 15% reduction in the number of OLIg2-positive cells in iron-loaded slice cultures compared with vehicle (123 ± 4.840 and 104.6 ± 4.916, respectively; Fig. 4.13A & B). Meanwhile, GFAP-positive astrocytes were unaffected by iron loading. There was no change in the area of GFAP-positive staining between treatment groups (Fig. 4.13A & B).

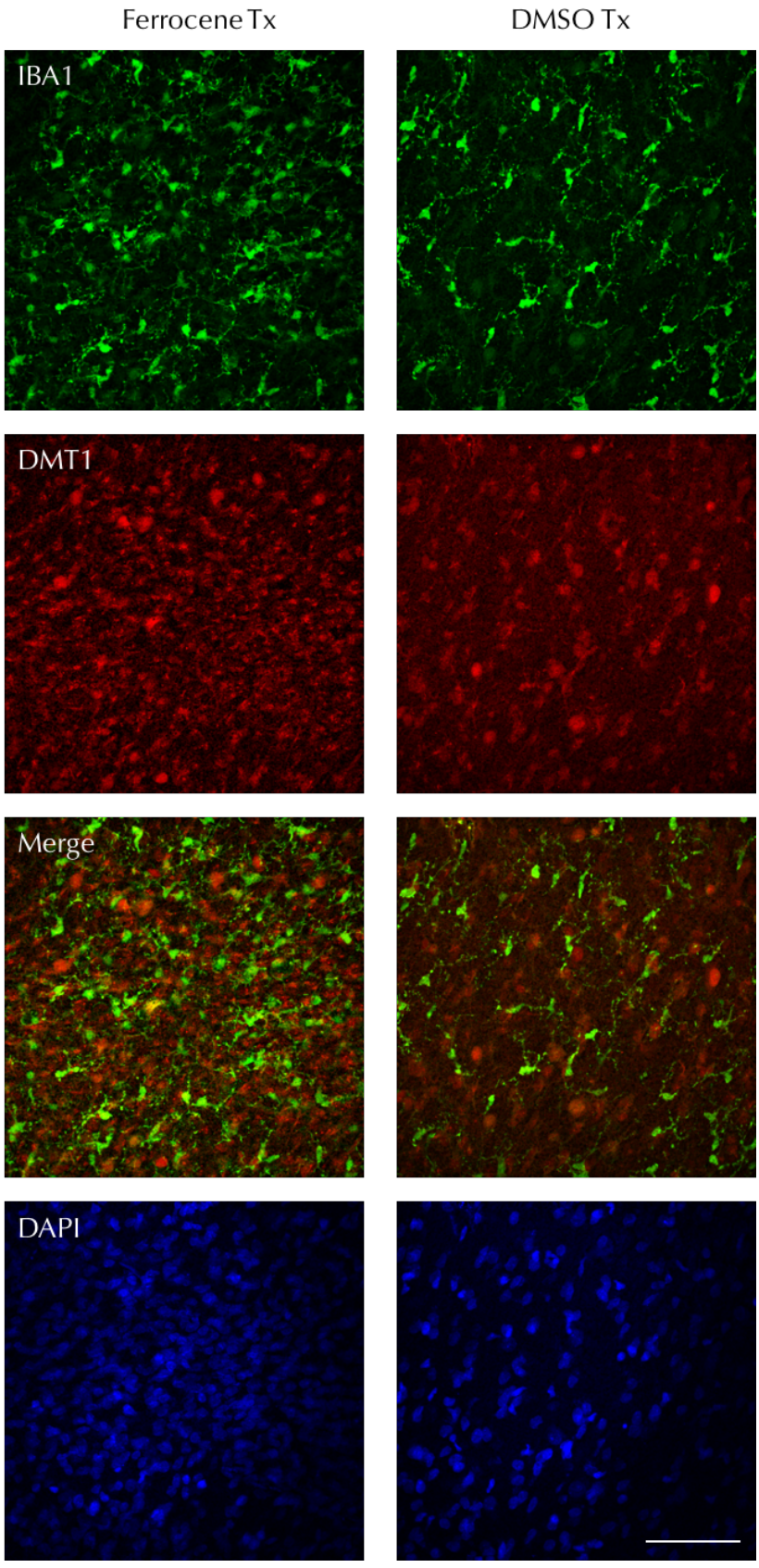

Figure 4.8: Dual immunofluorescent detection of DMT1 in microglia in vehicle and iron-loaded slice cultures. DMT1 expression was seldom seen in microglia in the control. Although DMT1 expression was seen more abundantly seen after iron-loading, the number of microgliahad also increased. Slice cultures were counterstained with DAPI (blue) to visualise the nuclei. Scale bar =

100 µm.

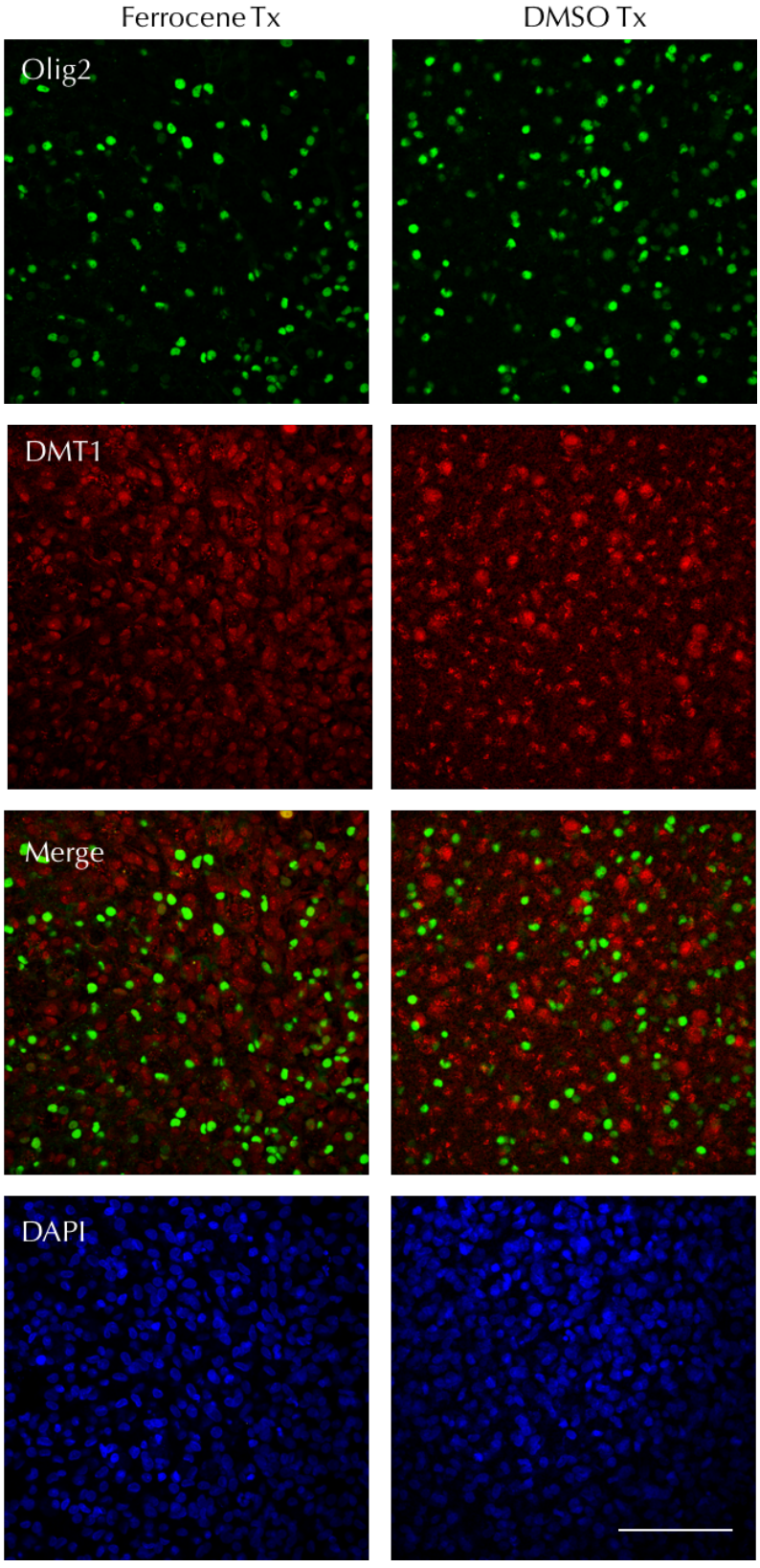

Figure 4.9: Dual immunofluorescent detection of DMT1 in oligodendrocyte-linage cells in vehicle and iron-loaded slice cultures. Very few oligodendrocyte-lineage cells were seen to be DMT1-positive. Iron loading was not seen to have any effect on numbers of DMT1-positive cells. Cultured

were counterstained with DAPI (blue) to visualise the nuclei. Scale bar = 100 µm.

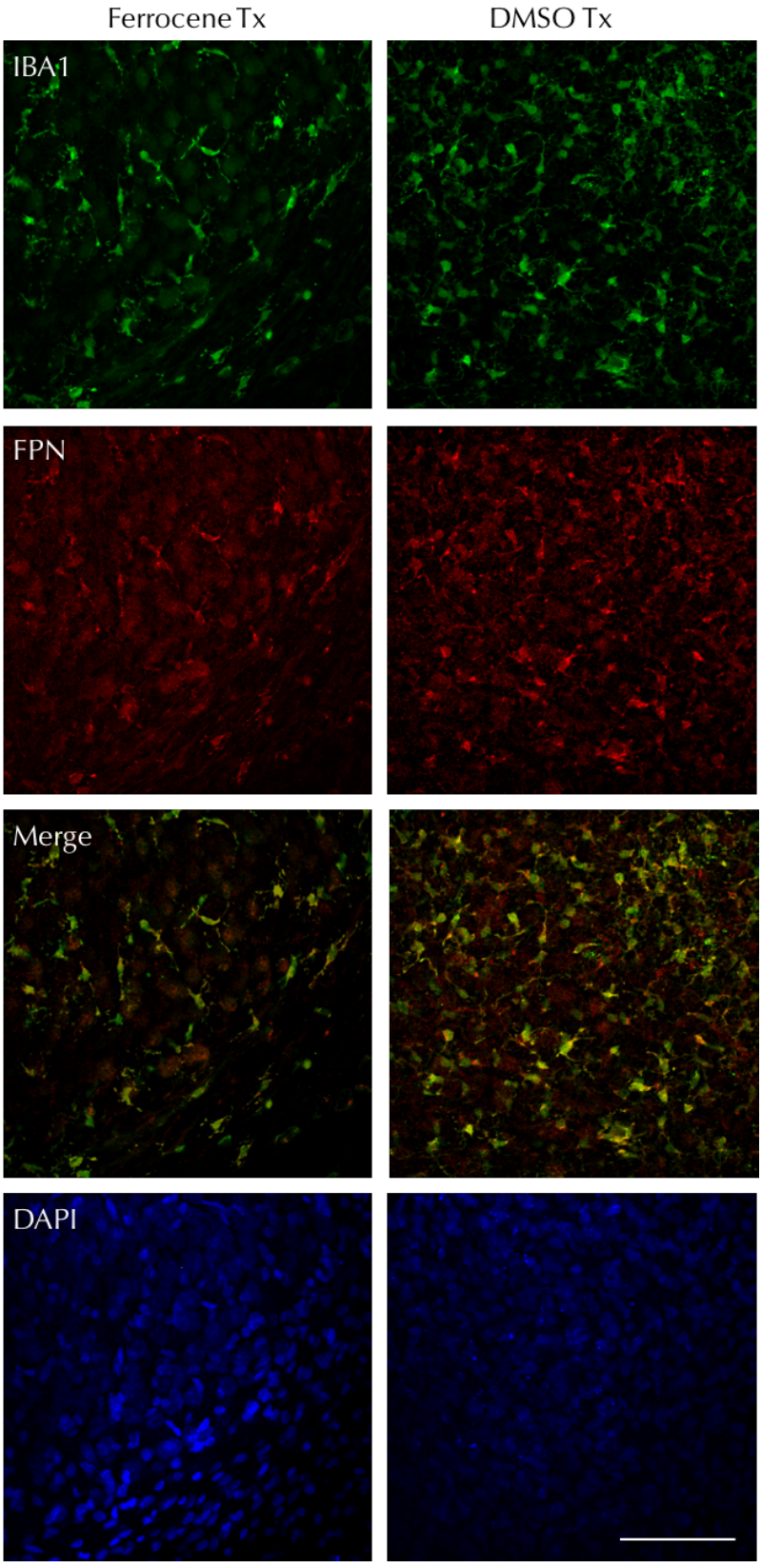

Figure 4.10: Dual immunofluorescent detection of ferroportin in microglia in vehicle and iron-loaded slice cultures. A reduction in ferroportin staining was seen in microglia in iron-loaded slice cultures compared with vehicle. Cultures were counterstained with DAPI (blue) to visualise the nuclei. Scale bar = 100 µm.

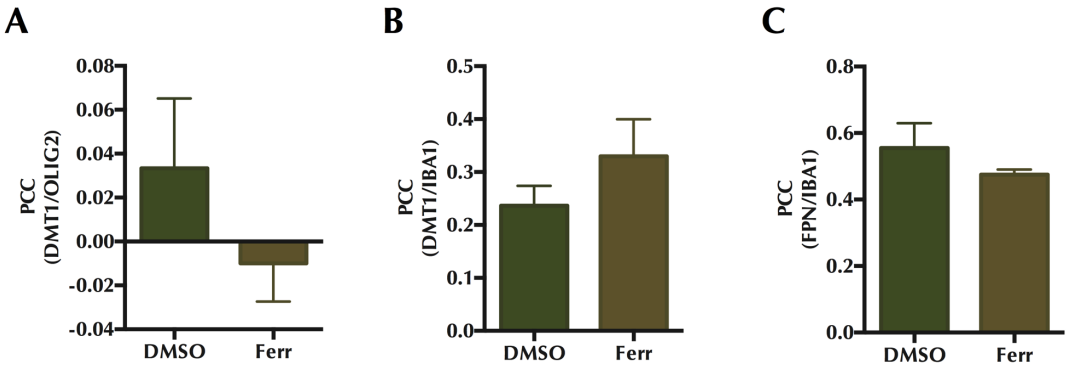

Figure 4.11: Colocalisation analysis of iron molecules with oligodendrocytes and microglia. (A) DMt1/OLIG2 colocalisation. (B) DMT1/IBA1 colocalisation. (C) FPN/IBA1 colocalisation. Preliminary colocalisation analysis using Pearson colocalisation correlation (PCC) indicates that is not any colocalisation between DMT1 and OLIG2-positive cells. There is a weak possible colocalisation with IBA1-positive cells in control conditions and a trend towards an increase after iron loading. There is moderate colocalisation of FPN and IBA1 in control conditions that seems to decrease after iron loading. Values are mean ± SEM from 2 replicate wells (n=1 experiment).

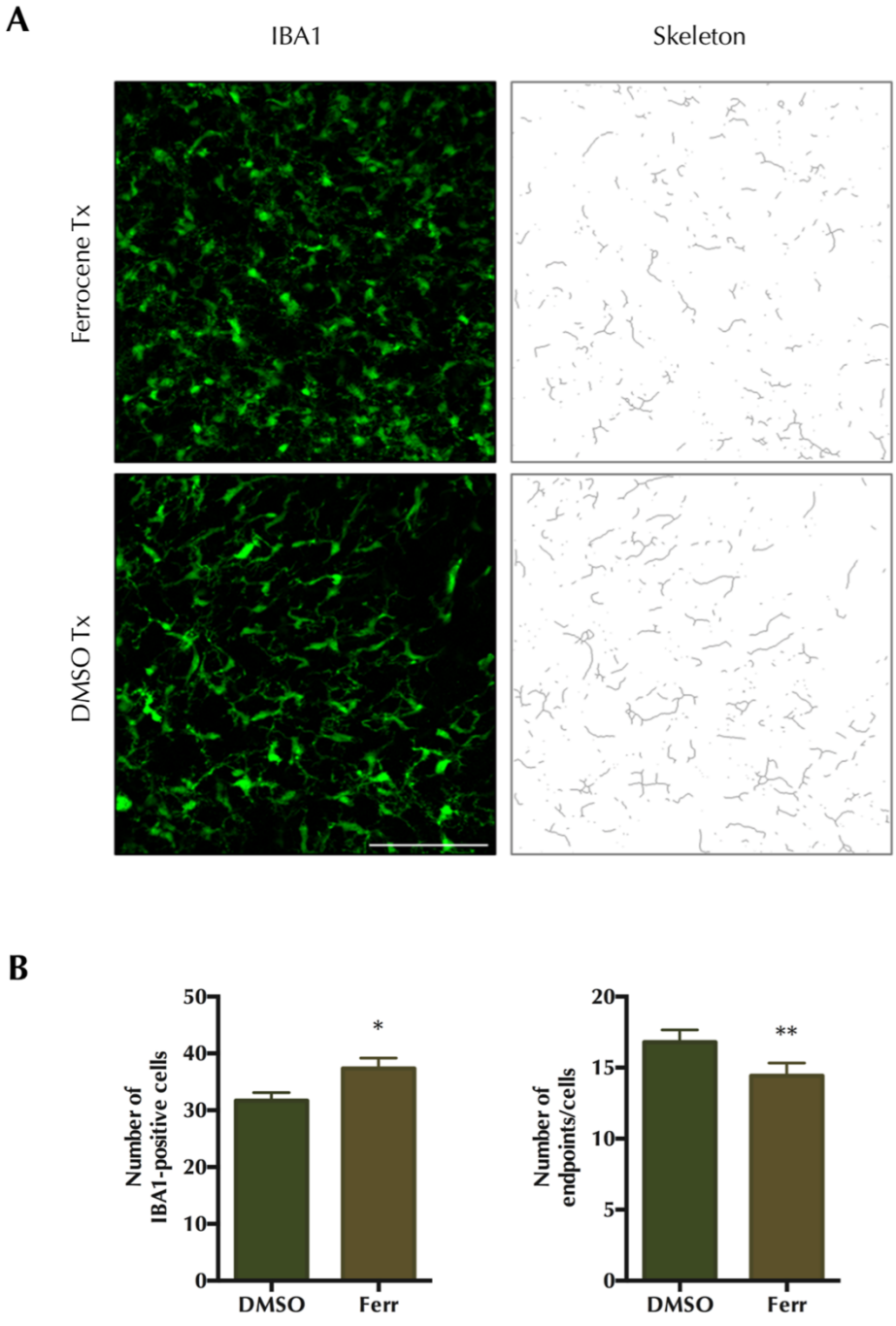

Figure 4.12: Effect of 1 μM ferrocene loading on the number and morphology of microglia. (A) Representative confocal maximum intensity projection images of microglia and skeletonised images. (B) Quantification of the number of the number and branching complexity of IBA1-positive microglia per field. Iron loading increases number of microglia and reduces microglia branching complexity. Endpoint is defined as voxel that only has one neighbour and is used as measure to detect the number of branches and thus branching complexity. Values are mean ± SEM from 3 experiments. * denotes $P<0.05$ and ** $P<0.01$ compared with vehicle. Scale = 100 μm.

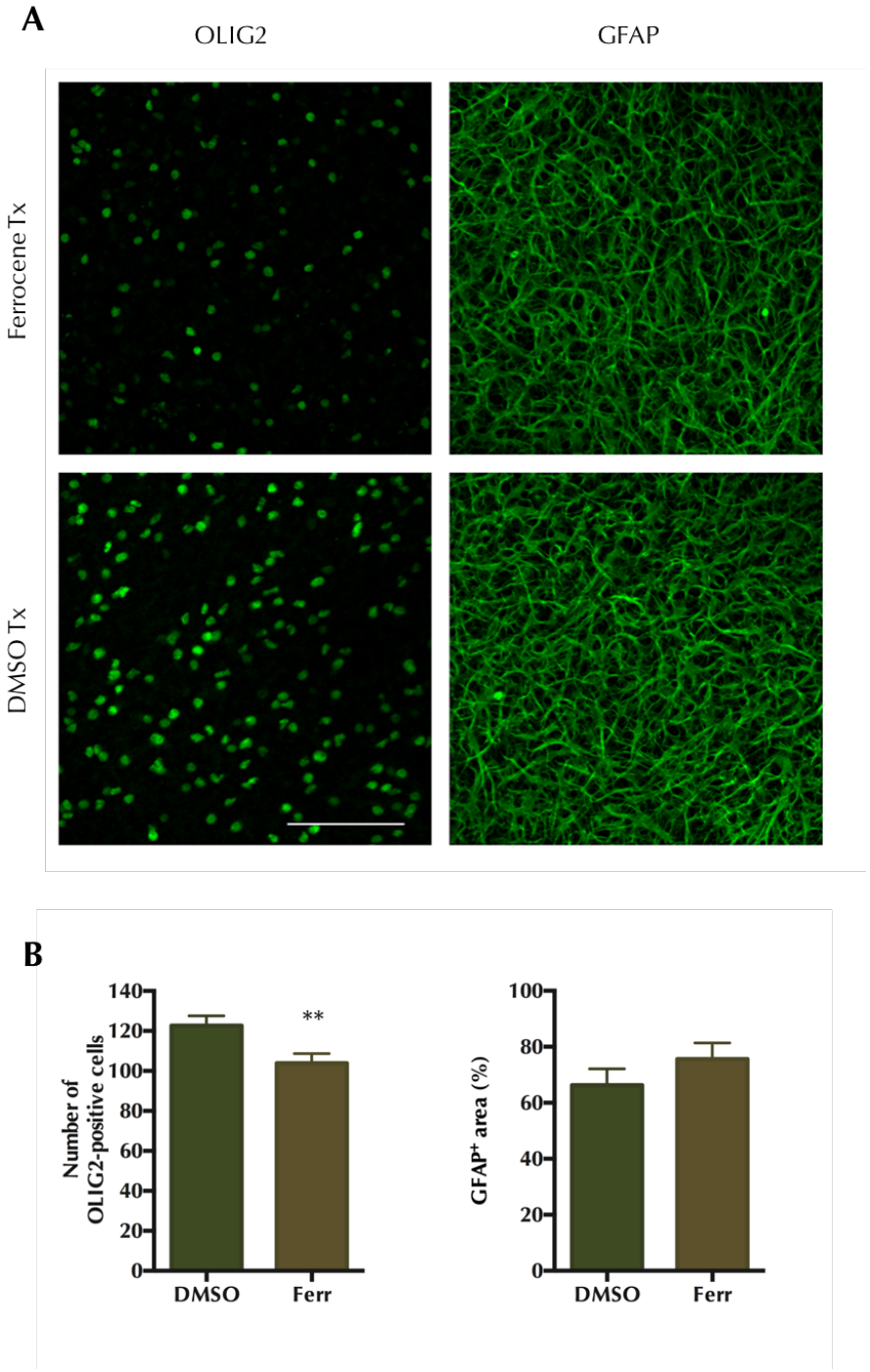

Figure 4.13: Effect of 1 μM ferrocene loading on the number and morphology of glial cells. Representative confocal maximum intensity projection images of (A) oligodendrocyte-lineage cells and astrocytes in vehicle and iron-loaded slice cultures. (B) Quantification of the number of OLIG2-positive cells and the GFAP-positive area per field. Iron loading reduces the number of OLIG2-positive cells but has no effect of astrocyte morphology/number. Values are mean ± SEM from 3 experiments . ** denotes $P<0.01$ compared with vehicle. Scale = 100 μm.

4.5 Discussion

Organotypic cultures have demonstrated great potential as models of pathology in neurological disease, such as demyelination in Multiple Sclerosis (Birgbauer et al. 2004), amyloid deposition in Alzheimer's disease (Humpel 2015b) and degeneration of dopaminergic neurons in Parkinson's disease (Stahl et al. 2009). However, to date, these *ex vivo* cultures have not been realized as a platform to study iron handling in the CNS. Consequently, this study sought to establish and optimise a novel model of iron loading using hippocampal slice-based methodology to mimic the iron deposition and aberrant distribution that can occur in aging and neurodegenerative disease.

Firstly, we report a differential accumulation of iron in slice cultures following 10 µM, ferrocene, ferrous ammonium sulphate (FAS) and ferric citrate loading. Ten µM ferrocene caused maximal incorporation of iron into cultured hippocampus slices, when compared to FAS or FC, with a consequent modest reduction in slice viability. This same pattern was replicated when this experiment was repeated later using 1 µM iron reagent exposure for 12 h.

Before proceeding to discuss the follow-on experimental data of ferrocene concentration on iron-loading, it must be noted, however, that there is approximately a 2-fold difference in the iron content that was detected in the DMSO and H_20 controls between the 1 µM and 10 µM iron reagent comparison studies. This may have been due to technical variability as opposed to any biological effect. The ferrozine assays on the 1 µM experiments were conducted quite some time later and used a new batch of reagents and aliquots. The iron content that was detected in the DMSO controls in another iron-loading study (i.e. optimisation of ferrocene concentration for iron-loading study and this study that used the same batch of reagents) was in line with that detected in the 10 µM iron comparison study. Similarly, in chapter 5, the iron content in the DMSO controls in this iron-loading study (Fig 5.5) matched that of the 1 µM study when the raw data was compared – again the ferrozine assay in both studies used reagents from the same batch. Such absolute differences may indeed be considered negligible because the iron levels in the DMSO controls of all these studies have been in line with the values reported for the basal iron content in primary CNS cells (Fig. 3.1). With respect to the variability and validity of using the ferrozine assay to detect iron, we emphasise that the experimental differences in iron content in the control samples, or indeed, the iron-loaded samples, was minimal. Such findings demonstrate the consistency of the

ferrozine assay between attempts given identical reagents from the same batch and aliquot preparation.

Next, as already indicated, ferrocene caused the greatest increase in iron content out of the three iron reagents tested. This superior ability of ferrocene to cause iron overload may be due to its lipophilic structure (Table 1.2), which makes it membrane-permeable and therefore able to bypass the rigorous iron homeostasis system that acts to keep iron levels under tight control until it is metabolised. Previous studies have shown that iron is released from the ferrocene nucleus by enzymatic hydroxylation (Cable & Isom 1999; Nielsen & Heinrich 1993; Stepnicka 2008; Madinaveitia 1965; Hanzlik & Soine 1978). The resultant hydroxylated metabolite of ferrocene, which is unstable and oxygen dependent, undergoes spontaneous decomposition and releases solvated iron atoms that are available for normal physiological processing and metabolism (Cable & Isom 1999; Nielsen & Heinrich 1993; Stepnicka 2008; Madinaveitia 1965; Hanzlik & Soine 1978). On the other hand, ferrous and ferric iron (Table 1.2), are not lipophilic and must be taken up via DMT1 and transferrin receptor, respectively. Iron loading from these reagents is therefore immediately subjected to the iron homeostasis machinery, which acts to down-regulate DMT1 and the transferrin receptor-mediated uptake of iron under conditions of excess iron (Batista-Nascimento et al. 2012; Gaasch et al. 2007).

Next, in a ferrocene dose-response follow-on study, 1 μM ferrocene, which is slightly elevated compared with normal CSF iron, was discovered to be equally potent at causing iron overload, as both 1 and 10 μM ferrocene caused significant increases in iron content. Unsurprisingly, the addition of 0.1 μM ferrocene (i.e. normal iron load in CSF) did not cause iron accumulation. However, unexpectedly, neither did the addition of 100 μM ferrocene. Since ferrocene is known to pass through cell membranes by diffusion, it is possible that concentration gradients, rather than molarity, dictate the uptake of this compound into a cell.

The degree of iron accumulation in our iron-loaded organotypic cultures is on a par with the increase in iron concentration detected in the post-mortem brain of people suffering from neurodegenerative disease. For example, iron content is elevated by approximately 1.5-fold in the AD hippocampus, 1.6-fold in MS grey matter structures and periplaque white matter, and 1.6-fold in PD substantia nigral tissue, when compared with control brain (Hametner et al. 2013; Ayton et al. 2013; Ge et al. 2007). Also, a similar increase in the iron levels in subcortical white matter of healthy people with aging has been reported (Hametner et al. 2013).

Several groups have reported similar increases in iron-loaded CNS monocultures. Different studies using primary astrocytes and microglia exposed to 10-33 μM FC or FAS for treatment periods ranging from 8-24 h reported a 2-fold increase (Hoepken et al. 2004; Rathore et al. 2012; Riemer et al. 2004). Similarly, 20 μM TMPH-ferrocene 24 h exposure lead to a 1.2-fold increase in oligodendrocyte precursor cells (OPCs) (Zhang et al. 2005). However, Bishop *et al.* demonstrated much higher 57- 35- and 19-fold increases in microglia, astrocytes and neurons, respectively, after 24 h incubation with 33 μM FAC(Bishop et al. 2011). While these large increases in iron content are impressive, the magnitude of iron accumulation in our model more closely matches that seen in human brain disorders.

In our iron-loaded slice cultures, we detected an increase and possible redistribution of ferritin expression in glial cells when compared to vehicle. Notably, we observed a modest increase in ferritin-positive microglia, which is in line with the reported 1.65-fold increase in iron influx in 20 μM ferric chloride-treated cultured primary microglia (Rathore et al. 2012), but is much less than the 57-fold increase in iron content in primary microglia exposed to 33 μM ferric ammonium citrate reported by Bishop *et al.* (2011). Furthermore, we have also shown differences in the expression of iron import and export proteins in microglia. Fluorescent dual labelling and colocalsiation analysis provides evidence that is indicative of an increased expression of DMT1 in microglia and no change in oligodendrocyte-lineage cells. Furthermore, ferroportin expression seems to be decreased in microglia, a pattern indicative of microglia mopping up and retaining excess iron.

This cellular differential regulation likely accounts for why statistical significance was not achieved with our qPCR analysis – the opposing alterations in protein expression within the different cell types might be masked and/or diluted at the slice level, suggesting that total measurements at transcript or protein level within slice cultures do not provide reliable indicators of perturbations in the iron homeostasis. Nevertheless, we note modest up-regulation in several uptake proteins, that, although not significant, are still interesting and helped us select a subset of proteins to investigate at a cellular level using dual-labelling. This is important given the resource and feasibility limitations with regard sample and antibody availability to assess each homeostasis protein in each cell type for each condition.

In addition to iron loading having an impact on the iron homeostasis system, iron loading also led to more general cellular effects. Ferrocene treatment was seen to

cause a significant increase in the number of microglia. We hypothesise, that in a slice culture system, proliferation is the only feasible source for the increased number of microglia cells. Hydrogen peroxide, which is produced by the oxidation of iron in ferritin (Bou-Abdallah 2010; Zhao et al. 2001), has been described an important regulator of microglial proliferation (Groeger et al. 2009; Mander et al. 2006) and might be responsible for the increase in microglia cells that we detected in our iron-loaded slice cultures.

When the morphology of microglia was examined following exposure to ferrocene, there was an obvious change that appeared to be consistent with activation (Perry et al. 2010; Streit et al. 2009). This observation was confirmed using an objective Image J-based skeleton analysis (Morrison & Filosa 2013) of images from over 200 fields. The significant reduction in microglial 'end-points', when vehicle- and ferrocene-treated cultures were compared, suggests that some microglia were in an iron-induced activated state. This data is consistent with reports that ferritin positivity and iron accumulation are associated with activated and dystrophic microglia in aged brains, as well as in brains from individuals who had AD, MS or Huntington's disease (Hametner et al. 2013; Streit et al. 2009; Morrison & Filosa 2013; Simmons et al. 2007).

Similarly, with regard to oligodendrocyte-lineage cells, we more frequently observed ferritin in OLIG2-positive cells in the iron-loaded slice cultures compared with vehicle. Furthermore, in an unbiased quantification of oligodendrocyte-lineage cells using ImageJ, we demonstrated a significant 15% reduction in the number of OLIG2 positive cells, suggesting that the lower level of slice viability could be a result of oligodendrocyte-lineage cell death. It is also possible that the loss of OLIG2-positive cells could be attributable to differentiation of early progenitors into other cell types, in response to iron-loading. However, at this stage of development in the hippocampus it is not expected that many of these multipotent cells would be present. Also, such a degree of differentiation would result in measurable increases in other cell types, which were not seen, suggesting that this change is largely due to loss of cells committed to the oligodendrocyte cell line. This is the first time, to our knowledge, that an iron-induced loss of oligodendrocytes from cultured hippocampal slices has been documented. Our data is consistent with reduced numbers of oligodendrocytes that has been previously reported in active MS lesions in post-mortem human tissue (Hametner et al. 2013). In that particular study, the loss of oligodendrocytes was accompanied by an up-regulation of iron-exporting ferroxidases and extracellular accumulation of iron (so-called iron liberation) followed by uptake of iron into microglia and macrophages. This is of interest

since, in our brain slice model, we have observed increased ferritin staining in microglial cells following ferrocene treatment.

Astrocytes have previously been reported to accumulate large amounts of iron without any compromise in cell viability (Bishop et al. 2010; Keenan et al. 2010; Riemer et al. 2004; Bishop et al. 2011). They respond somewhat similarly in our *ex vivo* slice culture model of iron-loading. On the one hand, we demonstrate only modest ferritin expression in iron-treated astrocytes, which is undetectable in control slices. On the other hand, in agreement with the previous reports regarding the robustness of astrocytes when it comes to iron toxicity, we do not show any difference in astrocyte morphology or number between iron- and vehicle-loaded slices. This implies that astrocytes, unlike oligodendrocytes, do not contribute towards the 1.6-fold increase in LDH release in iron-loaded cultures. It might also partially explain the apparently contradictory MTT and LDH assay results, since the metabolic activity of the plentiful astrocyte population in the slices may have obscured the reduced metabolism in other cell types.

4.6 Conclusion

Iron-loading slice cultures with ferrocene produces a maximal increase in iron content when compared to other commonly used iron reagents. The accumulation of iron was accompanied by alterations in transcripts of iron homeostasis protein, increased ferritin in glia, mild toxicity, leading to oligodendrocyte loss, and microglia activation and proliferation. No appreciable effects were seen with astrocytes.

We believe that use of hippocampal slice-based methodology to produce a novel model of *ex vivo* iron accumulation is a significant advance on the mono- or dual-culture-based approaches that have been used up to now and that it will be an invaluable tool for researchers attempting to alleviate suffering caused by iron overload in the human brain.

5 Iron metabolism and the UPR in the CNS

5.1 Introduction

The unfolded protein response (UPR) is a 'check-and-balance' program activated upon disturbed homeostasis in the endoplasmic reticulum (i.e. ER stress). It acts to alleviate stress and restore normal ER function. Recently, the interplay between the UPR and iron metabolism has been identified in a hepatocyte cell line and in murine spleen (Oliveira et al. 2009). Nevertheless, this intriguing reciprocal relationship has remained underexplored and unappreciated in the CNS (Y. Liu & Connor 2012). A better understanding of this crosstalk might provide further clues into disease pathogenesis given that aberrant iron metabolism and increased expression of markers of the UPR have been independently reported in several neurodegenerative diseases, including multiple sclerosis, Alzheimer's disease and Parkinson's disease (Mercado et al. 2013; Lin & Popko 2009; Hetz & Mollereau 2014; Stephenson et al. 2014; R. Ward et al. 2014)..

5.2 Aims

The overall goal of this work was to confirm and characterise the reciprocal relationship between UPR and iron homeostasis within the CNS as a foundation for a future studies.

Specific aims:

i. Define the profile of expression of UPR associated molecules (BiP, CRT, CHOP, ATF4, ATF6, XBP1 and XBP1) at an mRNA level in iron-loaded slice cultures.

ii. Identify the putative binding sites of UPR transcript factors on a cohort of iron homeostasis proteins *in silico*.

iii. Localise the cellular expression of UPR transcription factors CHOP and ATF6 in iron-loaded and UPR activated cultures.

iv. Investigate whether or not a concurrent activation of a UPR in iron-loaded *ex vivo* brain slice cultures recapitulate the same iron deposition, modest toxicity and glial perturbations previously characterised.

5.3 Summary of Methodology

Iron-loaded brain slices, which were established, characterised and described in chapter 4, were used as an experimental platform to investigate iron-UPR interplay. Slice culture preparation and processing methods have been summarised in chapter 2. Five μg/ml tunicamycin (Tm) exposure was used to activate a UPR response. Slice cultures were harvested for comprehensive molecular, immunohistochemical, viability and biochemical analyses using methods described in chapter 2. Glial cell image analysis (see chapter 6 for optimisation and complete image analysis workflow methodology) was carried out on a total of 32 images from only 2 independent experiments (i.e. 4 images/slice culture 2 slice cultures/well and 2 wells/treatment). This is a less comprehensive and robust sampling and analysis than previously described in chapter 2. Identification of UPR transcription factor binding sites in promoter elements of iron homeostasis molecules was performed by computer search using Alggen Promo software, available on web page: www.alggen.lsi.upc.es.

5.4 Results

5.4.1 Impact of iron loading on the UPR

The effect of iron metabolism on the transcript expression of UPR-associated molecules was investigated by real-time PCR analysis using cDNA generated from iron-loaded slice culture experiments. There was approximately a 1.5-fold increase in mRNA expression in BiP/Grp78 and CRT in the iron-loaded slice cultures compared with control although this up-regulation did not reach statistical significance (Fig. 5.1). Similarly, increased expression of the transcripts of UPR-associated transcription factors was also seen, but again failed to reach statistical significance. CHOP transcripts were increased by approximately 1.5-fold. ATF4 and ATF6 were up-regulated 1.4- and 2.1-fold, respectively (Fig. 5.2). There was also an upward trend of increased expression of spliced and unsliced forms XBP1.

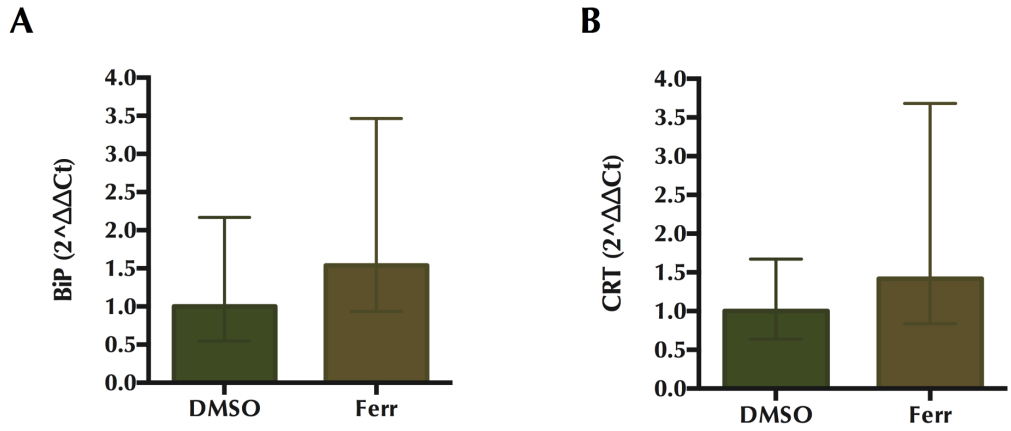

Figure 5.1: UPR chaperone mRNA expression in iron-loaded slice cultures. (A) BiP and (B) CRT. There was a trend towards increased transcript expression of BiP and CRT in iron-loaded slice cultures compared with control. Data expressed mean ± 95% confidence interval from 3 experiments.

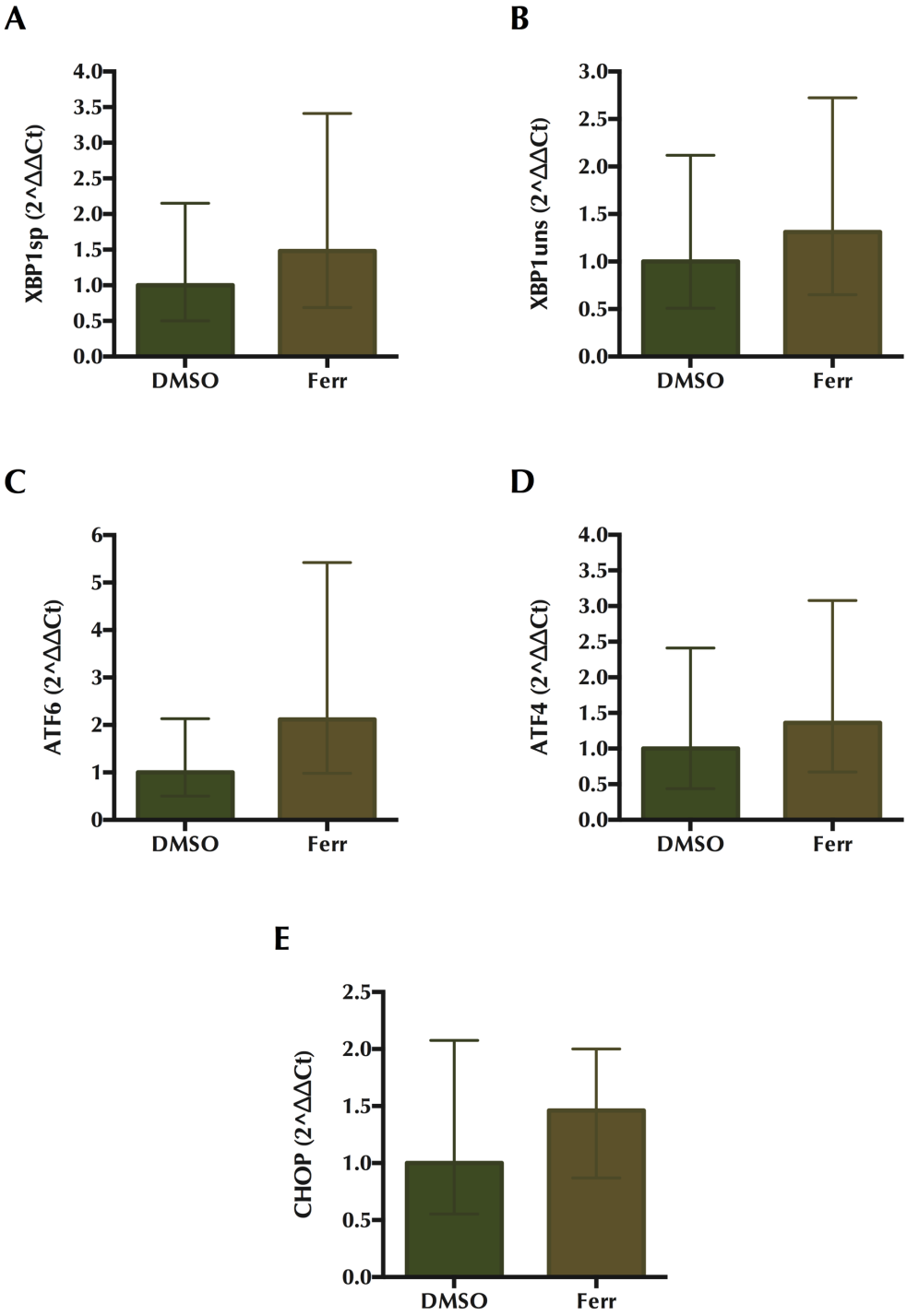

Figure 5.2: UPR transcription factor mRNA expression in iron-loaded slice cultures. (A) XBP1sp, (B) XBP1unsp, (C) ATF6, (D) ATF4 and (E) CHOP. There was a trend towards increased transcript expression of spliced XBP1,unspliced XBP1, ATF6, ATF4 and CHOP in iron-loaded slice cultures compared with control. Data expressed mean ± 95% confidence interval from 3 experiments.

5.4.2 Impact of the UPR on iron metabolism

Preliminary data generated from *in silico* (5.4.2.1) and real-time PCR (section 5.4.2.2) analyses have yielded evidence that is consistent with the idea that the UPR modulates iron metabolism.

5.4.2.1 In silico analysis for UPR transcription factor binding sites

Using the ALGGEN PROMO algorithm (with version 8.3 of TRANSFAC data) for predicting consensus protein binding sequences, we have demonstrated the presence of a number of putative binding sites for transcription factors commonly induced during the UPR in the DNA sequence of iron homeostasis molecules (Table 5.1). Only hits that had a dissimilarity index <15% and a random expectation <0.5 were included in this analysis. None of the transcription factors were found to be commonly expressed on all the genes of the iron homeostasis molecules that were tested. ATF3 and C/EBP-alpha were found on six of the eight genes (the exception of FTL and TfR1 for ATF3 and Hepc and Tf for C/EBP-alpha). XBP1, ATF and ATF2 were found on only two genes, CREB on three genes and C/EBP-beta was not found on any. There was not a consistent pattern of transcription factors hits across the different genes.

Table 5.1 Putative binding sites of UPR transcription factors in iron homeostasis molecules

Gene	Factor name	Start	End	Dissimilarity	String	RE equally	RE query
Hepc	ATF3 [T01313]	23	60	6.74	tgacacaa	0.0821	0.0616
	ATF3 [T01313]	445	45	13.48	tgctgtca	0.164	0.132
	XBP-1 [T00902]	379	384	6.47	atgccc	0.292	0.318
	XBP-1 [T00902]	448	453	1.58	tgtcat	0.22	0.231
FTH	ATF3 [T01313]	497	504	10.12	tgacaaaa	0.222	0.225
	ATF3 [T01313]	521	528	10.12	tgacttca	0.222	0.225
	C/EBPα [T00105]	301	307	3.55	accaatc	0.1367	0.225
	C/EBPα [T00105]	425	431	7.47	tgcaatg	0.273	0.29
	C/EBPα [T00105]	527	533	2.44	cattgag	0.273	0.278
	C/EBPα [T00105]	571	577	2.37	aattggg	0.273	0.279
	C/EBPα [T00105]	1063	1069	8.00	tccaatg	0.137	0.141
FTL	XBP-1 [T00902]	494	499	6.48	atgagg	0.401	0.4339
	C/EBPα [T00105]	211	217	5.58	gtcaatt	0.401	0.283
	C/EBPα [T00105]	754	760	5.78	gccaata	.401	0.283
TfR1	C/EBPα [T00105]	1609	1615	1.22	tattgag	0.345	0.42
	C/EBPα [T00105]	1822	1828	0	gattgag	0.345	0.334
	CREB [T00163];	2347	2355	3.08	tgacgtttg	0.086	0.091
Tf	C/EBPα [T00105]	1410	1416	4.56	gacaatc	0.28	0.27
	ATF3 [T01313]	1040	1047	8.31	gtatgtca	0.316	0.311
	ATF3 [T01313]	1397	1404	10.12	tgacctca	0.45584	0.445
	ATF3 [T01313]	1887	1894	0.00	ttacgtca	0.035	0.033
	CREB [T00163]	1886	1894	2.66	attacgtca	0.070	0.0687
	ATF-2 [T00167]	1886	1895	4.17	attacgtcaa	0.0395	0.037
	ATF [T00051]	1887	1898	8.419	ttacgtcaacag	0.08876	0.08748
FPN	ATF3 [T01313]	2376	2383	8.31	atatgtca	0.455	0.429
	ATF3 [T01313]	2745	2752	8.31	atatgtca	0.455	0.429
	ATF3 [T01313]	3237	3244	3.37	tgacataa	0.151	0.179
	C/EBPα [T00105]	759	765	5.024	cacaatc	0.404	0.37
	C/EBPα [T00105]	777	783	3.55	gattgga	0.404	0.533
	C/EBPα [T00105]	1433	1439	4.56	gattggc	0.404	0.367
Cp	C/EBPα [T00105]	74	80	8.00	cattgga	0.405	0.505
	C/EBPα [T00105]	935	941	0.54	cacaatc	0.405	0.361
	C/EBPα [T00105]	1421	1427	1.22	tattgag	0.405	0.361
	C/EBPα [T00105]	1430	1436	0.54	gattggg	0.405	0.361
	ATF3 [T01313]	932	939	6.74	tgacacaa	0.456	0.519
DMT1	C/EBPα [T00105]	2	8	3.55	accaatc	0.463	0.566
	CREB [T00163];	3116	3124	2.664	tgacgtgat	0.116	0.119
	ATF3 [T01313]	2716	2723	3.372	tgacataa	0.173	0.192
	ATF-2 [T00167]	3115	3124	4.17	ttgacgtgat	0.065	0.075
	ATF [T00051]	3112	3123	5.46	gcattgacgtga	0.048	0.047

Summary of the putative binding site of the UPR-associated transcription factors in the gene sequence of an iron-homeostasis molecule with a dissimilarity index < 15% and random expecation <0.5. Transcription factors tested: C/EBP-beta, C/EBP-α, CREB, XBP1, ATF, ATF3, ATF-2 and ATF1.

5.4.2.2 Real-time PCR analysis of the transcript expression of iron homeostasis molecules following UPR activation

The effect of UPR activation on the transcript expression of iron homeostasis molecules was investigated by real-time PCR analysis using cDNA generated from slice culture cultures exposed to 5 µg/ml tunicamycin. Firstly, we demonstrated that the transcript expression of BiP and CHOP, classical markers of UPR activation, were present at significantly higher levels, being 30- and 40-fold compared with control (Fig. 5.3). After confirming an activated UPR, we sought to investigate the production of iron homeostasis molecule transcripts. Tm exposure led to a 1.3- and 1.5-fold increase in FTL and FTH transcripts, respectively, compared with the DMSO control (Fig 5.4). Although there was a trend towards significance, this was not reached.

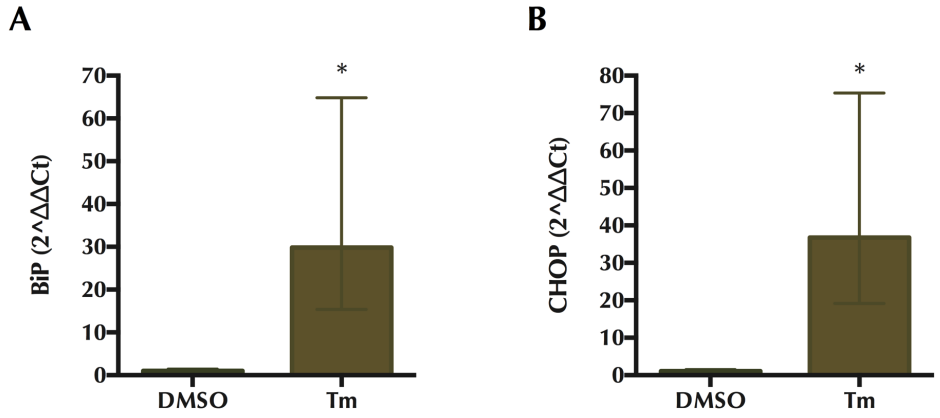

Figure 5.3: Activation of the UPR. Slice cultures were exposed to 5 µg/ml Tunicamycin for 12 h and immediately harvested without a recovery period. Under these conditions, there was a significant up-regulation of transcripts of BiP and CHOP compared with control. Data expressed mean ± 95% confidence interval from 3 experiments. * denotes a significant difference.

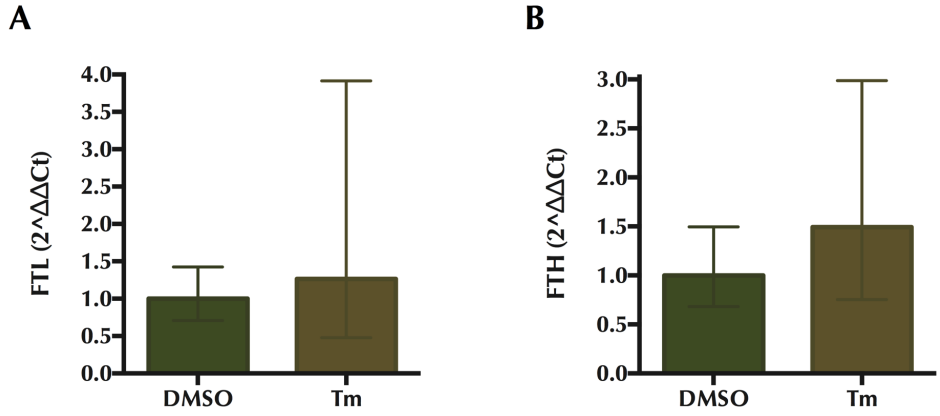

Figure 5.4: Effect of UPR activation on mRNA expression of iron storage molecules. There was a trend towards an up-regulation in FTL and FTH transcripts following 5 µg/ml tunicamycin exposure compared with control, although this did not reach statistical significance. Data expressed mean ± 95% confidence interval from 2 experiments.

5.4.3 UPR activation prevents ferrocene-induced iron accumulation and glial perturbations

5.4.3.1 Iron content and toxicity

In line with our previous findings, 1 μM ferrocene produced a 1.3-fold increase in the levels of iron in slice cultures when compared to vehicle. Similarly, we confirmed that ferrocene-induced a significant 1.5-fold increase in LDH release, and, once again, did not report any iron-induced loss in metabolic activity as assessed by MTT assay. Intriguingly, a concurrent 5 μg/ml Tm-induced UPR activation (TmF) resulted in amelioration in iron accumulation and toxicity (Fig. 5.5). We report that TmF exposure led to a significant difference in iron content and LDH release compared with ferrocene but not when compared with the DMSO control. Tm exposure alone did not lead to a significant difference in iron content or viability. There were no significant differences in metabolic activity or protein content between groups.

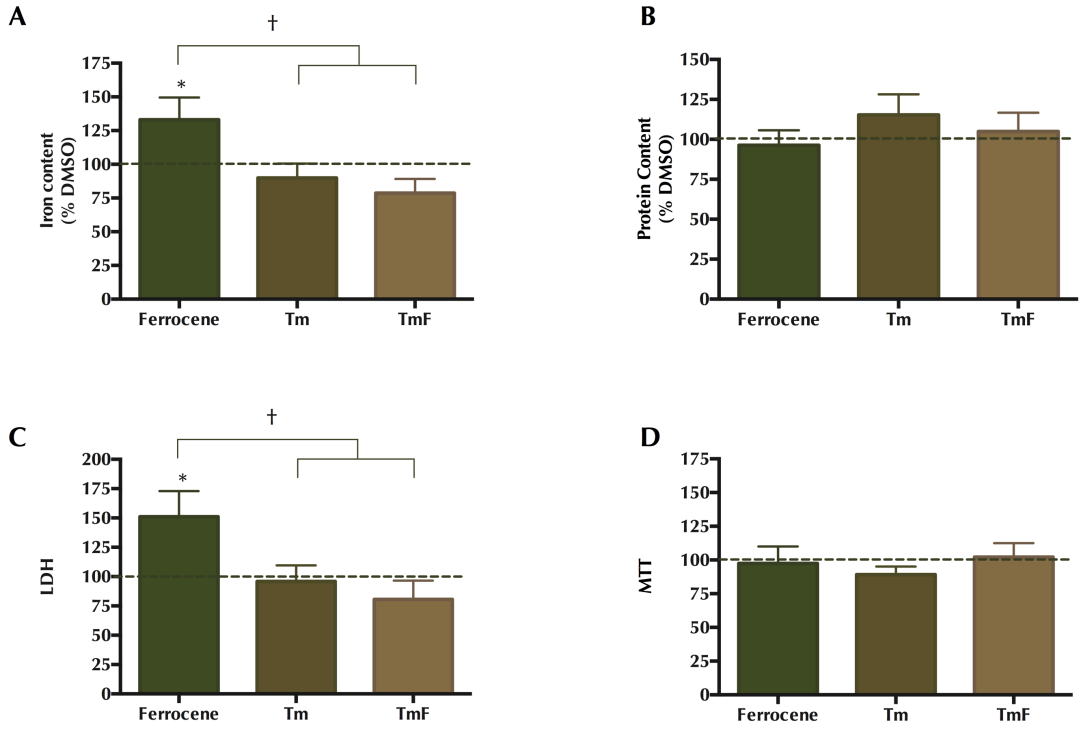

Figure 5.5: Effect of UPR activation on iron loaded slice cultures. Cultures were loaded with 1 μM ferrocene, 5 μg/ml Tm or both treatments concurrently (TmF). (A) Iron content. (B) Protein. (C) LDH assay. (D) MTT assay. Data expressed as percentage of DMSO control, which is indicated by the dashed line. Values are mean ± SEM from 3 experiments. * denotes a significant difference compared with DMSO and † denotes significance between groups ($P<0.05$).

5.4.3.2 Transcription factor expression in glia cells

CHOP-positive staining was not detected in control slice cultures. Similarly, there were minimal CHOP positive cells observed in iron-loaded slice cultures. Unsurprisingly, CHOP staining was abundant in the UPR-activated slice cultures and was most often seen in the nuclei or cytoplasm of cells but was rarely detected in processes (Fig. 5.6 & 5.7). Using dual immunofluorescent labelling, we have demonstrated that the CHOP positivity seen in nuclei following Tm exposure was occasionally colocalised with OLIG2-positive cells (Fig. 5.6). but only rarely colocalised with IBA1-positive microglia (Fig. 5.7). Intriguingly, we have observed slightly more CHOP-positive oligodendrocyte-lineage cells following TmF exposure compared with Tm.

Non-nuclear ATF6-positive staining was observed in slice cultures under all conditions (Fig 5.8 and 5.9). However, we observed an increased number of ATF6-positive nuclei following ferrocene, Tm or TmF exposure. Using dual immunofluorescent labelling, we further demonstrated that this nuclear and non-nuclear ATF6 expression is associated with oligodendrocyte-lineage cells following iron-loading or UPR activation, but was not detectable in the oligodendrocyte-lineage cells in the control (Fig. 5.9).

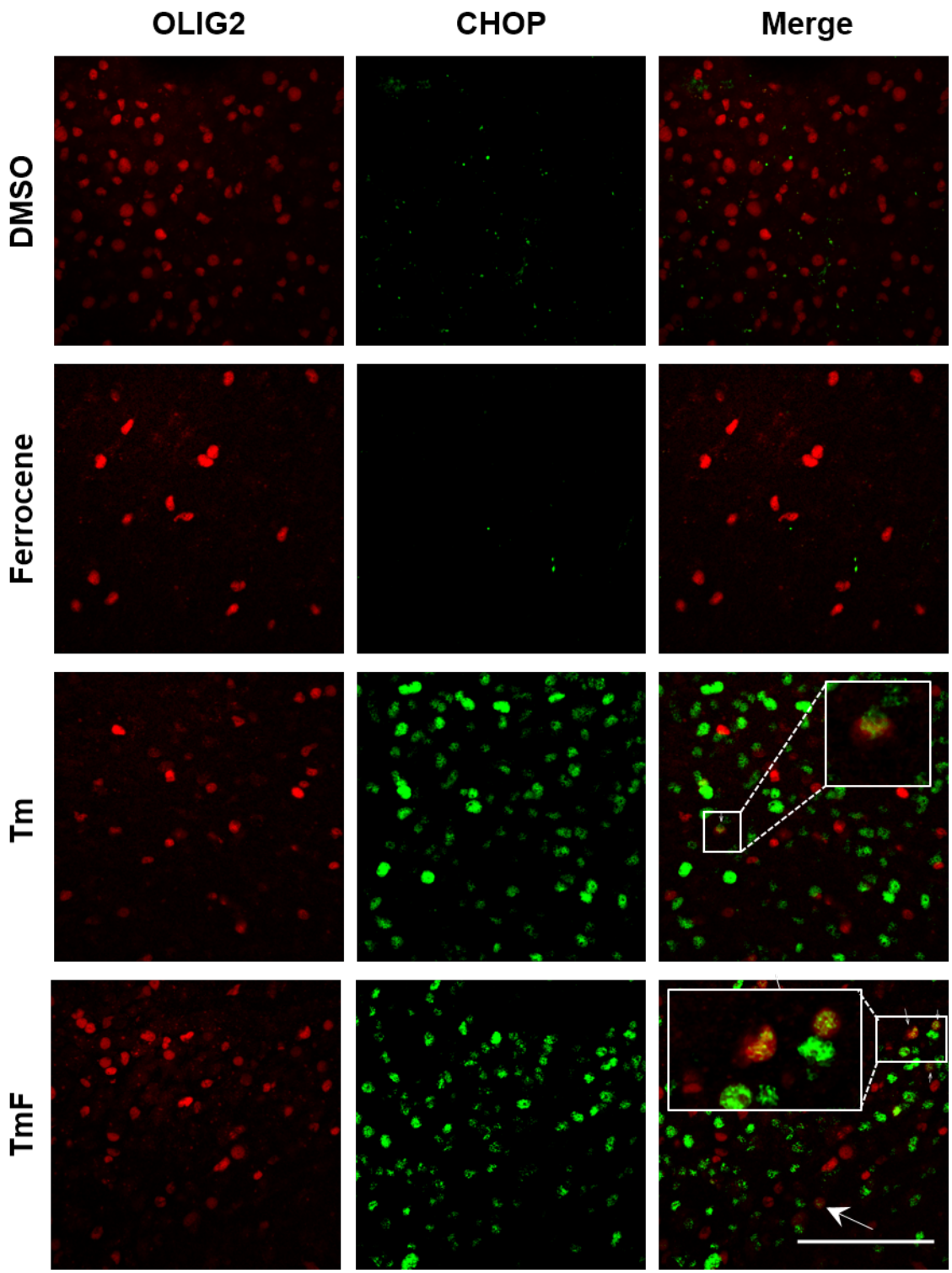

Figure 5.6: Dual immunofluorescent detection of CHOP in oligodendrocyte-lineage in vehicle, iron-loaded and UPR activated slice cultures. There is no detectable CHOP expression in OLIG2-positive cells in control or iron-loaded slice cultures. CHOP expression is occasionally seen following Tm exposure or concurrent iron/Tm exposure (TmF). The insets and white arrow denote colocalisation in merged images. Scale bar = 100 μm.

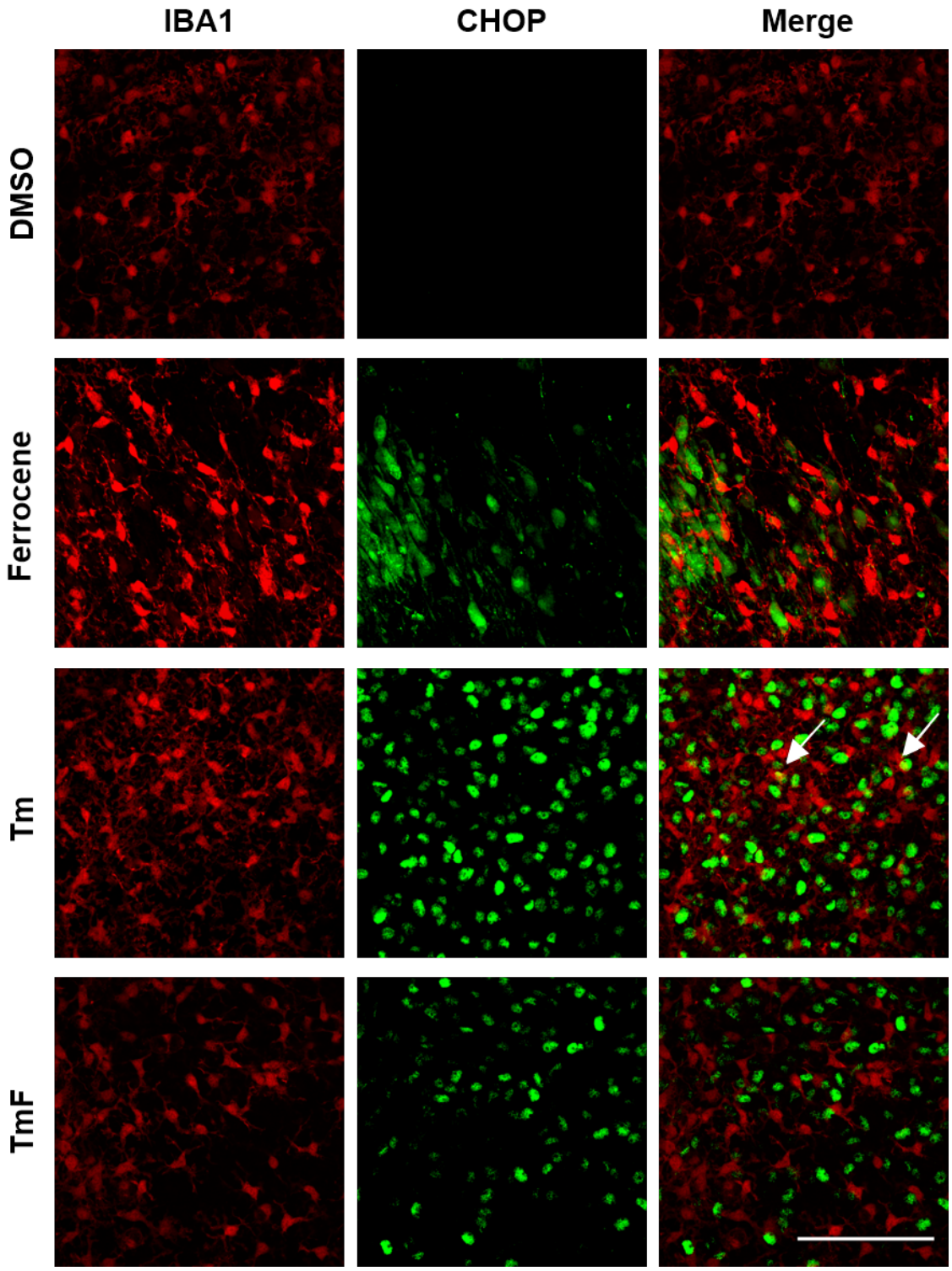

Figure 5.7: Dual immunofluorescent detection of CHOP in microglia in vehicle, iron-loaded and UPR activated slice cultures. There is no detectable CHOP expression in microglia cells in control or iron-loaded slice cultures. CHOP expression is rarely detectable in microglia (arrows) following Tm exposure or concurrent Tm/iron exposure (TmF). Scale bar = 100 μm.

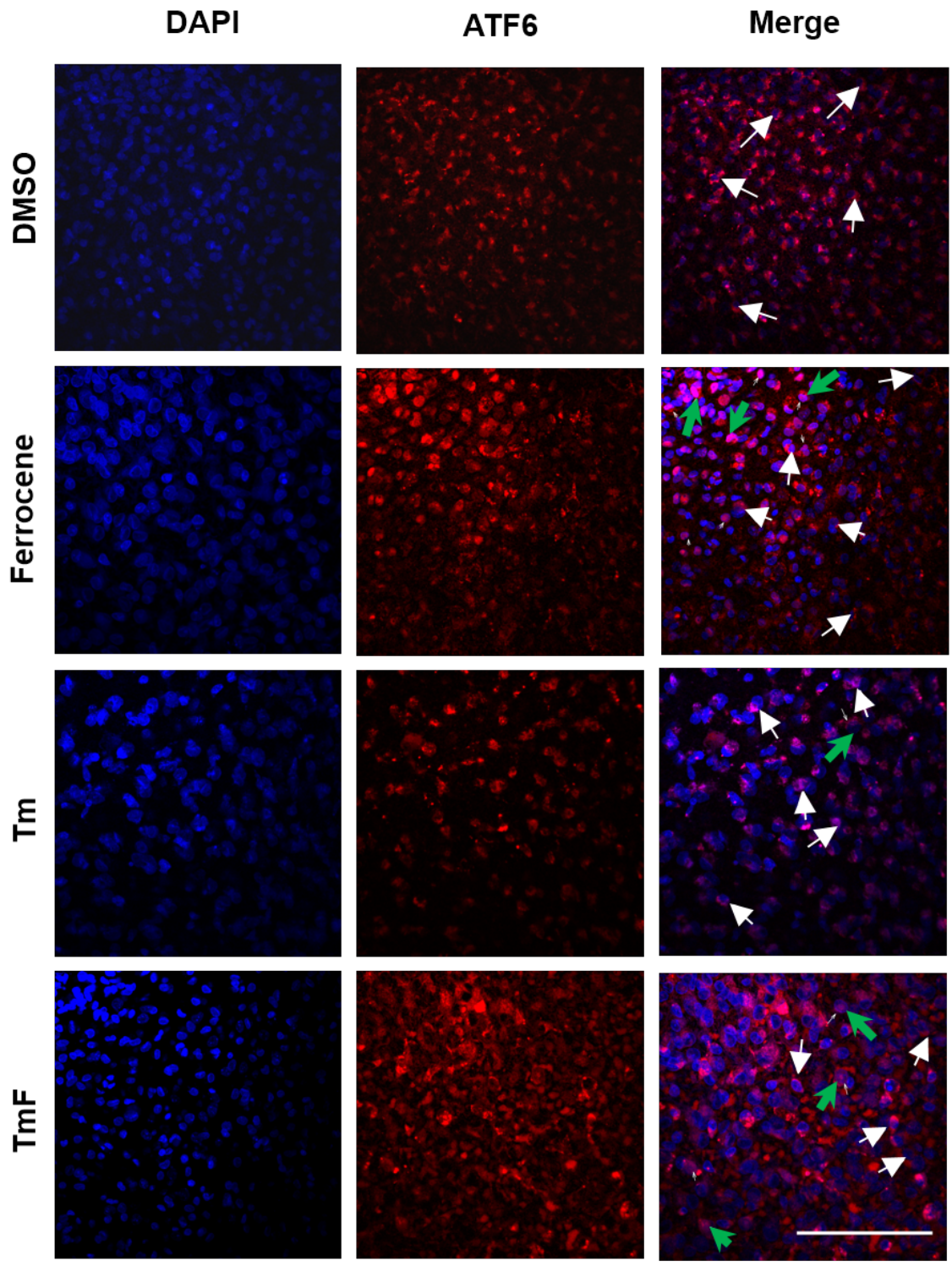

Figure 5.8: Dual immunofluorescent detection of ATF6 in nuclei of neurons and glial cells in vehicle, iron-loaded and UPR activated slice cultures. Both nuclear (green arrows) and non-nuclear (white arrows) localised ATF6 expression is observed following ferrocene and TmF exposure and occasionally following Tm exposure while only non-nuclear ATF6 is observed in the control. Scale bar = 100 µm.

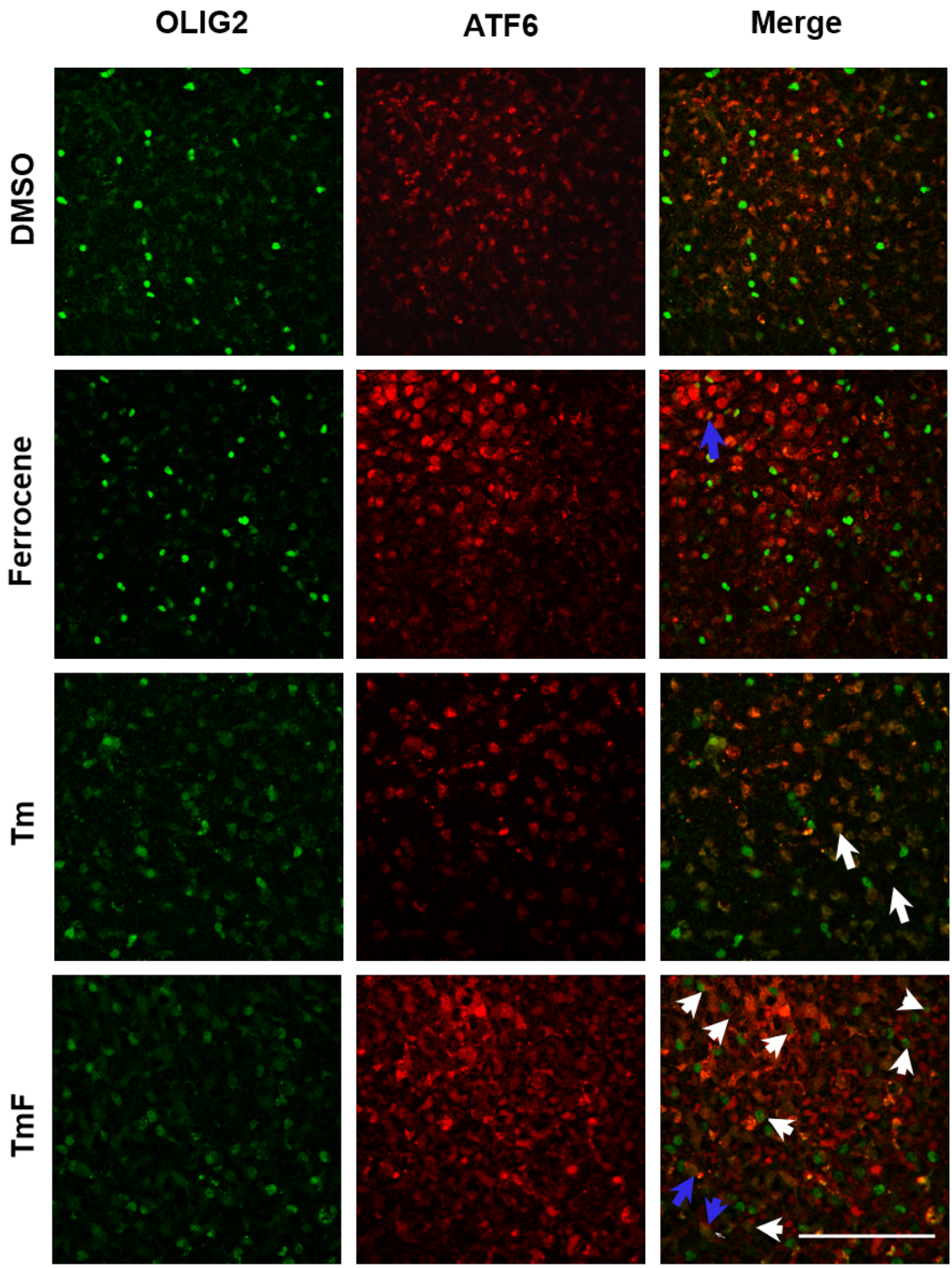

Figure 5.9: Dual immunofluorescent detection of ATF6 in oligodendrocyte-lineage cells in vehicle, iron-loaded and UPR activated slice cultures. Both nuclear (blue arrows) and non-nuclear (white arrows) localised ATF6 expression is observed in OLIG2-positive cells following TmF exposure and occasionally following Tm and ferrocene exposure, but is not detectable in the control conditions. Scale bar = 100 µm.

5.4.4 Glial morphology

Having previously established that iron loading with ferrocene leads to perturbed glial morphology and number in *ex vivo* slice cultures (Healy et al. 2016), we have re-confirmed these findings in a new set of independent experiments, and now extend our studies to investigate the effect of UPR activation on these iron-induced glial alterations.

The lowest number of OLIG2-positive cells was detected in slice cultures following ferrocene exposure, and was not further decreased by concurrent Tm exposure (Fig. 5.10). Indeed, the number of OLIG2-positive cells was significantly lower in iron-loaded slice cultures compared with the other conditions. Although we note an apparent loss in number of OLIG2-positive cells following Tm and TmF exposure compared with the DMSO control, this decrease did not reach statistical significance.

Although we were unable to fully replicate our earlier data on iron-loading leading to microglia activation and proliferation, we nevertheless still detected a trend towards decreased number of endpoints in iron-loaded slice cultures (Fig. 5.11). An endpoint is defined as the end of a microglia process/branch (i.e. a voxel with only one neighbour) and is used a numerical measurement of branching complexity, which is an indicator of microglia activation. On a qualitative basis, we observed that microglia in iron-loaded slice cultures had fewer, thicker processes compared with the cells in the control slice cultures whose processes were more numerous and quite thin. Similarly, there was an evident visual alteration in microglia morphology from a resting-like state into one more consistent with an activated state following Tm exposure, both alone and concurrently with iron-loading. Quantitatively as measured by endpoint number, we also report a trend towards decreased endpoints, but again this did not reach statistical significance.

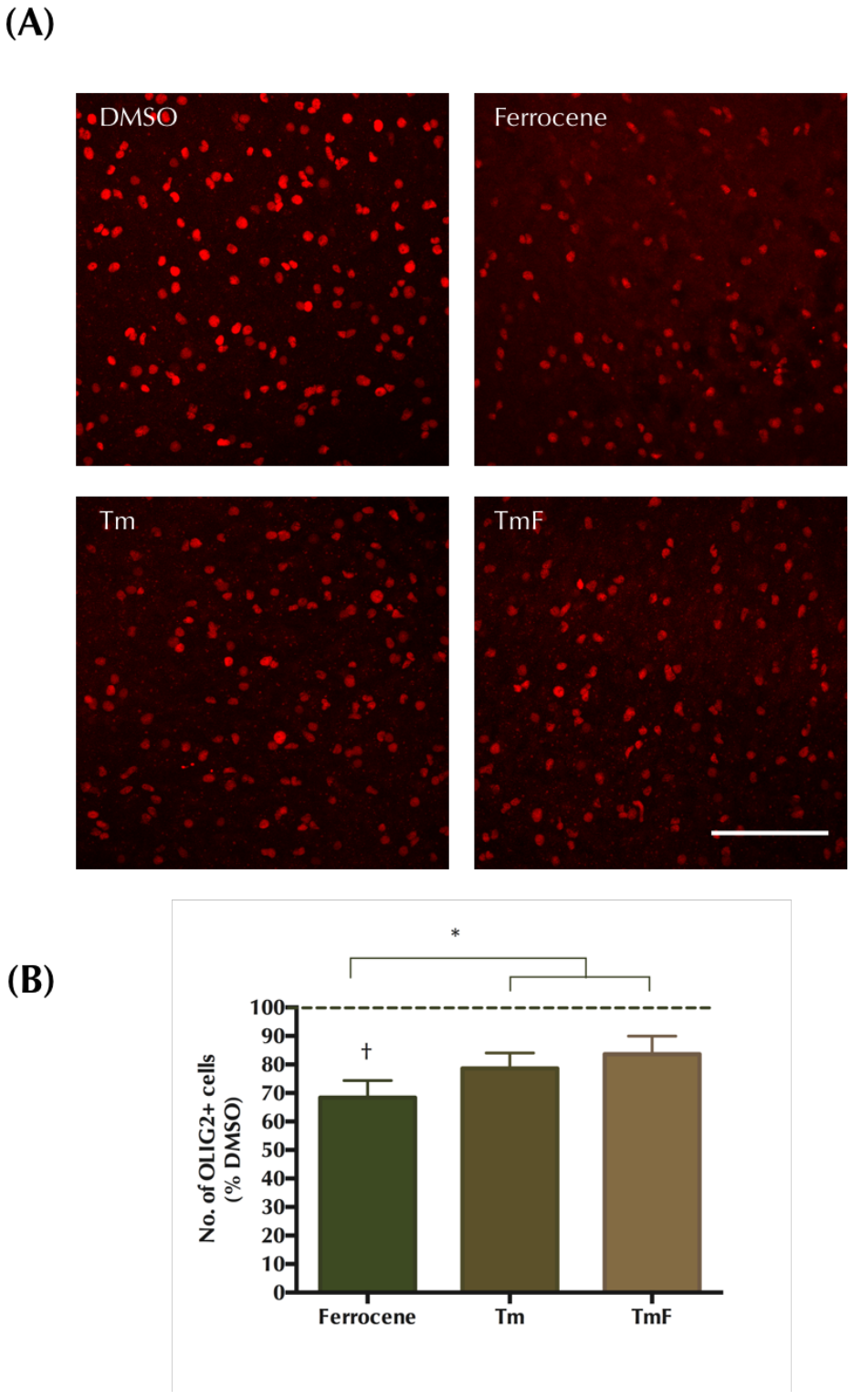

Figure 5.10: Effect of concurrent UPR activation and iron-loading on the number of OLIG2-positive cells. (A) Representative confocal maximum intensity projection images of oligodendrocyte-lineage cells. (B) Quantification of the number of OLIG2-positive cells. Data expressed as percentage of DMSO control, which is indicated by the dashed line. Values are mean ± SEM from 2 experiments. * denotes a significant difference compared with DMSO and † denotes significance between groups ($P<0.05$). Scale = 100 µm.

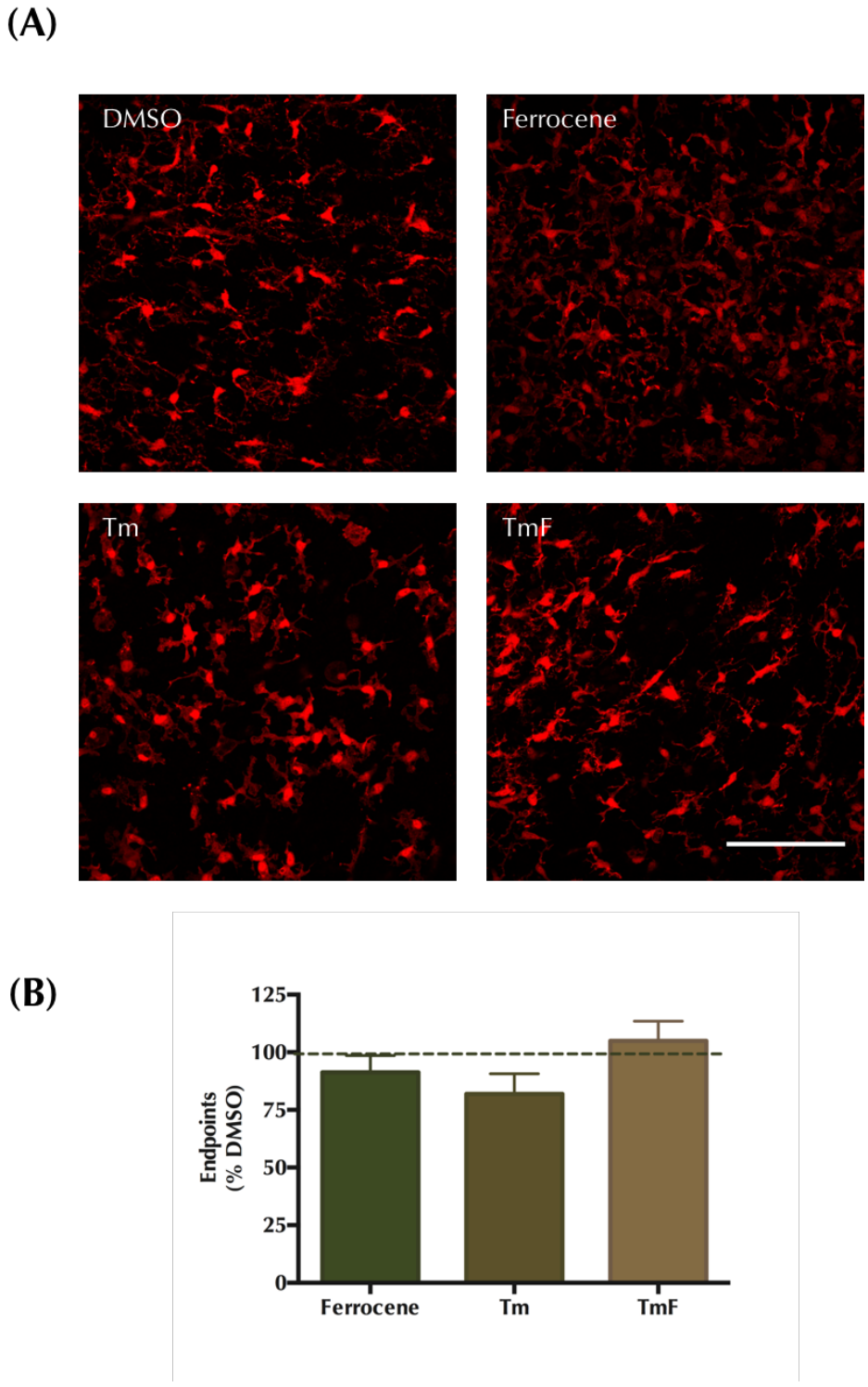

Figure 5.11: Effect of concurrent UPR activation and iron-loading on the number and morphology of microglia (A) Representative confocal maximum intensity projection images of microglia. (B) Quantification of the number and branching complexity of IBA1 microglia (endpoint is defined as the end of a microglia branch and the number of ends is a measure of branching complexity). Data expressed as percentage of DMSO control, which is indicated by the dashed line. Values are mean ± SEM from 2 experiments. Scale = 100 µm.

5.5 Discussion

The unfolded protein response (UPR) is a highly specialised program activated upon disturbed homeostasis in the endoplasmic reticulum (Schröder & Kaufman 2005). The UPR acts to alleviate stress and restore normal ER function. Compelling evidence, however, has extended the UPR beyond its classical role of handling protein misfolding to multifaceted roles in cell differentiation, metabolism, inflammation (Oliveira et al. 2011; Y. Liu & Connor 2012). Moreover, suggestive evidence has emerged for the existence of an interplay with iron metabolism (Oliveira et al. 2009; Vecchi et al. 2009; You 2003; Ye & Connor 2000). Details of this association remain unclear, which prompted us to exploit our novel iron-loaded *ex vivo* slice culture model to explore the putative intersection between the UPR and iron the CNS. In this chapter, we have investigated 1) the effect of iron loading on the activation of the UPR, 2) the effect of UPR activation on iron metabolism and 3) the concurrent effect of both processes on iron accumulation and glial perturbations.

Firstly, we have confirmed and extended on earlier reports that iron loading leads to an altered UPR profile. The 1.5-fold increase in the mRNA expression of BiP/GRP78 and CRT detected in our iron-loaded slice cultures corroborates with earlier evidence that these chaperones were up-regulated in iron-burdened astrocytoma cells (Ye & Connor 2000). In addition, our data is also in line with previous reports that BiP/FRP78 is up-regulated in the hepatocytes of mice that were fed excess iron in their diet and in iron-loaded hypoxic oligodendrocytes (Petrak et al. 2007; Rathnasamy et al. 2015). Our study builds on this evidence by providing a detailed profile of the effect of iron-loading on the mRNA expression of a cohort of transcription factors associated with the 3 arms of the UPR pathway. Generally, we found a modest increase in expression of these transcription factors in the iron-loaded slice cultures when compared with control, and this ranged from 1.3- to 2-fold of that detected in the control. These increases, while interesting, did not reach statistical significance.

We propose that the UPR is modulated by iron-loading but this is not homogeneous across the oligodendrocytes, neurons, astrocytes and microglia present in slice cultures. Different cell types express different levels of UPR sensors. For instance, oligodendrocytes, which produce vast amounts of myelin as an extension of their plasma membrane, a process for which iron metabolism and UPR activation are critical (Lin & Popko 2009; Todorich et al. 2011; Naughton et al. 2015; Schröder & Kaufman 2005), have been shown to be particularly sensitive to disruption of protein translation and protein secretory pathways. Given that oligodendrocytes only represent a proportion of the cells

present in hippocampal slice cultures, any oligodendrocyte-specific effects would be "diluted out" due to the masking effect of the other glial and neuronal cells that might be unaffected. A global assessment of UPR expression, at the mRNA level, by real-time PCR, or at the protein level, by western blot, might not be sufficiently sensitive and therefore unsuitable for detection of such changes. If a follow-on study was to be completed, a more precise analysis may be obtained from a dual-labelling approach of the UPR associated proteins in the different cell types, which is beyond the scope of this study given the limited samples and time available to complete such work.

Following on from this preliminary data that iron loading leads to modulation of UPR activation, we next characterised the opposite situation i.e. whether UPR activation effects iron metabolism in the brain. To our knowledge, this would be a novel contribution to the literature as the limited evidence that has been reported to date has not yet been generated from brain tissue and it is currently unclear whether this putative UPR-iron signalling is of relevance in the brain. The main intersection that has been described between the UPR and iron metabolism is the action of CHOP on hepcidin (via modulation of C/EBPα binding and/or through CREBH) in the liver and spleen (Vecchi et al. 2009; Oliveira et al. 2009). Less attention, however, has been given towards the UPR modulation of the other iron homeostasis proteins with the exception of the study by Oliveira et al. (2009) which reported an up-regulation in FPN, FTH and hepcidin transcripts following UPR activation and demonstrated the presence of several putative binding sites on the FTH and FPN genes for transcription factors associated with the UPR.

Accordingly, we performed a similar *in silico* analysis and were able to confirm the presence of binding sites for C/EBPα but not ATF on these genes. Furthermore, we demonstrated the presence of the putative binding sites of not only these transcription factors, but also XBP1 and CREB, on several of the other iron homeostasis genes. The presence of such regulatory elements is consistent with the idea that these genes might be responsive to the UPR. As proof-of-concept, and in line with the findings from the Oliveira study and our own *in silico* analysis, we selected both ferritin storage proteins, FTH and FTL, as interesting and promising candidates that might be modulated by the UPR in the CNS. Although we showed a modest increase in transcript expression of FTH and FTL following Tm-induced activation of the UPR, this increase did not reach statistical significance. Taken together, our results do not provide conclusive evidence for the presence or, indeed, the absence of UPR modulation of iron metabolism in the CNS, and further work is required in a more comprehensive follow-on study.

Our third goal was to investigate a concurrent UPR activation and iron loading in *ex vivo* slice cultures. Intriguingly, we found that Tm exposure led to the amelioration of ferrocene-induced iron accumulation, toxicity, oligodendrocyte loss and microglia activation. Such findings are indicative of a UPR protective effect to counter the perturbed cellular iron levels. Given the relevance of iron metabolism and UPR activation in oligodendrocyte-lineage-cells, which are actively myelinating and maturing in postnatal hippocampus, we focused our dual-staining efforts on this cell type. Intriguingly, we observed a slightly greater number of CHOP-positive oligodendrocyte-lineage cells following TmF exposure compared with Tm. However, we do note that there were only a few CHOP-positive cells compared with the total number of CHOP-positive nuclei seen with DAPI in both these conditions, suggesting that CHOP action in oligodendrocytes is relatively minor with respect to the global slice effect. Similarly, we also observed the occasional nuclear expression of ATF6 following iron-loading or Tm exposure in OLIG2-positive cells, an effect that was increased following TmF exposure, although no nuclear staining was seen in the control slices. Under all experimental conditions, cytoplasmic, that is non-active, ATF6 expression was seen associated with OLIG2. Taken together, these results indicate that the UPR may indirectly modulate iron metabolism of oligodendrocyte-lineage cells under conditions of toxic iron accumulation, and this intriguing finding warrants further investigation.

5.6 Conclusion

In summary, our data is consistent with, but does not strongly support, the existence of a reciprocal UPR-iron metabolism interplay in the CNS and this subject requires further investigation, which is outside the scope of this thesis. Of particular interest, however, is that the concurrent UPR activation leads to the amelioration of iron accumulation and the resulting toxicity and glial perturbations seen following iron-loading.

6 Evaluation of binarisation algorithms for image analysis of glial cells in *ex vivo* slice cultures

6.1 Introduction

Despite recent advances, an agreed standard for digital image analysis of glial morphology and cell number has not been described. Stringent evaluation and detailed reporting of such protocols, notably image segmentation and feature extraction, can quite critically affect the performance of successive steps in the image analysis workflow. However, sufficient description is seldom included in publications reporting data derived from image analysis, which raises concerns about the repeatability and definitiveness of reported information.

Segmentation, i.e. the process of detecting objects in the images, produces a binary image in which each pixel is assigned one of two values to indicate whether it is part of the background or object. Although this binary output is more meaningful and simple to analyse than the input fluorescence micrograph, inappropriate segmentation can inadvertently (or intentionally) affect the outcome of the analysis. This is exemplified in a recent report by Johnson and Walker (2015) that showed how two reasonable segmentation approaches to demarcate microglia in the rat brain resulted in opposing scientific conclusions being drawn regarding the experimental intervention.

A plethora of segmentation algorithms have been developed for use in a variety of applications, e.g. text recognition, object detection and tracking, medical diagnostics and image compression, and have been comprehensively categorized and compared (Sezgin and Sankur 2004, Sahoo 1988). Briefly, automatic thresholding can be broadly divided into global and local algorithms. Global algorithms compute a single threshold using the complete image information, while local algorithms compute a various threshold values from different partitions of the image. Global algorithms can then be further sub-grouped by their methodology e.g. histogram, clustering, entropy, object-attribute and spatial methods (Table 6.1).

Given that image segmentation is often imperfect, particularly in complex image sets, i.e. micrographs of glial immunohistochemistry acquired from thick 3D *ex vivo* hippocampal slice cultures, the focus of this chapter is to critically appraise FIJI's automatic image segmentation algorithms in order to develop, optimise and validate an image analysis workflow.

6.2 Aims of this study

To this end, and more broadly, to further develop a way of selecting the optimal threshold segmentation algorithm for correctly identifying glial cells in hippocampal *ex vivo* slice cultures, we have employed Brocher's Bio-Voxxel plugin available in FIJI.

Specific aims:

i. Develop, optimize and appraise the image analysis workflow for handling and quantifying micrographs of glial immunohistochemistry taken from *ex vivo* slice cultures.

ii. Compare user-selected and automatic threshold approaches for segmentation.

iii. Evaluate the capacity of 16 global and 9 local algorithms to successfully segment staining for astrocytes, oligodendrocytes and microglia using relative quality, accuracy, specificity and sensitivity as our test parameters.

iv. Validate the automated cell count of oligodendrocyte-lineage cells that was determined from maximum intensity projections using unbiased stereology principles.

6.3 Summary of methodology

Ex vivo slice cultures were immunolabelled with cell specific markers, i.e. astrocytes (GFAP), oligodendrocytes (OLIG2) and microglia (IBA1), and imaged on a laser scanning confocal microscope (Olympus Fluoview 1000). Z-projection images were acquired to encompass the staining detectable within the slice culture and subsequently processed using FIJI software (version 2.0.0-rc-49/1.51d). Brocher's semi-quantitative color-coded evaluation of segmentation (Brocher 2014), available within the Bio-Voxoxel plugin on ImageJ and FIJI platforms, was used to assess the relative quality, accuracy, specificity and sensitivity of 16 global and 9 local automatic thresholding algorithms (Fig 6.1).

Briefly, z-projections were converted into 8-bit grey scale maximum intensity projections. Pre-processing was minimal and restricted to background subtraction, using a rolling ball of 50 pixels, and despeckling. Sixteen maximum intensity projection images (i.e. 2 fields/slice, 2 slices/well, 2 wells/2 experiments) were used to evaluate threshold segmentation performance for astrocytes (GFAP), oligodendrocytes (OLIG2) and microglia (IBA1). The full details of methods used are provided in chapter 2.

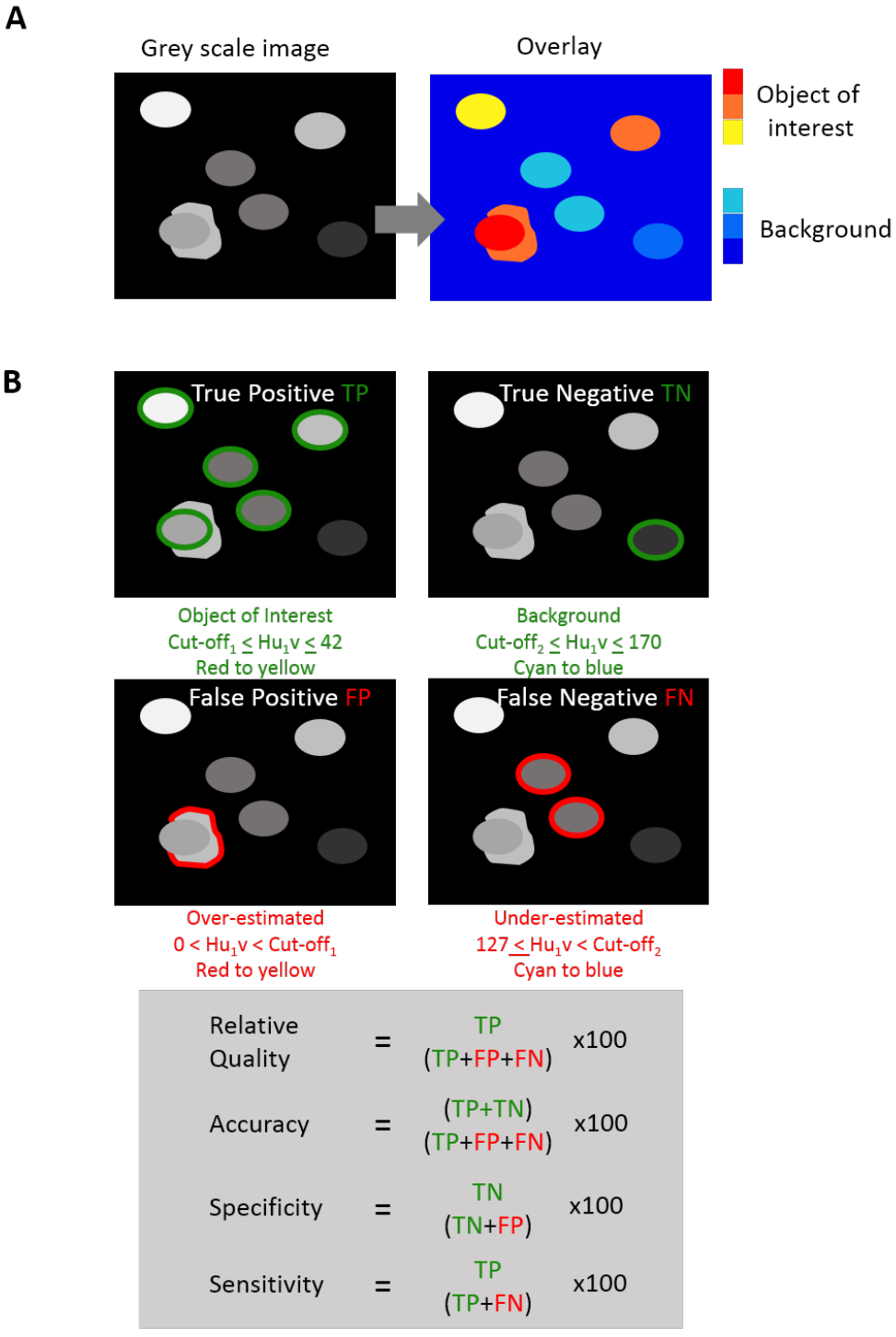

Figure 6.1: Brocher's semi-quantitative colour-coded evaluation of segmentation comparing 16 global and 9 local autothresholding algorithms in FIJI. (A) Each pixel is classed an as an object (coloured red-to-yellow) or non-object (i.e. background; coloured blue-to-cyan). (B) There are 4 categories for each pixel: object-of-interest/cellular staining, (true positive), background (true negative) over-estimated (false positive) and under-estimated (false negative;). To evaluate performance, the number of pixels assigned to each category is counted, and the following metrics are calculated: sensitivity, specificity, accuracy and relative quality. Accuracy is derived from sensitivity (i.e. correctly identified positives) and specificity (correctly identified negatives) parameters. Relative quality is a measurement of absolute quality where 100% represents a perfect binary production of the test image.

Table 6.1 Sub-division of Global auto-threshold algorithm by methodology

Histogram	Cluster	Entropy	Attribute	Misc.
Intermodes	Default	Shanbhag	Moments	Percentile
Minimum	Isodata	Li	Triangle	
Mean	MinimumErr	Yen		
	Otsu	Huang		
		RenyEntropy		
		MaxEntropy		

6.4 Results

6.4.1 Qualitative evaluation of image presentation approaches for representing the z-stack data of astrocyte, oligodendrocyte and microglial staining in slice cultures

Intensity projection images display 3D information as a 2D image. Theoretically, a projection image can convey more information about a z-stack in the same visual space than a representative single plane image (Fig. 6.2A). Note, however, that projections alter the original ground truth data of the IHC Z-stack in that volume becomes surface area, surface area becomes a line, and a line a point. The accuracy and sensitivity of the resulting projection depend on the nature of raw data and projection algorithm applied.

For astrocyte quantitation, using GFAP immunohistochemistry, the *maximum intensity* projection (MIP) and *average* projection algorithms best preserve the sharpness and quality of detail from the z-stack. *Standard deviation* and *sum* algorithms result in projections that are slightly dimmer and more blurred. *Minimum* and *median* algorithms lose considerable detail and sharpness (Fig. 6.2A). Similarly, for oligodendrocyte immunohistochemistry, *maximum intensity* algorithm best preserves detail. *Standard deviation* and *sum* algorithms preserve detail well but are not quite as sharp or bright. *Average* and *median* algorithms lead to considerable dimming and blurring of the OLIG2-positive staining and the *minimum* algorithm results in the loss of most detail (Fig. 6.2B). For IBA1, *maximum intensity* and *standard deviation* best preserve detail and sharpness, which is especially critical given the morphology of microglia. The branches and processes of the microglia are not as readily apparent in the projections from the *average* and *sum* algorithms and these details are barely present in the *minimum* and *median* projections (Fig. 6.2C).

In summary, *maximum intensity* is the best projection to concisely, sensitively and accurately convey z-stack information of single 2D image representation of astrocytes, oligodendrocyte-lineage cell nuclei and microglia in z-stacks.

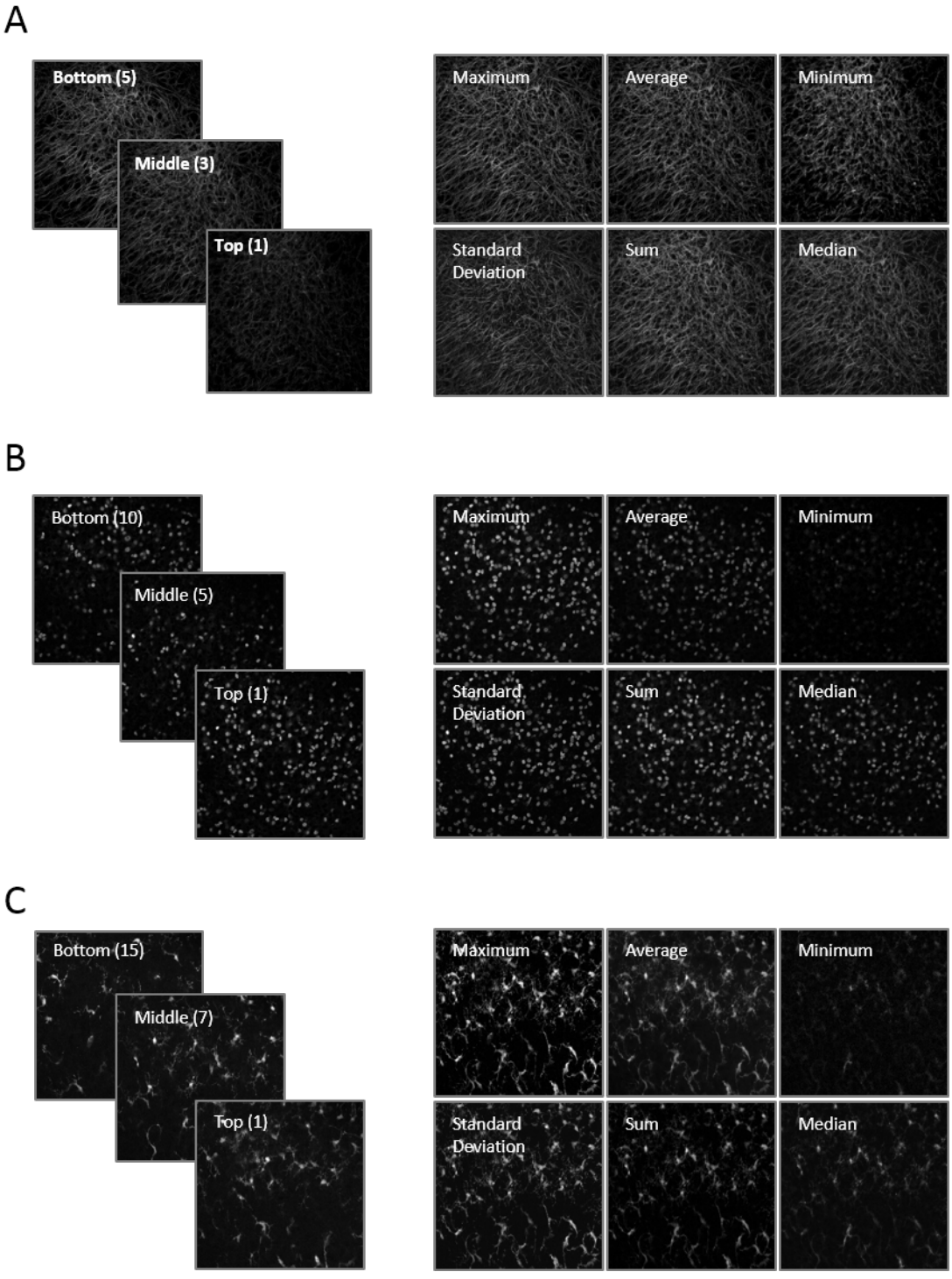

Figure 6.2: Qualitative evaluation of the available approaches for image presentation of glial cells in *ex vivo* slice cultures. Eight-bit grey-scale images of immunofluorescent cell-specific staining can be visualized at selected planes to represent the z-stack acquired from *ex vivo* slice cultures (left) or z-projected using 6 different project algorithms (right). (A) astrocytes stained with GFAP antibody, (B) oligodendrocytes stained with OLIG-2 antibody and (C) microglia stained with IBA1 antibody.

6.4.2 Qualitative visual evaluation of binarisation output of MIP IHC

Projection is useful, not only for presenting data in publications, but also for simplifying implementation of automated image analysis macros within the FIJI platform. Image segmentation and feature extraction by binarisation are key steps in automated image processing (Eliceiri 2012).

We demonstrated that a single user-chosen threshold value does not consistently produce an acceptable and valid binary representation of the ground truth image. In Fig. 6.3A two very different examples of astrocyte (GFAP) staining, that were taken using the same acquisition parameters in the same slice culture, are provided. Three single value thresholds were tested (25, 50, 75; chosen to maximally cover the range of reasonable thresholds within the 0-256 range of an 8 bit image) and all failed to produce reasonable binary representations across both images. Conversely, the threshold value calculated automatically using *default* algorithm, produced reasonable binary representations of the GFAP staining.

OLIG2-staining, which results in a more discrete and defined nuclear stain, was not as badly affected by single arbitrary thresholds as GFAP had been. Nevertheless, the best binary representation for two images was generated by relying on the default algorithm rather than a user chosen threshold values (Fig. 6.3B).

For staining of microglia (IBA1), 50, 75 and 100 were used as reasonable threshold values for two test images, i.e. one acquired from control and one from iron-loaded slice culture, that depict differing microglia morphology (Fig. 6.3C). As already described for GFAP staining, each of the single-value thresholds tested produced an inconsistent output quality between both images while the automatic value from default threshold algorithm produced the best representation (the calculated values were 65 and 105). Compared with the other available threshold algorithms, however, the default algorithm, as operator-assessed using subjective and visual approach, also produced a relatively poor representation of the original.

There are 16 global and 9 local thresholds available for the binarisation of images in FIJI. A subjective visual user comparison of the threshold options on a subset of images clearly indicated the obviously unsuitable thresholds such as Intermodes and *Sauvola* for GFAP (Fig. 6.4A), *MinError* and *Shanbhag* for OLIG2 (Fig. 6.4B) and *Yen* and *Contrast* for Iba1 (Fig 6.4C). This approach, however, is quite poor at differentiating between subtle quality differences, such as those between *Default, Bernsen* or *Huang* algorithms for GFAP staining. These thresholds all produce reasonable binary

representations and appear to be equally valid choices (Fig. 6.4) until further evaluation (Fig. 6.5).

The BioVoxxel plugin for FIJI offers a threshold check feature that tests each algorithm relative to a user-chosen reference value and produces colour coded images (Fig. 6.5, 6.7 and Fig. 6.9). The object-of-interest is coloured yellow-to-red and background is blue-to-cyan, which allows a more sensitive user-based discrimination of thresholds. Moreover, the visual partition also serves as a quantitative partition; the number of pixels grouped correctly (or incorrectly) either as object-of-interest or background are used as evaluation metrics.

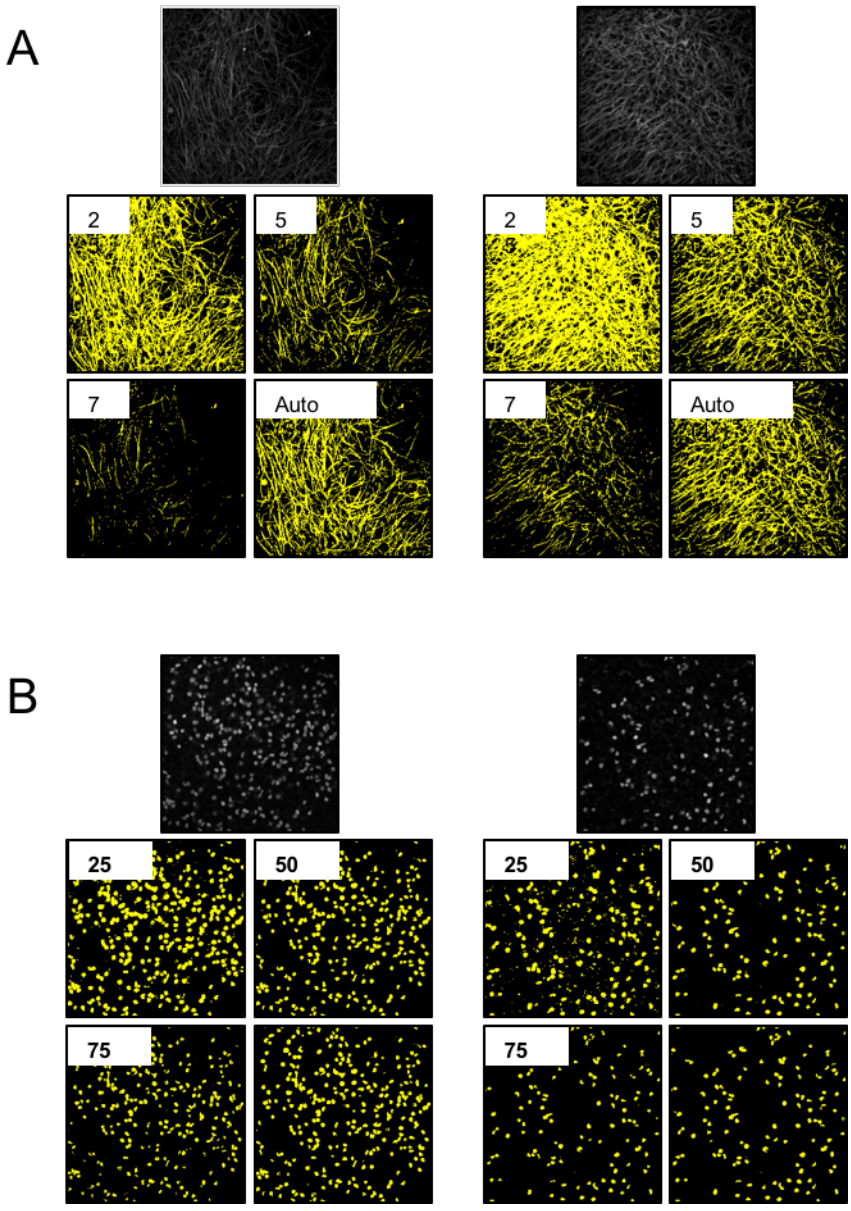

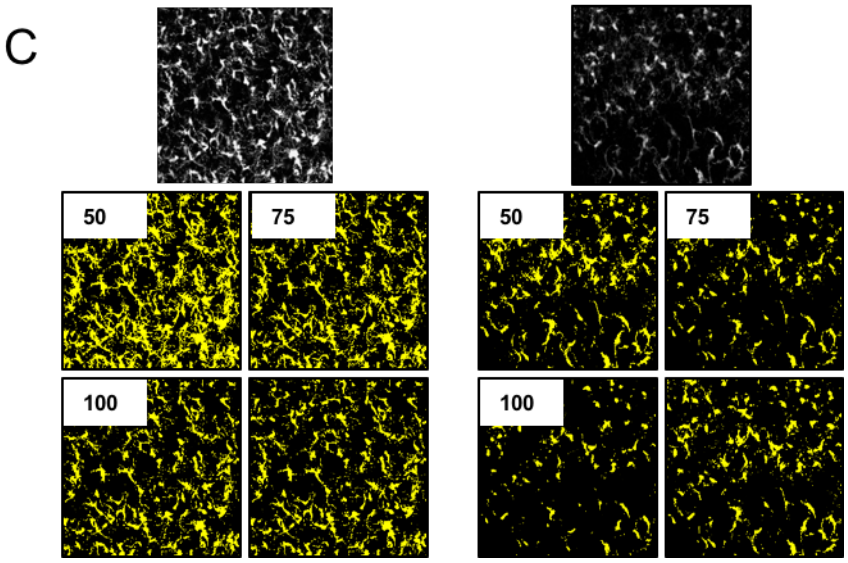

Figure 6.3: Representative maximum intensity projections and subsequent output binarisation generated from single user-chosen arbitrary numerical thresholds. (A) astrocytes stained with GFAP antibody, (B) oligodendrocytes stained with OLIG-2 antibody and (C) microglia stained with IBA1 antibody. It is evident that application of a single user-chosen threshold value does not consistently produce an acceptable representation of glial cell immunohistochemistry in different images whereas the automatic default segmentation algorithm produces an acceptable representation.

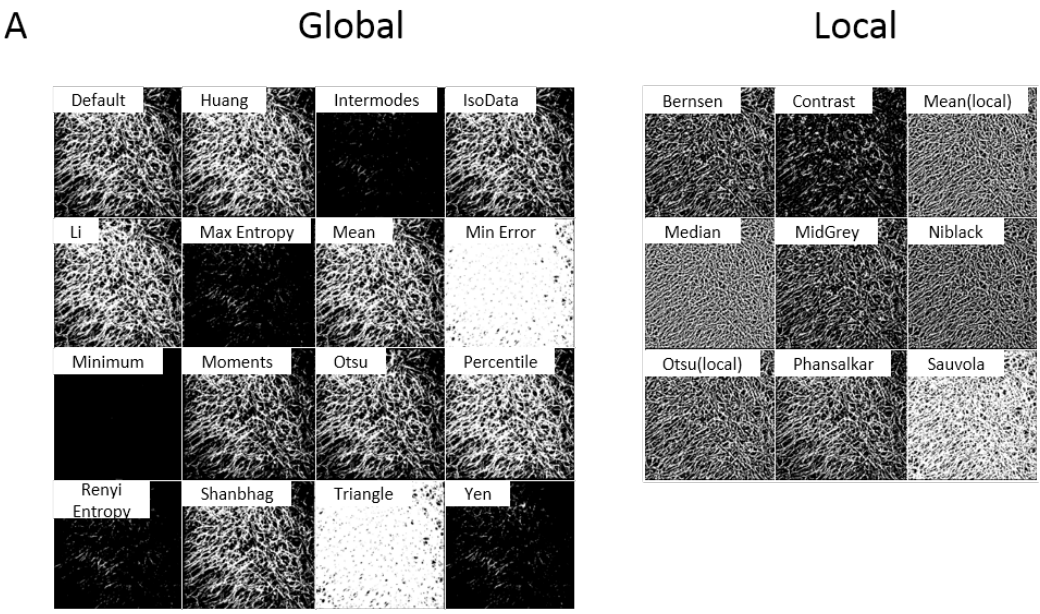

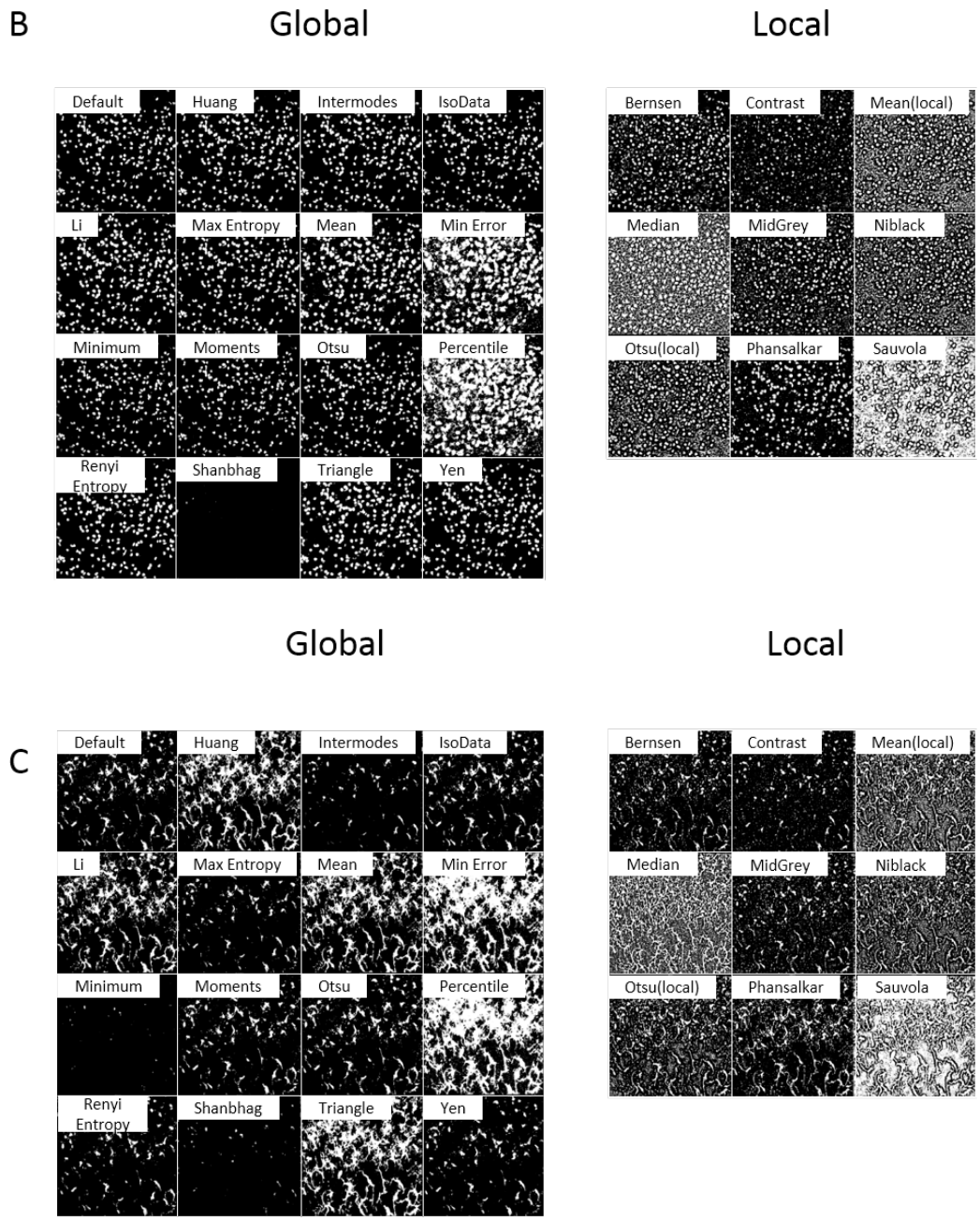

Figure 6.4: Representative binarisation of glial cell staining staining produced from different 16 global and 9 local threshold algorithms available on Image J. (A) astrocytes stained with GFAP antibody, (B) oligodendrocytes stained with OLIG-2 antibody and (C) microglia stained with IBA1 antibody.

6.4.3 Quantitative evaluation of algorithm binarisation of astrocyte images

The 16 global and 9 local threshold algorithms in FIJI were evaluated to determine the best approach to create optimal binary images of confocal z-stack images of GFAP-stained astrocytes in *ex vivo* slice cultures for downstream automated image analysis. Threshold performance was scored on 4 metrics – relative quality, accuracy, specificity and sensitivity (Fig. 6.6).

A one-way ANOVA was conducted to compare the performance of each algorithm on the relative quality of the thresholded output based on a user-selected reference value. There was a significant difference at the P<0.05 between algorithms ($F_{(24, 375)}$ = 62.43, P<0.0001; Fig. 6.6). Post hoc comparisons were carried out using the Dunnett's test. The *Percentile* algorithm was chosen as a comparator because it had the highest combined average score across the 4 test metrics. The average relative quality score of the *Percentile* algorithm was not significantly higher than *Huang, Li* or *Mean* (P>0.05). However, the relative quality score of *Percentile* was significantly higher than the other 21 algorithms (P<0.05) i.e. *Default, Intermodes, IsoData, Max Entropy, MinError, Minimum, Moments, Otsu, RenyiEntropy, Shanbhag, Triangle, Yen, Bernsen, Contrast, Mean (local) Median, Midgrey, Niblack, Otsu (local), Phansalkar* and *Sauvola.*

Similarly, a one-way ANOVA conducted to compare the accuracy of each algorithm indicated that there was a significant difference at the P<0.05 between algorithms ($F_{(24,375)}$=11.08, P<0.0001; Fig. 6.6). Post-hoc comparison using Dunnett's test indicated that the accuracy score for the *Percentile* algorithm was not significantly higher than *Default, Huang, Li, Mean,Otsu, Mean (local), Median, Niblack, Otsu (local), Phansalkar* or *Sauvola* (P>0.05). The accuracy score of *Percentile*, however, was significantly higher than the following algorithms: *Intermodes, Isodata, MaxEntropy, MinError, Minimum, Moments RenyiEntropy, Shanbhag, Triangle, Yen, Bernsen, Contrast* and *Midgrey* (P<0.05).

A one-way ANOVA conducted to compare the specificity of each algorithm indicated that there was a significant difference at the P<0.05 level ($F_{(24,375)}$=17.33, P<0.0001; Fig. 6.6). Post-hoc comparison using Dunnett's test indicated that specificity score for the *Percentile* algorithm was only significantly higher than *MinErro*r and *Sauvola* algorithms (P<0.0001) and that it was equally and non-significantly different from the other options (P>0.05).

Finally, a one-way ANOVA conducted to compare the sensitivity of each algorithm indicated that there was a significant difference at the P<0.05 between algorithms ($F_{(24,375)}$=29.95, P<0.0001; Fig. 6.6). Post-hoc comparison using Dunnett's test indicated that the sensitivity score for the *Percentile* algorithm was not significantly higher than *Huang, Li, Mean, MinError, Mean (local), Median, Niblack, Otsu (local)* or *Sauvola*. However, the sensitivity was significantly better than *Default, Intermodes, Isodata, Max Entropy, Minimum, Moments, Otsu, RenyiEntropy, Shanbhag, Triangle, Yen, Bernsen, Contrast, Midgrey* and *Phansalkar* (P<0.05).

Taken together, these results indicate the relative performance of *Percentile, Huang, Li* and *Mean* algorithms were comparable to each other (based on relative quality, accuracy, specificity and sensitivity metrics) but performed significantly better than the other global, and all of the local, threshold options for GFAP-stained astrocytes (Fig. 6.5 & 6.6).

Indeed, binarisation either by *Percentile* or *Mean* algorithms of images from experimental slice cultures, that had been either treated with iron-loading reagent, ferrocene, or DMSO control, led to the same experimental outcome i.e. that treatment did not affect the percentage coverage of GFAP, a measure of astrocyte area/reactivity (Fig. 6.3A). Conversely, *Otsu* binarisation of the same images resulted in the alternative conclusion that GFAP area was altered. *Sauvola* and *Bernsen* algorithms, which performed at a comparable level to *Otsu* but below the *Percentile* and *Mean*, did not replicate these spurious results.

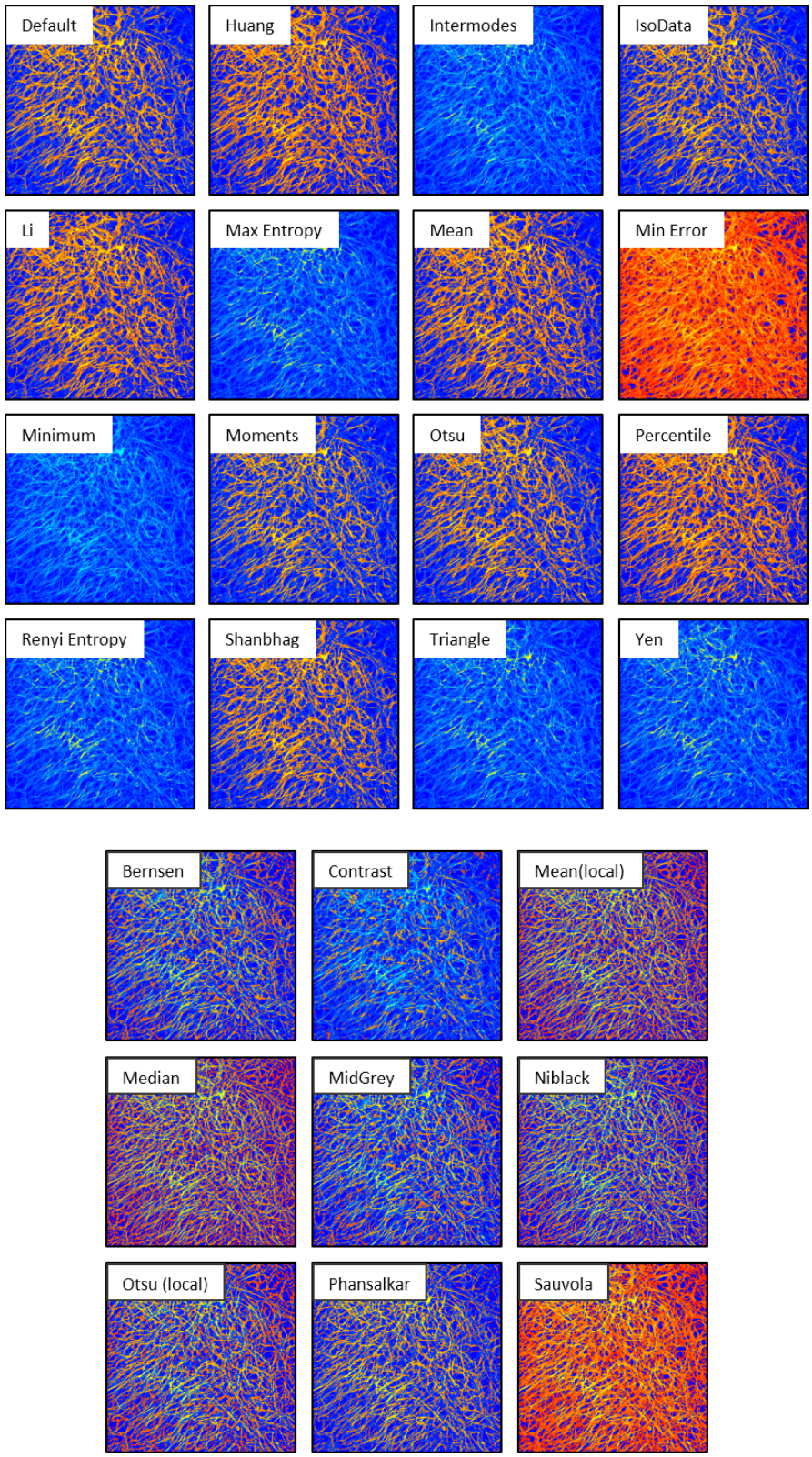

Figure 6.5: Performance evaluation of image segmentation algorithms on z-stack micrographs of astrocytes in *ex vivo* slice cultures. Bio-Voxxel colour-coded plugin aids the subjective comparison of threshold algorithms to select optimal method and serves as a visual cue supporting quantitative assessment.

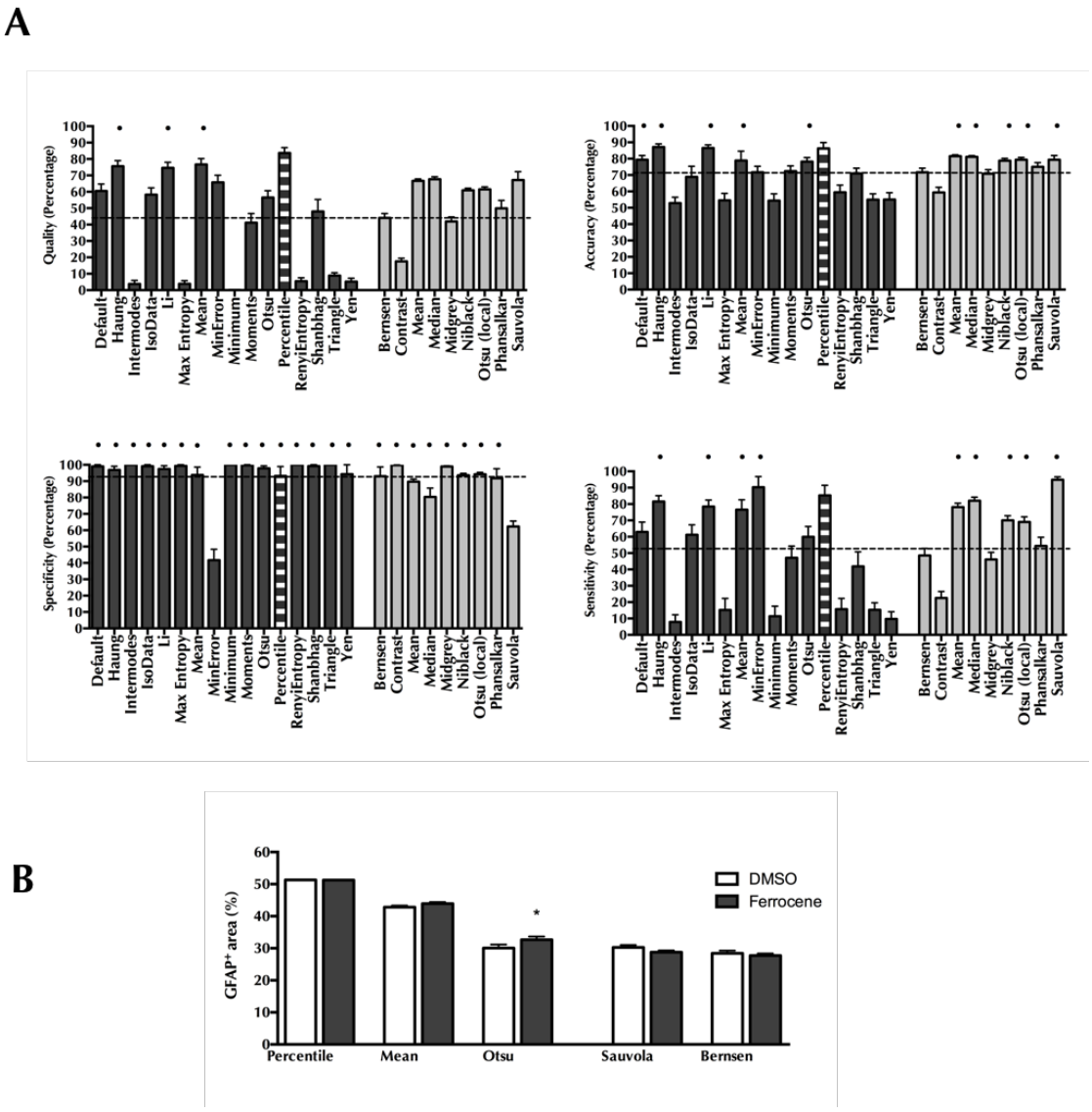

Figure 6.6: Quantitative assessment of threshold performance using relative quality, specificity, accuracy and sensitivity parameters. (A) Dashed line represents average performance of all thresholds collectively. The *Percentile* algorithm, i.e. the white and grey striped bar, performs the best across the 4 evaluation metrics. Statistical evaluation using a one-way ANOVA with a Dunnett's multiple comparison post test against *Percentile* indicates that this threshold does not perform significantly better than *Huang, Li, Mean* (denoted by the black dot) in the 4 metrics, whereas it is significantly better than the other 21 in-built FIJI threshold algorithms. Dark grey bars represent FIJI AutoThreshold Global methods and light grey columns the AutoThreshold Local methods. Values represent the mean and standard error of the mean (SEM) from n=16 test images of GFAP staining. Significance at $P<0.05$. (B) Quantification of GFAP area from the *Otsu* binarisation images results in the spurious finding that iron-loading with ferrocene leads to a significant increase in GFAP area compared with control group; this difference is not replicated from *Percentile, Mean, Sauvola* or *Bernsen* binarisation outputs.

6.4.4 Quantitative evaluation of algorithm binarisation of oligodendrocyte images

The same approach used for the evaluation threshold performance in astrocyte imaging was also applied to oligodendrocyte-lineage cells i.e. 16 global and 9 local thresholds were evaluated on the relative quality, accuracy, specificity and sensitivity of the output binary images (Fig. 6.7 and 6.8).

A one-way ANOVA was conducted to compare the performance of each algorithm on the relative quality of the thresholded output based on a user-selected reference value. There was a significant difference in relative quality for the 25 algorithms assessed ($F_{(24, 375)}$ = 37.11, P<0.0001; Fig. 6.8A). Post hoc comparisons were carried out using the Dunnett's test. *Otsu* was chosen as a comparator because it had the highest combined average score across the 4 test metrics. The average relative quality score of the *Otsu* algorithm was not significantly higher than *Default, Huang, IsoData, Li, MaxEntropy, Moments, RenyiEntropy, Yen* or *Phansalkar* (P>0.05). However, the relative quality score of *Otsu* was significantly higher than the other 14 algorithms (P<0.05) i.e. *Intermodes, Mean, MinError, Minimum, Percentile, Shanbhag, Bernsen, Contrast, Mean (local) Median, Midgrey, Niblack, Otsu (local), Sauvola and Triangle* (Fig. 6.8A).

Similarly, a one-way ANOVA conducted to compare the accuracy of each algorithm indicated that there was a significant difference at the P<0.05 level between algorithms ($F_{(24,375)}$=36.61, P<0.0001; Fig. 6.8A). Post-hoc comparison using Dunnett's test indicated that the accuracy score for the *Otsu* algorithm was significantly higher than only 7 of the 25 algorithms (i.e. *MinError, Percentile, Mean (local), Median, Niblack, Otsu (local)* and *Sauvola*; P<0.01) but was not the other 17 algorithms.

A one-way ANOVA, conducted to compare the specificity of each algorithm, indicated that there was a significant difference at the P<0.05 level between algorithms ($F_{(24,375)}$=30.03, P<0.0001). Post-hoc comparison using Dunnett's test indicated that the specificity score for the *Otsu* algorithm, matching the accuracy score pattern, was significantly higher than only 7 of the 25 algorithms (i.e. *MinError, Percentile, Mean (local), Median, Niblack, Otsu (local)* and *Sauvola*; P<0.01) but was not significantly better than the other 17 algorithms.

Finally, a one-way ANOVA conducted to compare the sensitivity of each algorithm indicated that there was a significant difference at the P<0.05 between algorithms ($F_{(24,375)}$ =21.24, P<0.0001; Fig. 6.8A). Post-hoc comparison using Dunnett's test indicated that the accuracy score for the *Otsu* algorithm was significantly higher than

only 4 other algorithms – i.e. *Intermodes, Minimum, Shanbhag* and *Contrast* ($P<0.001$) and was comparable with the other 20 algorithms ($P>0.05$).

Taken together, these results indicate that the relative performance of *Otsu, Default, Huang, Isodata, Li, MaxEntropy, Moments, RenyiEntropy, Yen* and *Phansalkar* algorithms were comparable to each other (based on relative quality, accuracy, specificity and sensitivity metrics) but performed significantly better than the other global and local threshold options for OLIG2 staining (Fig. 6.7 & 6.8A).

Finally, the accuracy of automated count of OLIG2-positive cells in *Otsu* binarisation of the *maximum intensity projection* was validated against the gold standard unbiased stereological approach (Howard & Reed 2004; Mayhew 1992; Schmitz & Hof 2005). A Pearson correlation coefficient was computed to assess the relationship between the two counting methods. There was a moderate positive correlation between the two approaches ($r=0.54$, $n=11$, $p=0.01$; Fig. 6.8B; upper panel). Having previously reported a loss of OLIG2-positive cells in slice cultures that were exposed to iron reagent compared to vehicle (chapter 4), we have since reanalysed a subset of these images using both methods and now report that the relative loss of OLIG2-positive cells between treatment groups is maintained in the stereology count (Fig. 6.8B; lower). We note, however, that stereology gives a lower total number, approximately 30% lower than the number detected in maximum intensity projection count. In DMSO slice cultures, cell counts using stereology principles and the automated methodology, in *maximum intensity* projection, gives values of 109± 14 and 163± 19 oligodendrocyte-lineage cells, respectively. In ferrocene treated slice cultures, the cell number is reduced by 11% and 14%, respectively, with values of 97± 15. and 140±12.

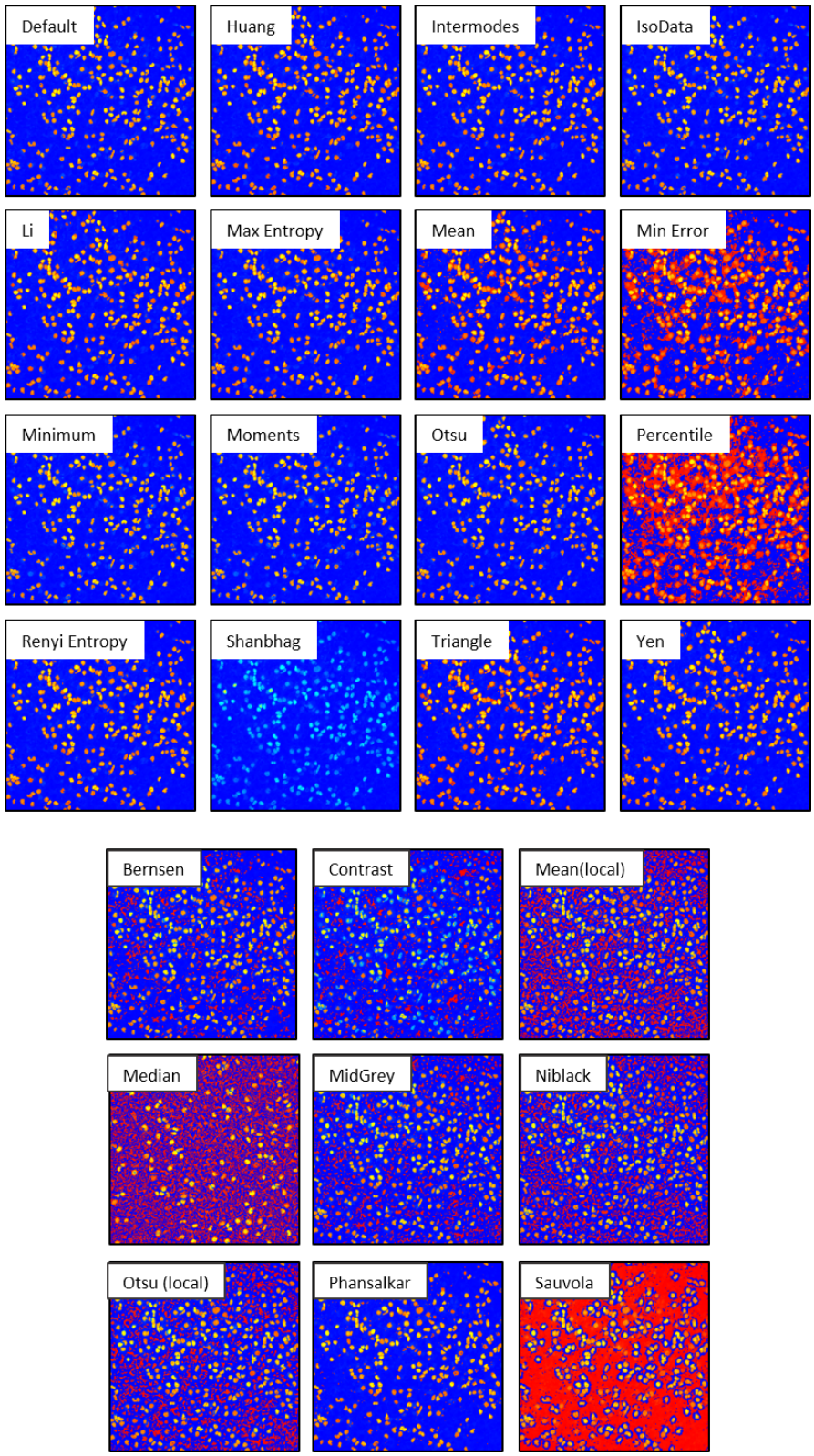

Figure 6.7: Performance evaluation of image segmentation algorithms on z-stack micrographs of oligodendrocyte-lineage cell nuclei in *ex vivo* slice cultures. Bio-Voxxel colour-coded plugin aids the subjective comparison of threshold algorithms to select optimal method and serves as a visual cue supporting quantitative assessment.

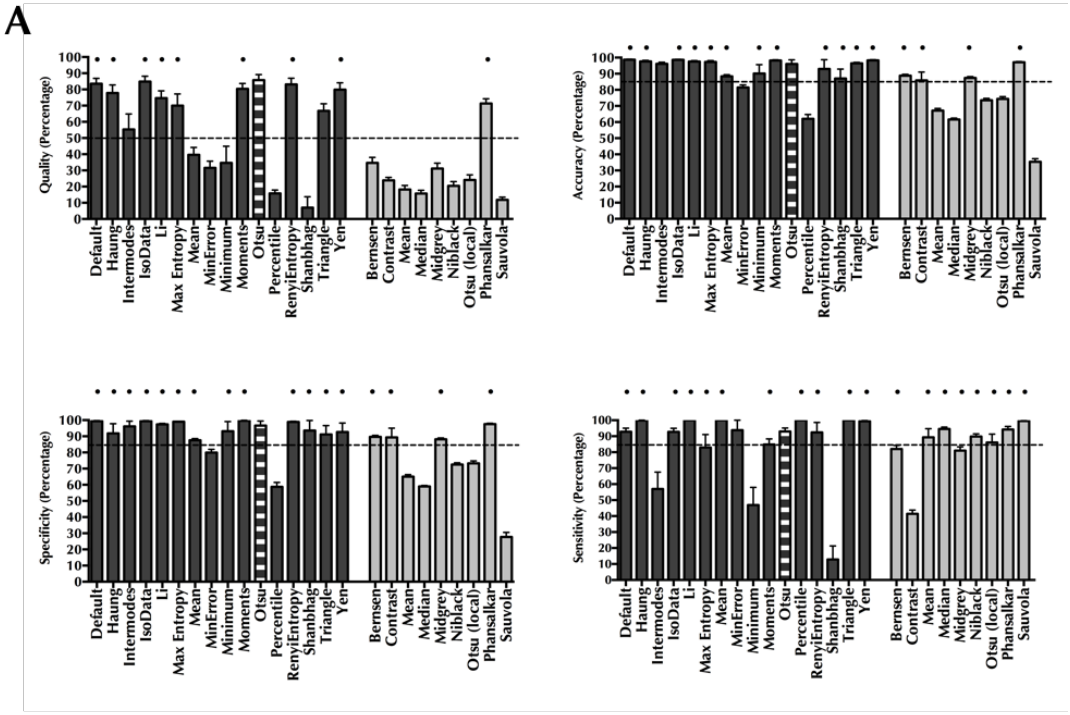

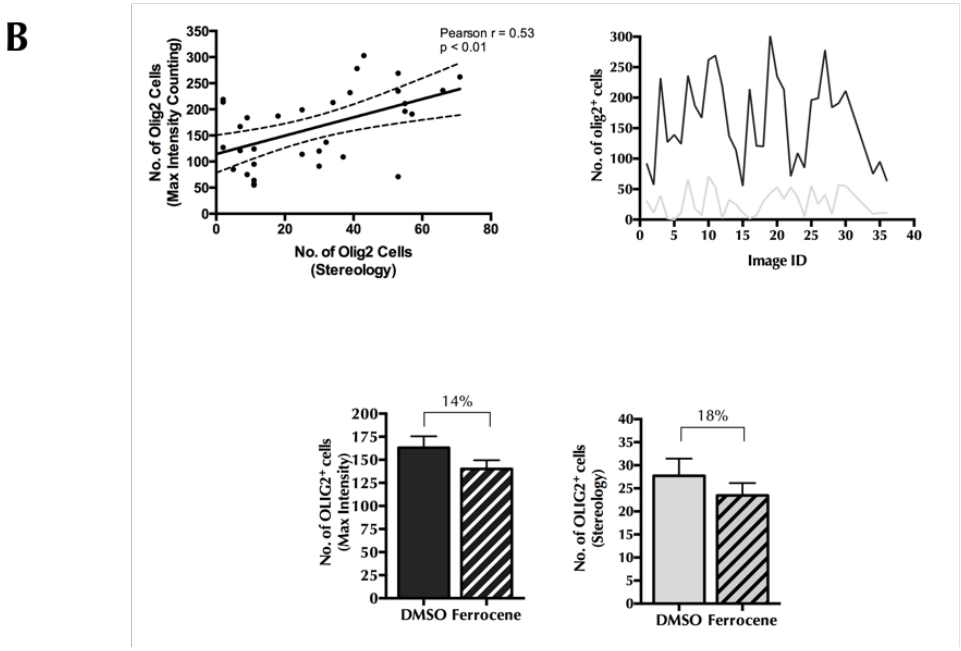

Figure 6.8: Quantitative assessment of threshold performance using relative quality, specificity, accuracy and sensitivity parameters. (A) Dashed line represents average performance of all thresholds collectively. Dark grey bars represent FIJI AutoThreshold Global methods and light grey columns the Auto Local Thresholds. Values represent the mean and standard error of the mean (SEM) from n=16 test images of OLIG2 staining. Black dot denotes non-significance; significance at $P<0.05$. (B) Comparison of maximum intensity projection auto-threshold and stereology methodologies for quantification of oligodendrocyte lineage cells. Top left: correlation calculations. Top right: total cells counted per image using both methodologies (black line = maximum intensity projections; grey line = stereology). Bottom: quantification of numbers of OLIG2-positive cells in iron-treated (diagonal striped bars) vs vehicle-treated (solid bars) ex vivo brain slices.

6.4.5 Quantitative evaluation of algorithm binarisation of microglia

The same approach that was taken to evaluate threshold performance for astrocytes and oligodendrocyte-lineage cells was also applied to IBA1 immunohistochemistry i.e. 16 global and 9 local thresholds were evaluated on the relative quality, accuracy, specificity and sensitivity of the output binary images (Fig. 6.10).

A one-way ANOVA was conducted to compare the performance of each algorithm on the relative quality of the thresholded output based on a user-selected reference value. There were a significant differences in relative quality between the 25 algorithms assessed ($F_{(24, 375)} = 24.25$, $P<0.0001$; Fig. 6.10B). Post hoc comparisons were carried out using the Dunnett's test to compare all other algorithms with the *Li* algorithm. This was chosen as a comparator because it had the highest combined average score across the 4 test metrics. The average relative quality score of the *Li* algorithm was not significantly higher than *Huang, Mean, Triangle* and *Phansalkar* ($P>0.05$). However, the relative quality score of *Li* was significantly higher than the other 20 algorithms ($P<0.01$) i.e. *Default, Intermodes, IsoData, MaxEntropy, MinError, Minimum, Moments, Otsu, Percentile, RenyiEntropy, Shanbhag, Yen, Bernsen, Contrast, Mean (local) Median, Midgrey, Niblack, Otsu (local*), and *Sauvola*.

Similarly, a one-way ANOVA conducted to compare the accuracy of each algorithm indicated that there was a significant difference at the $P<0.05$ between algorithms ($F_{(24,375)}=5.253$, $P<0.0001$; Fig. 6.10B). Post-hoc comparison using Dunnett's test indicated that the accuracy score for the *Li* algorithm was significantly higher than only 3 of the 25 algorithms (i.e. *MinError, Median* and *Sauvola*; $P<0.05$) but was not better significantly than the other 21 algorithms ($P>0.05$).

A one-way ANOVA conducted to compare the specificity score for each algorithm indicated that there was a significant difference at the $P<0.05$ level ($F_{(24,375)}=24.71$, $P<0.0001$; Fig. 6.10). Post-hoc comparison using Dunnett's test indicated that specificity score for Li algorithm was significantly higher than 6 of the 25 algorithms (i.e. *MinError, Percentile, Mean (local), Median*, *Niblack* and *Sauvola*; $P<0.01$) but was not better significantly than the other 18 algorithms ($P>0.05$).

Finally, a one-way ANOVA conducted to compare the sensitivity of each algorithm indicated that there was a significant difference at the $P<0.05$ between algorithms ($F_{(24,375)}=70.65$, $P<0.0001$; Fig. 6.10). Post-hoc comparison using Dunnett's test indicated that the accuracy score for the *Li* algorithm was significantly higher than 15 other algorithms – i.e. *Default, Intermodes, Isodata, MaxEntropy, Minimum, Moments,*

Otsu, RenyiEntropy, Shanbhag, Yen, Bernsen, Contrast, Midgrey, Niblack and *Otsu (local)* ($P<0.001$). The sensitivity score was not significantly higher than *Huang, Mean, MinError, Percentile, Triangle, Mean (local), Median, Phansalkar* or *Sauvola*.

Taken together, these results indicate the relative performance of *Li, Huang, Triangle* and *Phansalkar* algorithms were comparable to each other (based on relative quality, accuracy, specificity and sensitivity metrics) but performed significantly better than the other global and local threshold options for IBA1 stained microglia (Fig. 6.9 and 6.10)

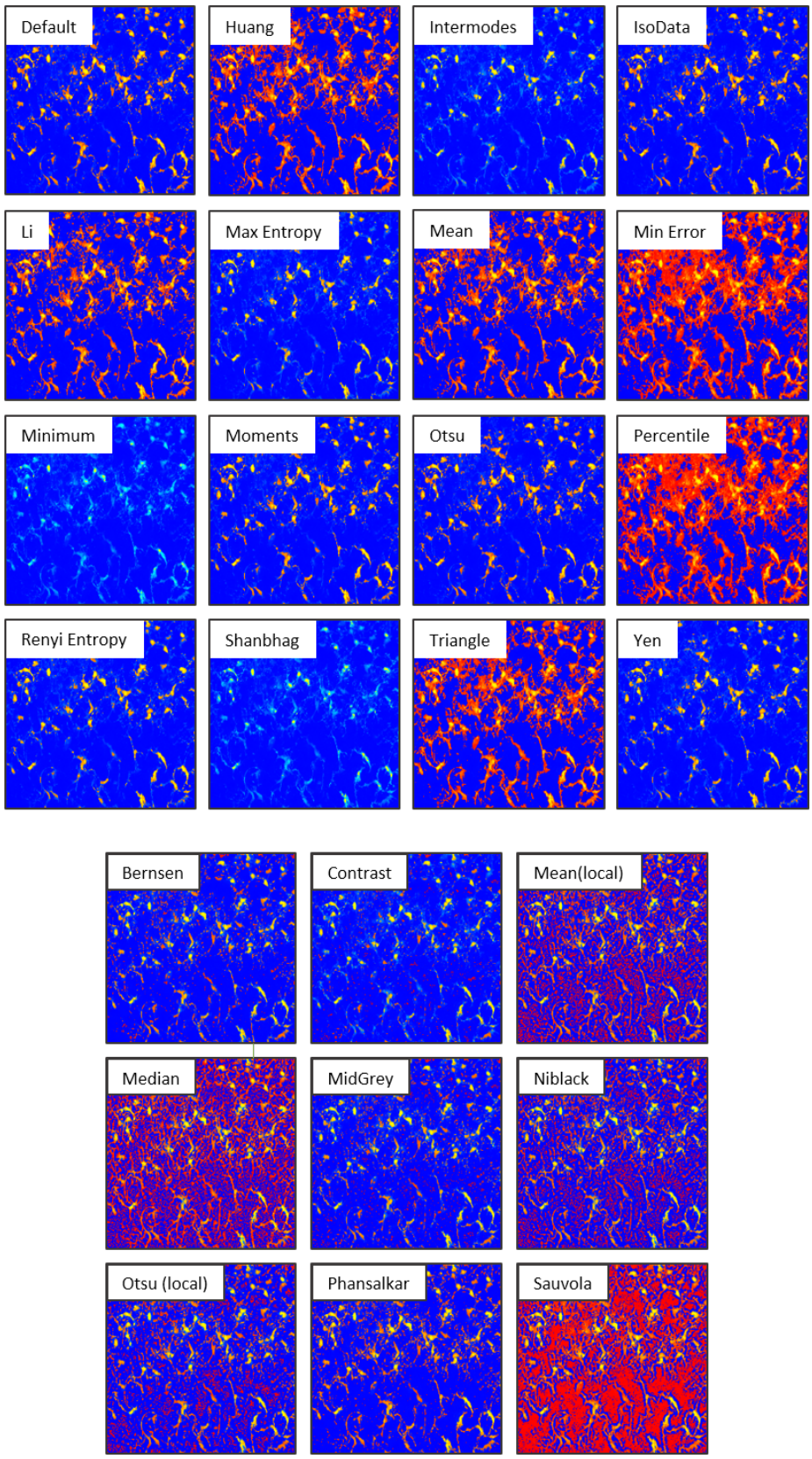

Figure 6.9: Performance evaluation of image segmentation algorithms on z-stack micrographs of IBA1 staining in *ex vivo* slice cultures. Bio-Voxxel colour-coded plugin aids the subjective comparison of threshold algorithms to select optimal method and serves as a visual cue supporting quantitative assessment.

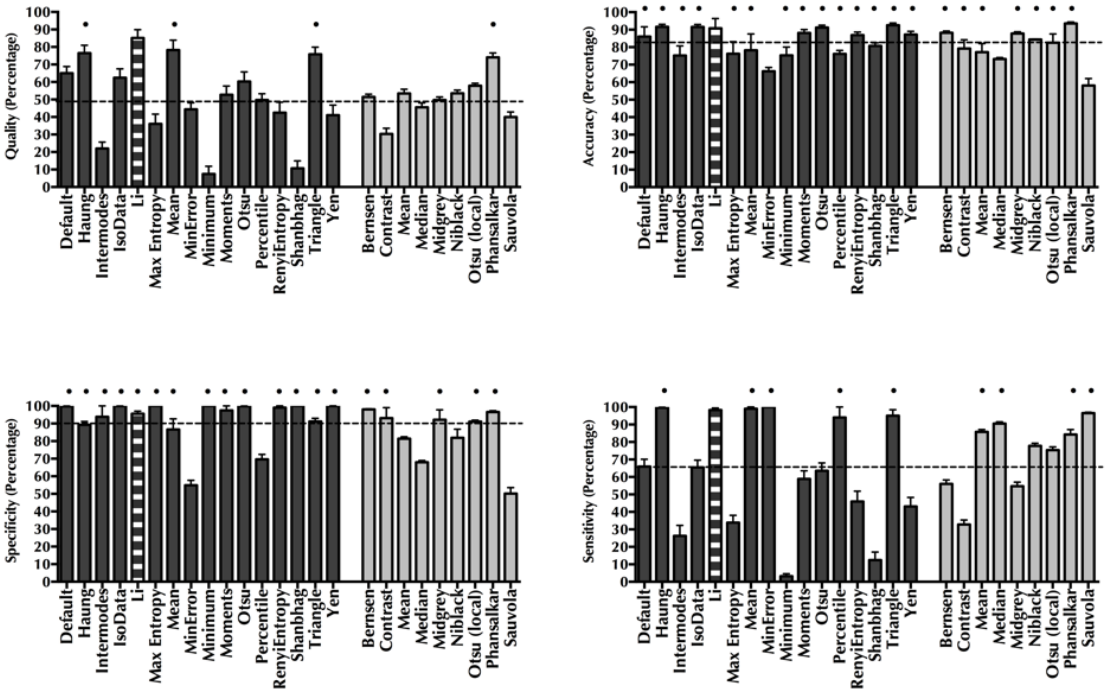

Figure 6.10: Quantitative assessment of threshold performance using relative quality, specificity, accuracy and sensitivity parameters. Dashed line represents average performance of all thresholds collectively. The *Li* algorithm, i.e. the white and black striped bar, performs the best across the 4 evaluation metrics. Statistical evaluation using a one-way ANOVA with a Dunnett's multiple comparison post test against *Li* indicates that this threshold does not perform significantly better than 4 in built FIJI threshold algorithms (i.e. *Huang, Mean, Triangle* and *Phansalkar*; denoted by black dot) in the 4 metrics, whereas it is significantly better than the other 20 options. Dark grey bars represent FIJI AutoThreshold Global methods and light grey columns the Auto Local Thresholds. Values represent average and standard error of the mean (SEM) from n=16 images. Significance at $P < 0.05$.

6.5 Discussion

Modern imaging and culturing techniques in neuroscience research have allowed unprecedented appreciation of the structure, function and importance of glial cells in the CNS and spawned a plethora of software tools for automatic and semi-automatic image analysis (Cho et al. 2007; Gähwiler et al. 1997; Humpel 2015a; Eliceiri et al. 2012; Faure et al. 1AD; WIESMANN et al. 2014; Schindelin et al. 2015). Despite these considerable advances, an agreed standard for digital image analysis of glial morphology and cell number has not been described. Consequently, the aim of this study was to develop, optimise and validate image analysis paradigms (using pre-existing and popular plugins and tools) in order to facilitate automated characterisation of glia within these *ex vivo* slice cultures.

The image analysis workflow includes several image-processing tasks (Eliceiri et al. 2012). This begins with immuno-labelling and image acquisition and ends with object recognition and quantitative measurements of aspects of the objects of interest e.g. spatial location, size, compartment morphology, and length and branching pattern of cell processes. There are clear, explicit standards in place for staining and imaging steps, e.g. identical antibody incubations and acquisition parameters, so we have focused our efforts on the downstream imaging handling processes of z-stack micrographs taken from *ex vivo* slice cultures once they have been acquired.

Intensity projection, which is a popular choice for 3D data visualisation, theoretically provides more information than a single section viewed alone and thereby allows a better understanding of the data, especially when viewing and comparing large datasets. It can offer a concise and accurate way to present data for publication. Despite these advantages, projection inherently alters the original ground truth data of a fluorescent z-stack micrograph because it collapses 3D as 2D. In doing so, it might not necessarily generate an accurate or sensitive visualization, depending on the nature of raw data and projection algorithm applied.

Here, we report that the maximum intensity projection gives the clearest rendering of a z-stack micrograph of immunolabelled glial cells in *ex vivo* slice cultures out of the 6 projections visualized. Despite considerable morphological differences and cellular distribution and densities between the glial markers, we report the maximum intensity projection consistently generated superior projections, particularly compared with minimum algorithm that was consistently poor, while the other algorithms varied. useful. The problematic features that might be generated from this type of projection, i.e.

maximizing noise, speckling the background or over-saturating the image, did not unduly effect our images. Consequently, these maximum intensity projections were considered acceptable representations of z-stacks and were then used for subsequent analysis steps, with the most important of these being that of segmentation.

The fundamental goal of image segmentation is to partition the input image in order to detect objects for further analysis or visualisation. It produces a binary image in which each pixel is assigned one of two values to indicate whether it is part of the background or object. Although this binary output is more meaningful and simple to analyse than the input fluorescence micrograph, inappropriate segmentation can inadvertently (or intentionally) affect the outcome of the analysis. As already mentioned in section 6.1, this is exemplified in a recent report by Johnson and Walker (2015) that showed how two reasonable segmentation approaches to demarcate microglia in the rat brain resulted in opposing scientific conclusions being drawn regarding the experimental intervention.

In line with their work, we have demonstrated here how using a single numerical user-chosen threshold results in compromised representation of the original immnolabelling if this same threshold is applied to several similar images. For relatively simple cellular morphologies, such as those of oligodendrocyte-lineage cell nuclei, this is not a considerable problem, but is unacceptable for astrocytes and microglia because the threshold either omits too much relevant information or includes noise and artefact. Images vary too much for a single manual arbitrary threshold, to be always applicable. This is especially true for the challenging task presented here i.e. delineation of cellular structures in a large of number of complex micrographs. These images of *ex vivo* slice cultures have problematic features such as noise, inter-image variability, ambient illumination, busyness of grey levels and inadequate contrast.

These difficulties however, can be readily circumvented using one of the variety of image segmentation threshold algorithms available in FIJI. These algorithms can account for image variations, enable convenient and quick batch processing, avoid user bias and still offer dozens of flexible options. The problem, therefore, becomes that of which is the optimal algorithm and how that choice can be identified and validated. By applying all 25 algorithms to test images of oligodendrocyte-lineage cells, astrocytes and microglia, it is evident that only a subset of these algorithms produce reasonable binary representations of the input image, and that no one threshold algorithm appears consistently suitable for all glial cells.

It is not always evident, easy or practical to evaluate the quality of segmentation by eye, especially when several of the algorithms result in visually similar outputs. Quantitative evaluation helps discriminate between any subtle superiority in binarisation performance that is not visually evident to the user. Therefore, we have exploited Brocher's colour-coded evaluation method (Brocher 2014), which is the first time, to our knowledge, that this toolkit has been applied to fluorescent micrographs, let alone to analysis of glia in *ex vivo* cultures. We can confirm that this toolkit does offer a relatively user-friendly, easy and quick evaluation of several binarisation methods by providing a qualitative output for visual analysis of colour-coded images and numerical quantification of binarisation performance (relative quality, accuracy, sensitivity and specificity).

After identifying the highest scoring algorithm for each cell type based on an average score of the 4 metrics for 16 images, we statistically assessed the performance of the other 24 algorithms against this comparator algorithm (*Otsu, Percentile* and *Li* for OLIG2, GFAP and IBA1, respectively). We found that a considerable number of the algorithms performed badly, particularly the local algorithms, but that several global algorithms were equally successful as the comparator. The simplest morphology, that of OLIG2-positive nuclei, was equally successfully binarised by 9 of the 25 algorithms tested (8 global and 1 local), whereas the abundant cell body staining of astrocytes by GFAP and intricate IBA1-positive microglial processes were successfully binarised only by 4 algorithms (all global). *Li* and *Huang* algorithms (both entropy-based algorithms) performed as well at the best algorithm for each cell type, suggesting that these two might be the optimal algorithms for segmenting maximum intensity projections of immuolabelled glial cells in *ex vivo* cultures for image analysis despite cellular differences.

Nevertheless, the 25 algorithms applied to each cell type (regardless of morphological complexity), performed markedly below 100% on relative quality parameter. For instance, *Li* and *Huang* both scored approximately 80%. This demonstrates imperfect quality of automated segmentation. This imperfect segmentation was not so evident on the subjective visual level when assessing the colour-coded output, and not much worse than the scores obtained by Brocher on his battery of test images, indicating these scores may be the best scores obtainable given the nature and complexity of the images. Regardless, this uniform and consistent imperfect segmentation method represents an improvement over the very variable

manual thresholding output, and introduces only relative, seemingly consistent, error, and therefore still allows reasonable relative measurements to be detected between groups.

With this in mind, a cohort of images was used to compare how the different threshold segmentation methods might influence the quantification of the total area of GFAP positivity, a measure of astrocyte reactivity and/or number, in iron-loaded compared with control slice cultures. Despite modest absolute differences in the precise areas calculated, most algorithms reproduced the experimental finding that there was no effect of iron-loading on astrocytes despite subpar segmentation used in the analysis. Notably, the Otsu algorithm, produced flawed binary outputs because a significance different was found between groups. Such findings demonstrate the need to validate that appropriate segmentation has taken place in order to ensure that genuinely valid results are obtained. However, it also provides evidence that non-optimal analysis does not always introduce spurious results.

This type of automated cell count, in a *maximum intensity* projection employed here, is based on well-established and robust image protocols that are widely used in the literature. It must be noted that such an approach, although well suited to detecting relative differences between groups, does not necessarily lend itself to all counting paradigms in that in can produce an inflated representation of the total number of cells present. Therefore, we have confirmed the validity of this counting paradigm by double-counting a cohort of images using an alternative design-based stereological enumeration method (Mayhew 1992; Howard & Reed 2004; Schmitz & Hof 2005). Indeed, we did find a considerable 5-fold difference in the total number of cells counted, but this was consistent across each image that was counted. Moreover, the relative loss of OLIG2 positive cells in iron-loaded compared with control *ex vivo* slice cultures was the same. This suggests this methodology is a suitable approach for measuring relative differences between treatment groups, but cannot provide reliable information about precise numbers.

Indeed, this 14% loss in OLIG2-positive cells in this cohort of images using the maximum intensity projection counting methodology is in excellent agreement with the 15% loss that had been detected using this method in the complete image set (chapter 4, section 4.4.7; n=126 images) However, the mean number of OLIG2-positive cells was not as precisely replicated. In the subset if images tested in this chapter, we detected 163±19 and 140±12 in the control and iron-loaded slice cultures respectively; while in the complete image set, we had detected 123±5 and 105±5, respectively, i.e. a mean 32%

increase in the number of OLIG2-positive cells detected. These results, along with the discrepancy with the stereology count, further confirm the validity of using this method for detecting relatively differences but that it is not suitable to detect absolute numbers. If precise and absolute quantification is required, e.g. if the research question is concerned with the number of OLIG2-positive cells in the hippocampus during myelination, stereology (and/or a flow cytometry count) would be the more appropriate strategy. However, for the purposes of this study, which is concerned with relative differences, either approach is acceptable given that both methodologies gave 14 and 11% relative loss in OLIG2-positive cells. Given that stereology methods, particularly the physical dissector method employed, is considerably more time-consuming, the maximum intensity projection count methodology is more feasible and appealing option.

The development of a 3D segmentation strategy would be an improvement over the 2D strategy that we have developed and employed here. However, such an approach was not as feasible with these tools available (i.e. the in-built FIJI threshold algorithms and Bio-Voxxel toolbox were designed for a single image) and presents additional difficulties for automatic segmentation. Nonetheless, our preliminary testing using these tools on confocal z-stacks of *ex vivo* glial was promising and such an approach is likely to emerge as the new and better counting method in the near future once computer processing power and FIJI plugins are improved and optimised for use in this context.

In summary, the specific image analysis workflow employed here, based around segmentation of glial cells in *ex vivo* slice cultures, as performed by automatic threshold functions in FIJI, has a number of specific advantages. The software required for this analysis is all open source, which has obvious cost saving benefits, but also aids in openness and transparency in reporting the outcome of analysis. Any other investigator can inspect, replicate, modify and redistribute the workflow without have little to no knowledge of algorithms or scripting language. Also, unlike stereological approaches, this does not require extensive manual sampling or an assumption of homogeneity in the tissue studied, which, in the case of hippocampus, is erroneous. It also has a better capacity to cope with multidimensional images. Our approach allows for complete and exact repeatability, with a series of precise and defined experimental parameters from the tissue preparation, through imaging and finally data extraction and analysis, including visual outputs for each step that can be scrutinised in addition to the raw original images and the numerical outputs, and thereby represents an excellent strategy for quantifying glial cells within the complex *ex vivo* environment.

6.6 Conclusion

There is a critical need to provide (and often a paucity of) sufficient details of image segmentation and thresholding parameters in quantitative image analysis of *ex vivo* slice cultures to allow independent repeatability and appraisal. To address this situation, we have developed, optimised and evaluated an image analysis workflow for handling and quantifying z-stack micrographs of glial immunohistochemistry taken from *ex vivo* slice cultures using the pre-existing tools i.e. the BioVoxxel plugin available in FIJI, which is an open and user-friendly software platform. The 25 threshold plugins available within FIJI were used to quantify the suitability of several segmentation strategies. Broadly speaking, there is no one strategy that is always applicable and each new immunofluorescent label must be evaluated in this respect. However, *Li* and *Huang* algorithms may be considered as first-line segmentation algorithms in analysis of glial cells stained with standard cell-specific antibodies. We can also conclude that, assuming a reasonable visual output, a quality score over 80%, is a likely to be acceptable for downstream analysis.

7 Discussion

7.1 Discussion

Iron is the most abundant transition metal in the CNS and indispensable for normal function. It exists in two redox-active forms: ferrous (Fe2+) and ferric (Fe3+), which grants iron with the aptitude and responsibility for numerous metabolic process and enzymatic systems (Núñez et al. 2012; Crichton et al. 2011; Rouault 2013). Indeed, iron acts as a co-factor or catalyst for functions including oxygen transport, energy metabolism, DNA synthesis and repair, myelin production and neurotransmitter synthesis. The dark side is that the redox-active nature of iron means that iron is potentially quite treacherous, especially in the brain. The high oxygen consumption of the brain and its high polyunsaturated fat content in the form of myelin and make it sensitive to damage caused by reactive oxygen species generated from rogue iron in the Fenton reaction. Therefore, iron metabolism requires a tightly controlled regulatory system to minimize potential deleterious effects without compromising the availability of iron. Consequently, neurons astrocytes, microglia and oligodendrocytes are all equipped with different sets of iron-related molecules to manage their needs and safety (R. Ward et al. 2014; Crichton et al. 2011; Rouault 2013). Nonetheless, aberrant iron has been proposed as important and common factor contributing to the neuropathology of multiple sclerosis, Alzheimer's disease and Parkinson's disease and other neurodegenerative disorders (Stephenson et al. 2014; Oshiro et al. 2011; Jiang et al. 2016).

Although brain iron research dates back to the late nineteenth century when Zaleski (1886) first made a quantitative analysis of iron content in human brain, research efforts did not truly take off until nearly a hundred years later following seminal work by Hallgren quantifying regional iron content that lay foundations for subsequent researchers who began to link iron deposition with neurodegenerative disease (Koeppen 1995; Hallgren & Sourander 1958). Due to the lack of sensitivity of the methods available and the complexity of the topic, there were considerable discrepancies and disputes in the published reports, in particular (Walton and Kaufman (1984) and Adams (1988) that followed Craelius' (1980) original observations of positive iron staining adjacent to demyelinated plaques and near lesions in multiple sclerosis brains. In the recent two decades, more sensitive histochemical staining methods have been developed and utilized, and methods such as MRI, are being increasing used and optimized for the detection of iron. Nevertheless, we are still far from understanding the putative role of iron in the progression of multiple sclerosis or in the disease phenotype of many other neurodegenerative disorders.

Designing an appropriate model system best suited to studying the pathological effect of iron is likely to be critical for generating further insights into the role of iron in neurodegenerative disorders. Indeed, a number of studies have exploited *in vitro* and *in vivo* models in conjunction with, or as an alternative, to investigation of the human brain. However, this reductionist approach for studying iron, although useful, is also inherently limited in attempting to replicate the complexity of the iron homeostasis system or disease. Hence, caution is necessary when extrapolating *in vitro* data to physiological scenarios. Organotypic brain slice cultures are robust and reliable *ex vivo* models that share the advantages of both *in vitro* and *in vivo* platforms. They match the accessibility, convenience and control of *in vitro* models without overtly compromising the complexity of the brain milieu (Cho et al. 2007; Gähwiler et al. 1997; Humpel 2015a). Similarly, the use of *ex vivo* models avoids the necessity of lengthy and expensive surgeries required to model neuropathology *in vivo*. Such advantages have been increasingly appreciated by the research community and have spawned a plethora of disease-relevant slice models that simulate features of neurodegenerative disease, such as demyelination in multiple sclerosis (Birgbauer et al. 2004), amyloid deposition in Alzheimer's disease (Humpel 2015b) and degeneration of dopaminergic neurons in Parkinson's disease (Stahl et al. 2009). However, to date, these *ex vivo* cultures have not been appreciated as a platform to study iron handling in the CNS. Only Li et al. (2003) have exploited the use of this platform for loading iron and their study focused only on iron in oxidative stress and did not attempt to model or measure iron deposition or changes in iron molecules. Consequently, the overarching aim of my PhD project was to establish, validate and optimise a novel model of iron loading using *ex vivo* methodology to mimic the facets of iron deposition and aberrant distribution that can occur in aging and neurodegenerative disease.

The first goal was to define iron and the iron homeostasis system operating in slice cultures (chapter 3). After confirming that basal iron content in *ex vivo* slice cultures was in line with the physiological iron content that has been reported from monocultures of CNS cells, we next demonstrated that the iron content *ex vivo* slice cultures was equivalent to the iron content of age-matched tissue but that there were differences in the transcript expression of several iron related molecules. To put these perturbations into context, we assessed the levels of transcripts encoding the 11 iron homeostasis proteins in postnatal hippocampus and cerebellum. This represents a novel and comprehensive characterization and a considerable contribution to brain iron research as most work has only considered these molecules in adult tissue or has studied

one or two molecules at only one postnatal age and compared results with adult tissue (Connor et al. 1990; S. M. Wang et al. 2009; Connor et al. 1992; Piñero et al. 2000; Cheepsunthorn et al. 1998; Connor & Menzies 1995; Siddappa et al. 2002; Wu et al. 2004; Kaur & Ling 1995; Burdo et al. 2001; Chang et al. 2005). Generally, we did not find a consistent pattern of expression of the importer, exporter or storage proteins in either region, nor did the transcript profiles match each other. The latter is not wholly unexpected given that these are quite distinctive structures. However, it does provide evidence that the region and tissue age to be used for *ex vivo* studies is not solely an arbitrary and/or technical choice (e.g. viability, consistency and yield can vary considerably), but that it must be considered with respect to iron homeostasis. Specifically, the region must be reasonably reflective of the global iron homeostasis system and not skewed by specific regional idiosyncrasies; for instance, the midbrain structures like the substantia nigra and globus pallidus have iron levels are on a par with the liver while medulla oblongata has low iron content (Hallgren & Sourander 1958). Although we found regional differences in iron content throughout the P10 brain, the expression of iron homeostasis molecules was quite homogeneous, which is quite different from the pattern of expression described in adult brain. Presumably, the regional differences that have been described for several of these molecules in the adult must emerge at an older age.

Collectively, these experiments led us to generate slice cultures from P10-11 hippocampus for 10 days, which is a relatively stereotypical set-up for *ex vivo* experiments. Our iron-related justification was as follows: 1) P10 hippocampus has a moderate iron content; 2) there is heterogeneous expression of iron homeostasis proteins compared with other regions; 3) there are minimal differences in the transcript of iron homeostasis proteins between adult and P21 hippocampal tissue (i.e. temporal equivalent of P10/11 ex vivo tissue cultured for 10 days); 4) the hippocampus is relevant to several neurodegenerative diseases, notably multiple sclerosis and Alzheimer's disease and 5) the hippocampus is a popular region to study iron allowing ready comparison with the literature. Nonetheless, we acknowledge that there are differences in the expression of iron homeostasis molecules present in *ex vivo* hippocampal tissue compared with the P21 aged-equivalent tissue but speculate that this alteration isn't a consequence of immature or delayed development because the expression levels are necessarily in line with those detected in P10 hippocampus. Rather, it is that most likely due to documented astrocyte proliferation from the culture preparation skewing cellular composition and over- or underrepresenting cell-specific iron homeostasis proteins. It

may be that the mechanical transection of fibres obtained during slice preparation has induced sustained hippocampal injury in the slice cultures, and this might account for the changes in the expression of the iron homeostasis detected compared with age matched tissue. Thus, this model does not perfectly reflect the iron homeostasis system in the mature hippocampus. However, it does offer a reasonable version of this system given that all the elements of the iron homeostasis machinery are present at mostly appropriate levels, and therefore our model represents a considerable improvement over current *in vitro* primary monoculture alternatives, but it not necessarily a model of homeostatic iron handling even prior to iron-loading.

Next, having characterized and validated the iron homeostasis system in *ex vivo* cultures compared with postnatal and adult tissue, we were tasked with identifying suitable iron loading paradigms (chapter 4). In the literature, a multitude of different iron reagents have been added to *in vitro* systems with their concentrations and exposure periods varying dramatically between studies. To this end, 10 μM of 3 different iron reagents was used as a starting point to define the optimal iron loading conditions. Although this 10 μM concentration is relatively low compared with that previously reported in the literature (see Chapter 1 tables 1.3-1.8), 10 μM still vastly exceeds the normal physiological iron content that has been detected in the CSF (Bradbury 1997; Núñez et al. 2012; Gaasch et al. 2007) by a magnitude of 10- to 100-fold and could be representative of iron levels that CNS cells might experience in neurodegenerative disease. A series of optimisation experiments led us to 1 μM ferrocene for 12 h in serum-free medium as our preferential iron-loading condition because it produced the maximal fold-increase in iron content matched with mild toxicity.

The degree of iron accumulation in our iron-loaded organotypic cultures is comparable with the increase in iron concentration detected in the post-mortem brain of people suffering from neurodegenerative disease. For example, iron content is elevated by approximately 1.5-fold in the AD hippocampus, 1.6-fold in MS grey matter structures and periplaque white matter, and 1.6-fold in PD substania nigral tissue, when compared with control brain (Hametner et al. 2013; Ayton et al. 2013; Ge et al. 2007). Also, a similar increase in the iron levels in subcortical white matter of healthy people with aging has been reported (Hametner et al. 2013).

The maximal *ex vivo* iron accumulation achieved following iron loading, although on a par with previous reports of iron-loaded monocultures, is nonetheless more modest. Different studies using primary astrocytes and microglia exposed to 10-33 μM FC or FAS for treatment periods ranging from 8-24 h reported a 2-fold increase (Hoepken et al.

2004; Rathore et al. 2012; Riemer et al. 2004). Similarly, 20 μM TMPH-ferrocene 24 h exposure lead to a 1.2-fold increase in oligodendrocyte precursor cells (OPCs) (Zhang et al. 2005). However, Bishop et al. demonstrated much higher 57- 35- and 19-fold increases in microglia, astrocytes and neurons, respectively, after 24 h incubation with 33 μM FAC (Bishop et al. 2011). While these large increases in iron content are impressive, the magnitude of iron accumulation in our model more closely matches that seen in human brain disorders. We propose that our *ex vivo* platform, by virtue of being a better mimicry of the mature iron homeostasis system in the CNS than cell culture models, is inherently better equipped to model the regulation and restoration of iron homeostasis and attempts to limit abnormal iron accumulation.

Although, by design, monocultures in themselves are limited in their capacity to model iron loading, we note that the execution of several studies in monocultures are further limited by an unelaborate experimental design. The researchers (Bishop et al. 2011; Bishop et al. 2010; Riemer et al. 2004; Hohnholt et al. 2010; Tulpule et al. 2010; Kress et al. 2002) typically have measured only iron content and toxicity, did not address the expression of iron homeostasis proteins, nor did they attempt to detangle the molecular mechanisms underlying such iron accumulation. Thus, the conclusions and relevance of these studies to iron in neurodegenerative disease, and the very basic characterisation of normal iron homeostasis in these oversimplified model systems, are relatively superficial. Therefore, we sought to extend on the body of work in monocultures, by focusing attention in our *ex vivo* slice culture model not on total iron accumulation and toxicity alone but localised iron accumulation to oligodendrocyte-lineage cells and microglia within the slice culture and examined the transcript expression of iron homeostasis molecules mediating cellular uptake, efflux and storage. In general, there was an upward trend towards increased mRNA levels. However, these modest increases, while interesting, did not reach statistical significance. Although differential cellular regulation might account for our inability to detect statistical significance with this qPCR analysis, it must also be noted that there was considerable variability in these results that this may also contribute towards detecting potential false negatives. The source of this variability is unclear.

The technical replicates in the qPCR plate were precise and accurate. Similarly, the housekeeping gene, beta-actin, was consistent between all samples (i.e. the technical replicates and the sample replicates from an experiment and was consistent between different experiments). Biological variability may be more likely cause of this variability although this had not previously been problematic in other measurements, i.e. viability

and biochemical assays or immunohistochemical analysis. For all studies, prior to experimental treatment, the wells were inspected the data before the experiment and discarded if the slice quality was considered visually unacceptable e.g. holes, hypoxia, touching slices together or against walls. Only acceptable and consistent slices were included in the experimental and assigned to different treatment groups, which was typically sufficient in the other scenarios to generate adequate data. Increasing the number of biological replicates to 5 independent experiments (from the original 3 experiments) did not improve the variability in this data. Although this variability continued to be problematic in later qPCR analyses (chapter 5), it was not especially critical in the earlier qPCR work on the *in vivo* postnatal tissue (chapter 3). The differences between these hippocampal samples is that *ex vivo* slice cultures only represent a small region of hippocampus, while the *in vivo* work sampled a complete hippocampus. Also, the cDNA generated from the *ex vivo* work used tissue indiscriminately from both the right and left hippocampi; while the cDNA from the *in vivo* work, only came from one hippocampal – the other had been snap-frozen with the intention of generating complementary protein analyses to accompany the RNA work. These factors together may have contributed towards the variability that is evident here. Pooling 3 slice cultures per insert, 2 inserts per sample and 3 samples per treatment group was expected to account for such anatomical variability, but evidently may not been adequate for qPCR analysis. The source of this variability should be addressed in future work – the variability in the expression of iron handling molecules in *ex vivo slice* cultures that were specifically identified selected from left/right dorsal/ventral hippocampus should be compared to clarify the source of variability. Ideally, such findings would be confirmed and extended to the protein level with western blot and immunohistochemistry. This data would more robust and reliable given that changes at the gene level are frequently not reflected at the protein level and vice versa.

Consequently, the modest increases detected here may be quite interesting but did not yield significant differences. Nevertheless, of particular interest, were ferritin, DMT1, FPN and hepcidin. Although we were unable to optimize hepcidin staining, a flaw in our work given our subsequent study investigating the UPR, we have shown interesting cellular differences at the protein level for DMT1 and FPN. The expression pattern of these molecules in microglia is indicative of increased uptake and storage and reduced export. This is consistent with the reported protective role of microglia and in line with the iron accumulation being localized mostly in microglia and macrophages in

multiple sclerosis brain and its primary animal model EAE (Stephenson et al. 2014; Zarruk et al. 2015; Hametner et al. 2013; Schuh et al. 2014).

Given the evidence that increased iron in macrophages and microglia can polarize them to a pro-inflammatory phenotype (Sindrilaru et al. 2011; Mehta et al. 2013; Kroner et al. 2015) and also reports of iron accumulation associated with activated and dystrophic microglia in aged brain, as well as from individuals with AD MS of Huntington's disease (Hametner et al. 2013; Streit et al. 2009; Lopes et al. 2008; Simmons et al. 2007), we were motivated to investigate if and how iron loading would affect the morphology and number of these glial cells in our hands and in this model. Our findings were in agreement with these reports. Quantitative analysis of microglia endpoints demonstrated a decreased in branching complexity, suggestive of microglia activation, a change consistent with our initial qualitative observations of activated-like morphology.

Furthermore, we also assessed perturbations in the other glial cells present: the oligodendrocyte-lineage cells and astrocytes. We found a loss in oligodendrocyte-cell number, which is consistent with previously reported reduction in numbers of oligodendrocytes that has been previously reported in active MS lesions in post-mortem human tissue (Hametner et al. 2013). In that particular study, the loss of oligodendrocytes was accompanied by an up-regulation of iron-exporting ferroxidases and extracellular accumulation of iron (so-called iron liberation) followed by uptake of iron into microglia and macrophages. This is of interest since, in our brain slice model, we have observed increased ferritin staining in microglial cells following ferrocene treatment. Astrocytes, meanwhile, showed little iron accumulation and no difference on morphology, as assessed by percentage GFAP area. Our findings support those already described for astrocyte near lesions in EAE (Zarruk et al. 2015). In this situation, the astrocytes do not accumulate iron, but markedly upregulate the expression of FPN and ferroxidases and can apparently safely acquire and recycle iron and remain unaffected.

Undoubtedly, our novel *ex vivo* slice culture model of iron loading, and our extensive characterization of the same, represents an intriguing body of work and an extension to the literature in this field. We have shown that accumulation of iron was accompanied by alterations in transcripts of iron homeostasis protein, increased ferritin in glia, mild toxicity, leading to oligodendrocyte loss, and microglia activation and proliferation while no appreciable effects were seen with astrocytes. Although this study could certainly be improved with further quantitative analysis of several of the iron homeostasis molecules in the glial cells, it serves as a distinct and thorough body of work

and believe that our model will be an invaluable tool for researchers attempting to alleviate suffering caused by iron overload in the human brain.

Following on from this work, in chapter 5, we were finally able to address the research question that inspired and demanded the development of the iron-loaded slice culture platform described, that is, the intersection of iron metabolism with UPR activation in the CNS and whether this interplay is of any particular significance with respect to neurodegeneration (Oliveira et al. 2011). Our data, although preliminary, generally supports the idea that iron loading modulates the UPR profile. We have confirmed and extended existing studies by showing increased levels not only of transcript expression of resident ER chaperones, BiP and CRT, but also a cohort of transcription factors – ATF6, ATF4, XBP1 and CHOP. These increases, however, did not reach statistical significance. This may have been because of the masking effect of the other cells in this global slice mRNA assessment, when only one cell type may be modulated, and warrants stronger evidence at not only a protein level, but also at a cell-specific level. We also provided preliminary data supporting the reciprocal modulation of the UPR on iron metabolism, but were unable to fully develop the work.

Intriguingly, we also found that tunicamycin exposure led to the amelioration of ferrocene-induced iron accumulation, toxicity, oligodendrocyte loss and microglia activation. Such findings are indicative of a UPR protective effect to counter the perturbed cellular iron levels and may prove useful in furthering the understanding of the neurodegenerative processes. Indeed, increased expression of UPR associated proteins and iron mismanagement have been demonstrated to be commonalities in neuropathology such as multiple sclerosis, Alzheimer's disease and Parkinson's disease. To date, however, these processes have not been linked together with each in the context of neurodegeneration. Although such mechanisms are unclear, it may be that the UPR triggers the transcriptional reshaping of iron homeostasis molecules to maintain adequate iron levels. This may be in conjunction with, or as a back-up to, the iron homeostasis system managing its own levels.

This is a potentially fascinating interplay that deserves further, more substantial, investigation. This preliminary work requires further investigation to clarify the protective role of the UPR modulating iron metabolism and characterise the specific mechanism of action of how this effect is achieved. At minimum, it would be necessary to count the number of oligodendrocyte-lineage cells in each experimental condition that express UPR transcription factors and chaperones in three independent experiments as an extension to the qualitative observation that we have reported here. It would also

be useful to investigate whether a different mode of UPR activation, such dithiothreitol or homocysteine exposure, which interfere with disulphide bond formation, induce a similar protective effect. Such an experiment, along with siRNA knockdown of several UPR proteins, would help to clarify and strengthen our idea that the UPR modulates iron metabolism to maintain homeostasis – it may be that this response is just one relating to a stochastic drug interaction between tunicamycin and ferrocene and not a protective response. Furthermore, given our *in silico* data that the iron homeostasis genes all display putative binding sites that are recognised by various transcription factors activated during the UPR, it would also be interesting to extend our original profile of expression of iron homeostasis molecules after iron loading (chapter 4) to include tunicamycin and the co-treatment of tunicamycin and ferrocene at a RNA, protein and cellular level. Such work would represent a marked improvement on the studies described here.

Finally, of relevance throughout the work described in chapters 4 and 5 although under-described until now, was our development and validation of an image analysis workflow for handling and quantifying micrographs of immunolabeleld glial cells. There is a critical need to provide (and often a paucity of) sufficient details of image segmentation and thresholding parameters in quantitative image analysis of *ex vivo* slice cultures to allow independent repeatability and appraisal (Johnson & Walker 2015; Eliceiri et al. 2012; Brocher 2014). Firstly, we report that a single numerical manual user-selected threshold is inadequate to cope with the complexity found in images such as these and fails to produce a consistently acceptable binary output that matches the fluorescent staining. These difficulties however, can be readily circumvented using one of the variety of image segmentation threshold algorithms available in FIJI. These algorithms can account for image variations, enable convenient and quick batch processing, avoid user bias and still offer dozens of flexible options. The problem, therefore, is which is the optimal algorithm and how can this choice can be identified and validated. To this end, we employed Brocher's colour-coded evaluation method (Brocher 2014), which is the first time, to our knowledge, that this toolkit has been applied to fluorescent micrographs, let alone to analysis of glia in *ex vivo* cultures. We can confirm that this toolkit does offer a relatively user-friendly, easy and quick evaluation of several binarisation methods by providing a qualitative output for visual analysis of colour-coded images and numerical quantification of binarisation performance (relative quality, accuracy, sensitivity and specificity). Broadly speaking, we found that there was no one strategy that was always applicable and each new

immunofluorescent label must be evaluated in this respect. However, *Li* and *Huang* algorithms may be considered as first-line segmentation algorithms in analysis of glial cells stained with standard cell-specific antibodies. We can also conclude that, assuming a reasonable visual output, a quality score of over 80%, is a likely to be acceptable for downstream analysis, and this is how ultimately, we selected the thresholds used to segment and measure the morphology and number of glial cells in chapters 4 and 5 and was critical in the quantification of glial cells following iron-loading.

7.2 Concluding remarks

Over the last decades, the molecular components of both iron metabolism and the UPR and have been steadily explained. There is now a clearer, albeit incomplete, understanding and insight into their respective operations both physiologically and in the context of neurodegenerative disease. As part of this collective endeavour, our work has mostly focused on development of a new *ex vivo* model of CNS iron loading. By doing so, we have helped demonstrate, elucidate and consolidate knowledge of glial management of excess iron. Using this model, we have initiated preliminary studies that confirm the intersection of iron metabolism and UPR in the CNS and have paved the way for future research on this topic. The biological relevance of this reciprocal UPR/iron metabolism signaling must be thoroughly characterized, warranting promising and exciting research directions.

7.3 Future perspectives

Undoubtedly, further studies are needed to explore the putative interplay between iron metabolism and the unfolded protein response in the CNS and its functioning in pathological conditions. Our work, which primarily developed an *ex vivo* model of glial iron mismanagement, has certainty paved the way for future research on this topic and has now highlighted several intriguing related research questions that ought to be considered that were beyond the scope of this work.

Of critical interest, is the loss of oligodendrocyte-lineage cells. Which stage of the cellular maturation lineage is affected by iron-loading and by what mechanism do these cells die? Ferroptosis, which is a recently recognised form of cell death that is dependent upon intracellular iron, and shown to be morphologically, biochemically and genetically distinct from other forms of cell death – i.e. apoptosis, necrosis and autophagy – is an

intriguing explanation for the loss that we detected. It would be interesting to undertake a morphological characterization using markers of oligodendrocyte-lineage and cell death to confirm whether it is oligodendrocyte precursor cells, immature oligodendrocytes or mature oligodendrocytes that are lost and which cell death mechanism is involved.

To date, and to the best of our knowledge, ferroptosis has not been well-studied in the context of neurodegeneration, Therefore, basic studies attempting to characterise ferroptosis following its induction and/or inhibition by experimental compounds in *ex vivo* slice cultures would generate simple but critical data. This data would allow specific, well-designed follow-up studies to investigate the role of ferroptosis in iron mismanagement and vice versa, and further link these processes to that of UPR activation. In these studies, it would also be useful to employ an iron chelator to further validate the iron-specific effects of ferrocene-loading, ferroptosis and UPR activation.

Similarly, it would be ideal to re-optimize this *ex vivo* iron-loading model using postnatal mouse hippocampal cultures rather than rat that was used here. This would allow brain tissue from knock-out mice, e.g. of cell-specific UPR associated proteins, to be used in generating slice cultures for iron-loading and/or ferroptosis experiments and allow us to answer several interesting research questions. This approach, along with siRNA and pharmacological manipulation, would provide several lines of persuasive and comprehensive evidence supporting (or rejecting) our hypothesis.

Nonetheless, it must be emphasized that the next critical steps relevant to this work involve repeating the preliminary studies and generating comprehensive and quantitative profiles of UPR associated transcription factors in glial cells following iron-loading and/or activation of the unfolded protein response and elucidating how exactly the UPR is linked to iron metabolism and vice-versa. Such data would allow future studies to be more critically designed and focused. This is essential given that this research is still uncovering the “tip of the iceberg” and below lie numerous possibilities of exciting and innovative research ahead that must be critically considered and identified.

8 References

Adams, C.W., 1988. Perivascular iron deposition and other vascular damage in multiple sclerosis. *Journal of Neurology, Neurosurgery & Psychiatry*, 51(2), pp.260–265.

Aguirre, P. et al., 2005. Iron homeostasis in neuronal cells: a role for IREG1. *BMC Neuroscience*, 6, p.3.

An, L. et al., 2009. Expression and localization of lactotransferrin messenger RNA in the cortex of Alzheimer's disease. *Neuroscience Letters*, 452(3), pp.277–280.

Ayton, S. et al., 2013. Ceruloplasmin dysfunction and therapeutic potential for Parkinson disease. *Annals of Neurology*, 73(4), pp.554–559.

Bagnato, F., Hametner, S. & Welch, E.B., 2013. Magnetic Resonance Imaging. *Magnetic Resonance Imaging*, 31(3), pp.376–384.

Baleriola, J. et al., 2014. Axonally Synthesized ATF4Transmits a Neurodegenerative Signal across Brain Regions. *Cell*, 158(5), pp.1159–1172.

Batista-Nascimento, L. et al., 2012. Iron and Neurodegeneration: From Cellular Homeostasis to Disease. *Oxidative Medicine and Cellular Longevity*, 2012(1), pp.1–8.

Belaidi, A.A. & Bush, A.I., 2016. Iron neurochemistry in Alzheimer"s disease and Parkinson"s disease: targets for therapeutics. *Journal of Neurochemistry*, 139 Suppl 1, pp.179–197.

Birgbauer, E., Rao, T.S. & Webb, M., 2004. Lysolecithin induces demyelination in vitro in a cerebellar slice culture system. *Journal of Neuroscience Research*, 78(2), pp.157–166.

Bishop, G.M. et al., 2011. Accumulation of non-transferrin-bound iron by neurons, astrocytes, and microglia. *Neurotoxicity Research*, 19(3), pp.443–451.

Bishop, G.M. et al., 2010. Synergistic accumulation of iron and zinc by cultured astrocytes. *Journal of Neural Transmission*, 117(7), pp.809–817.

Boll, M.C. et al., 1999. Reduced ferroxidase activity in the cerebrospinal fluid from patients with Parkinson's disease. *Neuroscience Letters*, 265(3), pp.155–158.

Boserup, M.W. et al., 2011. Heterogenous distribution of ferroportin-containing neurons in mouse brain. *BioMetals*, 24(2), pp.357–375.

Bou-Abdallah, F., 2010. Biochimica et Biophysica Acta. *BBA - General Subjects*, 1800(8), pp.719–731.

Braakman, I. & Hebert, D.N., 2013. Protein Folding in the Endoplasmic Reticulum. *Cold Spring Harbor Perspectives in Biology*, 5(5), pp.a013201–a013201.

Bradbury, M.W., 1997. Transport of iron in the blood-brain-cerebrospinal fluid system. *Journal of Neurochemistry*, 69(2), pp.443–454.

Bradford, M.M., 1976. A rapid and sensitive method for the quantitation of microgram quantities of protein utilizing the principle of protein-dye binding. *Analytical Biochemistry*, 72, pp.248–254.

Brand, A. et al., 2008. Docosahexaenoic acid-dependent iron accumulation in

oligodendroglia cells protects from hydrogen peroxide-induced damage. *Journal of Neurochemistry*, 105(4), pp.1325–1335.

Brocher, J., 2014. Qualitative and Quantitative Evaluation of Two New Histogram Limiting Binarization Algorithms. *International Journal of Image Processing (IJIP)*.

Brunner-Döpper, L. et al., 1998. Pitfalls in assessing specificity and affinity of non-transferrin-bound iron uptake. *Analytical Biochemistry*, 261(1), pp.128–130.

Burdo, J.R. et al., 2001. A light and electron microscopic study of divalent metal transporter-1 distribution in the rat hippocampus, after kainate-induced neuronal injury. *Journal of Neuroscience Research*, 177(6), pp.1198–1207.

Cable, E.E. & Isom, H.C., 1999. Metabolism of 3,5,5-trimethylhexanoyl-ferrocene by rat liver: release of iron from 3,5,5-trimethylhexanoyl-ferrocene by a microsomal, phenobarbital-inducible cytochrome P-450. *Drug Metabolism and Disposition*, 27(2), pp.255–260.

Cable, E.E.E., Connor, J.R.J. & Isom, H.C.H., 2007. Accumulation of iron by primary rat hepatocytes in long-term culture: changes in nuclear shape mediated by non-transferrin-bound forms of iron. *The American Journal of Pathology*, 152(3), pp.781–792.

Chakrabarty, A., Danley, M.M. & LeVine, S.M., 2004. Immunohistochemical localization of phosphorylated protein kinase R and phosphorylated eukaryotic initiation factor-2? in the central nervous system of SJL mice with experimental allergic encephalomyelitis. *Journal of Neuroscience Research*, 76(6), pp.822–833.

Chang, Y.Z. et al., 2005. Effects of development and iron status on ceruloplasmin expression in rat brain. *Journal of Cellular Physiology*, 204(2), pp.623–631.

Cheepsunthorn, P. et al., 2001. Characterization of a novel brain-derived microglial cell line isolated from neonatal rat brain. *Glia*, 35(1), pp.53–62.

Cheepsunthorn, P., Palmer, C. & Connor, J.R., 1998. Cellular distribution of ferritin subunits in postnatal rat brain. *The Journal of comparative neurology*, 400(1), pp.73–86.

Cho, S., Wood, A. & Bowlby, M.R., 2007. Brain slices as models for neurodegenerative disease and screening platforms to identify novel therapeutics. *Current neuropharmacology*, 5(1), p.19.

Comporti, M., 2002. Introduction-serial review: iron and cellular redox status. *Free Radical Biology and Medicine*, 32(7), pp.565–567.

Connor, J.R. & Benkovic, S.A., 1992. Iron regulation in the brain: Histochemical, biochemical, and molecular considerations. *Annals of Neurology*, 32(S1), pp.S51–S61.

Connor, J.R. & Menzies, S.L., 1990. Altered cellular distribution of iron in the central nervous system of myelin deficient rats. *Neuroscience*, 34(1), pp.265–271.

Connor, J.R. & Menzies, S.L., 1995. Cellular management of iron in the brain. *Journal of the neurological sciences*, 134 Suppl, pp.33–44.

Connor, J.R. et al., 1990. Cellular distribution of transferrin, ferritin, and iron in normal and aged human brains. *Journal of Neuroscience Research*, 27(4), pp.595–611.

Connor, J.R. et al., 1992. Regional distribution of iron and iron-regulatory proteins in the brain in aging and Alzheimer's disease. *Journal of Neuroscience Research*, 31(2), pp.327–335.

Craelius, W., Jacobs, R.M. & Jones, A.O., 1980. Mineral composition of brains of normal and multiple sclerosis victims. *Proceedings of the Society for Experimental Biology and Medicine. Society for Experimental Biology and Medicine (New York, N.Y.)*, 165(2), pp.327–329.

Crichton, R.R., Dexter, D.T. & Ward, R.J., 2011. Brain iron metabolism and its perturbation in neurological diseases. *Journal of Neural Transmission*, 118(3), pp.301–314.

Cunnea, P. et al., 2011. Expression profiles of endoplasmic reticulum stress-related molecules in demyelinating lesions and multiple sclerosis. *Multiple Sclerosis Journal*, 17(7), pp.808–818.

Cwiklinska, H., 2003. Heat shock protein 70 associations with myelin basic protein and proteolipid protein in multiple sclerosis brains. *International Immunology*, 15(2), pp.241–249.

Dang, T.N. et al., 2011. Neurochemistry International. *Neurochemistry International*, 58(7), pp.804–811.

Dang, T.N. et al., 2010. The putative heme transporter HCP1 is expressed in cultured astrocytes and contributes to the uptake of hemin. *Glia*, 58(1), pp.55–65.

Daviaud, N. et al., 2013. Experimental Neurology. *Experimental Neurology*, 248(C), pp.429–440.

de Los Monteros, A.E. et al., 1988. Transferrin: An early marker of oligodendrocytes in culture. *International Journal of Developmental Neuroscience*, 6(2), pp.167–175.

De Simoni, A. & MY Yu, L., 2006. Preparation of organotypic hippocampal slice cultures: interface method. *Nature Protocols*, 1(3), pp.1439–1445.

Dringen, R. et al., 2007. The Pivotal Role of Astrocytes in the Metabolism of Iron in the Brain. *Neurochemical Research*, 32(11), pp.1884–1890.

Du, F. et al., 2011. Hepcidin directly inhibits transferrin receptor 1 expression in astrocytes via a cyclic AMP-protein kinase a pathway. *Glia*, 59(6), pp.936–945.

Du, F. et al., 2014. Hepcidin Suppresses Brain Iron Accumulation by Downregulating Iron Transport Proteins in Iron-Overloaded Rats. *Molecular Neurobiology*.

Du, F. et al., 2009. L-DOPA Neurotoxicity Is Mediated by Up-Regulation of DMT1–IRE Expression U. Mueller, ed. *PLoS ONE*, 4(2), p.e4593.

Duce, J.A. et al., 2010. Iron-Export Ferroxidase Activity of b- Amyloid Precursor Protein Is Inhibited by Zinc in Alzheimer's Disease. *Cell*, 142(6), pp.857–867.

Duran-Aniotz, C., Martínez, G. & Hetz, C., 2014. Memory loss in Alzheimer's disease: are the alterations in the UPR network involved in the cognitive impairment? *Frontiers in aging neuroscience*, 6, pp.8–8.

Eliceiri, K.W. et al., 2012. Biological imaging software tools. *Nature Methods*, 9(7), pp.697–710.

Erikson, K.M. & Aschner, M., 2006. Increased manganese uptake by primary astrocyte cultures with altered iron status is mediated primarily by divalent metal transporter. *Neurotoxicology*, 27(1), pp.125–130.

Faucheux, B.A. et al., 1995. Expression of lactoferrin receptors is increased in the mesencephalon of patients with Parkinson disease. *Proceedings of the National Academy of Sciences of the United States of America*, 92(21), pp.9603–9607.

Faure, E. et al., 1AD. A workflow to process 3Dþtime microscopy images of developing organisms and reconstruct their cell lineage. *Nature Communications*, 7, pp.1–10.

Fhlathartaigh, M.N. et al., 2013. Calreticulin and other components ofendoplasmic reticulum stress in rat and humaninflammatory demyelination. *Acta neuropathologica communications*, 1(1), pp.1–1.

Fillebeen, C. et al., 2001. Lactoferrin is synthesized by activated microglia in the human substantia nigra and its synthesis by the human microglial CHME cell line is upregulated by tumor necrosis factor alpha or 1-methyl-4-phenylpyridinium treatment. *Brain research. Molecular brain research*, 96(1-2), pp.103–113.

Finazzi, D. & Arosio, P., 2014. Biology of ferritin in mammals: an update on iron storage, oxidative damage and neurodegeneration. *Archives of Toxicology*, 88(10), pp.1787–1802.

Fish, W.W., 1988. Rapid colorimetric micromethod for the quantitation of complexed iron in biological samples. *Methods in Enzymology*, 158, pp.357–364.

Friedman, A. et al., 2011. Ferritin as an important player in neurodegeneration. *Parkinsonism and Related Disorders*, 17(6), pp.423–430.

Frohman, E.M., Racke, M.K. & Raine, C.S., 2006. Multiple sclerosis—the plaque and its pathogenesis. *New England Journal of Medicine*, 354(9), pp.942–955.

Gaasch, J.A. et al., 2007. Brain Iron Toxicity: Differential Responses of Astrocytes, Neurons, and Endothelial Cells. *Neurochemical Research*, 32(7), pp.1196–1208.

Gähwiler, B.H. et al., 1997. Organotypic slice cultures: a technique has come of age. *Trends in neurosciences*, 20(10), pp.471–477.

Gähwiler, B.H.B., Thompson, S.M.S. & Muller, D.D., 2001. Preparation and maintenance of organotypic slice cultures of CNS tissue. *Current protocols in neuroscience / editorial board, Jacqueline N. Crawley ... [et al.]*, Chapter 6, pp.Unit–Un11.

Ge, Y. et al., 2007. Quantitative Assessment of Iron Accumulation in the Deep Gray Matter of Multiple Sclerosis by Magnetic Field Correlation Imaging. *American Journal of Neuroradiology*, 28(9), pp.1639–1644.

Gebril, O.H. et al., 2011. Brain Iron Dysregulation and the Risk of Ageing White Matter Lesions. *NeuroMolecular Medicine*, 13(4), pp.289–299.

Gething, M.J., 1997. Protein folding. The difference with prokaryotes. *Nature*, 388(6640), pp.329–331.

Gething, M.J., 1999. Role and regulation of the ER chaperone BiP. *Seminars in cell & developmental biology*, 10(5), pp.465–472.

Gray, C.W. & Patel, A.J., 1993. Induction of beta-amyloid precursor protein isoform mRNAs by bFGF in astrocytes. *Neuroreport*, 4(6), pp.811–814.

Groeger, G., Quiney, C. & Cotter, T.G., 2009. Hydrogen Peroxide as a Cell-Survival Signaling Molecule. *Antioxidants & Redox Signaling*, 11(11), pp.2655–2671.

Haass, C., Hung, A.Y. & Selkoe, D.J., 1991. Processing of beta-amyloid precursor protein in microglia and astrocytes favors an internal localization over constitutive secretion. *The Journal of neuroscience*, 11(12), pp.3783–3793.

Haider, L. et al., 2014. Multiple sclerosis deep grey matter: the relation between demyelination, neurodegeneration, inflammation and iron. *Journal of Neurology, Neurosurgery & Psychiatry*.

Hallgren, B. & Sourander, P., 1958. The effect of age on the non-haemin iron in the human brain. *Journal of Neurochemistry*, 3(1), pp.41–51.

Halliday, M. & Mallucci, G.R., 2015. Review: Modulating the unfolded protein response to prevent neurodegeneration and enhance memory. *Neuropathology and Applied Neurobiology*, 41(4), pp.414–427.

Hametner, S. et al., 2013. Iron and neurodegeneration in the multiple sclerosis brain. *Annals of Neurology*, 74(6), pp.848–861.

Han, J. et al., 2002. H and L ferritin subunit mRNA expression differs in brains of control and iron-deficient rats. *The Journal of nutrition*, 132(9), pp.2769–2774.

Hanzlik, R.P. & Soine, W.H., 1978. Enzymic hydroxylation of ferrocene. *Journal of the American Chemical ….*

Harding, H.P. et al., 2000. Regulated translation initiation controls stress-induced gene expression in mammalian cells. *Molecular cell*, 6(5), pp.1099–1108.

Hare, D., Ayton, S., et al., 2013. A delicate balance: Iron metabolism and diseases of the brain. *Frontiers in aging neuroscience*, 5, p.34.

Hare, D.J., Gerlach, M. & Riederer, P., 2012. Considerations for measuring iron in post-mortem tissue of Parkinson's disease patients. *Journal of Neural Transmission*, 119(12), pp.1515–1521.

Hare, D.J., Grubman, A., et al., 2013. Profiling the iron, copper and zinc content in primary neuron and astrocyte cultures by rapid online quantitative size exclusion chromatography-inductively coupled plasma-mass spectrometry. *Metallomics*, 5(12), p.1656.

Healy, S. et al., 2016. Significant glial alterations inresponse to iron loading in a novelorganotypic hippocampal sliceculture model. *Scientific Reports*, pp.1–12.

Hetz, C. & Mollereau, B., 2014. Disturbance of endoplasmic reticulum proteostasis in neurodegenerative diseases. *Nature Reviews Neuroscience*, 15(4), pp.233–249.

Hoepken, H.H., 2005. *Untersuchungen zum Eisenstoffwechsel neuraler Zellen*. Tubingen.

Hoepken, H.H. et al., 2004. Iron accumulation, iron-mediated toxicity and altered levels of ferritin and transferrin receptor in cultured astrocytes during incubation with ferric ammonium citrate. *Journal of Neurochemistry*, 88(5), pp.1194–1202.

Hohnholt, M., 2011. *Metabolism of iron and iron oxide nanoparticles in glial cells*.

Hohnholt, M., Geppert, M. & Dringen, R., 2010. Effects of Iron Chelators, Iron Salts, and Iron Oxide Nanoparticles on the Proliferation and the Iron Content of Oligodendroglial OLN-93 Cells. *Neurochemical Research*, 35(8), pp.1259–1268.

Hoozemans, J.J.M. et al., 2009. The Unfolded Protein Response Is Activated in Pretangle Neurons in Alzheimer's Disease Hippocampus. *The American Journal of Pathology*, 174(4), pp.1241–1251.

Horvath, R.J. et al., 2008. Differential migration, LPS-induced cytokine, chemokine, and NO expression in immortalized BV-2 and HAPI cell lines and primary microglial cultures. *Journal of Neurochemistry*, 107(2), pp.557–569.

Howard, V. & Reed, M., 2004. *Unbiased Stereology*, Garland Science.

Huang, E. et al., 2006. Upregulation of iron regulatory proteins and divalent metal transporter-1 isoforms in the rat hippocampus after kainate induced neuronal injury. *Experimental Brain Research*, 170(3), pp.376–386.

Huang, E., Ong, W.Y. & Connor, J.R., 2004. Distribution of divalent metal transporter-1 in the monkey basal ganglia. *Neuroscience*, 128(3), pp.487–496.

Hulet, S.W., Menzies, S. & Connor, J.R., 2002. Ferritin Binding in the Developing Mouse Brain Follows a Pattern Similar to Myelination and Is Unaffected by the Jimpy Mutation. *Developmental Neuroscience*, 24(2-3), pp.208–213.

Hulet, S.W., Powers, S. & Connor, J.R., 1999. Distribution of transferrin and ferritin binding in normal and multiple sclerotic human brains. *Journal of the neurological sciences*, 165(1), pp.48–55.

Humpel, C., 2015a. Organotypic brain slice cultures: A review. *Neuroscience*, 305, pp.86–98.

Humpel, C., 2015b. Organotypic vibrosections from whole brain adult Alzheimer mice (overexpressing amyloid-precursor-protein with the Swedish-Dutch-Iowa mutations) as a model to study clearance of beta-amyloid plaques. *Frontiers in aging neuroscience*, 7(98), p.46.

Hwang, I.K. et al., 2004. Ischemia-related change of ceruloplasmin immunoreactivity in neurons and astrocytes in the gerbil hippocampus and dentate gyrus. *Neurochemistry International*, 44(8), pp.601–607.

Jefferies, W.A. et al., 1996. Reactive microglia specifically associated with amyloid plaques in Alzheimer's disease brain tissue express melanotransferrin. *Brain Research*, 712(1), pp.122–126.

Jeong, S.Y., 2006. Age-Related Changes in Iron Homeostasis and Cell Death in the Cerebellum of Ceruloplasmin-Deficient Mice. *Journal of Neuroscience*, 26(38), pp.9810–9819.

Jeong, S.Y., 2003. Glycosylphosphatidylinositol-anchored Ceruloplasmin Is Required for Iron Efflux from Cells in the Central Nervous System. *Journal of Biological Chemistry*, 278(29), pp.27144–27148.

Jeong, S.Y. et al., 2009. Dysregulation of Iron Homeostasis in the CNS Contributes to Disease Progression in a Mouse Model of Amyotrophic Lateral Sclerosis. *Journal of Neuroscience*, 29(3), pp.610–619.

Jiang, H. et al., 2016. Brain Iron Metabolism Dysfunction in Parkinson. *Molecular Neurobiology*, pp.1–24.

Johnson, S.J. & Walker, F.R., 2015. Strategies to improve quantitative assessment of immunohistochemical and immunofluorescent labelling. *Scientific Reports*, pp.1–5.

Kaur, C. & Ling, E.A., 1995. Transient expression of transferrin receptors and localisation of iron in amoeboid microglia in postnatal rats. *Journal of anatomy*, 186 (Pt 1), pp.165–173.

Kawamata, T. et al., 1993. Lactotransferrin immunocytochemistry in Alzheimer and normal human brain. *The American Journal of Pathology*, 142(5), pp.1574–1585.

Keenan, B.M., Robinson, S.R. & Bishop, G.M., 2010. Neurochemistry International. *Neurochemistry International*, 56(6-7), pp.843–849.

Kleizen, B. & Braakman, I., 2004. Protein folding and quality control in the endoplasmic reticulum. *Current Opinion in Cell Biology*, 16(4), pp.343–349.

Klomp, L.W. et al., 1996. Ceruloplasmin gene expression in the murine central nervous system. *The Journal of clinical investigation*, 98(1), pp.207–215.

Koeppen, A.H., 1995. The history of iron in the brain. *Journal of the neurological sciences*, 134 Suppl, pp.1–9.

Kraskiewicz, H. & FitzGerald, U., 2011. Partial XBP1 knockdown does not affect viability of oligodendrocyte precursor cells exposed to new models of hypoxia and ischemia in vitro. *Journal of Neuroscience Research*, 89(5), pp.661–673.

Kress, G.J., Dineley, K.E. & Reynolds, I.J., 2002. The relationship between intracellular free iron and cell injury in cultured neurons, astrocytes, and oligodendrocytes. *Journal of Neuroscience*, 22(14), pp.5848–5855.

Kroner, A. et al., 2015. TNF and Increased Intracellular Iron Alter Macrophage Polarization to a Detrimental M1 Phenotype in the Injured Spinal Cord. *Neuron*, 86(5), p.1317.

Lane, D. & Richardson, D., 2014. The Active Role of Vitamin C in Mammalian Iron

Metabolism: Much More Than Just En- hanced Iron Absorption! *Free Radical Biology and Medicine*, pp.1–78.

Lane, D.J.R. et al., 2010. Two routes of iron accumulation in astrocytes: ascorbate-dependent ferrous iron uptake via the divalent metal transporter (DMT1) plus an independent route for ferric iron. *Biochemical Journal*, 432(1), pp.123–132.

Lassmann, H. & van Horssen, J., 2011. The molecular basis of neurodegeneration in multiple sclerosis. *FEBS Letters*, 585(23), pp.3715–3723.

Lavados, M. et al., 2008. Mild cognitive impairment and Alzheimer patients display different levels of redox-active CSF iron. *Journal of Alzheimer's disease : JAD*, 13(2), pp.225–232.

LeBlanc, A.C. et al., 1991. Differential APP gene expression in rat cerebral cortex, meninges, and primary astroglial, microglial and neuronal cultures. *FEBS Letters*, 292(1-2), pp.171–178.

Leitner, D.F. & Connor, J.R., 2012. Biochimica et Biophysica Acta. *BBA - General Subjects*, 1820(3), pp.393–402.

LeVine, S.M., 1997. Iron deposits in multiple sclerosis and Alzheimer's disease brains. *Brain Research*, 760(1), pp.298–303.

LeVine, S.M. et al., 1999. Ferritin, transferrin and iron concentrations in the cerebrospinal fluid of multiple sclerosis patients. *Brain Research*, 821(2), pp.511–515.

LeVine, S.M., Bilgen, M. & Lynch, S.G., 2013. Iron accumulation in multiple sclerosis: an early pathogenic event. *Expert review of neurotherapeutics*, 13(3), pp.247–250.

LeVine, S.M., Wulser, M.J. & Lynch, S.G., 1998. Iron quantification in cerebrospinal fluid. *Analytical Biochemistry*, 265(1), pp.74–78.

Li, K. & Reichmann, H., 2016. Role of iron in neurodegenerative diseases. *Journal of Neural Transmission*, pp.1–11.

Li, L. et al., 2011. Hepcidin Treatment Modulates the Expression of Divalent Metal Transporter-1, Ceruloplasmin, and Ferroportin-1 in the Rat Cerebral Cortex and Hippocampus. *Biological Trace Element Research*, 143(3), pp.1581–1593.

Li, Y. et al., 2013. Transferrin receptor and ferritin-H are developmentally regulated in oligodendrocyte lineage cells. *Neural regeneration research*, 8(1), pp.6–12.

Lin, W. & Popko, B., 2009. Endoplasmic reticulum stress in disorders of myelinating cells. *Nature Neuroscience*, 12(4), pp.379–385.

Lin, W. et al., 2005. Endoplasmic reticulum stress modulates the response of myelinating oligodendrocytes to the immune cytokine interferon. *The Journal of Cell Biology*, 169(4), pp.603–612.

Lin, W. et al., 2010. Enhanced Integrated Stress Response Promotes Myelinating Oligodendrocyte Survival in Response to Interferon. *The American Journal of Pathology*, 173(5), pp.1508–1517.

Liu, R. et al., 2003. Iron toxicity in organotypic cultures of hippocampal slices: role of reactive oxygen species. *Journal of Neurochemistry*, 85(2), pp.492–502.

Liu, Y. & Connor, J.R., 2012. Iron and ER stress in neurodegenerative disease. *BioMetals*, 25(4), pp.837–845.

Loeffler, D.A. et al., 1996. Increased regional brain concentrations of ceruloplasmin in neurodegenerative disorders. *Brain Research*, 738(2), pp.265–274.

Loke, S.Y. et al., 2013. EXPRESSION AND LOCALIZATION OF DUODENAL CYTOCHROME BIN THE RAT HIPPOCAMPUS AFTER KAINATE-INDUCED EXCITOTOXICITY. *Neuroscience*, 245(C), pp.179–190.

Lopes, K.O., Sparks, D.L. & Streit, W.J., 2008. Microglial dystrophy in the aged and Alzheimer's disease brain is associated with ferritin immunoreactivity. *Glia*, 56(10), pp.1048–1060.

Luther, E.M. et al., 2013. Acta Biomaterialia. *Acta Biomaterialia*, 9(9), pp.8454–8465.

Madinaveitia, 1965. Ferrocenes as haematinics. *British journal of pharmacology and ...*.

Mander, P.K., Jekabsone, A. & Brown, G.C., 2006. Microglia Proliferation Is Regulated by Hydrogen Peroxide from NADPH Oxidase. *The Journal of Immunology*, 176(2), pp.1046–1052.

Marquardt, T., Hebert, D.N. & Helenius, A., 1993. Post-translational folding of influenza hemagglutinin in isolated endoplasmic reticulum-derived microsomes. *Journal of Biological Chemistry*.

Mayhew, T.M., 1992. A review of recent advances in stereology for quantifying neural structure. *Journal of neurocytology*, 21(5), pp.313–328.

McCarthy, R.C. & Kosman, D.J., 2014. Glial Cell Ceruloplasmin and Hepcidin Differentially Regulate Iron Efflux from Brain Microvascular Endothelial Cells P. A. Cobine, ed. *PLoS ONE*, 9(2), p.e89003.

McMahon, J. et al., 2012. Increased expression of ER stress- and hypoxia-associated molecules in grey matter lesions in multiple sclerosis. *Multiple Sclerosis Journal*, 18(10), pp.1437–1447.

McRae, R. et al., 2009. In Situ Imaging of Metals in Cells and Tissues. *Chemical Reviews*, 109(10), pp.4780–4827.

Meguro, R. et al., 2007. Nonheme-iron histochemistry for light and electron microscopy: a historical, theoretical and technical review. *Archives of histology and cytology*, 70(1), pp.1–19.

Mehta, V. et al., 2013. Iron Is a Sensitive Biomarker for Inflammation in Multiple Sclerosis Lesions M. Reindl, ed. *PLoS ONE*, 8(3), p.e57573.

Mercado, G., Valdés, P. & Hetz, C., 2013. An ERcentric view of Parkinson's disease. *Trends in molecular medicine*, 19(3), pp.165–175.

Mháille, A.N. et al., 2008. Increased expression of endoplasmic reticulum stress-related

signaling pathway molecules in multiple sclerosis lesions. *Journal of neuropathology and experimental neurology*, 67(3), pp.200–211.

Mita, S., Schon, E.A. & Herbert, J., 1989. Widespread expression of amyloid beta-protein precursor gene in rat brain. *The American Journal of Pathology*, 134(6), pp.1253–1261.

Mizuguchi, M. et al., 1992. Alzheimer's disease beta-amyloid precursor protein in rat neural cells in culture. *Gerontology*, 38 Suppl 1, pp.15–23.

Molina-Holgado, F. et al., 2007. Metals ions and neurodegeneration. *BioMetals*, 20(3-4), pp.639–654.

Moos, T., 1996. Immunohistochemical localization of intraneuronal transferrin receptor immunoreactivity in the adult mouse central nervous system. *The Journal of comparative neurology*, 375(4), pp.675–692.

Moos, T. et al., 2007. Iron trafficking inside the brain. *Journal of Neurochemistry*, 103(5), pp.1730–1740.

Moos, T., Trinder, D. & Morgan, E.H., 2000. Cellular distribution of ferric iron, ferritin, transferrin and divalent metal transporter 1 (DMT1) in substantia nigra and basal ganglia of normal and beta2-microglobulin deficient mouse brain. *Cellular and molecular biology (Noisy-le-Grand, France)*, 46(3), pp.549–561.

Morath, D.J. & Mayer-Pröschel, M., 2001. Iron Modulates the Differentiation of a Distinct Population of Glial Precursor Cells into Oligodendrocytes. *Developmental Biology*, 237(1), pp.232–243.

Morrison, H.W. & Filosa, J.A., 2013. A quantitative spatiotemporal analysis of microglia morphology during ischemic stroke and reperfusion. *Journal of Neuroinflammation*, 10(1), pp.1–1.

Mosmann, T., 1983. Rapid colorimetric assay for cellular growth and survival: application to proliferation and cytotoxicity assays. *Journal of Immunological Methods*, 65(1-2), pp.55–63.

Muller, M. & Leavitt, B.R., 2014. Iron dysregulation in Huntington's disease. *Journal of Neurochemistry*, 130(3), pp.328–350.

Mycko, M.P. et al., 2004. Microarray gene expression profiling of chronic active and inactive lesions in multiple sclerosis. *Clinical Neurology and Neurosurgery*, 106(3), pp.223–229.

Møllgård, K. et al., 1988. Synthesis and localization of plasma proteins in the developing human brain. Integrity of the fetal blood-brain barrier to endogenous proteins of hepatic origin. *Developmental Biology*, 128(1), pp.207–221.

Naughton, M.C., McMahon, J.M. & FitzGerald, U., 2015. International Journal of Developmental Neuroscience. *International Journal of Developmental Neuroscience*, 47(Part B), pp.347–360.

Nielsen, P. & Heinrich, H.C., 1993. Metabolism of iron from (3,5,5-trimethylhexanoyl)ferrocene in rats. A dietary model for severe iron overload. *Biochemical Pharmacology*, 45(2), pp.385–391.

Nijholt, D.A. et al., 2012. The unfolded protein response is associated with early tau pathology in the hippocampus of tauopathies. *The Journal of Pathology*, 226(5), pp.693–702.

Noraberg, J. et al., 2005. Organotypic hippocampal slice cultures for studies of brain damage, neuroprotection and neurorepair. *Current Drug Targets-CNS & Neurological Disorders*, 4(4), pp.435–452.

Núñez, M.T. et al., 2012. Iron toxicity in neurodegeneration. *BioMetals*, 25(4), pp.761–776.

Oliveira, S.J. et al., 2009. ER Stress-Inducible Factor CHOP Affects the Expression of Hepcidin by Modulating C/EBPalpha Activity M. Polymenis, ed. *PLoS ONE*, 4(8), p.e6618.

Oliveira, S.J., de Sousa, M. & Pinto, J.P., 2011. ER Stress and Iron Homeostasis: A New Frontier for the UPR. *Biochemistry Research International*, 2011(23), pp.1–10.

Olivieri, S. et al., 2011. Ceruloplasmin Oxidation, a Feature of Parkinson's Disease CSF, Inhibits Ferroxidase Activity and Promotes Cellular Iron Retention. *Journal of Neuroscience*, 31(50), pp.18568–18577.

Oshiro, S. et al., 2000. Glial cells contribute more to iron and aluminum accumulation but are more resistant to oxidative stress than neuronal cells. *Biochimica et biophysica acta*, 1502(3), pp.405–414.

Oshiro, S. et al., 2008. Microglia and astroglia prevent oxidative stress-induced neuronal cell death: Implications for aceruloplasminemia. *Biochimica et Biophysica Acta (BBA) - Molecular Basis of Disease*, 1782(2), pp.109–117.

Oshiro, S., Morioka, M.S. & Kikuchi, M., 2011. Dysregulation of Iron Metabolism in Alzheimer"s Disease, Parkinson"s Disease, and Amyotrophic Lateral Sclerosis. *Advances in Pharmacological Sciences*, 2011(1), pp.1–8.

Oyadomari, S. & Mori, M., 2004. Roles of CHOP/GADD153 in endoplasmic reticulum stress. *Cell Death & Differentiation*.

O'Connor, T. et al., 2008. Phosphorylation of the Translation Initiation Factor eIF2a Increases BACE1 Levelsand Promotes Amyloidogenesis. *Neuron*, 60(6), pp.988–1009.

Patel, B.N., 1997. A Novel Glycosylphosphatidylinositol-anchored Form of Ceruloplasmin Is Expressed by Mammalian Astrocytes. *Journal of Biological Chemistry*, 272(32), pp.20185–20190.

Pelizzoni, I. et al., 2012. Expression of divalent metal transporter 1 in primary hippocampal neurons: reconsidering its role in non-transferrin-bound iron influx. *Journal of Neurochemistry*, 120(2), pp.269–278.

Pelizzoni, I. et al., 2011. Iron handling in hippocampal neurons: activity-dependent iron entry and mitochondria-mediated neurotoxicity. *Aging Cell*, 10(1), pp.172–183.

Perry, V.H., Nicoll, J.A.R. & Holmes, C., 2010. Microglia in neurodegenerative disease. *Nature Publishing Group*, 6(4), pp.193–201.

Petrak, J. et al., 2007. Proteomic analysis of hepatic iron overload in mice suggests

dysregulation of urea cycle, impairment of fatty acid oxidation, and changes in the methylation cycle. *AJP: Gastrointestinal and Liver Physiology*, 292(6), pp.G1490–G1498.

Petters, C. et al., 2014. Uptake and Metabolism of Iron Oxide Nanoparticles in Brain Cells. *Neurochemical Research*.

Pike, C.J., Ramezan-Arab, N. & Cotman, C.W., 1997. Beta-amyloid neurotoxicity in vitro: evidence of oxidative stress but not protection by antioxidants. *Journal of Neurochemistry*, 69(4), pp.1601–1611.

Pincus, D. et al., 2010. BiP Binding to the ER-Stress Sensor Ire1 Tunes the Homeostatic Behavior of the Unfolded Protein Response J. W. Kelly, ed. *PLoS Biology*, 8(7), p.e1000415.

Pinkernelle, J. et al., 2012. Magnetic nanoparticles in primary neural cell cultures are mainly taken up by microglia. *BMC Neuroscience*, 13(1), p.32.

Piñero, D.J. et al., 2000. Variations in dietary iron alter brain iron metabolism in developing rats. *The Journal of nutrition*, 130(2), pp.254–263.

Prasanthi, J.R.P. et al., 2011. Silencing GADD153/CHOP Gene Expression Protects against Alzheimer's Disease-Like Pathology Induced by 27-Hydroxycholesterol in Rabbit Hippocampus S. T. Ferreira, ed. *PLoS ONE*, 6(10), p.e26420.

Qian, Z.M. & Shen, X., 2001. Brain iron transport and neurodegeneration. *Trends in molecular medicine*, 7(3), pp.103–108.

Qian, Z.M. et al., 2014. Lipopolysaccharides Upregulate Hepcidin in Neuron via Microglia and the IL-6/STAT3 Signaling Pathway. *Molecular Neurobiology*.

Raha, A.A. et al., 2013. The systemic iron-regulatory proteins hepcidin and ferroportin are reduced in the brain inAlzheimer's disease. 1(1), pp.1–1.

Rathnasamy, G. et al., 2015. Hypoxia-Induced Iron Accumulation in Oligodendrocytes Mediates Apoptosis by Eliciting Endoplasmic Reticulum Stress. *Molecular Neurobiology*.

Rathnasamy, G., Ling, E.-A. & Kaur, C., 2014. Neuropharmacology. *Neuropharmacology*, 77(C), pp.428–440.

Rathnasamy, G., Ling, E.A. & Kaur, C., 2011. Iron and Iron Regulatory Proteins in Amoeboid Microglial Cells Are Linked to Oligodendrocyte Death in Hypoxic Neonatal Rat Periventricular White Matter through Production of Proinflammatory Cytokines and Reactive Oxygen/Nitrogen Species. *Journal of Neuroscience*, 31(49), pp.17982–17995.

Rathore, K.I., Redensek, A. & David, S., 2012. Iron homeostasis in astrocytes and microglia is differentially regulated by TNF-α and TGF-β1. *Glia*, 60(5), pp.738–750.

Rice, M.E., 1999. Use of ascorbate in the preparation and maintenance of brain slices. *Methods (San Diego, Calif.)*, 18(2), pp.144–149.

Riemer, J. et al., 2004. Colorimetric ferrozine-based assay for the quantitation of iron in

cultured cells. *Analytical Biochemistry*, 331(2), pp.370–375.

Robb, S.J. & Connor, J.R., 1998. An in vitro model for analysis of oxidative death in primary mouse astrocytes. *Brain Research*, 788(1-2), pp.125–132.

Rohan de Silva, H.A. et al., 1997. Cell-specific expression of beta-amyloid precursor protein isoform mRNAs and proteins in neurons and astrocytes. *Brain research. Molecular brain research*, 47(1-2), pp.147–156.

Ron, D. & Walter, P., 2007. Signal integration in the endoplasmic reticulum unfolded protein response. *Nature Reviews Molecular Cell Biology*, 8(7), pp.519–529.

Roskams, A.J. & Connor, J.R., 1994. Iron, transferrin, and ferritin in the rat brain during development and aging. *Journal of Neurochemistry*, 63(2), pp.709–716.

Rouault, T.A., 2013. Iron metabolism in the CNS:implications for neurodegenerativediseases. *Nature Reviews Neuroscience*, 14(8), pp.551–564.

Salvador, G.A., 2010. Iron in neuronal function and dysfunction P. I. Oteiza, ed. *BioFactors*, 36(2), pp.103–110.

Santambrogio, P. et al., 2007. Mitochondrial Ferritin Expression in Adult Mouse Tissues. *Journal of Histochemistry & Cytochemistry*, 55(11), pp.1129–1137.

Sawcer, S., Franklin, R.J.M. & Ban, M., 2014. Multiple sclerosis genetics. *The Lancet Neurology*, 13(7), pp.700–709.

Schindelin, J. et al., 2015. The ImageJ ecosystem: An open platform for biomedical image analysis. *Molecular Reproduction and Development*, 82(7-8), pp.518–529.

Schmechel, D.E. et al., 1988. Cellular localization of messenger RNA encoding amyloid-beta-protein in normal tissue and in Alzheimer disease. *Alzheimer disease and associated disorders*, 2(2), pp.96–111.

Schmitz, C. & Hof, P.R., 2005. Design-based stereology in neuroscience. *Neuroscience*, 130(4), pp.813–831.

Schrag, M. et al., 2011. Progress in Neurobiology. *Progress in Neurobiology*, 94(3), pp.296–306.

Schröder, M. & Kaufman, R.J., 2005. THE MAMMALIAN UNFOLDED PROTEIN RESPONSE. *Annual Review of Biochemistry*, 74(1), pp.739–789.

Schuh, C. et al., 2014. Oxidative tissue injury in multiple sclerosis is only partly reflected in experimental disease models. *Acta Neuropathologica*, pp.1–17.

Schulz, K. et al., 2011. Iron Efflux from Oligodendrocytes Is Differentially Regulated in Gray and White Matter. *Journal of Neuroscience*, 31(37), pp.13301–13311.

Sheftel, A.D., Mason, A.B. & Ponka, P., 2012. The long history of iron in the Universe and in health and disease. *Biochimica et Biophysica Acta (BBA) - General Subjects*, 1820(3), pp.161–187.

Shoham, S. & Youdim, M.B.H., 2002. The effects of iron deficiency and iron and zinc

supplementation on rat hippocampus ferritin. *Journal of Neural Transmission*, 109(10), pp.1241–1256.

Siddappa, A.J.M. et al., 2002. Developmental changes in the expression of iron regulatory proteins and iron transport proteins in the perinatal rat brain. *Journal of Neuroscience Research*, 68(6), pp.761–775.

Simmons, D.A. et al., 2007. Ferritin accumulation in dystrophic microglia is an early event in the development of Huntington's disease. *Glia*, 55(10), pp.1074–1084.

Sindrilaru, A. et al., 2011. An unrestrained proinflammatory M1 macrophage population induced by iron impairs wound healing in humans and mice. *The Journal of clinical investigation*, 121(3), pp.985–997.

Skaper, S.D. et al., 2009. Oligodendrocytes are a Novel Source of Amyloid Peptide Generation. *Neurochemical Research*, 34(12), pp.2243–2250.

Snyder, A.M. et al., 2010. Regional and cellular distribution of mitochondrial ferritin in the mouse brain. *Journal of Neuroscience Research*, 88(14), pp.3133–3143.

Song, N. et al., 2007. Divalent metal transporter 1 up-regulation is involved in the 6-hydroxydopamine-induced ferrous iron influx. *Journal of Neuroscience Research*, 85(14), pp.3118–3126.

Song, N. et al., 2010. Free Radical Biology & Medicine. *Free Radical Biology and Medicine*, 48(2), pp.332–341.

Stahl, K., Skare, Ø. & Torp, R., 2009. Organotypic Cultures as a Model of Parkinson´s Disease. A Twist to an Old Model. *The Scientific World JOURNAL*, 9, pp.811–821.

Stephenson, E. et al., 2014. Iron in multiple sclerosis: rolesin neurodegeneration and repair. *Nature Publishing Group*, pp.1–10.

Stepnicka, P., 2008. *Ferrocenes*, John Wiley & Sons.

Streit, W.J. et al., 2009. Dystrophic (senescent) rather than activated microglial cells are associated with tau pathology and likely precede neurodegeneration in Alzheimer's disease. *Acta Neuropathologica*, 118(4), pp.475–485.

Streit, W.J. et al., 2014. Microglial pathology. *Acta neuropathologica communications*, 2(1), p.142.

Sun, C. et al., 2012. Toxicology Letters. *Toxicology Letters*, 212(3), pp.276–281.

Sundstrom, L. et al., 2005. Organotypic cultures as tools for functional screening in the CNS. *Drug discovery today*, 10(14), pp.993–1000.

Takeda, A., Devenyi, A. & Connor, J.R., 1998. Evidence for non-transferrin-mediated uptake and release of iron and manganese in glial cell cultures from hypotransferrinemic mice. *Journal of Neuroscience Research*, 51(4), pp.454–462.

Tenopoulou, M. et al., 2007. Does the calcein-AM method assay the total cellular "labile iron pool" or only a fraction of it? *Biochemical Journal*, 403(2), p.261.

Thornton, B. & Basu, C., 2011. Real-time PCR (qPCR) primer design using free online software. *Biochemistry and Molecular Biology Education*, 39(2), pp.145–154.

Todorich, B. et al., 2009. Oligodendrocytes and myelination: The role of iron. *Glia*, 57(5), pp.467–478.

Todorich, B. et al., 2008. Tim-2 is the receptor for H-ferritin on oligodendrocytes. *Journal of Neurochemistry*, 107(6), pp.1495–1505.

Todorich, B., Zhang, X. & Connor, J.R., 2011. H-ferritin is the major source of iron for oligodendrocytes. *Glia*, 59(6), pp.927–935.

TODORICH, B.M. & Connor, J.R., 2004. Redox metals in Alzheimer's disease. *Annals of the New York Academy of Sciences*, 1012, pp.171–178.

Tu, B.P. & Weissman, J.S., 2004. Oxidative protein folding in eukaryotes mechanisms and consequences. *The Journal of Cell Biology*.

Tulpule, K. et al., 2010. Uptake of ferrous iron by cultured rat astrocytes. *Journal of Neuroscience Research*, 88(3), pp.563–571.

Urrutia, P. et al., 2013. Inflammation alters the expression of DMT1, FPN1 and hepcidin, and it causes iron accumulation in central nervous system cells. *Journal of Neurochemistry*, 126(4), pp.541–549.

Vassault, A., 1974. Lactate dehydrogenase. UV-method with pyruvate and NADH. In H. U. Bergmeyer, ed. *Methods of Enzymatic Analysis*. New York: Academic Press, pp. 574–579.

Vecchi, C. et al., 2009. ER Stress Controls Iron Metabolism Through Induction of Hepcidin. *Science*, 325(5942), pp.877–880.

Walter, P. & Ron, D., 2011. The unfolded protein response: from stress pathway to homeostatic regulation. *Science*, 334(6059), pp.1081–1086.

Walton, J.C. & Kaufmann, J.C., 1984. Iron deposits and multiple sclerosis. *Archives of pathology & laboratory medicine*, 108(9), pp.755–756.

Wang, J. et al., 2013. Pro-inflammatory cytokines modulate iron regulatory protein 1 expression and iron transportation through reactive oxygen/nitrogen species production in ventral mesencephalic neurons. *Biochimica et biophysica acta*, 1832(5), pp.618–625.

Wang, J. et al., 2015. The protective effect of lactoferrin on ventral mesencephalon neurons against MPP. *Scientific Reports*, pp.1–11.

Wang, J., Jiang, H. & Xie, J.-X., 2007. Ferroportin1 and hephaestin are involved in the nigral iron accumulation of 6-OHDA-lesioned rats. *European Journal of Neuroscience*, 25(9), pp.2766–2772.

Wang, L. et al., 2011. Expression and Localization of Mitochondrial Ferritin mRNA in Alzheimer's Disease Cerebral Cortex A. I. Bush, ed. *PLoS ONE*, 6(7), p.e22325.

Wang, M. & Kaufman, R.J., 2016. Protein misfolding in the endoplasmic reticulum as a

conduit to human disease. *Nature*, 529(7586), pp.326–335.

Wang, S.M. et al., 2009. Role of hepcidin in murine brain iron metabolism. *Cellular and Molecular Life Sciences*, 67(1), pp.123–133.

Ward, D.M. & Kaplan, J., 2012. Biochimica et Biophysica Acta. *BBA - Molecular Cell Research*, 1823(9), pp.1426–1433.

Ward, R. et al., 2014. The role of iron in brain ageing and neurodegenerative disorders. *The Lancet Neurology*, 13(10), pp.1045–1060.

Way, S.W. & Popko, B., 2016. ReviewHarnessing the integrated stress response for the treatment of multiple sclerosis. *The Lancet Global Health*, pp.1–10.

WIESMANN, V. et al., 2014. Review of free software tools for image analysis of fluorescence cell micrographs. *Journal of Microscopy*, 257(1), pp.39–53.

Williams, A., 2015. Remyelination in multiple sclerosis: what do we know and where are we going? *Neurodegenerative Disease Management*, 5(1), pp.49–59.

Williams, R. et al., 2011. Iron deposition is independent of cellularinflammation in a cerebral model of multiplesclerosis. *BMC Neuroscience*, 12(1), p.59.

Wong, B.X. et al., 2014. β-Amyloid Precursor Protein Does Not Possess Ferroxidase Activity but Does Stabilize the Cell Surface Ferrous Iron Exporter Ferroportin M. K. Lakshmana, ed. *PLoS ONE*, 9(12), p.e114174.

Wu, L.J.-C. et al., 2004. Expression of the iron transporter ferroportin in synaptic vesicles and the blood–brain barrier. *Brain Research*, 1001(1-2), pp.108–117.

Ye, Z. & Connor, J.R., 2000. Identification of iron responsive genes by screening cDNA libraries from suppression subtractive hybridization with antisense probes from three iron conditions. *Nucleic acids research*, 28(8), pp.1802–1807.

You, K., 2003. Transcriptional regulation of the human transferrin gene by GADD153 in hepatoma cells. *Hepatology*, 38(3), pp.745–755.

Zarruk, J.G. et al., 2015. Neurobiology of Disease. *Neurobiology of Disease*, 81(C), pp.93–107.

Zecca, L. et al., 2004. The role of iron and copper molecules in the neuronal vulnerability of locus coeruleus and substantia nigra during aging. *Proceedings of the National Academy of Sciences of the United States of America*, 101(26), pp.9843–9848.

Zechel, S., Huber-Wittmer, K. & Bohlen und Halbach, von, O., 2006. Distribution of the iron-regulating protein hepcidin in the murine central nervous system. *Journal of Neuroscience Research*, 84(4), pp.790–800.

Zhang et al., 2006. Cellular iron status influences the functional relationship between microglia and oligodendrocytes. *Glia*, 54(8), pp.795–804. Available at: http://onlinelibrary.wiley.com/doi/10.1002/glia.20416/full.

Zhang, H.-Y. et al., 2013. 6-Hydroxydopamine promotes iron traffic in primary cultured astrocytes. *BioMetals*, 26(5), pp.705–714.

Zhang, X. et al., 2005. Cytokine toxicity to oligodendrocyte precursors is mediated by iron. *Glia*, 52(3), pp.199–208.

Zhang, Y. et al., 1993. Basic FGF, NGF, and IGFs protect hippocampal and cortical neurons against iron-induced degeneration. *Journal of Cerebral Blood Flow & Metabolism*, 13(3), pp.378–388.

Zhao, G. et al., 2001. Is Hydrogen Peroxide Produced during Iron(II) Oxidation in Mammalian Apoferritins? †. *Biochemistry*, 40(36), pp.10832–10838.